Investigation of turbulence-surface interaction noise mechanisms and their reduction using porous materials

Zamponi, R.

DOI
10.4233/uuid:d332c7e3-87be-4ed6-aa71-e629ef77e07a

Publication date
2021

Document Version
Final published version

Citation (APA)
Zamponi, R. (2021). *Investigation of turbulence-surface interaction noise mechanisms and their reduction using porous materials*. [Dissertation (TU Delft), Delft University of Technology]. https://doi.org/10.4233/uuid:d332c7e3-87be-4ed6-aa71-e629ef77e07a

Important note
To cite this publication, please use the final published version (if applicable).
Please check the document version above.

INVESTIGATION OF TURBULENCE-SURFACE INTERACTION NOISE MECHANISMS AND THEIR REDUCTION USING POROUS MATERIALS

INVESTIGATION OF TURBULENCE-SURFACE INTERACTION NOISE MECHANISMS AND THEIR REDUCTION USING POROUS MATERIALS

Proefschrift

ter verkrijging van de graad van doctor
aan de Technische Universiteit Delft,
op gezag van de Rector Magnificus Prof.dr.ir. T.H.J.J. van der Hagen,
voorzitter van het College voor Promoties,
in het openbaar te verdedigen
op maandag 26 april 2021 om 12:30 uur

door

Riccardo ZAMPONI

Master of Science in Mechanical Engineering,
Università Politecnica delle Marche, Italië,
geboren te Macerata, Italië.

Dit proefschrift is goedgekeurd door de promotoren.

Samenstelling promotiecommissie bestaat uit:

Rector Magnificus,	voorzitter
Prof.dr. F. Scarano,	Technische Universiteit Delft, promotor
Prof.dr. C. Schram,	von Karman Instituut, Belgie, promotor
Dr. D. Ragni,	Technische Universiteit Delft, promotor

Onafhankelijke leden:

Prof.dr. D. Casalino,	Technische Universiteit Delft
Prof.dr. M. Roger,	Centrale School Lyon, Frankrijk
Prof.dr. M. Azarpeyvand,	Universiteit Bristol, Verenigd Koninkrijk
Dr. L. J. Ayton,	Universiteit Cambridge, Verenigd Koninkrijk
Prof.dr. D. A. von Terzi,	Technische Universiteit Delft, reservelid

Keywords: Aeroacoustics; Turbulence-interaction noise; Porous materials; Beamforming; Rod-airfoil configuration; Rapid distortion theory

Front & Back: Instantaneous spanwise-vorticity field of a turbulent flow interacting with a porous wing profile

von Karman Institute for Fluid Dynamics
Environmental and Applied Fluid Dynamics Department

Waterloosesteenweg 72, 1640 Sint-Genesius-Rode
Phone: +32 359 96 11, https://www.vki.ac.be

D/2021/0238/733, T. Magin, Editor-in-Chief

Published by the von Karman Institute for Fluid Dynamics with permission.

ISBN 978-2-87516-163-5

An electronic version of this dissertation is available at http://repository.tudelft.nl/.

Complex numbers are important
because they remind us
that not everything in this world is real.

CONTENTS

List of Figures

LIST OF TABLES

NOMENCLATURE

LATIN LETTERS

$\boldsymbol{a}$	complex source-amplitude vector (GIBF)
$\boldsymbol{A}$	transfer matrix with radiation patterns (GIBF)
a	cylinder radius (RDT)
$\boldsymbol{a}^\star$	regularized complex source-amplitude vector (GIBF)
A_S	body-surface area (Curle's analogy)
b	airfoil half-chord (Amiet's theory)
c	airfoil chord
c_0	speed of sound
$\boldsymbol{C}$	Equation (D.14), Equation (D.15), Equation (D.18) (RDT)
C_d	zero-lift drag coefficient
c_{dip}	reduction coefficient for dipole radiation efficiency
c_e	phase velocity (JCAL)
C_p	pressure coefficient
c_p	specific heat of the fluid
d	airfoil semi-span (Amiet's theory)
d	cylindrical rod diameter
D_a	microphone-array maximum aperture
$\mathrm{d}\boldsymbol{l}$	fluid element length
E_L	elliptic integral of the second kind
E_w	hot-wire anemometer voltage
$\boldsymbol{F}$	point-force field density
$\boldsymbol{f}$	force field density
f	frequency

$\boldsymbol{F}$	Equation (D.8) (RDT)
f_{BF}	resulting D%S beamformer output
F_L	incomplete elliptic integral of the first kind
f_R	Rayleigh resolution-limit frequency
f_{us}	under-sampling frequency (PIV)
$\boldsymbol{G}$	Equation (6.22) (RDT)
$\boldsymbol{g}$	steering vector
G	time-domain Green's function (linear acoustics)
G_ω	frequency-domain Green's function
H_{12}	transfer function between the microphones
He_l	Helmholtz number
$\boldsymbol{I}$	identity matrix
I_n	modified Bessel function of the first kind
I_r	far-field acoustic intensity
J_n	Bessel function of the first kind
J_p	cost function (GIBF)
K	porous parameter in impedance boundary condition (RDT)
k	acoustic wavenumber
k_0	viscous permeability (JCAL)
k_0'	thermal permeability (JCAL)
K_e	dynamic bulk modulus (JCAL)
K_L	complete elliptic integral of the first kind
K_n	modified Bessel function of the second kind
$K^\star$	normalized static permeability (RDT)
K_θ	porous parameter in impedance boundary condition at the angle of interest (RDT)
$\mathscr{L}$	aeroacoustic transfer function
L	porous-sample length

l	wind-tunnel width
l_{p-n}	distance between microphone array and scanning grid
L_p	absolute sound-pressure level
L_x	streamwise integral length scale of turbulence
$\boldsymbol{M}$	Mach number vector
$\boldsymbol{M}$	velocity distortion tensor (RDT)
$\boldsymbol{M}_{\text{corr}}$	corrected Mach number vector
$\boldsymbol{n}$	outward-pointing normal
N	total number of microphones
n	Fourier series mode
n_{s}	number of samples in the PIV dataset
$\boldsymbol{P}$	fluid stress tensor
P	total number of scanning-grid points
p	hydrodynamic pressure
P_d	acquired dynamic pressure
P_s	acquired static pressure
$\hat{q}$	point-source strength
Q	mass source term
q	general source strength
Q_V	volumetric flow rate (JCAL)
R	anechoic-reflection coefficient
R	auto-correlation function
R	minimum-resolvable source separation
r	radial coordinate
$\bar{r}$	radial coordinate (integration variable) (RDT)
Re_d	rod-based Reynolds number
r_{LE}	leading-edge radius
$\mathbb{S}$	cylinder surface

$\mathbb{S}$	fluid-domain surface enclosing the volume $\mathbb{V}$
s	entropy
s	wind-tunnel span
S_{pp}	far-field acoustic power spectral density
S_S	porous-sample surface
S_s	super-sampling factor (PIV)
St	Strouhal number
$\boldsymbol{T}$	Lighthill's stress tensor
St	Strouhal number
T	acquired temperature
T	anechoic-transmission coefficient
t	airfoil maximum thickness
t	time
T_D	time taken for the flow to be distorted (RDT)
T_L	turbulence timescale (RDT)
T_w	hot-wire temperature
$\boldsymbol{U}$	normalized mean-velocity vector (RDT)
$\boldsymbol{u}$	normalized velocity fluctuations vector (RDT)
$\boldsymbol{u}$	velocity vector
$\boldsymbol{U}$	eigenvector matrix (GIBF)
U	hot-wire anemometer velocity
$\boldsymbol{v}$	eigenmode vector (GIBF)
$\mathbb{V}$	fluid-domain volume where the source term q is non-zero
V	wall-normal velocity
$\boldsymbol{W}$	Equation 4.11 (GIBF)
$\boldsymbol{w}$	normalized steering vector
$\boldsymbol{x}$	position vector (x, y, z)
$\boldsymbol{y}$	position vector (integration variable)

$y^\star$ vertical distance from the airfoil

$\hat{Z}$ normalized impedance

Z_{ce} characteristic impedance (JCAL)

Z_s complex characteristic impedance

GREEK LETTERS

α absorption coefficient (JCAL)

α angle between streamwise and upwash velocity components (HW)

$\boldsymbol{\alpha}$ turbulent streamfunction (RDT)

α_{CL} confidence level for statistical uncertainty

α_∞ tortuosity (JCAL)

β compressibility factor

$\boldsymbol{\beta}$ turbulent-velocity potential (RDT)

$\boldsymbol{\beta_R}$ Reduction factor (GIBF)

χ^2 Chi-square distribution

$\boldsymbol{\delta}$ Kronecker delta

δ Dirac function

Δ_n time delay in the D%S beamformer for the n^{th} microphone

ΔL_p relative sound-pressure level

Δp pressure gradient through the porous sample

Δ_T drift function (RDT)

Δ_T original time separation between image couples (PIV)

Δ_{Ts} resulting time step with super-sampling algorithm (PIV)

Δt_e emission time delay

$\delta\theta$ (small) angular variation

Δx_{i} scanning-grid spatial resolution

Δ_y fluid-particle deviation (RDT)

$\boldsymbol{\epsilon}$ Levi-Civita symbol

ϵ absolute error in the acoustic spectra

$\varepsilon_{\mathrm{CL}}$	Equation (A.3)
$\boldsymbol{\gamma}$	vorticity distortion tensor (RDT)
γ	heat-capacity ratio of the fluid
Γ	cross-spectral matrix
$\boldsymbol{\Gamma}_1; \boldsymbol{\Gamma}_3$	Equation (D.19) (RDT)
$\boldsymbol{K}$	specific wavenumber vector (Amiet's theory)
$\boldsymbol{k}$	wavenumber vector
$\boldsymbol{\kappa}$	normalized wavenumber vector (RDT)
κ	thermal conductivity of the fluid
$\hat{\boldsymbol{\kappa}}$	normalized wavenumber vector scaled with the turbulence scale (RDT)
$\boldsymbol{\lambda}$	eigenvalue vector (GIBF)
Λ	viscous characteristic length (JCAL)
λ	acoustic wavelength
Λ	diagonal eigenvalue matrix (GIBF)
λ_c	convergence factor (RDT)
Λ'	thermal characteristic length (JCAL)
μ	dynamic viscosity of the fluid
μ_{R}	regularization parameter (GIBF)
$\mu_{\mathrm{R,IRLS}}$	regularization parameter within the IRLS algorithm (GIBF)
ν	kinematic viscosity of the fluid
$\boldsymbol{\Omega}^{\star}$	Equation (2.60) (RDT)
$\boldsymbol{\Omega}$	normalized mean-vorticity vector (RDT)
$\boldsymbol{\omega}$	normalized vorticity vector (RDT)
ω	angular frequency
Ω_3	mean spanwise vorticity
Φ	mean-flow velocity potential (RDT)
ϕ	porosity (JCAL)
ϕ	velocity potential (RDT)

$\boldsymbol{\Psi}$	two-dimensional velocity spectrum (RDT)
$\boldsymbol{\psi}$	vortical streamfunction (RDT)
Ψ	mean-flow streamfunction (RDT)
ρ	density of the fluid
ρ_e	complex density (JCAL)
σ	standard deviation
σ	static air-flow resistivity (JCAL)
σ_0	distance between source and observer considering compressibility effects
$\boldsymbol{\tau}$	viscous stress tensor
τ	time (integration variable)
τ	time delay in the auto-correlation function
$\hat{\tau}$	retarded time
τ_{slip}	response time related to the tracer particle (PIV)
$\hat{\boldsymbol{\Theta}}$	one-dimensional velocity spectrum scaled with the turbulence scale (RDT)
$\boldsymbol{\Theta}$	one-dimensional velocity spectrum (RDT)
θ	angular coordinate
θ_F	angle between observer direction and force
$\theta^\star$	singular-point angle (RDT)
ξ	Equation (6.5) (RDT)
ξ	normalized streamwise location

ACRONYMS

BW	beam width
CAA	computational aeroacoustics
CFDBF	conventional frequency-domain beamforming
CSM	cross-spectral matrix
CTTM	Centre de Transferts de Technologie du Mans
D&S	delay-and-sum
DR	diagonal removal

EPN	effective perceived noise
EU	European Union
FOV	field of view
GIBF	generalized inverse beamforming
HW	hot-wire
IRLS	iterative reweighted least squares
JCAL	Johnson-Champoux-Allard-Lafarge
LAUM	Laboratoire d'Acoustique de l'Université du Mans
LE	leading edge
LES	large-eddy simulations
NI	National Instruments
OGV	outlet guide vane
PIV	particle image velocimetry
PSD	power spectral density
PSF	point-spread function
QFF	Quiet Flow Facility
RDT	rapid distortion theory
SADA	small-aperture directional array
SL	main-to-side lobe ratio
SNR	signal-to-noise ratio
TE	trailing edge
TKE	turbulent kinetic energy
TUD	Delft University of Technology
VKI	von Karman Institute for Fluid Dynamics
VS	vortex shedding

SUPERSCRIPTS

*	dimensional value
$^+$	upstream value

$^-$	downstream value
†	referred to the complex conjugate
$'$	referred to the fluctuations around the mean
^{n}	referred to the n^{th} iteration
^{p}	referred to the p^{th} power
$^{(\infty)}$	referred to the upstream conditions (RDT)
$^{(cn)}$	referred to the cosine terms for the n^{th} mode in the Fourier series (RDT)
$^{(d)}$	referred to the vorticity distortion effect (RDT)
$^{(s)}$	referred to the body blocking effect (RDT)
$^{(sn)}$	referred to the sine terms for the n^{th} mode in the Fourier series (RDT)

SUBSCRIPTS

$_0$	referred to the stagnation point
$_\infty$	referred to the upstream conditions
$_{\text{dip}}$	referred to a dipole source
$_{\text{max}}$	referred to the maximum value
$_{\text{mono}}$	referred to a monopole source
$_{\text{n}}$	referred to the n^{th} microphone
$_{\text{p}}$	referred to the p^{th} scanning-grid point
$_{\text{ref}}$	referred to a reference value
$_{\text{rms}}$	referred to the root-mean-square
$_a$	referred to the ambient conditions
$_i$	input value
$_o$	output value
$_p$	referred to the $\mathscr{L}^p$ norm (GIBF)
$_p$	referred to the porous airfoil
$_s$	referred to the solid airfoil
$_s$	referred to the source location
$_{1/3}$	referred to a one-third octave band basis

$_{\mathrm{i}}$ referred to the i^{th} source-amplitude vector (GIBF)

OTHERS

$^{-}$ referred to the mean quantity

$^{\hat{}}$ referred to the double Fourier Transform

$^{\sim}$ referred to a cylindrical coordinate system

SUMMARY

The interaction of an airfoil with incident turbulence is an important source of aerodynamic noise in numerous applications, such as turbofan engines, cooling systems for automotive and construction industries, high-lift devices on aircraft wings, and landing gear systems. In these instances, turbulence is generally produced by elements that are installed upstream of the wing profile and generate inflow distortions. A possible strategy for the reduction of turbulence-interaction noise, also referred to as leading-edge noise, is represented by the integration of porous media in the structure of the airfoil. However, the physical mechanisms involved in this noise mitigation technique remain unclear. The present thesis aims to elucidate these phenomena and, particularly, how porosity affects the incoming turbulence characteristics in the immediate vicinity of the surface. This problem has been addressed from different perspectives, namely from the technological, experimental, and analytical ones.

An innovative design for a porous NACA-0024 profile fitted with melamine foam is proposed. The noise reduction performance achieved with such a porous treatment is evaluated through a novel version of the generalized inverse beamforming (GIBF) implemented with an improved regularization technique. The algorithm is first applied to different experimental benchmark datasets in order to evaluate its ability to reconstruct distributed aeroacoustic sources and to assess its accuracy and variability in different conditions. Results indicate that the implemented method provides an enhanced representation of the distributed noise-source regions and higher performance in terms of accuracy and variability if compared with other common beamforming techniques. GIBF is then employed together with far-field microphone measurements to characterize the leading-edge noise radiated by solid and porous NACA-0024 profiles immersed in the wake of an upstream cylindrical rod at different free-stream velocities. A noise reduction of up to 2 dB is found for frequencies around the vortex-shedding peak, with a trend that is independent of the Reynolds number, whereas significant noise regeneration is observed at higher frequencies, most probably due to surface roughness.

Subsequently, the flow-field alterations due to porosity in the stagnation region of the airfoils are investigated by means of mean-wall pressure, hot-wire anemometry, and particle image velocimetry measurements. The porous treatment mostly preserves the integrity of the NACA-0024 profile's shape but yields a wider opening of the jet flow that increases the drag force. Moreover, porosity allows for damping of the velocity fluctuations near the surface and has limited influence on the upstream mean-flow field. In particular, the upwash component of the root-mean-square of the velocity fluctuations turns out to be significantly attenuated in a porous airfoil in contrast to a solid one, resulting in a strong decrease of the turbulent kinetic energy in the stagnation region. The present effect is more pronounced for higher Reynolds numbers. The mean spanwise vorticity close to the body appears also to be mitigated by the porous treatment. Furthermore, the comparison between the power spectral densities of the incident turbulent

velocities demonstrates that porosity has an effect mainly on the low-frequency range of the turbulent-velocity spectrum, with a spatial extent up to about two leading-edge radii from the stagnation point. In addition, the vortex-shedding frequency peak in the power spectrum of the streamwise velocity fluctuations close to the airfoil surface is found to be suppressed by porosity. The present results show analogies with the outcomes of the aeroacoustic analysis, highlighting the important role played by the attenuated turbulence distortion due to the porous treatment of the airfoil in the corresponding noise reduction.

An analytical model based on the rapid distortion theory (RDT) to predict the turbulent flow around a porous cylinder is formulated with the aim of improving the understanding of the effect of porosity on turbulence distortion and interpreting the experimental results. The porous treatment, characterized by a constant static permeability, is modeled as a varying impedance boundary condition applied to the potential component of the velocity that accounts for Darcy's flow within the body. The RDT implementation is first validated through comparisons with published velocity measurements in the stagnation region of an impermeable cylinder placed downstream of a turbulence grid. Afterwards, the impact of porosity on the velocity field is investigated through the analysis of the one-dimensional velocity spectra at different locations near the body and the velocity variance along the stagnation streamline. The porous surface affects the incoming turbulence distortion near the cylinder by reducing the blocking effect of the body and by altering the vorticity deformation caused by the mean flow. The former leads to an attenuation of the one-dimensional velocity spectrum in the low-frequency range, whereas the latter results in an amplification of the high-frequency components. This trend is found to be strongly dependent on the turbulence scale and influences the evolution of the velocity fluctuations in the stagnation region. The porous RDT model is finally adapted to calculate the turbulence distortion in the vicinity of the porous NACA-0024 profile leading edge. The satisfactory agreement between predictions and experimental results suggests that the present methodology can improve the understanding of the physical mechanisms involved in the airfoil-turbulence interaction noise reduction through porosity and can be instrumental in designing such passive noise-mitigation treatments.

SAMENVATTING

De interactie van een vleugelprofiel met inkomende turbulentie is een belangrijke bron van aerodynamisch geluid in talrijke toepassingen, zoals turbofanmotoren, koelsystemen voor de automobiel en bouwindustrie, welvingskleppen op vliegtuigvleugels, en landingsgestel-systemen. In deze gevallen wordt turbulentie over het algemeen veroorzaakt door elementen die stroomopwaarts van het vleugelprofiel zijn geïnstalleerd en die verstoringen van de instroom veroorzaken. Een mogelijke strategie voor de vermindering van turbulentie-interactieruis, ook wel "leading-edge noise"genoemd, is de integratie van poreuze media in de structuur van het aerodynamische vlak. De fysische mechanismen die een rol spelen bij deze geluidsverminderende techniek zijn echter nog onduidelijk. Deze dissertatie heeft tot doel deze verschijnselen op te helderen en, in het bijzonder, om vast te stellen hoe porositeit de inkomende turbulentiekarakteristieken in de onmiddellijke nabijheid van het oppervlak beïnvloedt. Dit probleem is vanuit verschillende invalshoeken benaderd, namelijk vanuit een technologische, experimentele en analytische invalshoek.

In het proefschrift wordt een innovatief ontwerp voor een poreus NACA-0024 profiel voorzien van melamine schuim gepresenteerd. De geluidsreductie die met een dergelijke poreuze behandeling wordt bereikt, wordt geëvalueerd met behulp van een nieuwe versie van generalized inverse beamforming (GIBF) techniek met daarin een een verbeterde data regularisatie. Het algoritme wordt eerst toegepast op verschillende experimentele referentiedatasets, teneinde zijn vermogen om gedistribueerde aeroakoestische bronnen te reconstrueren te evalueren, en om zijn nauwkeurigheid en variabiliteit in verschillende omstandigheden te beoordelen. De resultaten geven aan dat de geïmplementeerde methode een verbeterde representatie geeft van de gedistribueerde geluidsbrongebieden en hogere prestaties levert in termen van nauwkeurigheid en variabiliteit in vergelijking met gangbare beamforming technieken. GIBF wordt vervolgens gebruikt in combinatie met microfoonmetingen op afstand, om het geluid te karakteriseren dat wordt uitgestraald door de voorrand van zowel impermeabele als poreuze NACA-0024 profielen, geplaatst in het zog van een stroomopwaards cilindrische staaf. De metingen zijn verricht bij verschillende luchtstroomsnelheden. Een geluidsvermindering tot 2 dB wordt waargenomen voor frequenties rond de piek behorende bij de "vortex-shedding". De afname is onafhankelijk is van het Reynoldsgetal. Een belangrijke geluidsbron bij hogere frequenties wordt waargenomen, die hoogstwaarschijnlijk te wijten aan oppervlakteruwheid.

Vervolgens worden de veranderingen in het stromingsveld ten gevolge van porositeit in het stagnatiegebied van de vleugelprofielen onderzocht door middel van wandrukmetingen, warme-draadanemometrie en particle image velocimetry. Bij het gebruik van de poreuze voorrand wordt de vorm van het NACA-0024 profie grotendeels behouden l maar zorgt de wijdere opening van de jetstroming voor een hogere luchtweerstand. Bovendien zorgt de porositeit voor demping van de snelheidsfluctuaties aan het opper-

vlak. De porositeit heeft een beperkte invloed op het gemiddelde stroomopwaartse stromingsveld. Het blijkt dat de opwaartse component van het kwadratisch gemiddelde van de snelheidsfluctuaties aanzienlijk wordt gedempt in een poreus aerodynamisch vlak, in tegenstelling tot een massief en niet-doorlatend vlak. Dit resulteert in een sterke afname van de turbulente kinetische energie in het stagnatiegebied. De afname wordt groter voor hogere Reynoldsgetallen. De gemiddelde vorticiteit over de spanwijdte dicht bij het vleugelprofiel lijkt tevens te worden verminderd door de poreuze voorrand. Verder laat de spectrale analyse van de vermogensdichtheden van de invallende turbulente snelheden zien dat porositeit vooral effect heeft op de lage frequenties. Het verschijnsel wordt waargenomen tot een afstand van twee keer de straal van de voorrang gerekend vanaf het stagnatiepunt. Bovendien blijkt de piek in het vermogensspectrum van de luchtsnelheid vlak boven het oppervlak die hoort bij het loslaten van de wervelingen te worden onderdrukt. De huidige resultaten zijn analoog aan de uitkomsten van de aero-akoestische analyse, waarbij de belangrijke rol van de gedempte turbulentievervorming als gevolg van de poreuze staat van het aerodynamische vlak duidelijk werd.

Een analytisch model gebaseerd op de rapid distortion theory (RDT) om de turbulente stroming rond een poreuze cilinder te voorspellen is ontwikkeld met als doel om het inzicht in het effect van porositeit op turbulentievervorming te verbeteren en de experimentele resultaten beter te kunnen interpreteren. De poreuze buitenlaag, met zijn constante statische permeabiliteit, wordt gemodelleerd als een variërende impedantie randvoorwaarde toegepast op die component van de snelheid die hoort bij de Darcy stroming in het poreuze medium. De RDT implementatie wordt eerst gevalideerd door de resultaten te vergelijken met gepubliceerde snelheidsmetingen in het stagnatiegebied van een ondoorlaatbare cilinder, die stroomafwaarts van een turbulentierooster is geplaatst. Daarna wordt de invloed van porositeit op het snelheidsveld onderzocht door middel van het analyseren van de één-dimensionale snelheidspectra op verschillende plaatsen nabij het vleugelprofiel en van de snelheidsvariatie langs de stagnatiestroomlijn. Het poreuze oppervlak beïnvloedt de inkomende turbulentievervorming nabij de cilinderdoor het blokkerende effect van het object te verminderen en door de vervorming van de wervelingendoor de gemiddelde stroming te veranderen. Het eerste effect leidt tot een verzwakking van het het laagfrequente gebied in het een-dimensionale snelheidspectrum, terwijl het tweede resulteert in een versterking van de hoogfrequente componenten. Deze trend blijkt sterk afhankelijk te zijn van de turbulentieschaal en dit beïnvloedt de evolutie van de snelheidsfluctuaties in het stagnatiegebied. Het poreuze RDT model wordt uiteindelijk aangepast om de turbulentievervorming in de nabijheid van de poreuze NACA-0024 voorkant te berekenen. De redelijke overeenkomst tussen voorspellingen en experimentele resultaten suggereert dat de nieuw ontwikkelde methodologie een beter inzicht geeft in de fysische mechanismen die een rol spelen bij de vermindering van het geluidsnivo als gevolg van de interactie tussen turbulentie en het vleugelprofiel. Dit inzicht kan dan helpen bij het ontwerpen van optimale passieve geluidsverminderende oppervlakken.

PREFACE

The research presented henceforth has been mainly carried out at the von Karman Institute for Fluid Dynamics. It is a result of my own work and, when specifically indicated in the text, of the work conducted in collaboration with others. Parts of the material included in the manuscript have been published or presented at international conferences. This information is provided in the footnotes at the beginning of each chapter. The manuscript has not been submitted to any other university or place of learning for any degree, diploma, or other qualification. I would like to gratefully acknowledge the support of the European Commission's Framework Program "Horizon2020", through the Marie Skłodowska-Curie Innovative Training Networks (ITN) "SmartAnswer - Smart mitigation of flow-induced acoustic radiation and transmission" grant agreement No. 722401.

Riccardo Zamponi
Brussels, April 2021

1

INTRODUCTION

Art and science have their meeting point in method.

Edward G. Bulwer-Lytton

A possible strategy for the reduction of the noise generated by turbulence interacting with a wing profile, also referred to as leading-edge noise, is represented by the integration of a porous medium in the airfoil structure. After a description of the physical mechanisms characterizing the leading-edge noise production, the main studies involving porosity for sound mitigation are reviewed in this chapter. The objectives pursued in the thesis and the provided contributions are finally stated.

Parts of this chapter are included in [1–3].

1

1.1. NOISE REDUCTION CHALLENGE

Aerodynamic noise represents a critical problem involving a large number of sectors including air and ground transportation, building cooling and ventilation systems, and wind-energy production. Noise exposure affects humans causing several health problems, i.e. tinnitus, sleep disruption, cognitive and hearing impairment in children, and cardiovascular disease [4–7]. According to the World Health Organization, more than 1.6 million healthy years of life are lost in western Europe as a consequence of environmental noise [8]. Particularly, the inhabited areas in the vicinity of the airports are among the most affected by this issue, considering also the ever–increasing demand for flights. In 2017, approximately 3.2 million people suffered from aircraft-noise exposure, and 1.4 million encountered sleep-disturbance problems around the 47 major European airports [9].

Hence, numerous international organizations are implementing policies and strategies to tackle this problem. One such example is represented by Regulation (EU) No 598/2014 [10], adopted by the European Union (EU) in 2014 and concerning the introduction of noise-related operating restrictions, which also impact aircraft from non-EU countries. More recently, a report published by the European Commission, Flightpath 2050 [11], outlined the EU's vision for the future of aviation and highlighted the important role of the aeronautic industry in reducing noise pollution. The challenging goal set by this program is to achieve a 65 % reduction in the effective perceived noise (EPN) emissions of flying aircraft by 2050. A step-change in the existing noise-mitigation strategies is therefore required in order to meet these targets.

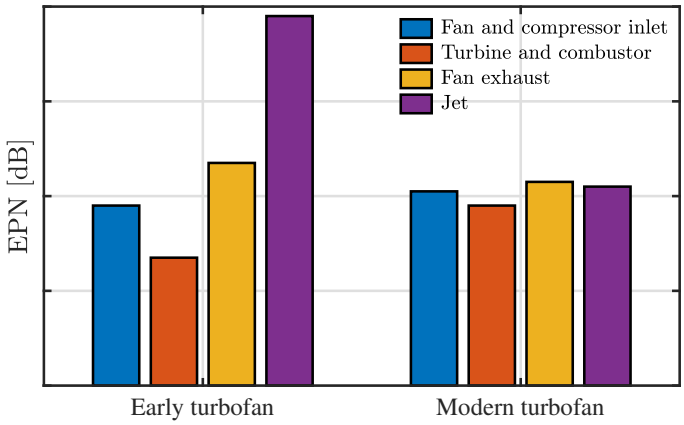

Figure 1.1: Historical changes in the contribution to the effective perceived noise (EPN) level from the different components of a turbofan engine. Taken from [12].

The investigation of the generation and propagation of flow-induced noise, a research field commonly denoted as aeroacoustics, started about 70 years ago with the work of Lighthill [13], triggered by the substantial noise emissions radiated from the aeroengines, which, at that time, were characterized by single-stream high-speed hot jets. In such configurations, the dominant noise source was represented by the jet mixing with the cooler ambient air [12]. Considerable investments have been made during

the following years to improve the aeroengines' design and to mitigate their noise. Modern turbofan engines involve a two-stream architecture with increasing values for the bypass ratio. This makes it possible to significantly reduce the jet noise but it also results in an increase in the relative contribution to the overall noise provided by the fan, as can be observed in Figure 1.1.

Several fan-related noise generation mechanisms can be distinguished for a subsonic flow, with both tonal and broadband components. Tonal noise is produced by periodic interactions mainly linked to the blade-passing frequency and its harmonics. For instance, the rotating blades induce force- and volume-displacement effects on the flow (fan self-noise), whereas the downstream outlet guide vanes (OGVs) (see Figure 1.2) exert a blockage effect on the momentum of the unsteady wake (fan-vane interaction noise) [12]. Broadband noise arises from random fluctuating mechanisms occurring in the engine, such as the scattering of the turbulent boundary layer on the rotor blade at the trailing edge (rotor self-noise), the interaction of the vortices at the blade tip with the boundary layer formed along the inlet duct (rotor casing boundary-layer interaction noise), and the impingement of the turbulent wake of the fan with the OGVs (rotor-stator interaction noise). The latter mechanism is typically the dominant broadband-noise source in a turbofan engine. An extensive review of how the different turbomachinery noise components can be predicted is provided by Moreau [14].

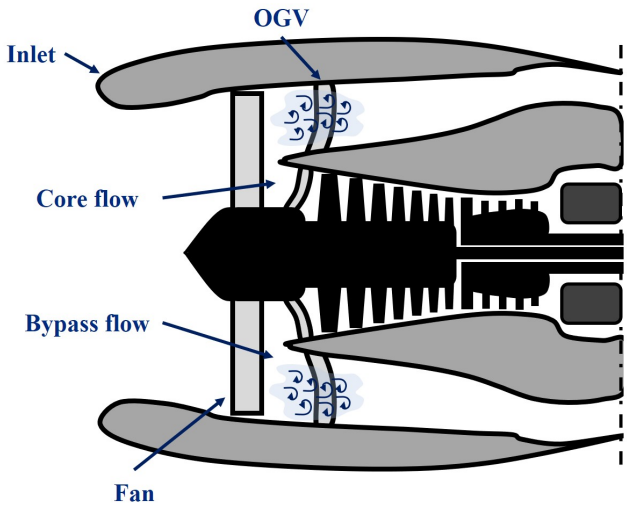

Figure 1.2: Detail of a high-bypass turbofan engine. The air flow supplied by the inlet is compressed by the fan and directed through the outlet guiding vanes (OGVs) into the engine and outer path. Adapted from [15].

1.1.1. AIRFOIL-TURBULENCE INTERACTION NOISE

The noise generated by the impingement of the fan wake on the OGV represents the typical application addressed in this thesis and will be investigated for an isolated wing profile. The so-called airfoil-turbulence interaction noise, denoted also as leading-edge

noise, involves numerous other sectors that have a high societal impact, such as cooling systems for automotive and construction industries [16, 17], high-lift devices on aircraft wings [18, 19], and landing gear systems [20, 21]. In these examples, turbulence is generally produced by elements that are installed upstream of the airfoil and generate inflow distortions.

From a physical perspective, the turbulent eddies interacting with the leading edge are subjected to a rapid deformation that scatters part of their kinetic energy into sound [22]. A fundamental study on the noise emitted by this mechanism was performed by Amiet [23], who proposed a theory to predict the far-field acoustic power spectrum produced by an airfoil immersed in a turbulent flow. In this case, the spanwise correlation length and integral length scale of the upwash velocity fluctuations constitute the key parameters for the prediction of the noise generated by the interaction with the incoming turbulence.

Experimentally, the leading-edge noise generation process has been addressed by several authors. Paterson and Amiet [24] measured the emitted far-field noise and unsteady surface pressure field of a NACA-0012 profile that was installed downstream of a turbulence grid and concluded that the prediction of incident turbulence-interaction noise can be carried out if the inflow properties are sufficiently documented. Olsen and Wagner [25] analyzed the broadband noise generated by the impingement of turbulence on airfoils characterized by different shapes and observed that an increasing thickness corresponded to reduced turbulence-interaction noise. Similar conclusions were drawn by Oerlemans and Migliore [26], who performed wind tunnel tests for six different airfoils at several angles of attack in a grid-generated turbulent flow. Moreau *et al.* [27] investigated the effect of the angle of attack and airfoil shape by studying the noise emitted by three different mock-ups (a flat plate, thin controlled-Diffusion airfoil, and NACA-0012 profile) interacting with a turbulent flow in a grid-airfoil configuration. The results of the experiments confirmed the previously mentioned thickness effect, whereas the impact of the angle of attack and camber was found to be limited. Devenport *et al.* [28] also confirmed the influence of the effects of these parameters by testing three airfoils in a wind tunnel that was equipped with a turbulence grid.

Additional numerical investigations on this influence were also carried out by Gill *et al.* [29] using computational aeroacoustics (CAA). The authors identified the stagnation region as the area where dominant leading-edge noise generation mechanisms occur. This region becomes larger with the increasing thickness of the airfoil, leading to a wider area where the turbulence distortion takes place and consequently to a reduced gradient for the variation of the upwash velocity fluctuations in the stagnation region. This effect is believed to play an important role in the high-frequency noise mitigation experienced by a wing profile due to the thickness effect. A similar approach has been adopted by Kim *et al.* [30], who numerically investigated the inflow noise generated by the interaction of a symmetric airfoil interacting with homogeneous, isotropic turbulence. They observed that the above-mentioned high-frequency noise attenuation reduces with the increasing Mach number as a consequence of the more significant relative contribution of the streamwise turbulent-velocity components.

The effective distortion of the turbulent vortical structures at the leading edge must be taken into account in order to obtain an accurate prediction of the leading-edge noise

when the airfoil exceeds a minimum thickness [27, 31, 32]. In this regard, a useful analytical tool that can be considered for estimating the turbulence distortion around an airfoil with a non-negligible thickness is the rapid distortion theory (RDT), formulated by Hunt [33] and based on the work of Ribner and Tucker [34] and Batchelor and Proudman [35].

In his original work, Hunt [33] performed a wavenumber analysis to calculate the homogeneous turbulent flow around a circular cylinder. Velocity spectra and variances were estimated in the asymptotic cases where the turbulence scale is much smaller or larger than the characteristic size of the body. The RDT predictions were shown in qualitative agreement with the results of Bearman [36], who experimentally investigated the distortion of grid-generated turbulence approaching the stagnation region of a bluff body. Goldstein [37] followed a similar methodology for modeling the turbulent flow around an obstacle of arbitrary shape and extended the theory to account for compressibility effects. Britter *et al.* [38] performed detailed comparisons between RDT asymptotic results and velocity measurements of grid-generated turbulence interacting with a circular cylinder. This type of problem was also addressed by Durbin and Hunt [39], who employed the RDT to calculate the surface pressure fluctuations of a round obstacle for large-scale and small-scale turbulence. Further applications of the theory for velocity and pressure calculations in turbulent flows approaching bluff bodies have been reviewed by Hunt *et al.* [40].

More recently, Ayton and Peake [41] formulated an asymptotic model based on the RDT to investigate the impingement of homogeneous isotropic turbulence on a thin elliptical solid body in a region close to the stagnation point. A method to compute the turbulent pressure spectra for a location near the leading edge of the body and for a location far from it was also proposed in this study. Moreover, Klettner *et al.* [42] studied the interaction of an array of solid circular cylinders characterized by a varying solid fraction with the wake produced by an upstream cylinder using both unsteady viscous simulations and inviscid RDT calculations.

1.1.2. POROUS MATERIALS FOR NOISE MITIGATION

Since acting on the turbulence intensity of the incident flow is typically unfeasible, one possible leading-edge noise mitigation strategy is to make the airfoil less affected by local disturbances. The usage of absorbing materials, e.g. porous media, as part of the airfoil structure has the potential to achieve such a goal. The idea of applying porosity for noise-attenuation strategies comes from the studies on the silent flight of owls by Kroeger *et al.* [43], who described the feather structure at the trailing edge of the owl wings as *wing porosity* (Figure 1.3) and classified this feature as one of the mechanisms responsible for silencing their flight. The beneficial sound-mitigation effects of the porous treatment of a wing profile were first demonstrated by Lee [44], who numerically investigated the influence that a porous leading-edge insert of a helicopter blade had on turbulence-interaction noise. He observed that a far-field noise reduction of up to 30 % was possible due to the suppression of the pressure fluctuations at the blade surface.

Geyer *et al.* [46, 47] manufactured numerous porous airfoils characterized by different materials and tested them with various grid-generated turbulent flows by means of microphone array techniques. They focused their attention on the influence of the

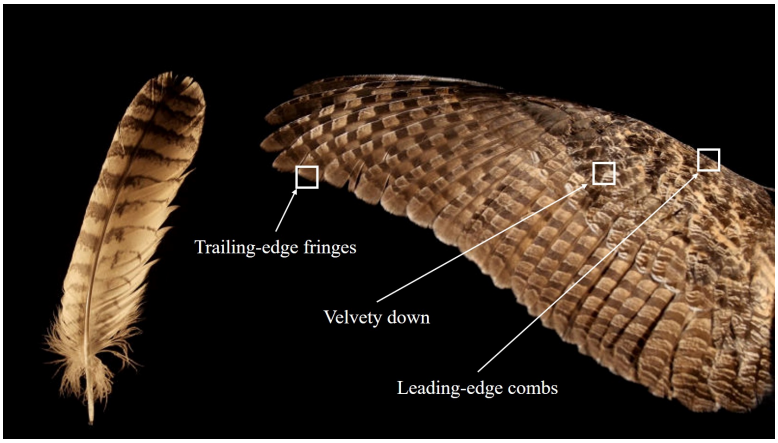

Figure 1.3: The three wing features that are thought to contribute to the owl's silent flight capability: a comb of stiff feathers along the wing leading edge; a soft, downy material distributed on the top of the wing; and a flexible fringe at the wing trailing edge [45]. Image copyrights: Josh Cassidy/KQED. Content: Lehigh University.

parameters characterizing the porous media, observing how the noise-reduction performance was strongly related to the material properties. Particularly, they found that lower values of static air-flow resistivity could lead to more significant noise reduction but also to noise regeneration at high frequencies, most likely associated with the increased roughness due to the interaction of the airfoil boundary layer with the open pores of the material. Subsequently, the leading-edge noise produced by the same porous airfoils was investigated by Sarradj and Geyer [48] through symbolic regression tools. They observed a dependency of the noise on the square of the turbulence intensity and from the fifth to the sixth power of the flow velocity. The ratio of the integral length scale of the incoming turbulent flow to the characteristic length of the porous structure, linked to the static air-flow resistivity, was found to have a significant influence on the acoustic frequency spectrum.

When porosity covers the full chordwise extent of the airfoil, a noticeable deterioration of the aerodynamic performance is expected, resulting in a decrease of the lift force and an increase of the drag force, especially at high angles of attack [46, 49–51]. The former effect is related to the communication between pressure and suction side of the wing profile through the pores of the material, whereas the latter effect is linked to the augmented surface roughness. Several researchers have already proposed technological solutions for the implementation of porous materials in the design of a wing profile with the aim of preserving its aerodynamic performance. Among them, Roger *et al.* [22, 52] filled a NACA-0012 profile with steel wool to study the leading-edge noise reduction from a grid-airfoil and cylinder-airfoil interaction. They found that a reduction ranging from 2.5 dB to 6 dB was achievable for the part of the frequency spectrum that was related to the characteristic length of the porous medium. A similar approach for the inclusion of porous materials in the structure of a thick airfoil has been proposed by Bampanis and Roger [53], who designed a rigid exoskeleton coated with a metallic wire mesh where melamine foam or metal wool could be fitted in. Likewise, a solid center plane was in-

cluded to avoid cross-flow between pressure and suction side in order to maintain the aerodynamic performance of the wing profile. Broadband-noise mitigation varying from 4 dB to 6 dB was observed in this case.

Additional research on the application of a porous treatment of the airfoil was performed by Geyer *et al.* [54], who experimentally and numerically tested the effectiveness of perforated leading-edge inserts for the attenuation of grid-generated turbulence-interaction noise. A noticeable mitigation of up to 8 dB was achieved for frequencies ranging from 1 kHz to 4 kHz. Similar to previous investigations, noise regeneration occurring at high frequencies for perforated leading-edge inserts with large pores was found due to the increased surface roughness. A different design for a flow permeable insert has been investigated by Avallone *et al.* [55] and Sinnige *et al.* [56] with the aim of suppressing the noise produced by the interaction of a pylon with a propeller slipstream. An attenuation of the tonal components of the emitted far-field noise was measured in this case. Chaitanya *et al.* [57] studied the turbulence-interaction noise reduction obtained by flat plates characterized by different extents of porous inserts. Notably, they observed that the use of a single row of holes situated downstream of the leading edge allows for a significant low-frequency attenuation without increasing the noise radiations at higher frequencies. Ayton *et al.* [58] found that smoothly varying chordwise porosity on a perforated flat plate can be beneficial for reducing the turbulent boundary-layer trailing-edge noise thanks to the more significant destructive interference of the back-scattered field generated by an impermeable leading edge [59, 60].

All the above-mentioned studies demonstrate the potential of the porous treatment of an airfoil as a turbulence-interaction noise reduction technique. However, no definitive explanation about the physical mechanisms involved in the noise mitigation for a thick wing profile has been found yet. The main goal pursued in this manuscript is to elucidate these mechanisms. One possible reason is linked to the dissipation of the acoustic energy by the viscous and thermal losses occurring during the oscillatory fluid motion in the pores of the material [61]. A second one is related to the hydrodynamic absorption by the turbulent eddies due to the interaction with a penetrable surface. As a consequence of this, the distortion experienced by the turbulence in the immediate vicinity of the airfoil may be affected by the porous treatment. The study described in this manuscript is based on the investigation of the latter mechanism.

1.2. THESIS OBJECTIVES AND OUTLINE

The methodology considered in the present research rests upon three research objectives:

1. **Perform detailed experiments to characterize the alterations in the distortion of turbulence interacting with the airfoil due to porosity and the corresponding noise attenuation**;

2. **Implement an accurate and robust acoustic beamforming technique for the localization and quantification of the noise sources generated by the impingement of a turbulent flow on a wing profile**;

3. **Develop an analytical model based on the RDT to predict the turbulent flow**

around a porous bluff body and apply it to interpret the experimental results of the turbulence distortion in the vicinity of the airfoil.

Considering the above-defined research objectives, the thesis is organized as follows.

- In Chapter 2, the theoretical framework of the topics addressed in the rest of the manuscript is discussed. Specifically, a brief overview of the linear acoustic theory provides the basis for computing the sound propagation models considered in acoustic beamforming techniques (**objective 2**). The use of aeroacoustic analogies makes it possible to derive a formulation for calculating the noise generated by a body that is immersed in a turbulent flow (**objective 1**). Finally, the governing equations of the RDT are presented. These constitute the starting point of the analytical model for the prediction of the distortion of turbulence interacting with a porous bluff body (**objective 3**).

- In Chapter 3, the experimental setups and measurement techniques employed for carrying out the different experiments (**objective 1**) are outlined. The facilities where the measurements take place as well as the benchmark configuration that is used for generating the turbulent flow are illustrated. The design and characterization of a NACA-0024 airfoil integrated with porous media are then described in detail. The measurement techniques include hot-wire anemometry, acoustic far-field microphones, and particle image velocimetry (PIV).

- In Chapter 4, the implementation of an improved version of an existing acoustic beamforming technique (**objective 2**) is described. After a short overview of the beamforming basic principles, the technique is validated through its application to two experimental benchmark datasets in order to evaluate its performance under different conditions. Subsequently, the noise sources produced by the impingement of turbulence on solid and porous NACA-0024 profiles are characterized by means of far-field microphone measurements and acoustic beamforming (**objective 1**).

- In Chapter 5, the results of the investigation of the turbulent flow interacting with solid and porous airfoils (**objective 1**) are reported and discussed. The flow around the NACA-0024 profiles is characterized to study the evolution of the boundary layer. A specific focus is then put on the stagnation region with the aim of analyzing the alterations in turbulence distortion triggered by porosity. The measurements are compared with the results of numerical simulations. The influence of the Reynolds number of the free-stream flow and the design elements of the porous airfoil configuration on the velocity field is also evaluated.

- In Chapter 6, the distortion of homogeneous isotropic turbulence impinging on a porous cylinder is calculated by means of the RDT (**objective 3**). The analytical formulation of the porous RDT model is presented and its assumptions and limitations are discussed. The implemented algorithm is validated through comparisons with published velocity measurements and is applied to a solid and porous cylinder in order to investigate the impact of porosity on the turbulent field. Finally, the method is adapted to model the turbulence distortion in the vicinity of

the leading edge of the porous NACA-0024 profile with the aim of interpreting the outcomes of the experimental investigation (**objective 3**).

- In Chapter 7, the conclusions drawn from the different investigations as well as the future perspectives and recommendations linked to the present research are outlined.

REFERENCES

[1] R. Zamponi, D. Ragni, N. Van de Wyer, and C. Schram, *Experimental Investigation of Airfoil Turbulence-Impingement Noise Reduction Using Porous Treatment,* in *25th AIAA/CEAS Aeroacoustics Conference* (American Institute of Aeronautics and Astronautics, Delft, The Netherlands, 2019).

[2] R. Zamponi, S. Satcunanathan, S. Moreau, D. Ragni, M. Meinke, W. Schröder, and C. Schram, *On the role of turbulence distortion on leading-edge noise reduction by means of porosity,* Journal of Sound and Vibration **485**, 115561 (2020).

[3] R. Zamponi, S. Moreau, and C. Schram, *Rapid distortion theory of turbulent flow around a porous cylinder,* Journal of Fluid Mechanics **915**, A27 (2021).

[4] M. M. Haines, S. A. Stansfeld, R. F. S. Job, B. Berglund, and J. Head, *Chronic aircraft noise exposure, stress responses, mental health and cognitive performance in school children,* Psychological Medicine **31**, 265 (2001).

[5] C. Clark, R. Martin, E. van Kempen, T. Alfred, J. Head, H. W. Davies, M. M. Haines, I. L. Barrio, M. Matheson, and S. A. Stansfeld, *Exposure-Effect Relations between Aircraft and Road Traffic Noise Exposure at School and Reading Comprehension,* American Journal of Epidemiology **163**, 27 (2006).

[6] W. R. O. f. Europe, L. Fritschi, World Health Organization, and Regional Office for Europe, *Burden of Disease from Environmental Noise Quantification of Healthy Life Years Lost in Europe.* (World Health Organization, Geneva, 2011).

[7] O. Hahad, S. Kröller-Schön, A. Daiber, and T. Münzel, *The cardiovascular effects of noise,* Deutsches Aerzteblatt Online (2019), 10.3238/arztebl.2019.0245.

[8] W. R. O. f. Europe, L. Fritschi, World Health Organization, and Regional Office for Europe, *Environmental noise guidelines for the European Region* (World Health Organization, 2018).

[9] European Aviation Safety Agency. and EAA., *European aviation environmental: report 2019.* (Publications Office, LU, 2019).

[10] C. of European Union, *Council regulation (EU) no 598/2014,* (2014), http://data.europa.eu/eli/reg/2014/598/oj.

[11] European Commission. Directorate General for Research and Innovation. and European Commission. Directorate General for Mobility and Transport., *Flightpath 2050 :Europe's vision for aviation : maintaining global leadership and serving society's needs.* (Publications Office, LU, 2011).

[12] N. Peake and A. B. Parry, *Modern Challenges Facing Turbomachinery Aeroacoustics,* Annual Review of Fluid Mechanics **44**, 227 (2012).

[13] *On sound generated aerodynamically I. General theory,* Proceedings of the Royal Society of London. Series A. Mathematical and Physical Sciences **211**, 10.1098/rspa.1952.0060.

[14] S. Moreau, *Turbomachinery Noise Predictions: Present and Future,* Acoustics **1**, 92 (2019).

[15] S. Garg, *Aircraft Turbine Engine Control Research at NASA Glenn Research Center,* Journal of Aerospace Engineering **26**, 422 (2013).

[16] A. Guédel, *Acoustique des ventilateurs - Génération du bruit et moyens de réduction (Acoustics of fans - Noise generation and reduction)* (1999).

[17] S. Caro and S. Moreau, *Aeroacoustic modelling of low pressure axial flow fans,* in *6th Aeroacoustics Conference and Exhibit* (American Institute of Aeronautics and Astronautics, Lahaina, HI, U.S.A., 2000).

[18] S. Perennes and M. Roger, *Aerodynamic noise of a two-dimensional wing with high-lift devices,* in *4th AIAA/CEAS Aeroacoustics Conference* (American Institute of Aeronautics and Astronautics, Toulouse,France, 1998).

[19] T. F. Brooks and W. M. Humphreys, *Flap-edge aeroacoustic measurements and predictions,* Journal of Sound and Vibration **261**, 31 (2003).

[20] M. Macaraeg, *Fundamental investigations of airframe noise,* in *4th AIAA/CEAS Aeroacoustics Conference* (American Institute of Aeronautics and Astronautics, Toulouse,France, 1998).

[21] K. Zhao, P. Okolo, E. Neri, P. Chen, J. Kennedy, and G. J. Bennett, *Noise reduction technologies for aircraft landing gear-A bibliographic review,* Progress in Aerospace Sciences **112**, 100589 (2020).

[22] M. Roger, C. Schram, and L. de Santana, *Reduction of Airfoil Turbulence-Impingement Noise by Means of Leading-Edge Serrations and/or Porous Material,* in *19th AIAA/CEAS Aeroacoustics Conference* (American Institute of Aeronautics and Astronautics, Berlin, Germany, 2013).

[23] R. K. Amiet, *Acoustic radiation from an airfoil in a turbulent stream,* Journal of Sound and Vibration **41**, 407 (1975).

[24] R. Paterson and R. Amiet, *Acoustic radiation and surface pressure characteristics of an airfoil due to incident turbulence,* in *3rd Aeroacoustics Conference* (American Institute of Aeronautics and Astronautics, Palo Alto, CA, U.S.A., 1976).

[25] W. Olsen and J. Wagner, *Effect of thickness on airfoil surface noise,* AIAA Journal **20**, 437 (1982).

[26] S. Oerlemans and P. Migliore, *Aeroacoustic Wind Tunnel Tests of Wind Turbine Airfoils,* in *10th AIAA/CEAS Aeroacoustics Conference* (American Institute of Aeronautics and Astronautics, Manchester, UK, 2004).

[27] S. Moreau and M. Roger, *Effect of Angle of Attack and Airfoil Shape on Turbulence-Interaction Noise,* in *11th AIAA/CEAS Aeroacoustics Conference* (American Institute of Aeronautics and Astronautics, Monterey, California, 2005).

[28] W. J. Devenport, J. K. Staubs, and S. A. Glegg, *Sound radiation from real airfoils in turbulence,* Journal of Sound and Vibration **329**, 3470 (2010).

[29] J. Gill, X. Zhang, and P. Joseph, *Symmetric airfoil geometry effects on leading edge noise,* The Journal of the Acoustical Society of America **134**, 2669 (2013).

[30] D. Kim, G.-S. Lee, and C. Cheong, *Inflow broadband noise from an isolated symmetric airfoil interacting with incident turbulence,* Journal of Fluids and Structures **55**, 428 (2015).

[31] J. Christophe, *Application of Hybrid Methods to High Frequency Aeroacoustics*, Ph.D. thesis, Université Libre de Bruxelles (2011).

[32] L. D. de Santana, J. Christophe, C. Schram, and W. Desmet, *A Rapid Distortion Theory modified turbulence spectra for semi-analytical airfoil noise prediction,* Journal of Sound and Vibration **383**, 349 (2016).

[33] J. C. R. Hunt, *A theory of turbulent flow round two-dimensional bluff bodies,* Journal of Fluid Mechanics **61**, 625 (1973).

[34] H. Ribner and M. Tucker, *Spectrum of turbulence in a contracting stream*, Tech. note no. 19 (N.A.C.A., 1953).

[35] G. K. Batchelor and I. Proudman, *The effect of rapid distortion of a fluid in turbulent motion,* The Quarterly Journal of Mechanics and Applied Mathematics **7**, 83 (1954).

[36] P. W. Bearman, *Some measurements of the distortion of turbulence approaching a two-dimensional bluff body,* Journal of Fluid Mechanics **53**, 451 (1972).

[37] M. E. Goldstein, *Unsteady vortical and entropic distortions of potential flows round arbitrary obstacles,* Journal of Fluid Mechanics **89**, 433 (1978).

[38] R. E. Britter, J. C. R. Hunt, and J. C. Mumford, *The distortion of turbulence by a circular cylinder,* Journal of Fluid Mechanics **92**, 269 (1979).

[39] P. A. Durbin and J. C. R. Hunt, *On surface pressure fluctuations beneath turbulent flow round bluff bodies,* Journal of Fluid Mechanics **100**, 161 (1980).

[40] J. Hunt, H. Kawai, S. Ramsey, G. Pedrizetti, and R. Perkins, *A review of velocity and pressure fluctuations in turbulent flows around bluff bodies,* Journal of Wind Engineering and Industrial Aerodynamics **35**, 49 (1990).

[41] L. J. Ayton and N. Peake, *Interaction of turbulence with the leading-edge stagnation point of a thin aerofoil,* Journal of Fluid Mechanics **798**, 436 (2016).

[42] C. A. Klettner, I. Eames, and J. C. R. Hunt, *The effect of an unsteady flow incident on an array of circular cylinders,* Journal of Fluid Mechanics **872**, 560 (2019).

[43] R. A. Kroeger, H. D. Grushka, and T. C. Helvey, *Low Speed Aerodynamics for Ultra-Quiet Flight*, Tech. Rep. AD893426 (Air force flight dynamics laboratory Wright-Patterson Air Force Base, Ohio, 1972).

[44] S. Lee, *Reduction of blade-vortex interaction noise through porous leading edge,* AIAA Journal **32**, 480 (1994).

[45] J. W. Jaworski and N. Peake, *Aerodynamic noise from a poroelastic edge with implications for the silent flight of owls,* Journal of Fluid Mechanics **723**, 456 (2013).

[46] T. Geyer, E. Sarradj, J. Giesler, and M. Hobracht, *Experimental assessment of the noise generated at the leading edge of porous airfoils using microphone array techniques,* in *17th AIAA/CEAS Aeroacoustics Conference (32nd AIAA Aeroacoustics Conference)* (American Institute of Aeronautics and Astronautics, Portland, Oregon, 2011).

[47] T. Geyer, E. Sarradj, and J. Giesler, *Application of a Beamforming Technique to the Measurement of Airfoil Leading Edge Noise,* Advances in Acoustics and Vibration **2012**, 1 (2012).

[48] E. Sarradj and T. Geyer, *Symbolic regression modeling of noise generation at porous airfoils,* Journal of Sound and Vibration **333**, 3189 (2014).

[49] R. E. Mineck and P. M. Hartwich, *Effect of Full-Chord Porosity on Aerodynamic Characteristics of the NACA 0012 Airfoil*, Technical Publication NASA/TP-3591.

[50] E. Sarradj and T. Geyer, *Noise Generation by Porous Airfoils,* in *13th AIAA/CEAS Aeroacoustics Conference (28th AIAA Aeroacoustics Conference)* (American Institute of Aeronautics and Astronautics, Rome, Italy, 2007).

[51] C. Teruna, F. Avallone, D. Casalino, and D. Ragni, *Numerical Investigation of Leading Edge Noise Reduction on a Rod-Airfoil Configuration Using Porous Materials and Serrations,* Journal of Sound and Vibration , 115880 (2020).

[52] M. Roger and S. Moreau, *Airfoil Turbulence-Impingement Noise Reduction by Porosity or Wavy Leading-Edge Cut: Experimental Investigations,* in *45th International Congress and Exposition on Noise Control Engineering* (Institute of Noise Control Engineering, Hamburg, Germany, 2016) pp. 6366–6375.

[53] G. Bampanis and M. Roger, *On the Turbulence-Impingement Noise of a NACA-12 Airfoil with Porous Inclusions,* in *26th AIAA/CEAS Aeroacoustics Conference* (American Institute of Aeronautics and Astronautics, Virtual event, 2020).

[54] T. F. Geyer, A. Lucius, M. Schrödter, M. Schneider, and E. Sarradj, *Reduction of Turbulence Interaction Noise Through Airfoils With Perforated Leading Edges,* Acta Acustica united with Acustica **105**, 109 (2019).

[55] F. Avallone, D. Casalino, and D. Ragni, *Impingement of a propeller-slipstream on a leading edge with a flow-permeable insert: A computational aeroacoustic study,* International Journal of Aeroacoustics **17**, 687 (2018).

[56] T. Sinnige, B. D. Corte, R. De Vries, F. Avallone, R. Merino-Martínez, D. Ragni, G. Eitelberg, and L. L. M. Veldhuis, *Alleviation of Propeller-Slipstream-Induced Unsteady Pylon Loading by a Flow-Permeable Leading Edge,* Journal of Aircraft **56**, 1214 (2019).

[57] C. Paruchuri, P. Joseph, T. P. Chong, M. Priddin, and L. J. Ayton, *On the noise reduction mechanisms of porous aerofoil leading edges,* Journal of Sound and Vibration **485**, 115574 (2020).

[58] L. J. Ayton, M. J. Colbrook, T. Geyer, P. Chaitanya, and E. Sarradj, *Reducing aerofoil–turbulence interaction noise through chordwise-varying porosity,* Journal of Fluid Mechanics **906**, A1 (2021).

[59] M. Roger and S. Moreau, *Back-scattering correction and further extensions of Amiet's trailing-edge noise model. Part 1: theory,* Journal of Sound and Vibration **286**, 477 (2005).

[60] S. Moreau and M. Roger, *Back-scattering correction and further extensions of Amiet's trailing-edge noise model. Part II: Application,* Journal of Sound and Vibration **323**, 397 (2009).

[61] M. Kuczmarski and J. Johnston, *Acoustic Absorption in Porous Materials*, Technical Report NASA/TM-2011-216995 (NASA Glenn Research Center, 2011).

2

THEORY

Nothing in life is to be feared, it is only to be understood.
Now is the time to understand more, so that we may fear less.

Marie Curie

The theoretical framework required for the understanding of the topics addressed in the manuscript is outlined in this chapter. First, the linear acoustic theory is briefly reviewed in order to describe how sound waves are generated and how they propagate in a quiescent fluid considering different point-source models. Subsequently, the noise generated by the interaction of a turbulent flow with a solid body is modeled by means of the aeroacoustic analogies. Finally, the linear theory describing the sudden changes in turbulence experienced by a turbulent flow impinging on a bluff body, or rapid distortion theory, is introduced.

Parts of this chapter are included in [1].

2.1. LINEAR ACOUSTIC THEORY

This section briefly reviews the fundamental concepts at the basis of linear acoustics. The formulation that follows is largely based on the work of Glegg and Deventport [2], for which an interested reader is referred to.

2.1.1. ACOUSTIC WAVE PROPAGATION EQUATION AND SOLUTION

For a fluid in motion characterized by incompressible behavior, i.e. at low Mach numbers, and without heat transfer and variation of internal energy, the equations of continuity and momentum can be written as

$$\frac{\partial \rho}{\partial t} + \frac{\partial (\rho u_\mathrm{i})}{\partial x_\mathrm{i}} = Q; \tag{2.1}$$

$$\frac{\partial (\rho u_\mathrm{i})}{\partial t} + \frac{\partial (-P_\mathrm{ij} + \rho u_\mathrm{i} u_\mathrm{j})}{\partial x_\mathrm{j}} = f_\mathrm{i} + Q u_\mathrm{i}, \tag{2.2}$$

where ρ is the fluid density, $\boldsymbol{u}$ is the flow velocity, $\boldsymbol{P}$ is the fluid stress tensor, and $\boldsymbol{f}$ is the density of the force field acting on the bulk of the fluid, such as the gravitational one. In this case, the mass source term Q [3] represents the rate of mass per unit volume that is injected inside the control volume through a permeable boundary portion and adds momentum by a quantity $Q\boldsymbol{u}$. Moreover, the fluid stress tensor can be expressed as the sum of the isotropic part $-p\boldsymbol{I}$, where p is the hydrostatic pressure and $\boldsymbol{I}$ is the identity matrix, and the deviatoric part $\boldsymbol{\tau}$, which contains the viscous stresses.

The present equations can be linearized by performing a decomposition of the involved quantities into mean values, denoted with the symbol $\bar{}$, and perturbations around them, indicated with the subscript $'$. This procedure will make it possible to derive the sound-propagation model for the acoustic beamforming technique described in Chapter 4. If the fluid is in a quiescent state, i.e. the mean velocity is zero, it follows that

$$\begin{aligned} p(\boldsymbol{x}, t) &= \bar{p} + p'(\boldsymbol{x}, t); \\ \rho(\boldsymbol{x}, t) &= \bar{\rho} + \rho'(\boldsymbol{x}, t); \\ \boldsymbol{u}(\boldsymbol{x}, t) &= \bar{\boldsymbol{u}} + \boldsymbol{u}'(\boldsymbol{x}, t) = \boldsymbol{u}'(\boldsymbol{x}, t). \end{aligned} \tag{2.3}$$

By substituting Equations (2.3) into Equations (2.1) and (2.2) and neglecting the higher-order terms, the linearized continuity and momentum equations read

$$\frac{\partial \rho'}{\partial t} + \bar{\rho} \frac{\partial u'_\mathrm{i}}{\partial x_\mathrm{i}} = Q; \tag{2.4}$$

$$\bar{\rho} \frac{\partial u'_\mathrm{i}}{\partial t} + \bar{\rho} \frac{\partial (u_\mathrm{i} u_\mathrm{j})}{\partial x_\mathrm{j}} = -\frac{\partial p'}{\partial {x_\mathrm{i}}^2} + \frac{\partial \tau'_\mathrm{ij}}{\partial x_\mathrm{j}} + f_\mathrm{i}. \tag{2.5}$$

It is now possible to avoid the dependency on the acoustic velocity perturbation $\boldsymbol{u}'$ by subtracting the divergence of Equation (2.5) from the time derivative of Equation (2.4), yielding

$$\frac{\partial^2 \rho'}{\partial t^2} - \frac{\partial^2 p'}{\partial {x_\mathrm{i}}^2} = -\frac{\partial f_\mathrm{i}}{\partial x_\mathrm{i}} - \frac{\partial^2 \tau'_\mathrm{ij}}{\partial x_\mathrm{i} \partial x_\mathrm{j}} + \frac{\partial Q}{\partial t}. \tag{2.6}$$

By explicating the density as a function of the pressure through the equation of state

$$p = p(\rho, s); \tag{2.7}$$

$$p' = \left(\frac{\partial p}{\partial \rho}\right)_s \rho' + \left(\frac{\partial p}{\partial s}\right)_\rho s' = c_0^2 \rho' + \left(\frac{\partial p}{\partial s}\right)_\rho s', \tag{2.8}$$

s being the entropy, and by inserting Equation (2.8) into Equation (2.6), the inhomogeneous wave equation can be derived as

$$\frac{1}{c_0^2}\frac{\partial^2 p'}{\partial t^2} - \frac{\partial^2 p'}{\partial x_i{}^2} = -\frac{\partial f_i}{\partial x_i} - \frac{\partial^2 \tau'_{ij}}{\partial x_i \partial x_j} + \frac{1}{c_0^2}\left(\frac{\partial p}{\partial s}\right)_\rho \frac{\partial^2 s'}{\partial t^2} + \frac{\partial Q}{\partial t}, \tag{2.9}$$

where c_0 is the speed of sound. The left-hand side of Equation (2.9) is the d'Alembertian operator applied to a pressure perturbation p' and the right-hand side represents all the possible sound sources. In particular, the term $\partial Q/\partial t$ describes an unsteady mass injection in the volume, while the term $\partial^2 s'/\partial t^2$ indicates entropy fluctuations that, due to thermal expansion in a process such as combustion or heat transfer, acts also as a volume source. These two terms are both represented by monopole-like sources. The term $-\nabla \cdot \boldsymbol{f}$, which is associated with the fluctuating non-uniform force field, induces dipole-like sources. The force density can also be used to represent the reaction force of a rigid wall to unsteady aerodynamic forces, which, as will be discussed later, constitutes the dominant sound source in numerous flows [2]. Finally, the term $-\nabla \cdot (\nabla \cdot \boldsymbol{\tau}')$ is associated with the fluctuating, non-uniform viscous stresses and represents the sound due to the turbulence modeled by quadrupole-like sources. The discussion about monopole, dipole, and quadrupole sources will be covered in greater details in Chapter 2.1.2.

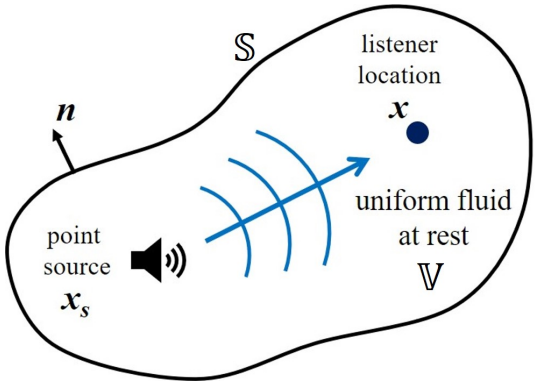

Figure 2.1: A control volume of size $\mathbb{V}$ bounded by the surface $\mathbb{S}$ with fluid in a quiescent state.

Equation (2.9) can be solved by using the Green's function method [2]. The Green's function is the fundamental solution of the wave propagation equation and represents the acoustic pressure that satisfies the wave equation for an impulsive point source located at $\boldsymbol{x}_s$ (see Figure 2.1) and emitting a sound pulse at time t_s ($t_s < t$). For a listener located at position $\boldsymbol{x}$ in space at time t, $G(\boldsymbol{x}, t|\boldsymbol{x}_s, t_s)$ is the solution of the following wave

equation:

$$\frac{1}{c_0^2}\frac{\partial^2 G}{\partial t^2} - \frac{\partial^2 G}{\partial {x_i}^2} = \delta(\boldsymbol{x}-\boldsymbol{x}_s)\delta(t-t_s), \tag{2.10}$$

δ being the Dirac function. The pulse response should also satisfy the causality conditions $G = 0$ and $\partial G/\partial t = 0$ for $t_s < 0$ since the pressure field observed at time t must be caused by source signals that have been emitted at the earlier times t_s. The Green's function is further determined by the linear boundary conditions that are imposed [2]. If these correspond to those of the acoustical field, G is denoted as *tailored*.

By replacing the source term in the right-hand side of Equation (2.9) with the general source term q and using the Green's theorem, it is possible to rewrite the equation in its integral form:

$$\begin{aligned} p'(\boldsymbol{x},t) = &\int_{t_0}^{t}\iiint_{\mathbb{V}} q(\boldsymbol{y},\tau)G\,dV\,d\tau - \int_{t_0}^{t}\iint_{\mathbb{S}}\left[p'(\boldsymbol{y},\tau)\frac{\partial G}{\partial y_i} - G\frac{\partial p'(\boldsymbol{y},\tau)}{\partial y_i}\right]n_i\,dS\,d\tau \\ &-\left\{\iiint_{\mathbb{V}}\left[p'(\boldsymbol{y},\tau)\frac{\partial G}{\partial \tau} - G\frac{\partial p'(\boldsymbol{y},\tau)}{\partial \tau}\right]dV\right\}_{\tau=t_0}, \end{aligned} \tag{2.11}$$

$\boldsymbol{n}$ being the outward-pointing normal on the surface $\mathbb{S}$ enclosing the volume $\mathbb{V}$ where q is non-zero (Figure 2.1). The second integral of the right hand side vanishes for a tailored Green's function, while the third one represents the effect of the initial conditions at $\tau = t_0$. For a tailored Green's function, and if $t_0 = -\infty$, Equation (2.11) becomes

$$p'(\boldsymbol{x},t) = \int_{-\infty}^{t}\iiint_{\mathbb{V}} q(\boldsymbol{y},\tau)G\,dV\,d\tau. \tag{2.12}$$

2.1.2. POINT-SOURCE MODELS

The Green's function for a quiescent fluid in free space is given by

$$G(\boldsymbol{x},t|\boldsymbol{x}_s,t_s) = \frac{\delta\left(t - t_s - \frac{||\boldsymbol{x}-\boldsymbol{x}_s||}{c_0}\right)}{4\pi||\boldsymbol{x}-\boldsymbol{x}_s||}. \tag{2.13}$$

where the term $\hat{\tau} = t - ||\boldsymbol{x}-\boldsymbol{x}_s||/c_0$ is called *retarded time*, $||-||$ denoting the norm of the vector. Equation (2.13) is an outward, traveling impulsive wave whose amplitude is inversely proportional to the distance. The evaluation of the time integral can be performed by using the sampling property of δ inside the Green's function expression. Starting from the expression for the acoustic pressure induced by a generic source distribution, it follows that

$$p'(\boldsymbol{x},t) = \iiint_{\mathbb{V}} \frac{q\left(\boldsymbol{y}, t - \frac{||\boldsymbol{x}-\boldsymbol{y}||}{c_0}\right)}{4\pi||\boldsymbol{x}-\boldsymbol{y}||}\,dV. \tag{2.14}$$

If the source is acoustically compact, i.e. the source dimensions are smaller than the wavelength of the emitted sound wave, it can be considered as a point source. The source function for the compact source is

$$q(\boldsymbol{x},t) = \hat{q}(t)\delta(\boldsymbol{x}-\boldsymbol{x}_s), \tag{2.15}$$

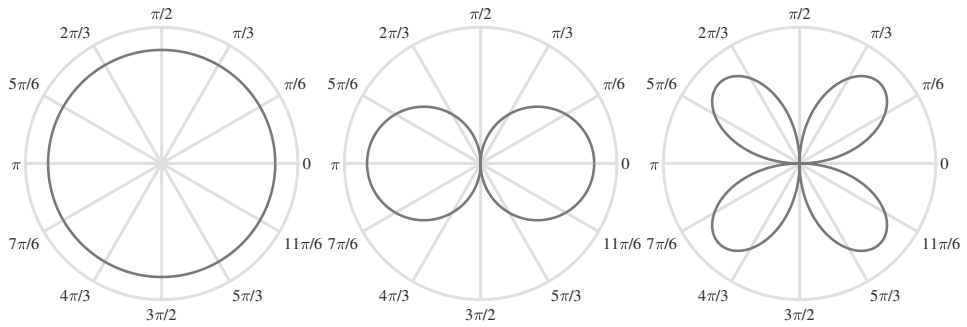

(a) Monopole-like source. (b) Dipole-like source. (c) Quadrupole-like source.

Figure 2.2: Directivity patterns for different point-source models.

where $\hat{q}(t)$ is the point-source strength. By substituting Equation (2.15) into Equation (2.14) and by evaluating the volume integral, the expression for the acoustic pressure induced by a point source in free field is derived as

$$p'(\boldsymbol{x},t) = \frac{\hat{q}\left(t - \frac{||\boldsymbol{x}-\boldsymbol{x}_s||}{c_0}\right)}{4\pi||\boldsymbol{x}-\boldsymbol{x}_s||}. \tag{2.16}$$

This is an omnidirectional or monopole sound field and its directivity pattern is illustrated in Figure 2.2a. Thus, the pressure field satisfies the homogeneous wave equation, obtained by considering the left-hand side of the equation equal to zero, everywhere except at the source position. A monopole can be thought of as a pulsating sphere with a vanishing radius but constant source strength. In the inhomogeneous wave equation, both sources due to mass injection and entropy fluctuations feature a monopole-like source behavior, with different expressions for the source strength.

For a point force in $\boldsymbol{x}_s$, the source term is $q(\boldsymbol{x},t) = -\nabla\cdot\boldsymbol{f}$, where $\boldsymbol{f}$ can be written as $\boldsymbol{f}(\boldsymbol{x},t) = \boldsymbol{F}(t)\delta(\boldsymbol{x}-\boldsymbol{x}_s)$. Since such a source can be formed by two adjacent opposite monopoles, a point-force source is denoted as a dipole source (Figure 2.2b). The strength q of the monopoles and the distance l between the two sources have to be such that $q(t)\,l = \boldsymbol{F}(t)$, where l goes to zero and q increases in order to keep $\boldsymbol{F}$ constant. A dipole can also be thought of as a small rigid sphere oscillating in the direction of the dipole axis. From Equation (2.14), the equation for the dipole acoustic pressure can be derived as

$$\begin{aligned} p'(\boldsymbol{x},\boldsymbol{x}_s,\theta_F,t) &= -\frac{\partial}{\partial x_i}\left[\frac{\boldsymbol{F}}{4\pi||\boldsymbol{x}-\boldsymbol{x}_s||}\right] \\ &= \frac{\cos\theta_F}{4\pi}\left\{\frac{1}{c_0||\boldsymbol{x}-\boldsymbol{x}_s||}\left[\frac{\partial F}{\partial t}\right] + \left[\frac{F}{||\boldsymbol{x}-\boldsymbol{x}_s||^2}\right]\right\}, \end{aligned} \tag{2.17}$$

where $F = ||\boldsymbol{F}||$ and θ_F is the angle between observer direction and force. The square brackets indicate that the function should be evaluated at the emission time $t - ||\boldsymbol{x} - \boldsymbol{x}_s||/c_0$.

Concerning the structure of the dipole field, several considerations can be made. First, the dipole pressure is composed of two terms, one falling off with $1/r$, where

$r = ||\boldsymbol{x} - \boldsymbol{x}_s||$, and one with $1/r^2$. The $1/r^2$ term dominates the field close to the source and is therefore indicated as the *near field*. At larger distances - in the *far field* -, the pressure decades with $1/r$, as for the monopole source in Equation (2.16). Second, the dipole field has a non-uniform directivity. The pressure field has a $\cos\theta_F$ dependence, with zero pressure at 90° with respect to the dipole axis. Third, the far-field pressure of the dipole (even for $\cos\theta_F = 1$) is much lower than the pressure of a single monopole having the same strength q. This can be understood from the partial cancellation of the two constituent monopoles. Thus, dipoles are less efficient than monopoles in free field conditions.

As a combination of two monopoles leads to a dipole, a combination of two dipoles yields a quadrupole, which models the sound generated by viscous stresses (Figure 2.2c). Since such a source can be formed by two adjacent opposite dipole sources, a turbulent-point source can be considered as a quadrupole source. Because the two dipoles can be combined in different ways due to their asymmetry, the term *quadrupole* more appropriately designates a family of sound sources. Quadrupole sources will not be discussed in this manuscript and, for more information, an interested reader can refer to [2].

2.1.3. HELMHOLTZ EQUATION IN THE FREQUENCY DOMAIN

The derivation of the wave equation and its fundamental solution has been carried out in the time domain so far. Similar considerations can be made for the frequency domain by computing the Fourier transform of the wave propagation equation. The homogeneous Helmholtz equation is

$$\nabla^2 \hat{p} + k^2 \hat{p} = 0, \tag{2.18}$$

where $\hat{p}$ is derived from $p'(\boldsymbol{x}, t) = \hat{p} e^{i\omega t}$ and $k = \omega/c_0$ is the acoustic wavenumber, ω being the angular frequency of the excitation. The inhomogeneous Helmholtz equation, computed by adding the source terms to Equation (2.18), can be solved by the means of the frequency-domain Green's function, according to

$$(\nabla^2 + k^2) G_\omega(\boldsymbol{x} - \boldsymbol{x}_s) = -\delta(\boldsymbol{x} - \boldsymbol{x}_s). \tag{2.19}$$

Equation (2.19) is subjected to the Sommerfeld radiation boundary condition, which ensures that waves are radiated and not absorbed by the sources. Hence, the radiated energy scatters to infinity. The present condition can be expressed as

$$\lim_{r \to +\infty} r \left(\frac{\partial p'}{\partial t} + c_0 \frac{\partial p'}{\partial r} \right) = 0. \tag{2.20}$$

By applying Equation (2.20), the fundamental solution of the non-homogeneous Helmholtz equation can be derived as

$$G_\omega(\boldsymbol{x} - \boldsymbol{x}_s) = \frac{e^{ik||\boldsymbol{x} - \boldsymbol{x}_s||}}{4\pi ||\boldsymbol{x} - \boldsymbol{x}_s||}. \tag{2.21}$$

Subsequently, the expression for the acoustic pressure given by a monopole in free-field conditions in frequency domain is

$$p_{\text{mono}}(\boldsymbol{x}, \boldsymbol{x}_s) = \frac{a_{\text{mono}}}{4\pi ||\boldsymbol{x} - \boldsymbol{x}_s||} e^{ik||\boldsymbol{x} - \boldsymbol{x}_s||}, \tag{2.22}$$

where a_{mono} is the complex source amplitude of the source, $\boldsymbol{x}$ is the receiver position, and $\boldsymbol{x}_s$ is the source position. A similar expression can be derived also for a dipole source as

$$p_{\text{dip}}(\boldsymbol{x},\boldsymbol{x}_s) = \frac{c_{\text{dip}}\, a_{\text{dip}}}{4\pi||\boldsymbol{x}-\boldsymbol{x}_s||}\frac{(\boldsymbol{x}-\boldsymbol{x}_s)\cdot(\cos\theta_F,\sin\theta_F,0)}{||\boldsymbol{x}-\boldsymbol{x}_s||^2}(-1+ik||\boldsymbol{x}-\boldsymbol{x}_s||)e^{ik||\boldsymbol{x}-\boldsymbol{x}_s||}, \tag{2.23}$$

where c_{dip} is a reduction coefficient which takes into account the lower radiation efficiency of the dipole with respect to the monopole [4] and θ_F determines the angle of the dipole orientation. Equations (2.22) and (2.23) can be used to model the sound propagation between source and receiver in noise-localization techniques, as will be illustrated in Chapter 4.1.

2.2. AEROACOUSTIC ANALOGIES

The linear acoustic theory presented in Chapter 2.1 provides a valid framework to understand the generation and the propagation of sound waves in a quiescent fluid. How this theory can also be transposed to model the noise generated by a turbulent flow through the aeroacoustic analogies is the topic of the present section.

2.2.1. LIGHTHILL'S ANALOGY

The concept at the basis of the analogy of Lighthill [5] is that the flow mechanisms responsible for the sound emitted by a turbulent flow can be represented, from the listener's point of view, by equivalent sources placed in a quiescent uniform medium. This approach has proven to be effective especially for low-Mach number applications. The mathematical formulation of the analogy is reported hereafter.

In absence of external forces acting on the flow and mass injecting in the control volume, Equation (2.6) may be rewritten in function of the density perturbation by adding the term $-c_0^2\nabla^2\rho'$ on both sides of the equation:

$$\frac{\partial^2\rho'}{\partial t^2} - c_0^2\frac{\partial^2\rho'}{\partial {x_{\text{i}}}^2} = \frac{\partial^2 T_{\text{ij}}}{\partial x_{\text{i}}\partial x_{\text{j}}} \tag{2.24}$$

$$\text{with} \qquad T_{\text{ij}} = \rho u_{\text{i}}u_{\text{j}} - \tau_{\text{ij}} + (p' - c_0^2\rho')\delta_{\text{ij}}, \tag{2.25}$$

where $\boldsymbol{T}$ is denoted as Lighthill's stress tensor. In this case, the reference state $(\bar{\rho};\ \bar{p})$ refers to a uniform medium at rest that is assumed to be far from the unsteady flow producing sound.

For high Reynolds numbers, the contribution of the viscous forces can be neglected and with the assumption of incompressible and isentropic flow, Lighthill's stress tensor can be approximated as $T_{\text{ij}} \approx \rho u_{\text{i}}u_{\text{j}}$. For an unbounded domain, Equation (2.24) can be then solved by means of the free-field Green's function in Equation (2.13), resulting in

$$\rho'(\boldsymbol{x},t) = \frac{\partial^2}{\partial x_{\text{i}}\partial x_{\text{j}}}\iiint_{\mathbb{V}}\frac{T_{\text{ij}}}{4\pi c_0^2||\boldsymbol{x}-\boldsymbol{y}||}\,dV. \tag{2.26}$$

Equation (2.26) indicates that, at low-Mach numbers, i.e. when the assumption of incompressibility is valid, free isentropic turbulent flows without solid bodies can be de-

scribed as a quadrupole-like source related to the fluctuating stresses. The present formulation can be further simplified by introducing the concept of acoustic compactness. A source region is defined acoustically compact when its size l is much smaller than the acoustic wavelength $\lambda = c_0/f$, hence $l/\lambda = He_l \ll 1$, He_l being the non-dimensional Helmholtz number. Under this condition, the source region can be considered as a single-point source and the sound field at the observer's location has a characteristic gradient length that is imposed by the plane wave behavior at the same position, resulting in the approximation $\partial/\partial x_i \approx -\partial/(c_0 \partial t)$. In this case, the homogeneous wave-propagation equation reduces to the Laplace equation describing an incompressible potential flow.

2.2.2. CURLE'S ANALOGY

Equation (2.26) corresponds to an acoustic field in absence of solid boundaries. In presence of a solid and stationary surface $\mathbb{S}$ in the control domain, the solution of Equation (2.24) can be expressed by [6]

$$\rho'(\boldsymbol{x},t) = \frac{1}{c_0^2}\int_{-\infty}^{t}\iiint_{\mathbb{V}} \frac{\partial^2 T_{ij}}{\partial y_i \partial y_j} G\, dV d\tau - c_0^2 \int_{-\infty}^{t}\iint_{\mathbb{S}} \left(\rho' \frac{\partial G}{\partial y_i} - G\frac{\partial \rho'}{\partial y_i}\right) n_i\, dS d\tau, \tag{2.27}$$

where $\boldsymbol{n}$ is the outward-pointing normal on the surface $\mathbb{S}$. The first term in the right-hand side of the equation indicates the incident acoustic field, while the second one is linked to the scattered acoustic field given by the surface response and vibration. The incident-field integral can be reformulated by performing an integration by parts as

$$\begin{aligned}\int_{-\infty}^{t}\iiint_{\mathbb{V}} \frac{\partial^2 T_{ij}}{\partial y_i \partial y_j} G\, dV d\tau &= \int_{-\infty}^{t}\iiint_{\mathbb{V}} T_{ij}\frac{\partial^2 G}{\partial y_i \partial y_j}\, dV d\tau \\ + \int_{-\infty}^{t}\iint_{\mathbb{S}} \left\{\left(-\frac{\partial \rho u_i}{\partial \tau} - c_0^2\frac{\partial \rho'}{\partial y_i}\right) G - \left[\rho u_i u_j + \left(p' - c_0^2\rho'\right)\delta_{ij} + \tau_{ij}\right]\frac{\partial G}{\partial y_j}\right\} n_i\, dS d\tau.\end{aligned} \tag{2.28}$$

The terms $-\partial \rho u_i/\partial \tau$ and $\rho u_i u_j$ inside the surface integral can be assumed equal to zero for a rigid and impermeable body.

Furthermore, if the free-field Green's function is applied and Equation (2.28) is substituted into Equation (2.27), Curle's solution to the Lighthill's equation for an incompressible and isentropic flow can be derived as [7]

$$\rho'(\boldsymbol{x},t) = \frac{\partial^2}{\partial x_i \partial x_j}\iiint_{\mathbb{V}} \frac{\rho u_i u_j}{4\pi c_0^2 ||\boldsymbol{x}-\boldsymbol{y}||}\, dV - \frac{\partial}{\partial x_i}\iint_{\mathbb{S}} \frac{p' n_i}{4\pi c_0^2 ||\boldsymbol{x}-\boldsymbol{y}||}\, dS. \tag{2.29}$$

The outcome of the analysis carried out by Curle is that, when a surface is immersed in a turbulent flow, a second term in addition to the Lighthill's stress tensor contributes to the radiated sound. Physically, this term is a distribution of dipoles that represents fluctuating forces acting on the fluid from the solid body and accounts for reflection and diffraction effects. Hence, the sound field is seen as a sum of a volume distribution of quadrupoles and a surface distribution of dipoles in a medium at rest. Moreover, if the solid body is considered acoustically compact, the surface integral reduces to a compact

dipole, which, at low Mach numbers, dominates over the volume integral. Therefore, Equation (2.29) can be rewritten as

$$\rho'(\boldsymbol{x},t) \approx \frac{x_\mathrm{i}}{4\pi||\boldsymbol{x}-\boldsymbol{x}_s||^2 c_0^3}\left[\frac{\partial}{\partial t}\iint_{\mathbb{S}} p' n_\mathrm{i}(\boldsymbol{y})\,dS\right]_{t=\hat{t}}. \tag{2.30}$$

From Equation (2.30), it is possible to derive a scaling law for the dipole source term considering (i) that the force on the surface typically scales with the square of the mean flow velocity around the body [2], i.e. the surface integral is proportional to $\bar{\rho}\bar{u}^2 A_S$, A_S being the surface area of the body, and (ii) that the timescale of the velocity fluctuations can be estimated by the ratio of the typical turbulence dimension L to the mean flow speed. By defining the acoustic intensity of the far field I_r as $I_r = p_\mathrm{rms}^2/\bar{\rho}c_0$, $p_\mathrm{rms} = |p'|/\sqrt{2}$ being the root mean square (r.m.s.) of the pressure fluctuations, it follows that

$$I_r \propto \frac{\bar{\rho}\bar{u}^6 A_S^2 \cos\theta_F{}^2}{(4\pi||\boldsymbol{x}-\boldsymbol{x}_s||)^2 c_0^3 L^2}. \tag{2.31}$$

As a consequence of Equation (2.31), when an acoustically compact rigid body is immersed in a turbulent flow, the resulting noise is expected to scale as the sixth power of the mean flow velocity.

2.3. RAPID DISTORTION THEORY

As mentioned in Chapter 1.1.1, the distortion of turbulence in the interaction with a thick airfoil can have a significant effect on the corresponding leading-edge noise. Indeed, it follows from Equation (2.30) that the flow noise radiated by a wing profile is directly related to the pressure fluctuations on its surface. These are, in turn, affected by the changes that turbulence experiences close to the body. The investigation of such modifications can, therefore, shed light upon the generated noise and, when porous materials are integrated into the volume of the airfoil, upon the sound-mitigation mechanism associated with this technology.

In view of the above, the RDT allows calculating the turbulent flow around a bluff body when this distortion occurs rapidly and will be employed in Chapter 6 to derive an analytical model that predicts the alterations in the turbulent flow due to porosity. The present section aims to briefly introduce the analytical framework at the basis of such a theory.

Figure 2.3 depicts the typical problem that is addressed by the RDT, where a two-dimensional isolated bluff body is immersed in a flow characterized by weak turbulence. Different flow regions can be identified: an outer region (E) where the normal and shear stresses are negligible compared with the inertial forces, a thin region (B) in correspondence with the boundary layer developing at the surface $\mathbb{S}$, and a separated region (W) in the wake of the body where large velocity fluctuations occur. The reference system is defined as follows: the x-axis is aligned with the streamwise direction, the z-axis is aligned with the spanwise direction, and the y-axis is oriented in the normal direction in order to form a right-handed coordinate system with the two previous axes, with the origin set at the body center.

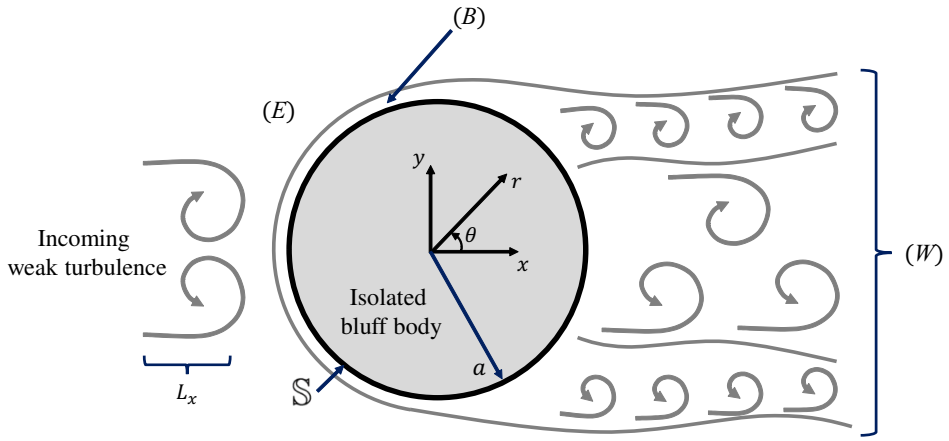

Figure 2.3: Schematic of the regions of flow surrounding a bluff body and the relevant dimensions represented by the body characteristic length and the scale of the incident turbulence. The different regions characterizing the flow field and the spatial reference systems considered in the present study are indicated. Adapted from [8].

2.3.1. ASSUMPTIONS OF THE THEORY

The RDT rests upon the following assumptions:

- the incoming turbulence is assumed to be weak:

$$\frac{u'_\infty}{\bar{u}_\infty} \ll 1, \tag{2.32}$$

  u'_∞ being the turbulence intensity and $\bar{u}_\infty$ being the mean value of the streamwise component of the upstream velocity;

- the Reynolds number based on the intensity of the upstream turbulence and turbulent integral length scale is assumed to be large:

$$\frac{u'_\infty L_x}{\nu} \gg 1, \tag{2.33}$$

  where L_x is the streamwise integral length scale and ν is the kinematic viscosity of the fluid;

- the time taken for the flow to be distorted, T_D, is much smaller than the timescale of turbulence, T_L. The former can be estimated as the ratio of the characteristic dimension of the cylinder, i.e. its radius a, to the mean value of the upstream velocity, i.e. $T_D = a/\bar{u}_\infty$, while the latter is the time taken for a fluid element to pass through a large eddy of scale L_x, i.e. $T_L = L_x/u'_\infty$, and amounts to approximately the time for the velocity autocorrelation of this element to be reduced to 1/3 [9]. Therefore, the present assumption may be rewritten as

$$\frac{u'_\infty}{\bar{u}_\infty} \ll \frac{L_x}{a}. \tag{2.34}$$

This equation does not need to be verified locally for every turbulence scale but rather constitutes an average criterion for the application of the linear theory [10].

Under the above conditions, the flow in the region (E) of Figure 2.3 is only slightly affected by the velocity fluctuations generated in the region (B) and (W) and can be represented by the solution of a well-posed boundary value problem determining the changes in a given fluctuating-velocity field [8].

2.3.2. GOVERNING EQUATIONS

The linearized momentum equations for an incompressible flow read[1]

$$\frac{\partial u_i'}{\partial t^*} + \bar{u}_j \frac{\partial u_i'}{\partial x_j^*} + u_j' \frac{\partial \bar{u}_i}{\partial x_j^*} = -\frac{1}{\rho^*} \frac{\partial p^*}{\partial x_i^*}. \tag{2.35}$$

By taking the curl of Equation (2.35) and considering the continuity equations

$$\frac{\partial \bar{u}_i}{\partial x_i^*} = 0 \quad \text{and} \quad \frac{\partial u_i'}{\partial x_i^*} = 0, \tag{2.36}$$

the dependence on pressure is avoided and the dimensionless linearized vorticity equations under the RDT assumptions can be derived as [8]

$$\frac{\partial \omega_i}{\partial t} + U_j \frac{\partial \omega_i}{\partial x_j} + u_j \frac{\partial \Omega_i}{\partial x_j} + \left\{ u_j \frac{\partial \omega_i}{\partial x_j} \right\} = \omega_j \frac{\partial U_i}{\partial x_j} + \Omega_j \frac{\partial u_i}{\partial x_j} + \left\{ \omega_j \frac{\partial u_i}{\partial x_j} \right\}, \tag{2.37}$$

where $\boldsymbol{U} = \bar{\boldsymbol{u}}/\bar{u}_\infty$, $\boldsymbol{u} = \boldsymbol{u}'/\bar{u}_\infty$, and $(x, y, z, t) = (x^*, y^*, z^*, t^*\bar{u}_\infty)/a$. $\boldsymbol{\Omega}$ and $\boldsymbol{\omega}$ are the corresponding vorticity terms and are defined as $\boldsymbol{\Omega} = \nabla \times \boldsymbol{U}$ and $\boldsymbol{\omega} = \nabla \times \boldsymbol{u}$. If Equation (2.32) is satisfied, the term in braces in the left-hand side of Equation (2.37), which represents the advection of the turbulence vorticity by the fluctuating velocity, is negligible. Likewise, the condition expressed by Equation (2.34) enables neglecting the term in braces in the right-hand side of Equation (2.37), which defines the rate of stretching and rotation of $\boldsymbol{\omega}$ by the fluctuating-velocity gradients. This is a consequence of the random variation of $\boldsymbol{u}$ during the period of the distortion given by T_L [8].

For bluff-body flows such as that around a circular cylinder, the irrotational component of $\boldsymbol{U}$ has typically the most substantial effect on turbulence and it is thus possible to assume

$$\boldsymbol{\Omega} = 0 \tag{2.38}$$

in Equation (2.37). The present assumption is also verified by the order-of-magnitude analysis carried out by Hunt [8]. The mean velocity field can then be determined as the solution to a potential flow problem subjected to appropriate boundary conditions. Since the upstream velocity U_∞ is specified, only one condition needs to be imposed. For an impenetrable cylinder, the normal component of the incident velocity must vanish at the wall:

$$\boldsymbol{u} \cdot \boldsymbol{n} = 0 \qquad \text{on} \quad \mathbb{S}, \tag{2.39}$$

[1] In this subsection, the superscript * for $\boldsymbol{x}$, t, p, and ρ denotes dimensional quantities.

$\boldsymbol{n}$ being the outward-pointing normal to the body surface $\mathbb{S}$. The resulting potential flow around a solid cylinder will be described in Chapter 6.2.1. Subsequently, $\boldsymbol{\omega}$ can be derived from Cauchy's equation as a function of its upstream value $\boldsymbol{\omega}_\infty$ [11] and the vorticity distortion tensor $\boldsymbol{\gamma}$:

$$\omega_\mathrm{i}\left(x,y,z,t\right) = \gamma_\mathrm{ij}\left(x,y\right)\omega_{\infty,\mathrm{j}}\left(x,y-\Delta_y,z,t-\Delta_T\right). \tag{2.40}$$

Δ_y is the deviation of a fluid particle in the y-direction as it travels around the body and is expressed by $\Delta_y = y + \Psi$, Ψ being the streamfunction of the irrotational mean flow, while Δ_T is the *drift* function [12] defined as

$$\Delta_T = \int_{-\infty}^{x}\left(\frac{1}{U_x(x',y')}-1\right)dx' \quad \text{where} \quad \Psi(x',y') = \Psi(x,y). \tag{2.41}$$

Analytical formulations for Δ_T and Δ_y as functions of Ψ for the flow around a circular cylinder are available and will be discussed in Chapter 6.3. In this case, $\boldsymbol{\gamma}$ can be expressed as a function of $\boldsymbol{U}$ and the derivatives of Δ_T along x and y [8]:

$$\gamma_\mathrm{ij} = \begin{bmatrix} U_x & -\partial\Delta_T/\partial y & 0 \\ U_y & 1+\partial\Delta_T/\partial x & 0 \\ 0 & 0 & 1 \end{bmatrix}. \tag{2.42}$$

Once $\boldsymbol{U}$ and $\boldsymbol{\omega}$ are known, $\boldsymbol{u}$ may be calculated by expressing its deviation from the upstream value in terms of a scalar velocity potential ϕ and a vortical streamfunction $\boldsymbol{\psi}$, specified by the gauge condition $\nabla\cdot\boldsymbol{\psi} = 0$ [13], such that

$$\Delta\boldsymbol{u} = \boldsymbol{u} - \boldsymbol{u}_\infty = -\nabla\phi + \nabla\times\boldsymbol{\psi}. \tag{2.43}$$

This Helmholtz decomposition of the velocity field is at the basis of the porous RDT model that will be described in Chapter 6. A new set of governing equations for the problem can now be derived by substituting Equation (2.43) into Equation (2.1) to give

$$\nabla^2\phi = 0 \tag{2.44}$$

and into Equation (2.37) to give

$$\nabla^2\boldsymbol{\psi} = -\Delta\boldsymbol{\omega} = -(\boldsymbol{\omega}-\boldsymbol{\omega}_\infty). \tag{2.45}$$

For Equation (2.44), the boundary conditions expressed by Equation (2.39) and by the imposition of the upstream velocity are satisfied separately, resulting in

$$\nabla\phi\cdot\boldsymbol{n} = \boldsymbol{u}_\infty\cdot\boldsymbol{n} \qquad \text{on} \quad \mathbb{S} \tag{2.46}$$

and

$$|\nabla\phi| \to 0 \qquad \text{as} \quad x^2+y^2\to\infty, \tag{2.47}$$

while the same conditions applied to Equation (2.45) yield

$$(\nabla\times\boldsymbol{\psi})\cdot\boldsymbol{n} = 0 \qquad \text{on} \quad \mathbb{S} \tag{2.48}$$

and

$$|\nabla \times \boldsymbol{\psi}| \to 0 \qquad \text{as} \quad x^2 + y^2 \to \infty. \tag{2.49}$$

Besides, an additional boundary condition has to be imposed on $\boldsymbol{\psi}$ in order to satisfy the gauge condition everywhere:

$$\nabla \cdot \boldsymbol{\psi} = 0 \qquad \text{on} \quad \mathbb{S} \qquad \text{and} \quad \text{as} \quad x^2 + y^2 \to \infty. \tag{2.50}$$

Four partial differential equations have then to be solved simultaneously: the Laplace equation for ϕ in Equation (2.44) and the three Poisson equations for $\boldsymbol{\psi}$ in Equation (2.45). More efficient approaches to solve the RDT equations have been proposed, for instance, by Goldstein [14], but it will be argued in Chapter 6.2.4 that the decomposition of the velocity field proposed in Equation (2.43) provides a better framework to account for porosity.

2.3.3. FOURIER ANALYSIS

If the upstream turbulence is homogeneous and stationary in time, the velocity field shall be described by means of spatial Fourier analysis in terms of the velocity distortion tensor $\boldsymbol{M}$:

$$\hat{\hat{u}}_\mathrm{i} = \int_{-\infty}^{\infty} M_\mathrm{ij}(x, y; \boldsymbol{\kappa})\, \hat{\hat{u}}_{\infty,\mathrm{j}}(\boldsymbol{\kappa})\, d\kappa_2, \tag{2.51}$$

where $\boldsymbol{\kappa} = (\kappa_1, \kappa_2, \kappa_3)$ is the wavenumber vector made dimensionless by the cylinder radius a and $\hat{\hat{\boldsymbol{u}}}_\infty$ is the spatial Fourier transform of the upstream velocity coming from

$$\begin{pmatrix} u_{\infty,\mathrm{i}} \\ \omega_{\infty,\mathrm{i}} \end{pmatrix}(x, y, z, t) = \iiint_{-\infty}^{\infty} e^{i(\kappa_1 x + \kappa_2 y + \kappa_3 z + \sigma t)} \begin{pmatrix} \hat{\hat{u}}_{\infty,\mathrm{i}} \\ \hat{\hat{\omega}}_{\infty,\mathrm{i}} \end{pmatrix}(\boldsymbol{\kappa})\, d\kappa_1\, d\kappa_2\, d\kappa_3. \tag{2.52}$$

In Equation (2.52), $\sigma = -\kappa_1$ as a result of the application of Taylor's hypothesis. Near the body, the turbulence becomes inhomogeneous in the x and y directions but remains homogeneous in the z direction since the mean velocity is invariant along z. Therefore, following the decomposition of the velocity field in Equation (2.43), the Fourier analysis on ϕ and $\boldsymbol{\psi}$ yields

$$\begin{pmatrix} \phi \\ \psi_\mathrm{i} \end{pmatrix}(x, y, z, t) = \iint_{-\infty}^{\infty} e^{i(\kappa_3 z - \kappa_1 t)} \begin{pmatrix} \hat{\hat{\phi}} \\ \hat{\hat{\psi}}_\mathrm{i} \end{pmatrix}(\boldsymbol{\kappa})\, d\kappa_1\, d\kappa_3. \tag{2.53}$$

Equations (2.44) and (2.45) can now be rewritten as

$$\left\{ \frac{\partial^2}{dx^2} + \frac{\partial^2}{dy^2} - \kappa_3^2 \right\} \hat{\hat{\phi}} = 0 \tag{2.54}$$

and

$$\left\{ \frac{\partial^2}{dx^2} + \frac{\partial^2}{dy^2} - \kappa_3^2 \right\} \hat{\hat{\psi}}_\mathrm{i} = -\left[\hat{\hat{\omega}}_\mathrm{i} - \delta_\mathrm{ij} \int_{-\infty}^{\infty} e^{i(\kappa_1 x + \kappa_2 y)}\, \hat{\hat{\omega}}_{\infty,\mathrm{j}}\, d\kappa_2 \right], \tag{2.55}$$

respectively, where $\partial / \partial z = i\kappa_3$ due to the homogeneity in the z direction and $\boldsymbol{\delta}$ is the Kronecker delta. From Equation (2.40), it follows that

$$\hat{\hat{\omega}}_\mathrm{i} = \gamma_\mathrm{ij}(x, y)\, e^{i\kappa_1(\Delta_T + x)} \int_{-\infty}^{\infty} e^{i\kappa_2(y - \Delta_y)}\, \hat{\hat{\omega}}_{\infty,\mathrm{j}}\, d\kappa_2. \tag{2.56}$$

Two new variables can be introduced in order to further simplify the governing equations:

$$\hat{\tilde{\phi}}(x,y,\kappa_1,\kappa_3) = \int_{-\infty}^{\infty} \beta_j(x,y,\boldsymbol{\kappa})\,\hat{u}_{\infty,j}(\boldsymbol{\kappa})\,d\kappa_2; \tag{2.57}$$

$$\hat{\tilde{\psi}}_i(x,y,\kappa_1,\kappa_3) = \int_{-\infty}^{\infty} \alpha_{ij}(x,y,\boldsymbol{\kappa})\,\hat{\omega}_{\infty,j}(\boldsymbol{\kappa})\,d\kappa_2. \tag{2.58}$$

The tensor $\boldsymbol{\alpha}$ is the turbulent streamfunction, while the vector $\boldsymbol{\beta}$ is the turbulent-velocity potential. Substituting Equation (2.57) into Equation (2.54), and Equations (2.58) and (2.56) into Equation (2.55) yields

$$\left\{\frac{\partial^2}{dx^2} + \frac{\partial^2}{dy^2} - \kappa_3^2\right\}\beta_j = 0; \tag{2.59}$$

$$\left\{\frac{\partial^2}{dx^2} + \frac{\partial^2}{dy^2} - \kappa_3^2\right\}\alpha_{ij} = -\Omega^\star_{ij} \qquad \text{with} \qquad \Omega^\star_{ij} = \left[\gamma_{ij}\,e^{i(\kappa_1\Delta_t - \kappa_2\Delta_y)} - \delta_{ij}\right] e^{i(\kappa_1 x + \kappa_2 y)}. \tag{2.60}$$

$\boldsymbol{\Omega}^\star$ is a known function that tends to zero as $x \to -\infty$ or $y \to \pm\infty$ since $\Delta_T, \Delta_y \to 0$ and $\boldsymbol{\gamma} \to \boldsymbol{\delta}$. For a formal statement of the problem, the boundary conditions need to be reformulated in terms of $\boldsymbol{\alpha}$ and $\boldsymbol{\beta}$. In Chapter 6.2, these will be derived for the case of a solid and porous circular cylinder.

Considering that $\hat{\boldsymbol{u}} = -\nabla\hat{\tilde{\phi}} + \nabla\times\hat{\tilde{\boldsymbol{\psi}}} + \hat{\boldsymbol{u}}_\infty$, it follows from Equations (2.57) and (2.58) that

$$\hat{u}_i = \int_{-\infty}^{\infty} \left\{\left(M^{(s)}_{ij} + M^{(\infty)}_{ij}\right)\hat{u}_{\infty,j} + a_{ij}\,\hat{\omega}_{\infty,j}\right\} d\kappa_2, \tag{2.61}$$

where

$$\begin{aligned} M^{(s)}_{ij} &= -\left(\frac{\partial\beta_j}{\partial x}, \frac{\partial\beta_j}{\partial y}, i\kappa_3\beta_j\right); \quad M^{(\infty)}_{ij} = \delta_{ij}e^{i(\kappa_1 x+\kappa_2 y)}; \\ a_{ij} &= \left(\frac{\partial\alpha_{3j}}{\partial y} - i\kappa_3\alpha_{2j}, i\kappa_3\alpha_{1j} - \frac{\partial\alpha_{3j}}{\partial x}, \frac{\partial\alpha_{2j}}{\partial x} - \frac{\partial\alpha_{1j}}{\partial y}\right). \end{aligned} \tag{2.62}$$

It is now convenient to express $\boldsymbol{\alpha}$ in terms of $\hat{\boldsymbol{u}}_\infty$. It follows from the definition of vorticity that $\hat{\omega}_{\infty,i} = \varepsilon_{ijk}\left(\partial\hat{u}_{\infty,k}/\partial x_j\right) = \varepsilon_{ijk}\left(i\kappa_j\hat{u}_{\infty,k}\right)$, ε_{ijk} being the Levi-Civita symbol. By defining

$$M^{(d)}_{il} = i\,a_{ij}\varepsilon_{kjl}\kappa_k, \tag{2.63}$$

Equation (2.51) is finally recovered with the notation

$$\boldsymbol{M} = \boldsymbol{M}^{(s)} + \boldsymbol{M}^{(d)} + \boldsymbol{M}^{(\infty)}. \tag{2.64}$$

2.3.4. SPECTRA AND VARIANCES

The solutions for $\boldsymbol{M}$ can then be used to calculate the two-dimensional spectra $\boldsymbol{\Psi}_{ij}$, the one-dimensional spectra $\boldsymbol{\Theta}_{ij}$, and the variances at two points $\overline{u_i u_j}(x,y)$ near the body as a function of the three-dimensional spectrum $\boldsymbol{\Theta}_\infty$ of the upstream turbulence:

$$\boldsymbol{\Psi}_{ij}(x,y;\kappa_1,\kappa_3) = \int_{-\infty}^{\infty} M_{il}(x,y;\boldsymbol{\kappa})^\dagger\,M_{jm}(x,y;\boldsymbol{\kappa})\,\boldsymbol{\Theta}_{\infty,lm}(\boldsymbol{\kappa})\,d\kappa_2; \tag{2.65}$$

$$\boldsymbol{\Theta}_{ij}(x,y;\kappa_1) = \int_{-\infty}^{\infty} \boldsymbol{\Psi}_{ij}(x,y;\kappa_1,\kappa_3)\, d\kappa_3; \tag{2.66}$$

$$\overline{u_i u_j}(x,y) = \int_{-\infty}^{\infty} \boldsymbol{\Theta}_{ij}(x,y;\kappa_1)\, d\kappa_1, \tag{2.67}$$

where the symbol † denotes the complex conjugate. For isotropic turbulence, $\boldsymbol{\Theta}_\infty$ may be represented by the von Kármán spectrum normalized in terms of the r.m.s. incident turbulent velocity and the cylinder characteristic dimension [15]:

$$\boldsymbol{\Theta}_{\infty,ij}(\boldsymbol{\kappa}) = \frac{55 g_1 (a/L_x)^{\frac{2}{3}} k^2}{36\pi \left[g_2 (a/L_x)^2 + k^2\right]^{\frac{17}{6}}} \left[\delta_{ij} - \frac{\kappa_i \kappa_j}{k^2}\right], \tag{2.68}$$

with $k^2 = \kappa_1^2 + \kappa_2^2 + \kappa_3^2 = |\boldsymbol{\kappa}|^2$ and g_1 and g_2 that are computed through the gamma function, namely $g_2 = \pi\Gamma^2(5/6)/\Gamma^2(1/3) = 0.5578$ and $g_1 = g_2^{5/6}/\pi = 0.1957$. The turbulence distortion can then be fully predicted by calculating $\boldsymbol{M}(x,y;\boldsymbol{\kappa})$ at each point around the body and for each wavenumber component. In Chapter 6, the RDT will be applied to calculate the velocity tensor for a solid and porous cylinder.

REFERENCES

[1] R. Zamponi, S. Moreau, and C. Schram, *Rapid distortion theory of turbulent flow around a porous cylinder,* Journal of Fluid Mechanics **915**, A27 (2021).

[2] S. A. L. Glegg and W. Devenport, *Aeroacoustics of low Mach number flows: fundamentals, analysis, and measurement* (Academic Press, London, 2017).

[3] A. Hirschberg, *Introduction to aeroacoustics of internal flows,* in *Basics of Aeroacoustics and Thermoacoustics*, Von Karman Institute Lecture series 2007-09 No. 0377-8312, edited by J. Anthoine (2007) pp. 1–112.

[4] T. Suzuki, *L1 generalized inverse beam-forming algorithm resolving coherent/incoherent, distributed and multipole sources,* Journal of Sound and Vibration **330**, 5835 (2011).

[5] *On sound generated aerodynamically I. General theory,* Proceedings of the Royal Society of London. Series A. Mathematical and Physical Sciences **211**, 10.1098/rspa.1952.0060.

[6] M. E. Goldstein, *Aeroacoustics*, NASA SP (Scientific and Technical Information Office, National Aeronautics and Space Administration, 1974).

[7] N. Curle, *The influence of solid boundaries upon aerodynamic sound,* Proceedings of the Royal Society of London. Series A. Mathematical and Physical Sciences **231**, 505 (1955).

[8] J. C. R. Hunt, *A theory of turbulent flow round two-dimensional bluff bodies,* Journal of Fluid Mechanics **61**, 625 (1973).

[9] H. Tennekes and J. L. Lumley, *A first course in turbulence* (MIT Press, Cambridge, Mass, 1972).

[10] J. Hunt, H. Kawai, S. Ramsey, G. Pedrizetti, and R. Perkins, *A review of velocity and pressure fluctuations in turbulent flows around bluff bodies,* Journal of Wind Engineering and Industrial Aerodynamics **35**, 49 (1990).

[11] G. K. Batchelor and I. Proudman, *The effect of rapid distortion of a fluid in turbulent motion,* The Quarterly Journal of Mechanics and Applied Mathematics **7**, 83 (1954).

[12] M. J. Lighthill, *Drift,* Journal of Fluid Mechanics **1**, 31 (1956).

[13] G. K. Batchelor, *An Introduction to Fluid Dynamics*, 1st ed. (Cambridge University Press, 2000).

[14] M. E. Goldstein, *Unsteady vortical and entropic distortions of potential flows round arbitrary obstacles,* Journal of Fluid Mechanics **89**, 433 (1978).

[15] G. K. Batchelor, *The theory of homogeneous turbulence*, Cambridge University Press. (Cambridge University Press, 1953).

3

EXPERIMENTAL SETUP

The true method of knowledge is experiment.

William Blake

This chapter has the objective to introduce the main tools and techniques that are employed for carrying out the measurement campaigns presented in the thesis. The experiments take place in two vertical open-jet wind tunnels that are briefly illustrated. The turbulent flow interacting with the wing profile is produced by placing an upstream cylindrical rod, in the so-called rod-airfoil configuration. The integration of porosity into the airfoil structure is performed by fitting melamine foam in a permeable hard-plastic exoskeleton with the shape of a NACA-0024 profile. The porous parameters and sound-absorbing behavior of the melamine foam are characterized by means of impedance tube measurements. Finally, a description of the different experimental setups is provided. These include hot-wire anemometry for the qualification of the nozzle-flow and the investigation of the flow field around the airfoils, microphone-array acquisitions for the study of the far-field noise emissions, and PIV for the flow-field visualization.

Parts of this chapter are included in [1–5].

3.1. EXPERIMENTAL FACILITIES

The experimental work described in this manuscript is carried out in two different facilities, namely the JAFAR anechoic chamber of the von Karman Institute for Fluid Dynamics (VKI) and the A-tunnel facility of Delft University of Technology (TUD).

3.1.1. VKI JAFAR FACILITY

The JAFAR testing facility has been originally developed by Schram [6] and subsequently adapted by de Santana [7] and Guariglia *et al.* [8], and consists of a vertical open-jet wind tunnel situated in a 4 m × 3 m × 4 m semi-anechoic room equipped with acoustic absorbing melamine foam. The chamber has a cutoff frequency of 200 Hz, i.e. free–field conditions apply for higher frequencies [9]. A sketch of the facility is illustrated in Figure 3.1. The circuit is initially fed by pressure at 35 bar. An electrical ball valve with a safety return battery is employed to turn on and off the system. The pressure is subsequently decreased by a pilot-controlled pressure regulator and flow enters a buffer tank set at 10 bar. The volume of the tank is 500 l, leading to a residence time of the flow of approximately 3.5 s.

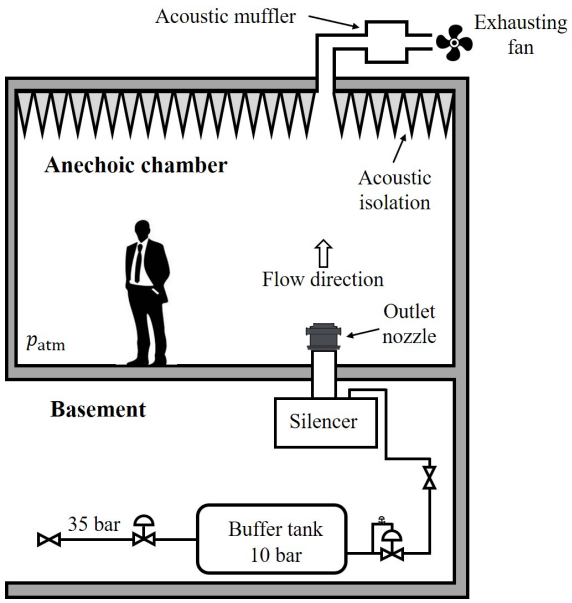

Figure 3.1: Sketch of JAFAR facility of VKI. Adapted from [8].

A pressure line is directed from the buffer tank to the silencer and is equipped with pressure regulators that allow for a variation of the mass-flow rate. The silencer has the function to provide an anechoic termination for the outlet nozzle by mitigating the noise generated by the air supply system and preventing spurious acoustic excitations of the flow [8]. A 0.3 m-diameter duct that guides the flow into the anechoic chamber is placed downstream of this component. A circular-to-rectangular contraction designed by De Santanta [7] adapts the circular geometry of the upstream duct to the desired rectangular

geometry of the exhaust nozzle. The contraction ratio is 2.35 to 1 and the outlet nozzle exit has a span of $s = 0.200\,\text{m}$ and a width of $l = 0.150\,\text{m}$. The qualification of the nozzle flow will be described in Chapter 3.5.1. Finally, the flow from the jet is extracted by an exhausting fan placed at the top of the chamber.

3.1.2. TUD A-TUNNEL FACILITY

The A-tunnel facility is a vertical open–jet wind tunnel that is situated in an anechoic chamber equipped with Flamex Basic acoustic absorbing foam and is characterized by a cutoff frequency of 250 Hz. A sketch showing the side view of the facility is illustrated in Figure 3.2, while a detailed description of its design and main features is provided by Merino-Martínez *et al.* [10].

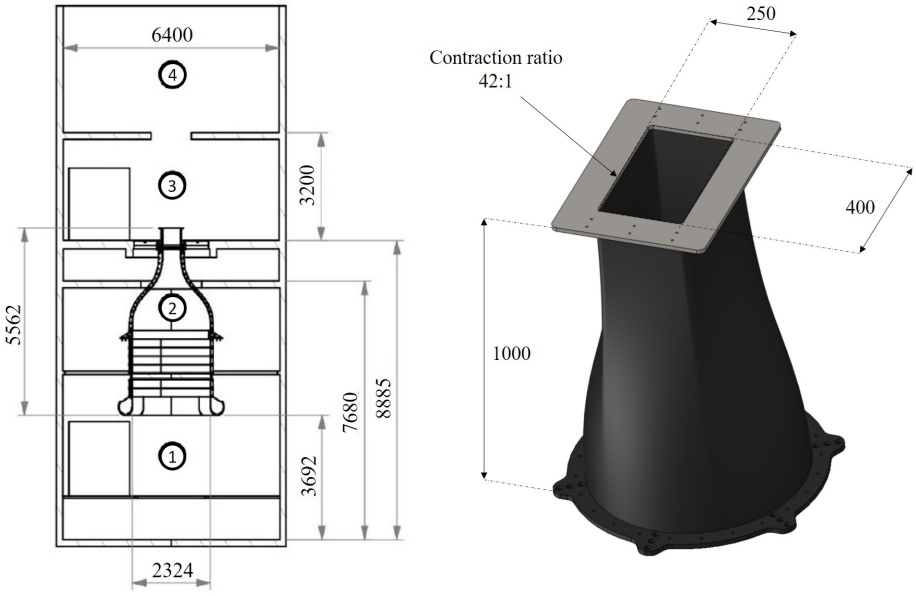

Figure 3.2: Sketch of the A-Tunnel facility of TUD and the outlet nozzle and exit plane employed for the measurements. The side view of the facility (adapted from [10]) includes the settling chamber (1), contraction (2), open-jet test section (3), and fans and collector room (4). The distances are expressed in mm.

The outlet nozzle of the wind tunnel is flush-mounted at the exit of the contraction. It has a height of 1 m and features a rectangular exit plane with a contraction ratio of 42 to 1, a span of $s = 0.250\,\text{m}$, and a width of $l = 0.400\,\text{m}$. A sketch of the nozzle is depicted in Figure 3.2. The maximum velocity that can be reached with this configuration is $72\,\text{m}\,\text{s}^{-1}$ [10]. The qualification of the nozzle flow will be described in Chapter 3.5.2.

3.2. ROD-AIRFOIL CONFIGURATION

The experimental setup considered in the turbulence-interaction noise investigation involves a thick NACA-0024 airfoil immersed in the turbulent wake of an upstream cylin-

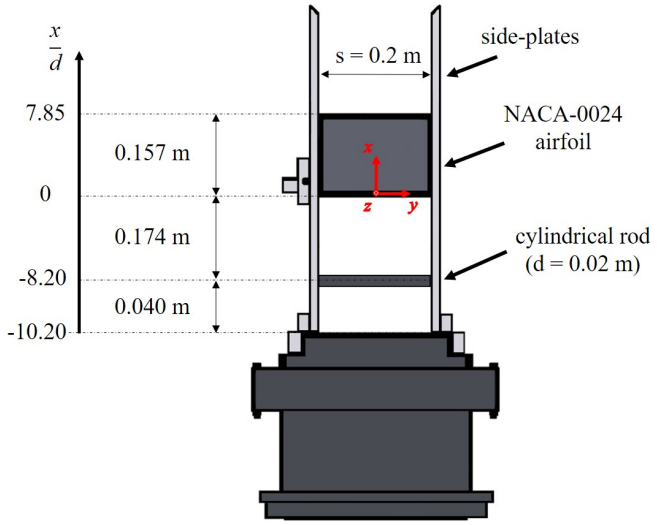

(a) Rod-airfoil configuration installed in the JAFAR facility of VKI.

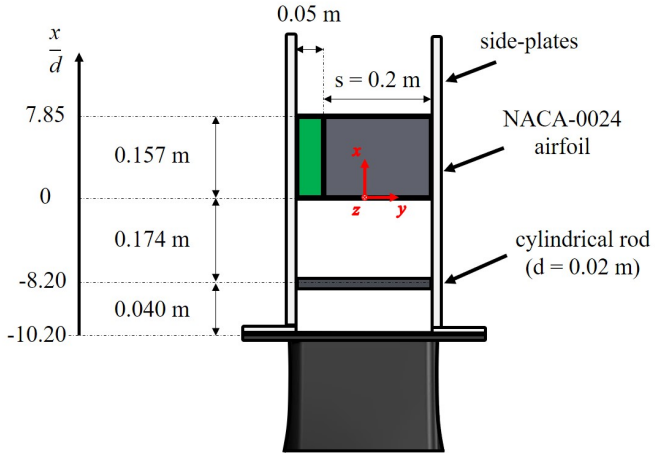

(b) Rod-airfoil configuration installed in the A-Tunnel facility of TUD.

Figure 3.3: Sketch of the experimental setups employed for airfoil-turbulence interaction noise measurements. The red arrows denote the coordinate axes of the reference system.

drical rod. In this arrangement, first proposed by Jacob *et al.* [11] as an aeroacoustic benchmark problem and addressed experimentally in several studies [7, 12–14], the airfoil undergoes a broadband perturbation dominated by a shedding frequency, similar to turbomachineries (e.g. the interaction between turbofan wake and OGVs discussed in Chapter 1.1), helicopter rotors, landing-gear applications, ventilating systems, and high-lift devices [15].

Figure 3.3a shows a sketch of the rod-airfoil configuration installed in the VKI JAFAR facility. Two side plates guide the flow from the outlet nozzle and support the $d = 0.020\,\mathrm{m}$

diameter rod and NACA-0024 profile, separated from each other by a distance of 0.174 m ($x/d = 8.20$). The airfoil chord is $c = 0.157$ m ($c/d = 7.85$) and the maximum thickness is approximately $t = 0.038$ m ($t/d = 1.90$). This value is designed in order to have the same radius for airfoil leading edge and rod.

Given the relatively low aspect ratio $s/c = 1.27$ of the airfoil, some precautions are taken to minimize the risk of contamination of the acoustic field by corner effects. Indeed, the junctions between airfoil and side plates are filled with a rounded fillet of clay with a radius approximately equal to 0.003 m that has the primary function to avoid gap noise [16]. Moreover, the thickness of the incoming boundary layer over the side plates is less than 0.002 m and is characterized by a turbulence intensity well below that of the incoming turbulence in the main stream.

The same rod-airfoil configuration installed in the JAFAR facility is adapted to be placed on the A-Tunnel outlet nozzle. A sketch of the setup is depicted in Figure 3.3b. Both NACA-0024 airfoil and cylindrical rod are held in place by Plexiglass side plates rigidly connected to the nozzle. The distances between rod and airfoil (0.174 m) and between outlet-nozzle exit and rod (0.040 m) are kept unchanged for comparison purposes. Nevertheless, an additional component is required to adapt the 0.200 m of the airfoil span to the 0.250 m of the exit plane width. A 3D-printed hard-plastic extension having the same shape as the NACA-0024 profile and a span of 0.050 m is manufactured to achieve this goal. Also in this case, clay is employed at the junctions between wing profile and side plate and between wing profile and hard-plastic extension in order to minimize gap noise.

The following reference system, indicated by the red arrows in Figure 3.3, is adopted for the presentation of the results: the x-axis is aligned with the flow direction, the z-axis is aligned with the spanwise direction of the airfoil, and the y-axis is oriented in the normal direction in order to form a right-handed coordinate system. The origin is set at the midspan leading edge of the airfoil mock-up.

3.3. DESIGN OF THE AIRFOILS

The same manufacturing technique is used to design the solid and porous versions of the airfoil. For both of them, a hard-plastic exoskeleton with a thickness of 0.002 m preserves the structural integrity of the model. This is made of two components, one per each side of the airfoil surface, that are glued together at the leading edge and trailing edge. The porous airfoil exoskeleton features hexagonal openings throughout its surface, with a side-to-side length of 0.004 m and an equivalent open area ratio of 80 % to allow for the penetration of the air flow into the inner region. Figure 3.4 illustrates a schematic of this component. The volume of the airfoil is filled with melamine foam. A hard-plastic impenetrable center-plane avoids the cross-flow between the two sides of the wing profile. However, its extent does not cover the first 6.4 % of the chord (one leading-edge radius) in order to enable the air-flow to penetrate at the stagnation point. Moreover, both airfoils are coated with the same metallic woven wire mesh, which protects the materials and guarantees an adequate quality surface roughness. This is characterized by an aperture of 0.198 mm, a wire diameter of 0.056 mm, and an open area ratio of 60.8 %. Figure 3.5 provides a sketch of the different parts of the porous airfoil.

Furthermore, a third airfoil just made of melamine foam is designed with the aim of

investigating the acoustic influence of exoskeleton and wire mesh. The melamine foam is cut in the shape of a NACA-0024 and glued on the solid center-plane, without any other hard-plastic component. Although this design does not represent a technological solution for the implementation of a porous material in the structure of the airfoil, it constitutes a basis of comparison for the study of the physical mechanisms involved in the flow field alterations due to the porous treatment. A picture of the three manufactured prototypes is shown in Figure 3.6.

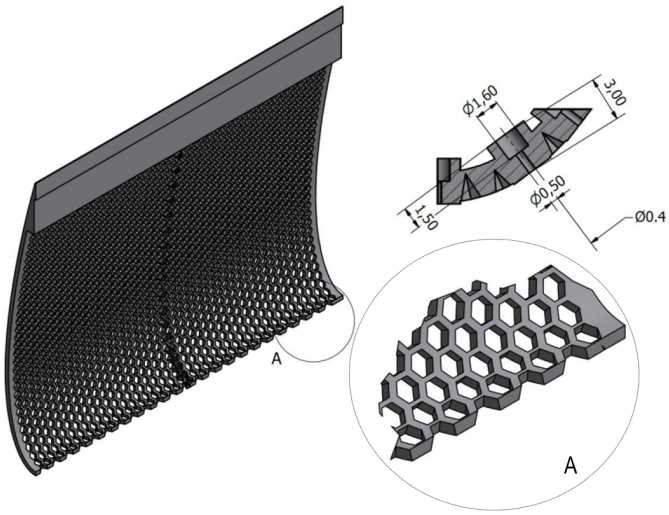

Figure 3.4: Structure of the permeable exoskeleton exhibiting the hexagonal openings and static-pressure ports.

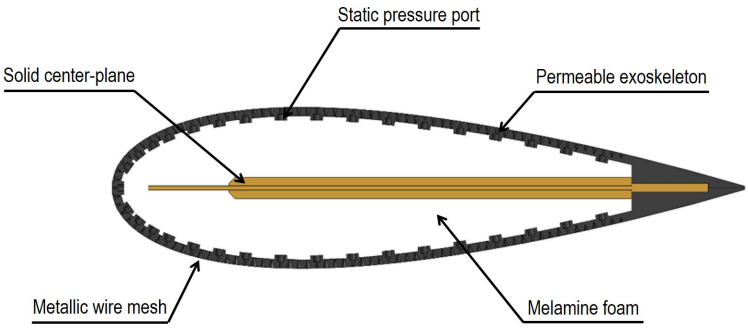

Figure 3.5: Representation of the porous NACA-0024 profile featuring solid center-plane, hard-plastic exoskeleton, metallic wire mesh, and static-pressure ports.

Finally, the solid and porous airfoils are equipped with 35 static pressure sensors distributed along both sides of the airfoils, at corresponding streamwise locations (Figure 3.5). The transducers are placed at the corners of the hexagonal openings in the midspan

Figure 3.6: Pictures of the solid (on the left), melamine (in the middle), and porous airfoils (on the right) manufactured at VKI.

of the exoskeleton, thereby minimizing the alterations in the local open area ratio, as shown in Figure 3.4. The x-coordinates of the sensors range from 1 % to almost 80 % of the chord. Furthermore, an additional measurement position is designed at the airfoil leading edge in order to acquire the stagnation pressure. The ports are then connected to an in-house signal conditioning and acquisition device for the evaluation of the mean wall-pressure distributions and data are acquired at a sampling frequency of 500 Hz for 15 s.

3.4. CHARACTERIZATION OF THE POROUS MEDIUM

In the present section, the main parameters defining a porous medium are listed and presented. Moreover, the experimental setups considered for the characterization of the porous material properties and the analysis of its sound-absorbing behavior are described. The measurements are conducted in collaboration with Centre de Transfert de Technologie du Mans (CTTM) and Laboratoire d'Acoustique de l'Université du Maine (LAUM). The results of the experiments have been used to calibrate and validate the direct hybrid LES/CAA method implemented by Satcunanathan *et al.* [17] in the framework of a collaboration between VKI and RWTH Aachen University.

3.4.1. JOHNSON-CHAMPOUX-ALLARD-LAFARGE MODEL

The Johnson-Champoux-Allard-Lafarge (JCAL) model describes visco-inertial and thermal dissipative effects inside a porous medium with a rigid frame. According to the model, the six parameters that are necessary to fully characterize the material are

- the static air-flow resistivity, σ, which is described by the relationship known as Darcy's law [18] and corresponds to the ratio of a pressure difference Δp across a sample of porous material in the presence of a static fluid flow through it to the product of the flow velocity and sample thickness;

- the porosity, ϕ, defined as the ratio of the accessible pore volume (since those pores that are closed and not accessible are not expected to have an influence on the acoustic and aerodynamic characteristics) to the total volume;

- the tortuosity, α_∞, which takes into account the sinuous fluid paths through the porous material;

- the viscous characteristic length, Λ, introduced by Johnson *et al.* [19], which considers the medium- and high-frequency viscous and inertial effects;
- the thermal characteristic length, Λ', defined by Champoux and Allard [20], which expresses the thermal exchanges between porous material frame and pore saturating fluid at medium- and high-frequencies;
- the thermal permeability, k_0', introduced by Lafarge *et al.* [21], which models the thermal exchanges between porous material frame and saturating fluid at low frequencies.

Besides these, another property used to define a porous medium is the static viscous permeability, k, which is directly linked to σ by the relationship $k = \mu/\sigma$, μ being the dynamic viscosity of air.

An expression to describe the complex density ρ_e of a porous material with a rigid frame having arbitrary pore shapes can be derived through the knowledge of the six parameters of the JCAL model as [19]

$$\rho_e(\omega) = \frac{\rho_0 \alpha_\infty}{\phi}\left[1 + \frac{\sigma\phi}{i\omega\rho_0\alpha_\infty}\sqrt{1 + i\frac{4\alpha_\infty^2\mu\rho_0\omega}{\sigma^2\Lambda^2\phi^2}}\right], \tag{3.1}$$

where ρ_0 and μ are the density and dynamic viscosity of the incompressible Newtonian fluid the material is saturated with, respectively. Similarly, a formulation for the dynamic bulk modulus for the same kind of porous material is [21]

$$K_e(\omega) = \frac{\gamma p_0}{\phi}\left\{\gamma - (\gamma - 1)\left[1 - i\frac{\phi\kappa}{k_0' c_P \rho_0 \omega}\sqrt{1 + \frac{4k_0' c_P \rho_0 \omega}{\kappa \Lambda'^2 \phi^2}}\right]^{-1}\right\}^{-1}, \tag{3.2}$$

where p_0, γ, κ, and c_P are the mean pressure, heat-capacity ratio, thermal conductivity, and specific heat of the fluid, respectively. Consequently, it is possible to determine the phase velocity c_e and characteristic impedance Z_{ce} from ρ_e and K_e:

$$c_e = \sqrt{\frac{K_e(\omega)}{\rho_e(\omega)}} \qquad Z_{ce} = \sqrt{K_e(\omega)\rho_e(\omega)}. \tag{3.3}$$

c_e and Z_{ce} will be employed in Chapter 3.4.3 to derive the absorption coefficient of the melamine foam predicted by the JCAL model.

3.4.2. STATIC AIR-FLOW RESISTIVITY TEST

The first experimental campaign for the characterization of the porous media included in the porous airfoil involves the determination of the static air-flow resistivity using the measurement unit of the standard ISO 9053-1:2018, which is depicted in Figure 3.7. The measurements have been performed in collaboration with J. Golliard from CTTM. σ is retrieved by measuring the pressure gradient Δp on both sides of a sample through which a stabilized flow with a volumetric rate Q_v passes:

$$\sigma = \frac{\Delta p S_S}{Q_v L}, \tag{3.4}$$

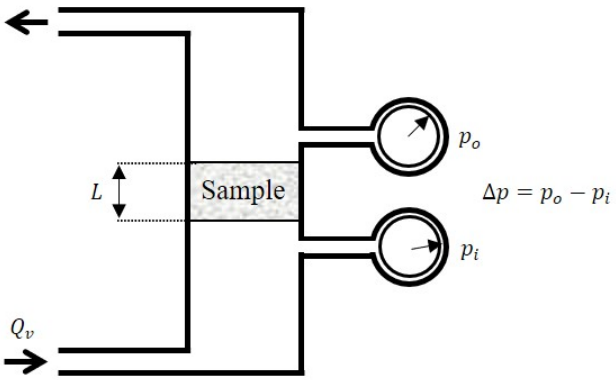

Figure 3.7: Schematic showing the static airflow resistivity measurement unit following the standard ISO 9053-1:2018.

where S_S is the cross-section area of the sample and L is its length. Three cylindrical samples of melamine foam with a diameter of 44.5 mm and a thickness of 15.5 mm are considered due to the anisotropic and inhomogeneous nature of the material. Furthermore, one additional sample composed of the hard-plastic exoskeleton (2.0 mm thick) coated with the metallic woven wire mesh (0.2 mm thick) and characterized by the same diameter is prepared to analyze the combination of the two layers.

The values of the static air-flow resistivity measured for the different samples are

- **Melamine sample** 1: $\sigma = 9215\,\mathrm{Pa\,s\,m^{-2}} \pm 700\,\mathrm{Pa\,s\,m^{-2}}$;
- **Melamine sample** 2: $\sigma = 8600\,\mathrm{Pa\,s\,m^{-2}} \pm 700\,\mathrm{Pa\,s\,m^{-2}}$;
- **Melamine sample** 3: $\sigma = 8233\,\mathrm{Pa\,s\,m^{-2}} \pm 700\,\mathrm{Pa\,s\,m^{-2}}$;
- **exoskeleton + wire mesh sample**: $\sigma \approx 0\,\mathrm{Pa\,s\,m^{-2}}$.

The retrieved parameters for the porous media are in agreement with the typical values associated with the melamine foam ($\sigma = 8000\,\mathrm{Pa\,s\,m^{-2}}$ - $\sigma = 12\,000\,\mathrm{Pa\,s\,m^{-2}}$). Regarding the fourth sample, the pressure acquired by the measurement unit is below the sensitivity of the transducers. For this reason, the static air-flow resistivity of these materials can be approximated to zero. This assumption is verified by further measurements conducted at LAUM on the same samples showing an estimation for the normalized pressure difference of $\Delta p/\rho_0 c_0 U = 0.012$, U being the flow velocity.

3.4.3. SOUND ABSORPTION ANALYSIS

The analysis of the sound-absorbing behavior of the porous material is performed by means of an impedance tube. The measurements have been carried out in collaboration with J. Golliard from CTTM. The corresponding setup is depicted in Figure 3.8 (configuration **A**). A loudspeaker is placed at one side of the tube, whereas the sample of the test material is at the opposite one. A standing wave pattern is generated from a broadband,

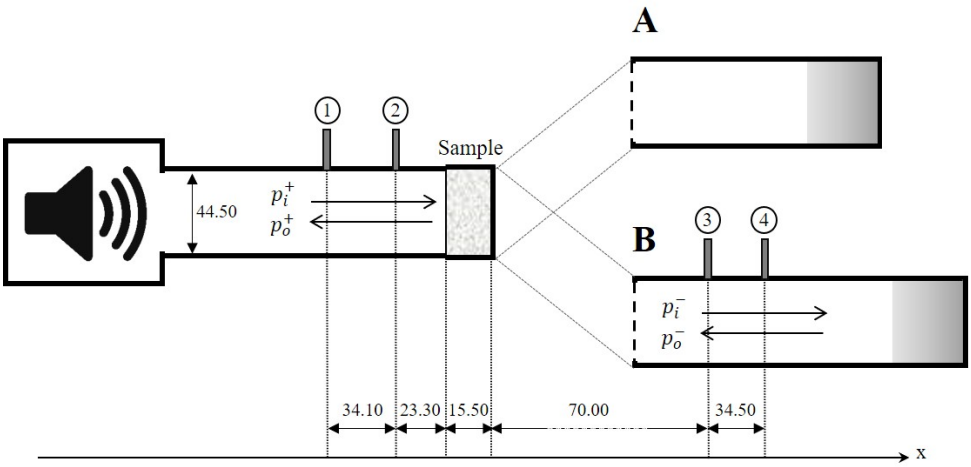

Figure 3.8: Configurations of the impedance tube for the determination of the sound-absorbing behavior (**A**) and characterization of the porous parameters (**B**) of the melamine foam. The distances are expressed in mm.

stationary noise signal being the result of a forward traveling sound wave and a backward, or reflected, sound wave. The frequency of the sound signal is kept lower than the cutoff frequency of the tube to assure the generation of plane propagating waves. Two fixed phase-calibrated microphones are located at two different positions along the tube wall (see Figure 3.8).

The above-mentioned method, labeled as *2p method* [22, 23], is based on the estimation of the transfer function between the microphones. The determination of this quantity allows for the mathematical separation of the incident and reflected waves, leading to the anechoic-reflection coefficient of the sample for the same frequency band as that characterizing the broadband signal. Indeed, since the mathematical problem of a sound wave propagating in a duct can be considered one-dimensional for frequencies up to the cutoff frequency, the total sound pressure at any point in the tube can be expressed by

$$p(x) = Ae^{-ikx} + Be^{ikx}, \tag{3.5}$$

A and B denoting pressure coefficients. The transfer function between the two microphones in the tube, indicated by the subscripts 1 and 2, is

$$H_{12} = \frac{p(x_2)}{p(x_1)} = \frac{Ae^{-ikx_2} + Be^{ikx_2}}{Ae^{-ikx_1} + Be^{ikx_1}} = \frac{e^{-ikx_2} + Re^{ikx_2}}{e^{-ikx_1} + Re^{ikx_1}}, \tag{3.6}$$

where $R = B/A$ is the pressure reflection coefficient of the material. Solving for R yields

$$R = \frac{e^{-ikx_2} - H_{12}e^{-ikx_1}}{H_{12}e^{ikx_1} - e^{ikx_2}}. \tag{3.7}$$

It is now possible to derive the expressions for the normalized impedance $\hat{Z}$ and for the sound-absorption coefficient α, which indicates the amount of sound absorbed by the

porous material, as

$$\hat{Z} = \frac{1+R}{1-R}; \qquad \alpha = 1 - R^2. \tag{3.8}$$

For the experimental campaign, the three melamine samples employed in the static air-flow resistivity test are considered. In addition, a fourth sample made of melamine foam and the combination of hard-plastic exoskeleton and metallic woven wire mesh is studied. A white noise signal is emitted by the loudspeaker with a frequency range of 50 Hz-5 kHz, while the range considered for the acquisition is 80 Hz-4.3 kHz. The sampling frequency is set to 51.2 kHz.

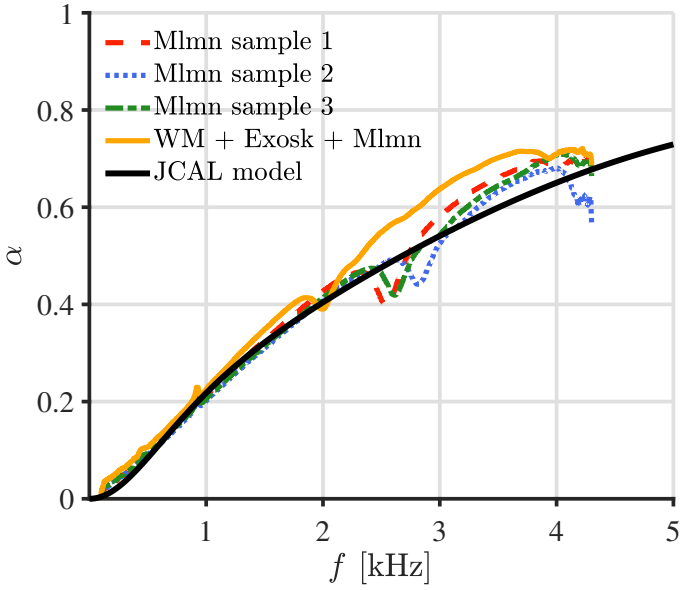

Figure 3.9: Sound absorption coefficient for the three samples of melamine foam and a sample including melamine foam, hard-plastic exoskeleton, and woven wire mesh compared to the JCAL model fitted to the experimental data.

The results of the sound-absorption coefficient for the four samples are depicted in Figure 3.9. These are compared with the analytical prediction of the JCAL model that is computed from Z_{ce} through

$$\alpha = 1 - \left(\frac{Z_s - Z_0}{Z_s + Z_0} \right)^2, \tag{3.9}$$

where $Z_0 = \rho_0 c_0$ and Z_s is the complex characteristic acoustic impedance defined as $Z_s = -iZ_{ce}\cot(kL)$ according to the fluid equivalent model [24]. Equation (3.9) is derived from Equation (3.8) considering $\hat{Z} = Z_s/Z_0$. The procedure to determine the porous parameters involved in the calculation of ρ_e and K_e (Equations 3.1 and 3.2) from the experiments will be discussed in the following section. The JCAL prediction exhibits a satisfactory agreement with the measurements of the three samples of melamine foam, especially at lower frequencies. The negative bumps that can be observed in the experiments in the range 2.5 kHz-3 kHz are not present in the model and are attributable

to resonance phenomena occurring in the impedance tube due to its finite length. Indeed, the absorption is a consequence of the acoustic attenuation by the porous layer, the reflection and transmission at the first fluid-porous layer, and the interaction with the solid back plate, the latter of which is not accounted for in the prediction. Moreover, the effect of the additional layers results in a shift of the bump to lower frequencies and in enhanced values of α, which deviate further from the JCAL model due to the increase in the sample thickness.

DETERMINATION OF MELAMINE FOAM PARAMETERS

The impedance tube in Figure 3.8 is set up for a second measurement with four phase-calibrated microphones (configuration **B**) in order to determine the porous model parameters through the inverse method developed by Niskanen et al. [25]. The characterization is carried out in collaboration with J.-P. Groby and Y. Aurégan from LAUM. The technique consists of fitting the JCAL model describing the porous medium to the measurement of the scattering matrix, which contains the anechoic reflection, R, and anechoic transmission, $T' = Te^{ikL}$, of the material. The statistical inversion is performed in the Bayesian framework and provides additional information on the uncertainty of the parameters. With reference to Figure 3.8, T' and R can be expressed by [26]

$$T' = \frac{p_o^- p_i^+ - p_o^+ p_i^-}{(p_i^+)^2 - (p_i^-)^2}; \qquad R = \frac{p_o^+ p_i^+ - p_o^- p_i^-}{(p_i^+)^2 - (p_i^-)^2}. \tag{3.10}$$

The measurements are conducted for one of the three samples of melamine foam and for the same sample but inverted in order to further investigate the inhomogeneity and anisotropy of the porous material. The considered excitation signal is a logarithmic swept sine over the frequency range of 100 Hz-4.3 kHz in order not to overcome the cutoff frequency of the tube ($\sim$ 5 kHz).

The porous parameters obtained from the characterization and uncertainty computed from the statistical inversion are listed in Table 3.1. The deviations experienced by

	Sample	**Inverted sample**
ϕ [-]	$9.85 \times 10^{-1} \pm 8.05 \times 10^{-3}$	$9.89 \times 10^{-1} \pm 6.44 \times 10^{-3}$
α_∞ [-]	$1.01 \pm 1.05 \times 10^{-2}$	$1.02 \pm 1.72 \times 10^{-2}$
Λ [m]	$1.28 \times 10^{-4} \pm 6.10 \times 10^{-6}$	$1.36 \times 10^{-4} \pm 1.10 \times 10^{-5}$
Λ' [m]	$1.82 \times 10^{-4} \pm 2.45 \times 10^{-5}$	$2.11 \times 10^{-4} \pm 2.05 \times 10^{-5}$
k_0 [m^2]	$1.41 \times 10^{-9} \pm 9.54 \times 10^{-12}$	$1.41 \times 10^{-9} \pm 1.03 \times 10^{-11}$
k_0' [m^2]	$2.31 \times 10^{-9} \pm 1.60 \times 10^{-10}$	$2.48 \times 10^{-9} \pm 1.36 \times 10^{-10}$

Table 3.1: JCAL model parameters characterizing a sample of the melamine foam fitted into the porous airfoil. The uncertainties are estimated from the statistical inversion.

the parameters for the different sample configurations fall within the uncertainty range. A significant mismatch between the value of k_0 computed by the inverse method and the corresponding static viscous permeability obtained from the measured static air-flow resistivity ($\approx 2.08 \times 10^{-9}$ m^2) can be however observed. The origin of this discrepancy requires further investigations to be clarified, although the relatively satisfactory match

seen for the absorption coefficient in Figure 3.9 suggests that the value of k_0 listed in Table 3.1 is closer to the real value of the melamine foam. Finally, additional measurements for the study of the effects of flow on the anechoic transmission and reflection of the sound waves in the porous media are presented in Appendix B.

3.5. NOZZLE-FLOW QUALIFICATION

The qualification of the nozzle flow is outlined separately for the VKI JAFAR facility and the TUD A-Tunnel facility.

3.5.1. JAFAR FACILITY

The experiments in the JAFAR facility are carried out at a free-stream flow velocity of $U_\infty = 30\,\mathrm{m\,s^{-1}}$ that corresponds to a Reynolds number based on the rod diameter of $Re_d = 4.1 \times 10^4$. This velocity is measured at the airfoil leading-edge height ($x = 0$) in the absence of the rod using a Prandtl probe. Additional information about the methodology followed for the quantification of the reference velocity is provided in Appendix A.1. The wing profile is set at a 0° angle of attack, which is verified by the mean wall-pressure distribution.

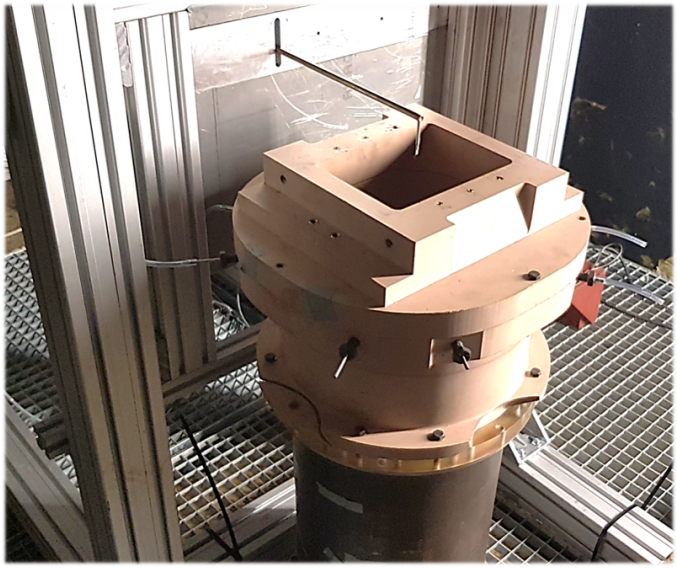

Figure 3.10: Carriage system installed in the JAFAR facility for the automatic movement of the hot-wire L-shaped probe within the yz plane for the qualification of the facility.

Profiles of the mean velocity, $\bar{U}$, and root-mean-square (r.m.s.) of the velocity fluctuations, U', are obtained at the nozzle exit with a single hot-wire L-shaped probe. This is connected to an in-house anemometer and installed in a carriage system, depicted in Figure 3.10, which enables automatically moving the sensor within the yz plane. The system is moved by two EPOS-controlled brushless DC electric motors and is characterized by an accuracy of 0.1 mm. The static calibration of the hot-wire is performed in-situ

on a daily basis, using a Prandtl tube to measure the reference velocity. The maximum frequency response of the anemometer, estimated through a dynamic calibration of the Wheatstone-bridge components, is found to be $f_{max} \approx 12.5\,\text{kHz}$. All the measurements are corrected in order to take into account the temperature variations during the tests by following the method proposed by Bruun [27], as will covered in greater detail in Appendix A.2.

The data are acquired through a National Instruments (NI) *cDAQ 9234* card having a dynamic range of $\pm 5\,\text{V}$ and a resolution of 24 bits. An analogical anti-alias filter is embedded in the card and provides an automatic value of the cutoff frequency depending on the selected sampling frequency. In this case, the sampling frequency is set to 51.2 kHz, which leads to an anti-aliasing filter set to 25.6 kHz, and the acquisition time to 5 s in order to keep the maximum relative statistical uncertainty below 0.4 % for the mean velocity in the potential core of the jet (see Appendix A.3).

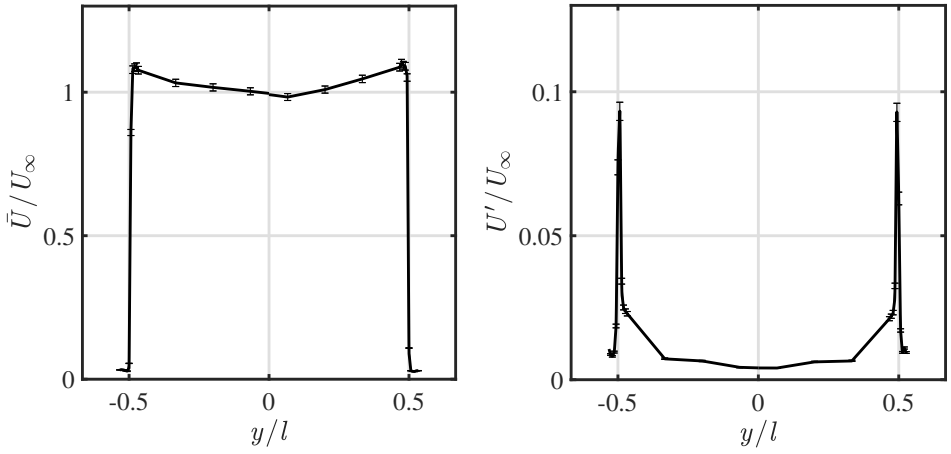

(a) Mean velocity profile.

(b) Turbulence intensity profile.

Figure 3.11: Velocity profiles at $x/d = -10.65$, corresponding to $x = -0.213\,\text{m}$, at the airfoil midspan.

Figure 3.11 presents the dimensionless mean velocity, $\bar{U}/U_\infty$, and turbulence intensity, U'/U_∞, along the y-axis at $z = 0$. The probe is placed 0.001 m downstream of the nozzle exit in the streamwise direction, corresponding to $x/d = -10.65$. The cylindrical rod is removed to allow for the movement of the sensor. The mean velocity remains within 4 % of U_∞ across the potential core of the jet, whereas an increase of up to 9 % in U_∞ can be observed in proximity to the outlet-nozzle edges. The sharp transition in the velocity between potential core and no-flow region indicates a limited width for the shear layer, as would be expected at such a short distance from the outlet-nozzle exit. In Figure 3.11b, the turbulence intensity is found to be about 0.4 % in the potential core of the jet. Finally, the peaks in turbulence intensity are located in the two shear layer regions and amount to almost 10 %, with an uncertainty below 1.4 % (see Appendix A.3). A more extensive analysis of the nozzle flow is reported in Appendix A.4. Finally, the present results are used as boundary conditions for the numerical prediction of the flow field by means of LES for the same experimental setup performed by Satcunanathan *et*

al. [17]. The LES results will be evaluated in Chapter 5.4 to supplement the experimental measurements and provide complementary information about the description of the different turbulent-velocity components.

3.5.2. A-TUNNEL FACILITY

The experiments in the A-tunnel facility are carried out at free-stream flow velocities of $U_\infty = 20\,\mathrm{m\,s^{-1}}$, $U_\infty = 30\,\mathrm{m\,s^{-1}}$, and $U_\infty = 40\,\mathrm{m\,s^{-1}}$, which correspond to a Reynolds number based on the rod diameter of $Re_d = 2.7 \times 10^4$, $Re_d = 4.1 \times 10^4$, and $Re_d = 5.4 \times 10^4$, respectively. The flow velocity is measured through a Pitot-static tube connected to a Mensor DPG 2400 pressure gauge and characterized by an accuracy of 0.03 % of the read value.

The full qualification of the outlet nozzle has been already performed by Merino-Martínez *et al.* [10]. In that case, the mean velocity in the streamwise was found to be uniform within 0.6 % independently of the free-stream velocity, while the turbulence intensity of the clean flow was below 0.1 % for free-stream velocities higher than $20\,\mathrm{m\,s^{-1}}$.

3.6. FLOW FIELD CHARACTERIZATION

The investigation of the boundary layer around the solid and porous airfoil configurations and the stagnation region surrounding their leading edge is conducted in the JAFAR facility using the same hot-wire anemometer and acquisition system employed for the nozzle-flow qualification (see Chapter 3.5.1). In this case, the carriage system is rotated in order to enable moving the probe along the x-direction. The wire is mounted on a straight probe oriented perpendicularly to the flow direction. The sampling frequency is kept at 51.2 kHz, while the acquisition time is extended to 10 s in order to ensure statistical convergence in the computation of the velocity power spectral density (PSD) of the incident velocity fluctuations. This quantity is processed by means of the Welch method [28], with blocks of 2^{13} samples windowed using a Hanning weighting function that is characterized by 50 % data overlap, thus providing a frequency resolution of 6.25 Hz. The same parameters are employed to compute the PSD from the LES data described in Chapter 5.4. Furthermore, the temperature variations are corrected by following the model proposed by Bruun [27] (see Appendix A.2).

Figure 3.12 shows the coordinates of the measurement positions considered for the characterization of the boundary layer. Nine chordwise coordinates are chosen along the wing profile. The traverses are designed at $z = 0.1\,s$ in order to avoid the influence of the static-pressure port on the measurement points close to the airfoil surface. As the wing profile is symmetric and installed with an angle of attack of 0°, only one surface is investigated. The x-axis locations along the airfoil correspond to the 2 %, 5 %, 10 %, 20 %, 30 %, 40 %, 50 %, 62.5 %, and 75 % of the chord. 30 measurement positions are considered in the y-direction for each traverse, resulting in 270 points in total. The distance between the points is variable and the step is 0.5 mm, 1 mm, and 4 mm for respectively the first 7.5 mm, the following 10 mm, and the last part as shown in Figure 3.12.

Furthermore, an additional traverse made of 35 measurement points is designed at $x/c = 1.05$ in order to characterize the wake of the airfoils. Indeed, the integration of the mean velocity profile $\bar{U}$ at this location provides an estimation of the zero-lift drag

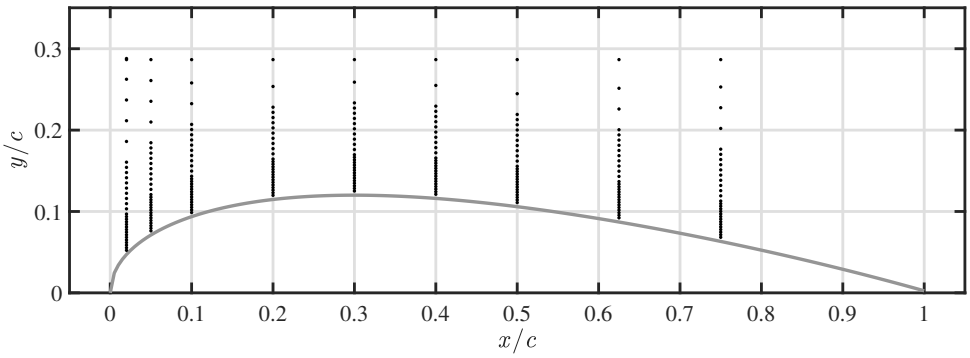

Figure 3.12: Traverses designed for the characterization of the airfoil boundary layer by means of hot-wire anemometry consisting of 55 points at $z = 0.1\,s$. The distance between the points is 4.0 mm, 1.0 mm, and 0.5 mm for respectively the first 50 mm ($5r_{LE}$), the following 10 mm ($1r_{LE}$), and the final 10 mm ($1r_{LE}$) of the traverse, while the minimum distance of the probe from the surface ranges from 0.5 mm to 0.8 mm.

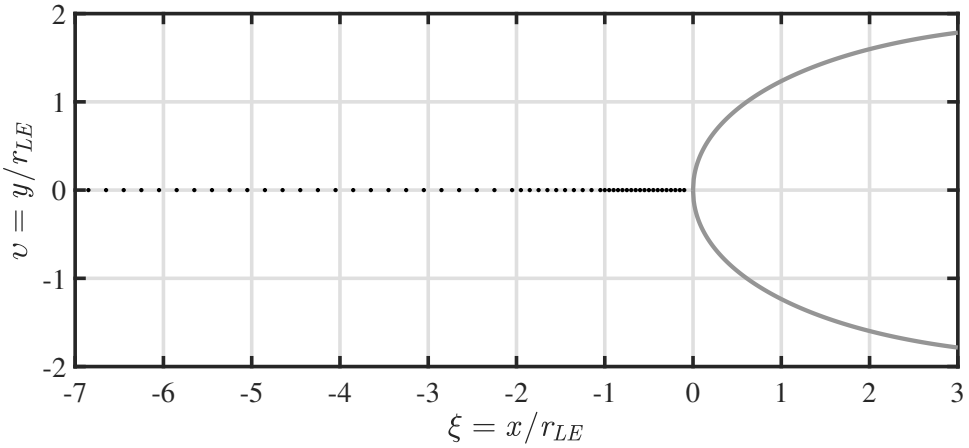

Figure 3.13: Traverse designed for the characterization of the stagnation streamline by means of hot-wire anemometry in the JAFAR facility consisting of 55 points at $z = 0.1\,s$. The distance between the points is 2.0 mm, 1.0 mm, and 0.5 mm for respectively the first 50 mm ($5r_{LE}$), the following 10 mm ($1r_{LE}$), and the final 10 mm ($1r_{LE}$) of the traverse, while the minimum distance of the probe from the surface is 0.5 mm.

coefficient C_d and, therefore, the loss in the aerodynamic performance experienced by the porous airfoil with respect to the solid one. For sufficiently high Reynolds numbers, the shear stresses acting on the airfoil surface can be considered negligible, yielding

$$C_d = \frac{\int_{-\infty}^{\infty} \rho \bar{U}(y) \left[\bar{U}_\infty - \bar{U}(y)\right] dy}{t \frac{1}{2} \rho \bar{U}_\infty^2}, \tag{3.11}$$

where $\bar{U}(y)$ is assumed to be independent from the spanwise direction. For practical calculations, the integration is performed from $y = 0$ to $y = 0.3\,c$ and the result is multiplied by a factor 2 assuming symmetry in the velocity profile.

Likewise, Figure 3.13 illustrates the measurement positions of the single traverse acquired along the stagnation streamline. The x-coordinate is normalized by the leading-edge radius, r_{LE}. Also in this case, the traverse is considered at $z = 0.1\,s$. 55 locations are designed, with the probe moving in the streamwise direction from the upstream flow region towards the airfoil leading edge. The distance between consecutive measurement points varies from 2.0 mm, to 1.0 mm, and finally to 0.5 mm as shown in Figure 3.13. For both experimental campaigns, the minimum distance of the probe from the surface less than 0.5 mm is evaluated using a dummy sensor having the same geometry as the hot-wire probe. In this way, it is possible to optically determine the exact position at which the prongs of the sensor touch the surface of the airfoil at the leading edge without harming the actual probe.

3.7. ACOUSTIC FAR-FIELD MEASUREMENTS SETUP

The far-field acoustic measurements are carried out in the A-tunnel facility with the solid, porous, and melamine airfoil configurations. A microphone array consisting of 64 G.R.A.S. *40 PH* analog free-field microphones with integrated constant-current power amplifiers is employed for the experiments. Each microphone features a diameter of 0.007 mm and a length of 0.059 mm, and is characterized by a flat frequency response within ±1 dB from 50 Hz to 5 kHz and within ±2 dB from 5 kHz to 20 kHz. The transducers are connected to a data acquisition system consisting of 4 NI *PXIe-4499 Sound and Vibration Modules* having a 24 bits resolution and a 204.8 kHz maximum sampling rate. The boards are controlled by a NI *RMC-8354* computer via a NI *PXIe-8370* board. All the microphones are calibrated in amplitude using a G.R.A.S. *42AA* pistonphone, which emits a sinusoidal wave of 114 dB at 250 Hz. The relative phase responses of the microphones are also calculated using a clapping device that generates an impulse broadband sound. This approach allows for the estimation of the phase difference between the expected received signal and the actual recorded signal by each microphone, using the center microphone as the reference. The calibration can be performed for all the frequencies of interest. Additional information about the present setup can be found in [29].

The structure of the phased microphone array features a 1 m × 2 m steel perforated plate with square holes arranged in a regular grid pattern to fit the microphones. The plate is characterized by a total of 8450 perforations with dimensions of 0.01 m × 0.01 m that provide as many potential positions for the microphone. The thickness of the plate is 0.004 m, leading to an approximate open area ratio of 51 %. The present design offers a compromise solution between minimization of the acoustic reflections and robustness of the array structure [10]. The array is installed in a rectangular steel frame structure that can be easily moved inside the anechoic room and whose borders are equipped with acoustic absorbing foam. Each G.R.A.S. microphone is located within a holder made of a hollow threaded metal rod having an outer diameter of 0.010 m and an inner diameter of 0.008 m. This can be tightly mounted to the array through a couple of M10 nuts, as can be observed in Figure 3.14a.

The microphone distribution for airfoil-turbulence interaction noise measurements extends for 1 m in the z-direction and 2 m in the x-direction, and features 64 microphones arranged on a 7-arm spiral array [30] with 9 microphones on each arm and an

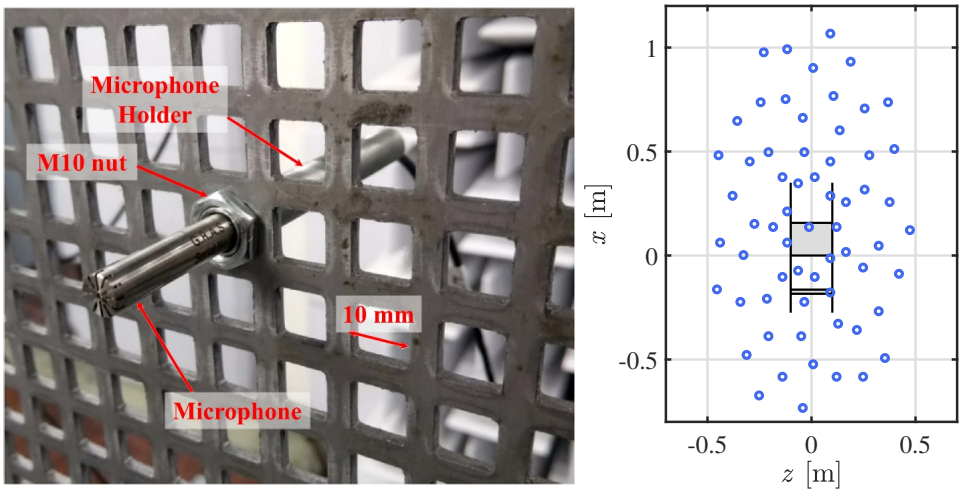

(a) Detail of the G.R.A.S. microphone holding system and steel perforated plate. Taken from [10].

(b) Distribution of microphones in the array as seen from behind.

Figure 3.14: Experimental setup for turbulence-interaction noise measurements. The 64-microphone array is placed at 1 m from the rod-airfoil configuration.

additional transducer placed at the center of the array. A schematic of the relative positions of the microphones with respect to the rod-airfoil configuration is depicted in Figure 3.14b. Considering the coordinate reference system introduced in Figure 3.3, the center microphone is located at $(x, y, z) = (0.137\,\text{m}, 1.000\,\text{m}, -0.012\,\text{m})$. In this configuration, the microphones are placed outside of the shear layer of the jet.

For each measurement, a sampling frequency of 50 kHz and 60 s of recording time are considered. The acoustic data are averaged in time blocks of 2^{13} samples, giving a frequency resolution of 6.10 Hz, and windowed using a Hanning weighting function with 50 % data overlap, following Welch's method [28].

3.8. PARTICLE IMAGE VELOCIMETRY SETUP

Stereoscopic time-resolved PIV experiments are conducted in the A-Tunnel facility for solid, porous, and melamine airfoil configurations. The measurements are taken on a plane at the midspan of the wing profiles, centered in the stagnation region. A sketch of the experimental setup is depicted in Figure 3.15. Two Photron *Fastcam SA 1-1* having a sensor of 1024 px × 1024 px and a pixel pitch of 20 µm are employed with a separation time between the camera exposures of 185 µs. The cameras are equipped with Nikon *NIKKOR* 105 mm focal distance macro-objectives set at $f_\# = 5.6$. Seeding is produced by a SAFEX *Twin-Fog Double Power* fog generator with a glycol-based solution. The generated mean drop diameter is 1 µm. The laser sheet is obtained through laser pulses with a wavelength of 527 nm and energy of 30 µJ per pulse that are generated by a Quantronix *Darwin Duo 527-80-M double cavity Nd:YLF* system using a spherical and a cylindrical optical lens, resulting in an approximate thickness of 1 mm.

Parameter	Quantity
Image rate	2.7 kHz
Pulse separation time	185 µs
Acquisition sensor	1024 px × 1024 px
Field of view	58 mm × 58 mm
Distance obj-FOV	0.6 m
Pixel pitch	20 µm
Magnification factor	0.34
Particle image size at $f_\# = 5.6$	0.5 px
Digital resolution	17.7 px mm^{-1}
Interrogation window	32 px × 32 px
Overlap factor	75 %
Spatial resolution	1.81 mm × 1.81 mm
Vector spacing	0.45 mm × 0.45 mm
Pixel displ. at $U_\infty = 30$ m s^{-1}	10 px

Table 3.2: Stereoscopic time-resolved PIV parameters.

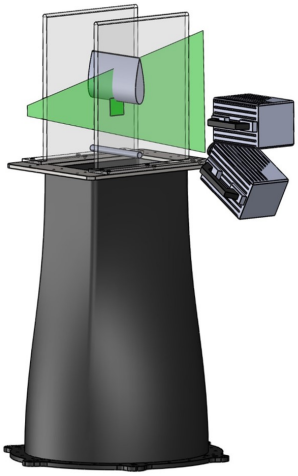

Figure 3.15: PIV measurement setup.

Data are acquired at a sampling frequency of 2.7 kHz for 1 s, corresponding to approximately 300 cycles of vortex shedding from the upstream rod at $Re_d = 4.1 \times 10^4$. A *LaVision* high-speed controller ensures the synchronization between image acquisitions and laser pulses. The field of view (FOV) has a dimension of 58 mm × 58 mm and a digital resolution of 17.7 px mm^{-1}, as shown by the raw image depicted in Figure 3.16. The calibration is done by acquiring static images of a plate situated in the FOV and equipped with a millimeter paper from both cameras. A mask is applied to neglect the region in the vicinity of the airfoil surface due to the high number of invalid points detected by the commercial software Davis 8.4 by *LaVision* and generated by laser light reflections, especially in the melamine configuration case. The mask also includes the shadow shed by the airfoil leading edge. Elsewhere, invalid points are either interpolated in time or reconstructed from adjacent points with the `smoothn` function by Garcia [31], which is based on a penalized least squares method. The processing of the raw images is performed with Davis 8.4 employing a multi-pass cross-correlation approach [32] with a final interrogation window of 32 px × 32 px and 75 % overlapping.

Furthermore, the time super-sampling algorithm by Scarano et al. [33] is used with a factor 3, leading to a final sampling frequency of 8.1 kHz. The super-sampling model is based on Taylor's frozen-turbulence approximation between two consecutive vector fields in time. The assumption is valid within timescales that are smaller than the flow-dissipation ones. This technique is suitable for investigating datasets where the dominant motion is aligned with the measurement plane. The resulting time step of the PIV measurements Δ_{Ts} is equal to $\Delta_{Ts} = \Delta_T / S_s$, where Δ_T is the original time separation between two images in a couple and S_s is the super-sampling factor. The typical scales of fluctuations reconstructed in the flow can be observed in Figure 3.16, which depicts the time evolution of the streamwise velocity component at a location upstream of the airfoil for $Re_d = 4.1 \times 10^4$.

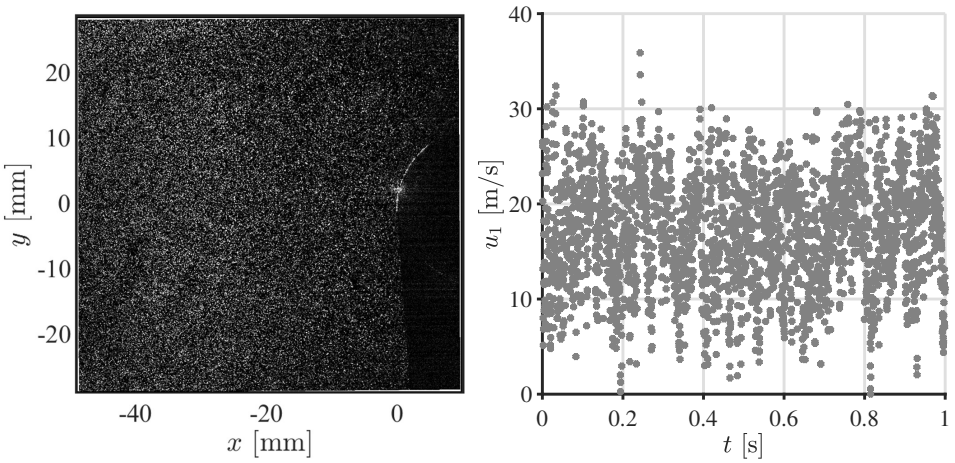

Figure 3.16: Raw PIV image sample (on the left) and time evolution of the streamwise velocity component extracted at $(x/R_{LE}, y/R_{LE}) = (-4, 0)$ (on the right) related to the solid airfoil configuration at $Re_d = 4.1 \times 10^4$.

The maximum frequency that can be inspected is however limited by the low-pass filtering effect of PIV, due to the averaging over the interrogation windows [34]. This frequency can be estimated by comparing the convection velocity with the resolution of the employed interrogation window and it puts a limitation on the size of turbulent eddies and frequencies that can be analyzed, which may be below the Nyquist one. In the present case, the maximum frequency to avoid spurious results is found to be approximately 0.9 kHz. This value represents the upper limit at which the PSD of the turbulent velocity obtained by the PIV measurements will be presented in Chapter 5.4. The PSD is computed using the Welch method [28], with blocks of 2^9 samples windowed using a Hanning weighting function that is characterized by 50 % data overlap, thus providing a frequency resolution of 15.8 Hz. The main PIV parameters are listed in Table 3.2.

PIV MEASUREMENT UNCERTAINTY

The uncertainty on PIV measurements is made of random and systematic errors. The main sources of systematic errors are typically peak-locking, particle slip, calibration errors, and finite spatial resolution.

- Peak-locking is due to the tendency of calculating velocity towards integer displacements caused by situations in which the particle image size is smaller than the camera pixel. According to Raffel *et al.* [35], a possible way to minimize this source of error is to keep the particle image larger than 2 px. In the present experiments, the particle size at the indicated magnification factor is found to be about 0.5 px. In order to avoid peak-locking issues, de-focusing of the particles has been carried out to reach a $1.5 - 2$ px particle diameter in the camera sensor [36].

- Particle slip [37] is a physical effect linked to the inertia of the seeding particles that may experience a lag with the flow. It can be estimated as the response time τ_{slip} related to the tracer particle multiplied by the particle acceleration. Given the

$\tau_{slip} \approx 0.5\,\mu s$ of the employed seeding, this phenomenon is expected to provide a negligible contribution to the overall uncertainty. For instance, the maximum estimated acceleration of the flow field at $Re_d = 4.1 \times 10^4$ amounts to approximately $5600\,m\,s^{-2}$, corresponding to an uncertainty of 0.01 % of the free-stream velocity.

- Calibration errors arise from the third-order polynomial mapping function that is generated to relate the pixel dimension to a geometrical coordinate. In the present case, *LaVision*'s self-calibration routine is applied to eliminate any potential misalignments in the original calibration. The uncertainty associated with the calibration errors is verified automatically with Davis 8.4 and corresponds to a residual error in the flow field of about 0.05 px.

- The finite spatial resolution is linked to the transfer function of the PIV correlation algorithm for scales ranging from the FOV to the interrogation window. The non-resolved smaller scales may, in turn, affect the measurement of the larger ones by introducing additional noise and aliasing. This issue can be tackled by using an iterative cross-correlation algorithm, which has proven to increase spatial resolution [38]. For the present study, structures with 1 mm scale length can be reconstructed with a 68 % confidence level.

Random errors are mainly due to the cross-correlation algorithm on which the PIV is based. Indeed, the cross-correlation analysis cannot provide an accurate representation of the stochastic nature of turbulence. An estimation of this error is based on the work of Westerweel [39] and amounts to 0.1 px. Moreover, the convergence of statistic quantities depends on the number of uncorrelated data points being processed. The present aspect will be further discussed in Appendix C.

The overall systematic and random components of PIV uncertainty can be approximately determined with Davis 8.4. The built-in method is based on correlation statistics and evaluates the differences in the correlation peaks computed from a pair of interrogation windows that are mapped back onto each other [40]. The uncertainty is provided for individual instantaneous velocity vectors and is quantified through propagation techniques [41]. Results indicate a maximum uncertainty on the velocity of $0.05\,U_\infty$ in the streamwise component and $0.04\,U_\infty$ in the upwash one at $Re_d = 4.1 \times 10^4$. Similar values are retrieved also at $Re_d = 2.7 \times 10^4$ and $Re_d = 5.4 \times 10^4$.

REFERENCES

[1] R. Zamponi, D. Ragni, N. Van de Wyer, and C. Schram, *Experimental Investigation of Airfoil Turbulence-Impingement Noise Reduction Using Porous Treatment,* in *25th AIAA/CEAS Aeroacoustics Conference* (American Institute of Aeronautics and Astronautics, Delft, The Netherlands, 2019).

[2] S. Satcunathan, R. Zamponi, M. Meinke, N. Van de Wyer, C. Schram, and W. Schröder, *Validation of a model for acoustic absorption in porous media,* in *48th International Congress and Exhibition on Noise Control Engineering* (Institute of Noise Control Engineering, Madrid, Spain, 2019) pp. 4329–4344.

[3] R. Merino-Martínez, S. Luesutthiviboon, R. Zamponi, A. Rubio Carpio, D. Ragni, P. Sijtsma, M. Snellen, and C. Schram, *Assessment of the accuracy of microphone array methods for aeroacoustic measurements,* Journal of Sound and Vibration **470**, 115176 (2020).

[4] R. Zamponi, S. Satcunanathan, S. Moreau, D. Ragni, M. Meinke, W. Schröder, and C. Schram, *On the role of turbulence distortion on leading-edge noise reduction by means of porosity,* Journal of Sound and Vibration **485**, 115561 (2020).

[5] S. Tamaro, R. Zamponi, D. Ragni, C. Teruna, and C. Schram, *Experimental investigation of turbulent coherent structures interacting with a porous airfoil,* Experiments in Fluids (2021), 10.1007/s00348-021-03170-2.

[6] C. Schram, *Aeroacoustics of subsonic jets: prediction of the sound produced by vortex pairing based on particle image velocimetry*, Ph.D. thesis, Technische Universiteit Eindhoven (2003).

[7] L. D. de Santana, *Semi-analytical methodologies for airfoil noise prediction*, Ph.D. thesis, KU Leuven (2015).

[8] D. Guariglia, A. Rubio Carpio, and C. Schram, *Design of a Facility for Studying Shock-Cell Noise on Single and Coaxial Jets,* Aerospace **5**, 25 (2018).

[9] K. Kucukcoskun, J. Christophe, J. Anthoine, C. Schram, and M. Tournour, *An Extension of Amiet's Theory for Spanwise-Varying Incident Turbulence Noise and Broadband Scattering Using BEM,* in *16th AIAA/CEAS Aeroacoustics Conference* (American Institute of Aeronautics and Astronautics, Stockholm, Sweden, 2010).

[10] R. Merino-Martínez, A. Rubio Carpio, L. T. Lima Pereira, S. van Herk, F. Avallone, D. Ragni, and M. Kotsonis, *Aeroacoustic design and characterization of the 3D-printed, open-jet, anechoic wind tunnel of Delft University of Technology,* Applied Acoustics **170**, 107504 (2020).

[11] M. C. Jacob, J. Boudet, D. Casalino, and M. Michard, *A rod-airfoil experiment as a benchmark for broadband noise modeling,* Theoretical and Computational Fluid Dynamics **19**, 171 (2005).

[12] M. Munekata, K. Kawahara, T. Udo, H. Yoshikawa, and H. Ohba, *An experimental study on aerodynamic sound generated from wake interference of circular cylinder and airfoil vane in tandem,* Journal of Thermal Science **15**, 342 (2006).

[13] M. Munekata, R. Koshiishi, H. Yoshikawa, and H. Ohba, *An experimental study on aerodynamic sound generated from wake interaction of circular cylinder and airfoil with attack angle in tandem,* Journal of Thermal Science **17**, 212 (2008).

[14] Y. Li, X.-n. Wang, Z.-w. Chen, and Z.-c. Li, *Experimental study of vortex–structure interaction noise radiated from rod–airfoil configurations,* Journal of Fluids and Structures **51**, 313 (2014).

[15] V. Lorenzoni, M. Tuinstra, and F. Scarano, *On the use of time-resolved particle image velocimetry for the investigation of rod–airfoil aeroacoustics,* Journal of Sound and Vibration **331**, 5012 (2012).

[16] W. J. Devenport, R. L. Simpson, M. B. Dewitz, and N. K. Agarwal, *Effects of a leading-edge fillet on the flow past an appendage-body junction,* AIAA Journal **30**, 2177 (1992).

[17] S. Satcunanathan, M. H. Meinke, and W. Schröder, *Prediction of Noise Mitigation by Porous Media based on a Direct-Hybrid CFD/CAA Method,* in *25th AIAA/CEAS Aeroacoustics Conference* (American Institute of Aeronautics and Astronautics, Delft, The Netherlands, 2019).

[18] A. Scheidegger, *The Physics of Flow Through Porous Media* (University of Toronto Press, 1963).

[19] D. L. Johnson, J. Koplik, and R. Dashen, *Theory of dynamic permeability and tortuosity in fluid-saturated porous media,* Journal of Fluid Mechanics **176**, 379 (1987).

[20] Y. Champoux and J. Allard, *Dynamic tortuosity and bulk modulus in air-saturated porous media,* Journal of Applied Physics **70**, 1975 (1991).

[21] D. Lafarge, P. Lemarinier, J. F. Allard, and V. Tarnow, *Dynamic compressibility of air in porous structures at audible frequencies,* The Journal of the Acoustical Society of America **102**, 1995 (1997).

[22] J. Y. Chung and D. A. Blaser, *Transfer function method of measuring in-duct acoustic properties. i. theory,* The Journal of the Acoustical Society of America **68**, 907 (1980).

[23] J. Y. Chung and D. A. Blaser, *Transfer function method of measuring in-duct acoustic properties. ii. experiment,* The Journal of the Acoustical Society of America **68**, 914 (1980).

[24] J. F. Allard and N. Atalla, *Propagation of Sound in Porous Media* (John Wiley & Sons, Ltd, Chichester, UK, 2009).

[25] M. Niskanen, J.-P. Groby, A. Duclos, O. Dazel, J. C. Le Roux, N. Poulain, T. Huttunen, and T. Lähivaara, *Deterministic and statistical characterization of rigid frame porous materials from impedance tube measurements,* The Journal of the Acoustical Society of America **142**, 2407 (2017).

[26] M. Åbom, *Measurement of the scattering-matrix of acoustical two-ports,* Mechanical Systems and Signal Processing **5**, 89 (1991).

[27] H. H. Bruun, *Hot-Wire Anemometry: Principles and Signal Analysis,* Measurement Science and Technology **7** (1996), 10.1088/0957-0233/7/10/024.

[28] P. Welch, *The use of fast Fourier transform for the estimation of power spectra: A method based on time averaging over short, modified periodograms,* IEEE Transactions on Audio and Electroacoustics **15**, 70 (1967).

[29] R. Merino-Martinez, *Microphone arrays for imaging of aerospace noise sources*, Ph.D. thesis, Delft University of Technology (2018).

[30] S. Luesutthiviboon, A. M. Malgoezar, R. Merino-Martinez, M. Snellen, P. Sijtsma, and D. G. Simons, *Enhanced HR-CLEAN-SC for resolving multiple closely spaced sound sources,* International Journal of Aeroacoustics **18**, 392 (2019).

[31] D. Garcia, *Robust smoothing of gridded data in one and higher dimensions with missing values,* Computational Statistics & Data Analysis **54**, 1167 (2010).

[32] F. Scarano and M. L. Riethmuller, *Advances in iterative multigrid PIV image processing,* Experiments in Fluids **29**, S051 (2000).

[33] F. Scarano and P. Moore, *An advection-based model to increase the temporal resolution of PIV time series,* Experiments in Fluids **52**, 919 (2012).

[34] J. M. Foucaut, J. Carlier, and M. Stanislas, *PIV optimization for the study of turbulent flow using spectral analysis,* Measurement Science and Technology **15**, 1046 (2004).

[35] M. Raffel, C. E. Willert, and J. Kompenhans, *Particle Image Velocimetry* (Springer Berlin Heidelberg, Berlin, Heidelberg, 1998).

[36] J. Westerweel, D. Dabiri, and M. Gharib, *The effect of a discrete window offset on the accuracy of cross-correlation analysis of digital PIV recordings,* Experiments in Fluids **23**, 20 (1997).

[37] A. Melling, *Tracer particles and seeding for particle image velocimetry,* Measurement Science and Technology **8**, 1406 (1997).

[38] F. F. J. Schrijer and F. Scarano, *Effect of predictor–corrector filtering on the stability and spatial resolution of iterative PIV interrogation,* Experiments in Fluids **45**, 927 (2008).

[39] J. Westerweel, *Fundamentals of digital particle image velocimetry,* Measurement Science and Technology **8**, 1379 (1997).

[40] B. Wieneke, *PIV uncertainty quantification from correlation statistics,* Measurement Science and Technology , 11 (2015).

[41] A. Sciacchitano and B. Wieneke, *PIV uncertainty propagation,* Measurement Science and Technology **27**, 084006 (2016).

4

ACOUSTIC BEAMFORMING DEVELOPMENT AND APPLICATION

We like no noise unless we make it ourselves.

Marie de Rabutin-Chantal, marquise de Sevigne

In this chapter, the implementation of an improved version of an existing acoustic beamforming technique, namely the generalized inverse beamforming (GIBF), is presented. After a brief overview of the beamforming basic principles, the GIBF algorithm is applied to two experimental benchmark datasets featuring trailing-edge noise and loudspeaker measurements. The ability of the method in reconstructing distributed aeroacoustic sources and its accuracy and variability in different testing conditions are evaluated. Subsequently, GIBF is employed together with far-field microphone measurements to extensively characterize the turbulence-interaction noise radiated by the solid, porous, and melamine NACA-0024 profiles immersed in the wake of the cylindrical rod at different free-stream velocities.

Parts of this chapter are included in [1–5].

4.1. BASICS OF BEAMFORMING

The basic principles of acoustic beamforming, as well as the main tools to evaluate and interpret a typical sound map, are outlined in this section.

4.1.1. DELAY-AND-SUM PRINCIPLE

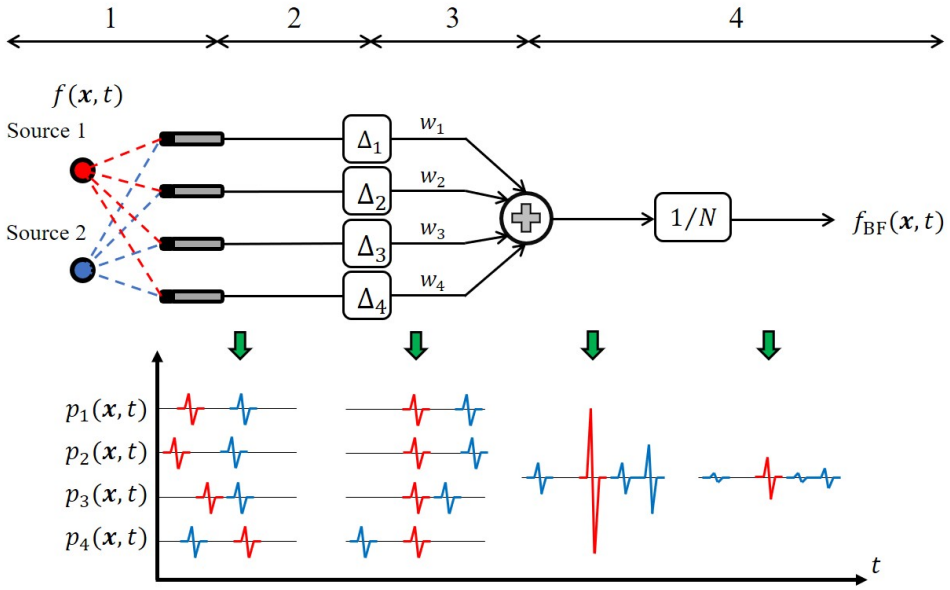

Figure 4.1: Visual description of the D&S principle with two potential sources and four microphones.

The principle of acoustic imaging techniques is best introduced through a description of the basic delay-and-sum (D&S) method [6–8]. The block diagram in Figure 4.1 illustrates the case of two-point sources situated in front of a linear microphone array, for which the D&S principle can be summarized in four steps as follows.

- The sound emitted by each source reaches every microphone of the array following different paths.
- The acquired signals are similar in waveform but exhibit different phases that are proportional to the travel distances. The time delays Δ_n can be computed from the speed of sound and the distance between microphones and sound sources. In the diagram in Figure 4.1, the beamformer targets the point where Source 1 is located.
- Subsequently, the signal of each microphone is shifted to account for the different relative Δ_n depending on the focus point. As a consequence, the components of the acoustic signal from Source 1 in all channels are in phase (red impulses), whereas those radiated from Source 2 are out of phase (blue impulses).
- Finally, the signals of all the microphone channels are summed up and averaged over the total number of microphones N. As depicted in Figure 4.1, the resulting

signal $f_{BF}(\boldsymbol{x}, t)$ features the same amplitude for Source 1 as that of the original signal, whereas the contributions coming from the signal components of Source 2 are negligible.

In a beamforming algorithm, the ensemble of potential sources that cover the expected noise-source locations is pre-defined by the user. The beamformer scans each of these sources and provides the resulting $f_{BF}(\boldsymbol{x}, t)$. If the potential source of this scanning grid actually contains a sound source at the considered location, the summed and normalized signals will provide a high amplitude. Conversely, if no sound source is present in the considered scanning-grid point, $f_{BF}(\boldsymbol{x}, t)$ will have low amplitude. The squared pressures of each scanning-grid point can then be computed, generating a sound map that indicates the position of the different noise sources included in the scanning grid.

4.1.2. CONVENTIONAL FREQUENCY-DOMAIN BEAMFORMING

If the D&S principle is transferred to the frequency domain through the Fourier transform of the recorded pressure signals, a formulation for the conventional frequency-domain beamforming (CFDBF) [6–9] can be derived. In this case, the sound propagation between each of the P scanning-grid points with position $\boldsymbol{x}_p$ and each of the N microphones with location $\boldsymbol{y}_n$ is modeled by means of the steering vector g_{pn}, a vector $P \times N$ that, for a stationary monopole-like source, can be represented by the free-field Green's function of the Helmholtz equation (see Chapter 2.1.3):

$$g_{pn} = \frac{-e^{ik||\boldsymbol{x}_p - \boldsymbol{y}_n||}}{4\pi||\boldsymbol{x}_p - \boldsymbol{y}_n||}. \tag{4.1}$$

The numerator of $\boldsymbol{g}_p$ induces the time delay, while the denominator gives the correction for the amplitude of the signal. The steering vector is typically normalized by its norm in order to obtain the same amplitude value for noise sources with the same strength but located at different positions. Several possible formulations for $\boldsymbol{g}_p$ are available in the literature depending on which aspect of the source characterization, i.e. localization accuracy or strength estimation, should be prioritized [10]. Moreover, additional modifications for $\boldsymbol{g}_p$ have been proposed in order to account for a dipole source [11] and for a moving source [12]. A recent application of beamforming for rotating sources can be found in the work of Amoiridis *et al.* [13].

The typical expression for the CFDBF output is given by

$$A(\boldsymbol{x}_p) = \boldsymbol{w}^{\dagger}(\boldsymbol{x}_p)\, \Gamma\, \boldsymbol{w}(\boldsymbol{x}_p) \quad \text{with} \quad \boldsymbol{w} = \frac{\boldsymbol{g}_p}{||\boldsymbol{g}_p||^2}, \tag{4.2}$$

where the symbol † denotes the complex conjugate and Γ indicates the cross-spectral matrix (CSM) of the acquired pressure signal. The CFDBF output expected from a given microphone array in ideal conditions can be theoretically determined through the point-spread function (PSF) [8], which represents the array response at a focus point $\boldsymbol{x}_P$ to a unitary–strength acoustic monopole-like source located in $\boldsymbol{x}_s$ and is a consequence of the finite number of microphones in the array. The PSF output features the main lobe located at the position of the source and side lobes decreasing with the distance from it, as can be observed in Figure 4.2, where the case of a monopole-like source centered at

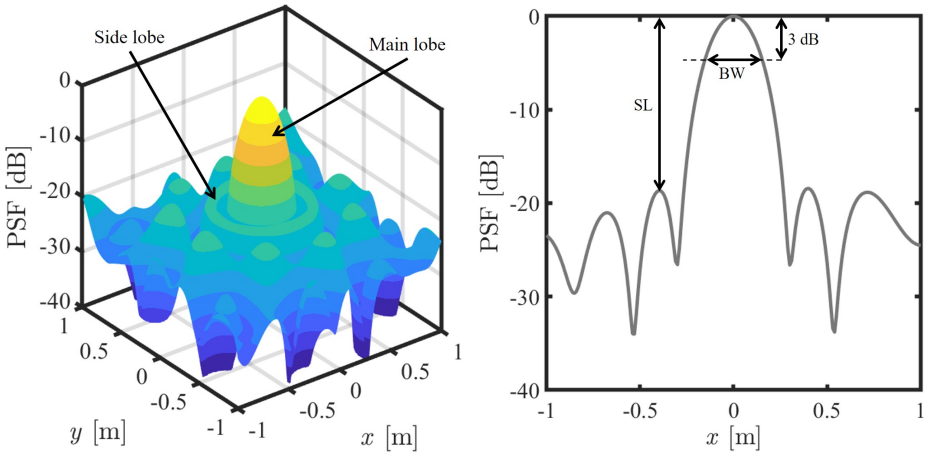

Figure 4.2: Schematic representation of a typical PSF at $f = 1\,\text{kHz}$ for a monopole source located at $(x,y) = (0\,\text{m},0\,\text{m})$. The array resolution is defined by the beam width (BW) at a position 3 dB lower than the main peak. The main-to-side lobe ratio (SL) indicates the capacity of the microphone array to distinguish sources of different amplitudes.

the origin of the coordinate system for $f = 1\,\text{kHz}$ is pictured. Several characteristic values defining the sound map are depicted in the plot:

- The beam width (BW) is defined as the width of the main lobe evaluated at 3 dB below its peak [8] and denotes the spatial resolution of the array and the associated capability to separate two sound sources situated at a small distance from each other. The lower the frequency is, the larger the BW will be. Furthermore, for planar arrays, the resolution in the direction perpendicular to the array plane is typically much lower than that in the lateral direction. A possible way to overcome this issue will be discussed in Chapter 4.2.3.

- The main-to-side lobe ratio (SL), or dynamic range, is defined as the difference in dB between the main-lobe peak and the highest side lobe [8]. In the PSF, the side lobes are coherent with the main lobe and this can lead to spatial aliasing effects that increase their amplitude at frequencies for which the minimum spacing between the microphones is larger than half the wavelength of the incoming wave. As a consequence, the higher the frequency is, the larger SL will be.

The use of advanced beamforming techniques like deconvolution approaches or inverse methods can significantly improve the spatial resolution and the dynamic range of the sound map, as will be shown in Chapter 4.3.1.

4.2. GENERALIZED INVERSE BEAMFORMING

The present section focuses on the implementation of the generalized inverse beamforming (GIBF), an acoustic beamforming inverse method first proposed by Suzuki [14].

4.2.1. INVERSE METHODS IN AEROACOUSTICS

Phased-array methods such as acoustic beamforming have proved to be standard noise mapping approaches in the aeronautic field. Indeed, the aeroacoustic community has always been active in this research topic and it is not inappropriate to state that some of the main findings on beamforming strategies have been obtained within this community. The above-mentioned CFDBF, deconvolution methods like CLEAN-SC [15–17], DAMAS [18, 19] and its evolution DAMAS-C [20] or others [21, 22], and, more recently, inverse approaches [23] such as GIBF [14, 24–26] are just some examples worth citing. An extensive review on acoustic beamforming methods for noise-source localization and their practical applications is provided by Merino-Martínez *et al.* [27, 28] and Chiariotti *et al.* [29].

Recently, an increased interest in inverse methods has grown as they make it possible to localize different kinds of source distributions and quantify their strengths. Although direct and inverse beamforming techniques start from the same source-receiver direct radiation formulation, they approach the problem in a completely different way. With respect to direct beamforming, in which each source is resolved as it is separated from the others (sources are implicitly assumed to be uncorrelated), inverse methods tackle the problem by considering all sources at once. Since source interference is thus potentially taken into account, inverse methods can deal with correlated/uncorrelated and sparse/spatially-distributed sources. This undoubtedly represents an incomparable advantage with respect to direct approaches, even though the mathematical implications linked to an inverse problem are numerous, like the necessity of some form of regularization and compliance with sparsity conditions (the source distribution is modeled by few non-zero components) to ensure a reliable strength reconstruction.

The latter aspect is undertaken in the present chapter, which has the objective to illustrate an improved version of GIBF characterized by an innovative, automated regularization method. Indeed, the determination of the optimized parameters involved in the solution of the inverse problem is of key importance for an accurate source strength estimation and has already been discussed by Zavala *et al.* [24], who compared the results of optimized regularization strategies for GIBF with numerical and experimental reference datasets.

4.2.2. DESCRIPTION OF THE ALGORITHM

A brief summary of the GIBF algorithm is reported hereafter. As most of the beamforming algorithms, also GIBF starts from the estimation of the microphone CSM. Since Γ is non-negative definite and Hermitian, it can undergo eigenvalue decomposition:

$$\Gamma = \boldsymbol{U}\Lambda\boldsymbol{U}^{\dagger}, \tag{4.3}$$

where $\boldsymbol{U}$ is a unitary matrix containing orthonormal eigenvectors on its columns, Λ is a diagonal matrix consisting of their eigenvalues, and $\boldsymbol{U}^{\dagger}$ is the complex conjugate transpose of $\boldsymbol{U}$. Each eigenvalue is proportional to the overall strength related to a coherent source distribution (under an orthogonality constraint) and the eigenvectors are associated with the sensor phase responses to these coherent source distributions. It is then possible to define the *eigenmode* as

$$\boldsymbol{v}_i = \sqrt{\lambda_i}\boldsymbol{u}_i, \tag{4.4}$$

$\boldsymbol{u}_\mathrm{i}$ being the i^{th} column vector of $\boldsymbol{U}$ and $\sqrt{\lambda_\mathrm{i}}$ the corresponding eigenvalue.

Assuming that the superposition of the equivalent sources at each grid point on the target domain produces an acoustic signal at the microphones as described by the eigenmodes, it is possible to formulate the mathematical model as

$$\boldsymbol{v}_\mathrm{i} = \boldsymbol{A}\boldsymbol{a}_\mathrm{i}, \tag{4.5}$$

where $\boldsymbol{a}_\mathrm{i}$ is the i^{th} source-amplitude vector and $\boldsymbol{A}$ is the $P \times N$ transfer matrix containing the source-receiver radiation patterns. If a monopole-like source is radiating in the presence of uniform flow, the radiation pattern should be modified in order to consider the effect of the flow convection. A possible formulation to take a uniform flow of velocity $\boldsymbol{U}_\infty$ into account is [30]

$$p = \frac{a_\mathrm{mono}}{4\pi\sqrt{(\boldsymbol{M}\cdot(\boldsymbol{x}-\boldsymbol{x}_s))^2 + \beta^2\left|\left|\boldsymbol{x}-\boldsymbol{x}_s\right|\right|^2}} e^{-2\pi i f \Delta t_e}, \tag{4.6}$$

where a_mono is the source strength from Equation (2.22), $\boldsymbol{M}$ is a vector of Mach numbers $\boldsymbol{M} = \boldsymbol{U}_\infty / c_0$, f is the frequency at which the source is radiating, $\boldsymbol{x}$ and $\boldsymbol{x}_s$ are the receiver and source locations, β is the compressibility factor defined as $\beta = (1 - ||\boldsymbol{M}||^2)^{1/2}$, and Δt_e is the emission time delay, which can be estimated as

$$\Delta t_e = \frac{1}{c\beta^2}\left(-\boldsymbol{M}\cdot(\boldsymbol{x}-\boldsymbol{x}_s) + \sqrt{(\boldsymbol{M}\cdot(\boldsymbol{x}-\boldsymbol{x}_s)^2 + \beta^2\left|\left|\boldsymbol{x}-\boldsymbol{x}_s\right|\right|^2}\right). \tag{4.7}$$

Nevertheless, for measurements performed in an open jet wind tunnel, the assumption of uniform Mach number cannot be considered valid anymore. In this case, the diffraction caused by the jet shear layer has to be incorporated in the source description. A possible method that takes into account the effect of the shear layer has been proposed by Sijtsma [30] and consists of replacing the uniform flow Mach number by the average Mach number between source and observer. The corrected Mach number can be expressed by

$$\boldsymbol{M}_\mathrm{corr} = \boldsymbol{M}\frac{z_s - z_{sl}}{z_s - z}, \tag{4.8}$$

where z_{sl} indicates the location of the shear layer and z_s and z are the z-coordinates of $\boldsymbol{x}_s$ and $\boldsymbol{x}$, respectively. The present formulation is assumed reliable for moderate Mach numbers less than 0.25 and for angles between shear layer and acoustic waves greater than 45°.

The numerical problem of Equation (4.5) is under-determined [1] and ill-posed in the sense of Hadamard [31]. Hence, it is common practice to find the minimum-norm solution of the problem addressed in Equation (4.5) by either exploiting the Moore-Penrose pseudoinverse (as $P \gg N$, the right-inverse is used) or regularization strategies like the Tikhonov approach. This regularization technique modifies the original formulation of the problem by adding a residual norm term and a regularization parameter that balances the residual and solution norms, thus providing a solution like

$$\boldsymbol{a}_\mathrm{i}^\star = \boldsymbol{A}^\dagger(\boldsymbol{A}\boldsymbol{A}^\dagger + \mu_\mathrm{R}^2\boldsymbol{I})^{-1}\boldsymbol{v}_\mathrm{i}, \tag{4.9}$$

[1] The number of potential sources - *unknowns* - is greater than the number of microphones - *equations*.

where μ_R is the regularization parameter and $\boldsymbol{I}$ is the identity matrix. Suzuki [14] suggested to determine μ_R as a fraction of the maximum eigenvalue $\mu_R = \epsilon \max\{\text{eig}(\boldsymbol{A}\boldsymbol{A}^\dagger)\}$, where ϵ typically ranges from 0.1 % to 5 %. Nonetheless, this method relies on a user-defined input that should be adapted to the specific test case addressed by the GIBF algorithm. An automatic procedure to estimate μ_R based on existing functions correlating the solution and error norms such as generalized cross-validation, L-Curve, quasi-optimality, etc. [26]) is therefore considered in this work. Several regularization tools are implemented through the commercial software MATLAB by MathWorks following the work of Hansen [32] and can be selected to solve the inverse problem.

The use of the least squares approach to find the cost function minimum is not accurate, since distributed sources will have their contributions squared and then summed. To increase the readability of the source-distribution map and to have a more accurate estimation of the overall strength of the source vector [14], the solution of the problem in Equation (4.5) can be rewritten in terms of $\mathscr{L}^1$ norm:

$$\boldsymbol{a}_i^\star = \text{argmin}\{|\boldsymbol{a}_i| + \mu_R^{-2}|\boldsymbol{v}_i - \boldsymbol{A}\boldsymbol{a}_i|^2\}. \tag{4.10}$$

This formulation excludes the possibility of an analytical solution but an iterative approach like the iteratively reweighted least squares (IRLS) algorithm solves the issue. The IRLS method computes the source-amplitude vector at the n^{th} iteration as

$$\boldsymbol{a}_i^{n+1} = \boldsymbol{W}^{(n)}\boldsymbol{A}^\dagger(\boldsymbol{A}\boldsymbol{W}^{(n)}\boldsymbol{A}^\dagger + \mu_{R,\text{IRLS}}^2\boldsymbol{I})^{-1}\boldsymbol{v}_i, \tag{4.11}$$

where $\boldsymbol{W}^{(n)}$ is a diagonal matrix whose diagonal components w_i are given by $w_i = |a_i^{(n)}|$, a_i being the component of the vector $\boldsymbol{a}_i$. At $n = 0$, the solution of Equation (4.9) is considered. The iteration process stops when the norm of the source-amplitude vector $\boldsymbol{a}$ starts increasing or the iteration counter reaches a pre-defined limit.

Likewise, an optimized value of the regularization parameter $\mu_{R,\text{IRLS}}$ has to be imposed at each iteration of the IRLS algorithm. However, the techniques associated with the Tikhonov regularization procedure are valid only for the $\mathscr{L}^2$ norm and cannot be directly applied to Equation (4.11). In this case, $\mu_{R,\text{IRLS}}$ is determined by evaluating the corner of the generalized L-curve that correlates solution and residual norms of the $\mathscr{L}^1$ norm minimization problem. The present method represents an original contribution and will be examined in Chapter 4.3.

In both $\mathscr{L}^2$ and $\mathscr{L}^1$ norm formulations, an iterative approach is followed in order to guarantee sparsity of the solution, minimize irregularities in the map, and save computational time. During these iterations, the smallest components of the source-amplitude vector are discarded on the basis of a reduction factor β_R ($0 < \beta_R < 1$). In this way, a reduced transfer matrix of size $(\beta_R P) \times N$ is retrieved at each stage. The algorithm stops when the source-amplitude vector reaches a pre-defined size that is chosen by the minimization of the following cost function:

$$J_p = |\boldsymbol{a}_i|_p^p + \mu_R^{-2}|\boldsymbol{v}_i - \boldsymbol{A}\boldsymbol{a}_i|_p^2, \tag{4.12}$$

where p refers to the norm that is minimized, i.e. $p = 2$ for the $\mathscr{L}^2$ norm or $p = 1$ for the $\mathscr{L}^1$ norm.

4.2.3. EXTENSION TO A THREE-DIMENSIONAL SCANNING GRID

The possibility to deal with three-dimensional calculation grids represents an attractive topic for aeroacoustic researchers since the three-dimensional environment makes it possible to better reconstruct the acoustic phenomena that generate noise. On the other hand, volumetric acoustic imaging brings in additional issues, such as the management of potential sources located at different distances from the array, the poor spatial resolution in the radial direction from the array center, and the increase in the number of potential sources with no contribution to the acoustic field.

Although the potentialities of a volumetric approach are clear, very few works can be found in the literature [10, 33–38]. All the previous papers refer to direct and deconvolution formulations. Indeed, deconvolution is necessary to cope with the reduced longitudinal resolution capability (the one perpendicular to the array) of a beamformer with respect to the lateral one, unless the microphone array arrangement encloses the source region under analysis. Inverse methods partially overcome this issue by taking into account all sources at once, even though better results can be obtained by combining microphone arrays placed perpendicularly to each other. This motivates the extension of the GIBF algorithm to account for a three-dimensional scanning grid in the so-called 3D-GIBF. To the author's knowledge, the only work comparing deconvolution methods and GIBF for the three-dimensional localization of simplified sources is that by and Padois and Berry [39].

Nonetheless, the employment of non-planar scanning grids requires different approaches to handle the regularization of the numerical problem and this often leads to the generation of spurious noise sources in the map. A possible solution to overcome this problem is through the exploitation of the *multiplicative beamforming* approach. The multiplicative beamforming principle has been proposed in the literature in different formulations and array/source configurations, from cross/star-shaped arrays [40, 41] targeted to aeroacoustic testing, to double-spherical arrays [42] for interior noise applications but always with the purpose of enhancing the computed acoustic map and reducing the effect of side-lobes and artifacts in the acoustic image. The approach proposed in this manuscript is the one suggested by Porteous *et al.* [37]. For sake of readability, the main steps of the method are reported hereafter. Subscripts 1 and 2 denote the first and second array, respectively. As a result of the GIBF algorithm, the output of each array referring to the i^{th} source-amplitude vector is

$$\begin{aligned} \boldsymbol{a}_{\text{i}1}^{\star} &= \boldsymbol{A}_1^{\dagger}(\boldsymbol{A}_1\boldsymbol{A}_1^{\dagger} + \mu_{\text{R}}^2\boldsymbol{I})^{-1}\boldsymbol{v}_{\text{i}1}; \\ \boldsymbol{a}_{\text{i}2}^{\star} &= \boldsymbol{A}_2^{\dagger}(\boldsymbol{A}_2\boldsymbol{A}_2^{\dagger} + \mu_{\text{R}}^2\boldsymbol{I})^{-1}\boldsymbol{v}_{\text{i}2}. \end{aligned} \tag{4.13}$$

The final i^{th} source-amplitude vector can be calculated as the square root of the product of the two, i.e.

$$\boldsymbol{a}_{\text{i}}^{\star} = \sqrt{\boldsymbol{a}_{\text{i}1}^{\star}\,\boldsymbol{a}_{\text{i}2}^{\star}}. \tag{4.14}$$

Also in this case, the minimization of $\mathscr{L}^1$ norm can be considered by using the IRLS algorithm, as showed before.

The technique outlined above makes it possible to eliminate the directional bias related to the poor depth resolution of each array and reduce side-lobe levels from the beamforming map, improving the three-dimensional localization accuracy and hence

easing the use of a three-dimensional scanning grid. A practical application of 3D-GIBF involves the aeroacoustic characterization of the noise sources on a Counter Rotating Open Rotor installed on a 1/7 scale aircraft model [4]. The model has been tested in a large Low-Speed Wind Tunnel at The Pininfarina Aerodynamic and Aeroacoustic Research Center in Turin, Italy, within the framework of the FP7 EU Clean-Sky WENEMOR project. In that instance, the present approach has proven to be able to provide noise distribution maps characterized by fine resolution and high dynamic range.

4.3. BENCHMARK VALIDATION

The implementation of the GIBF algorithm is validated through its application to two experimental benchmark datasets that are relevant for aeroacoustic applications. The first one features trailing–edge noise measurements and is considered to evaluate the capability of the method in localizing and accurately quantifying distributed sound sources. The second one involves experiments with speakers emitting a known sound signal as a reference solution and simulates airframe noise applications characterized by multiple point sources such as landing-gear systems [43].

4.3.1. AIRFOIL TRAILING-EDGE MEASUREMENTS

The first benchmark test case is labeled as NASA2 [44] and contains data corresponding to trailing-edge noise measurements of an airfoil immersed in a clean flow from the NASA Langley Quiet Flow Facility (QFF) open-jet wind tunnel. An exhaustive description of the setup can be found in previous trailing-edge noise experiments [18, 45] and will be briefly summarized in the following section.

EXPERIMENTAL SETUP

A schematic of the experimental setup is depicted in Figure 4.3. A NACA 63-215 Mod-B full-span airfoil with a $s = 0.127\,\text{mm}$ (16 in) span and $c = 0.406\,\text{m}$ (36 in) chord length is mounted at its zero-lift angle of attack ($-1.2°$) relative to the vertical flow in the QFF. The wing profile, installed in a clean configuration and hence without the use of any high-lift device, features a spanwise uniform sharp trailing edge with a $t = 0.127\,\text{mm}$ (0.005 in) thickness. Grid of size #90 is distributed over the first 5 % of the airfoil leading edge in order to allow for a fully turbulent boundary layer at the trailing edge.

A 33-microphone small-aperture directional array (SADA) is placed at an elevation angle of 90° with respect to the pressure side of the airfoil. Data are acquired with the SADA at a free-stream Mach number of 0.17 and at a temperature of 26.35°. The sampling rate for the signal is 142 857.71 Hz and a total of 2 048 000 samples are recorded simultaneously for all microphone channels, corresponding to an acquisition time of 14.3 s. The measurement parameters of the campaign are summarized in Table 4.1. Considering the zero-lift condition of the wing profile and its orientation in the facility, it is possible to assume that the mean shear layer bounding the flow remains planar and attached to the nozzle-lip line and is located at a constant distance of 0.305 m from the centerline of the nozzle. The airfoil itself is offset from the tunnel centerline by 0.133 m and the SADA is located 1.524 m from the trailing edge. Finally, an acquisition in the absence of airfoil is taken in order to apply background-noise removal techniques.

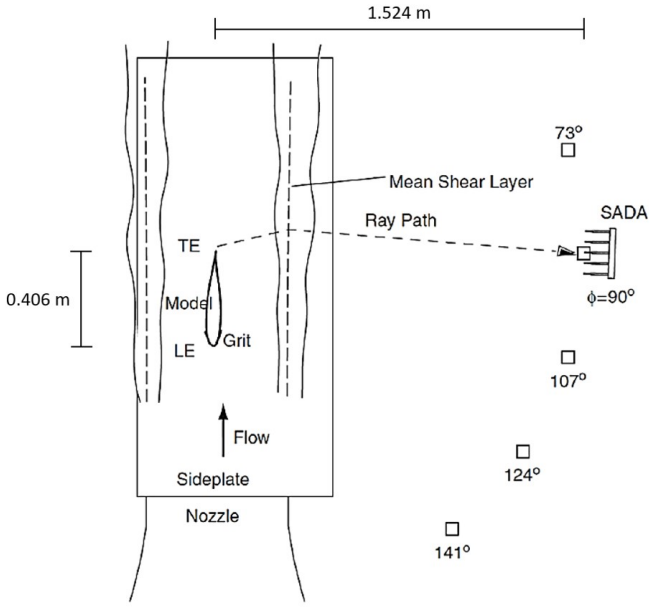

Figure 4.3: Setup for the trailing-edge measurements of the NACA 63-215 Mod-B full-span airfoil in NASA Langley QFF. The airfoil is installed in a clean configuration at its zero-lift angle of attack (−1.2°). The coordinate system origin is the center of the nozzle exit plane. Adapted from [44].

Configuration	Free Stream Mach	Angle of attack	Recording Time
Clean	0.17	−1.2°	14.3 s

Table 4.1: Measurement parameters used for the processing of the NASA2 benchmark dataset.

GIBF ALGORITHM SETTING

The GIBF algorithm requires some preliminary tuning in order to assess the optimal parameters and an automatic regularization procedure has been implemented. For the Tikhonov regularization in Equation (4.9), the quasi-optimality criterion is considered in order to determine the optimized value of μ_R, while the L-Curve approach described in Chapter 4.2.2 is employed to retrieve the optimized value of μ_R at each iteration of the IRLS algorithm.

Concerning the stop criterion for the iteration count, the resolution of the source localization increases with the number of iterations of the algorithm. Anyway, with the more significant reduction of the source-amplitude vector components, relevant physical sources risk being discarded, and, for this reason, a trade-off between readability of the map and loss of information has to be reached. The determination of the proper stop criterion is performed a posteriori, following a first run of the algorithm. From this, the cost function in Equation (4.12) is evaluated and the iteration counter corresponding to

its minimum is chosen for the second and definitive run. In the present case, β_R is set to 0.01 in order to allow for a smooth discard of the source-amplitude vectors.

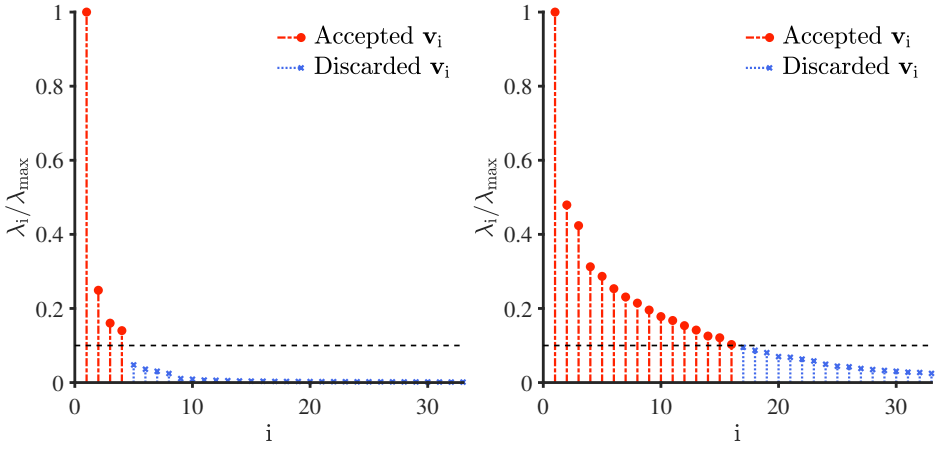

(a) $f = 3.15$ kHz. (b) $f = 12.5$ kHz.

Figure 4.4: Procedure for the determination of the total number of eigenmodes to be processed in the GIBF algorithm for two narrow frequencies. The different λ are normalized with the maximum eigenvalue λ_{max}. All the eigenvalues below the 10% of λ_{max} are discarded.

The choice of the number of eigenmodes to process determines how many coherent source distributions under the constraint of orthogonality are included in the computation. An automatic procedure is implemented to select this value based on the magnitude of the dominant eigenvalue λ_{max}. In particular, all the eigenmodes for which $\lambda > 0.1\,\lambda_{max}$ are considered, whereas the rest is discarded. The number of eigenmodes taken into consideration with this method is typically a function of the investigated frequency. The higher the frequency, the larger the number of non-negligible eigenmodes that are included will be. This trend can be observed in Figure 4.4, which provides a visualization of the present procedure for $f = 3.15$ kHz and $f = 12.5$ kHz.

Moreover, this feature makes it feasible to select a subset of eigenmodes that correspond only to the actual sources of interest, avoiding the contribution of spurious sources coming from the background noise. For instance, a region surrounding the airfoil could be defined in order to process only the coherent source distributions whose main lobes are embedded within this area. This possibility has not been exploited in the processing of the NASA2 benchmark dataset in order to allow for a direct comparison with other advanced beamforming methods.

SOURCE LOCALIZATION RESULTS

This section outlines the qualitative analysis of the source distributions processed on a one-third octave band basis. The objective of the study is to evaluate the performance of the algorithm in terms of source spatial resolution. Since the airfoil is installed in a clean configuration, the noise sources are expected in the trailing-edge regions of the wing profile. Moreover, the tripping procedure over the 5% of the airfoil leading edge is believed to lead to the generation of high-frequency noise contributions at this location.

In order to perform a preliminary assessment of the method capabilities, the results of GIBF are compared with those obtained by a CFDBF algorithm implemented at VKI. Four one-third octave band frequencies, namely $f_{1/3}$ = 3.15 kHz, $f_{1/3}$ = 8 kHz, $f_{1/3}$ = 12.5 kHz, and $f_{1/3}$ = 20 kHz are considered, in analogy with the work carried out by Brooks and Humphreys [18] on the same test case. The potential sources are displaced on a planar square scanning grid of 1.27 m per side placed at 1.524 m from the SADA. The grid contains 2601 points (51 points per each side) and extends beyond the side-plates where the wing profile is installed. The resulting spatial resolution is 0.0254 m. In both algorithms, a diagonal removal for the reduction of the microphone self-noise [8] and a conventional subtraction for the handling of background noise are applied to the CSMs of the recorded signals [46].

Figure 4.5 shows the source distributions processed by the CFDBF algorithm. The vertical black lines denote the test section side-walls, whereas the horizontal ones indicate the leading edge and trailing edge of the airfoil. In each plot, the flow goes from the bottom to the top of the map. A dynamic range of 10 dB is applied for presenting the sound-pressure level of the CFDBF source-distribution maps, expressed in dB with a reference pressure of $p_{\text{ref}} = 20\,\mu\text{Pa}$.

A general observation to be made is that the position of the main-source regions is variable according to the frequency. In addition, the noise is reflected by the two side-walls of the setup. Since these are not taken into account in the free-field Green's function, the reflected sources are interpreted by the CFDBF method as artifacts located in the regions at $|x/c| > 1.13$. The source distributions for each frequency are analyzed separately.

- At $f_{1/3}$ = 3.15 kHz (Figure 4.5a), the main noise sources are distributed downstream of the trailing-edge center. However, the difference in sound-pressure level between leading-edge and trailing-edge source regions is lower than 3 dB because of the limited dynamic range of the map. For this band, CFDBF is not able to properly isolate the noise source because of the frequency-dependent beamwidth characteristics of the antenna. Indeed, the SADA has been designed to have a 1 ft (0.3048 m) main lobe at 10 kHz. Hence, at frequencies below half of this value, the separation of multiple source contributions is problematic for non-advanced methods.

- At $f_{1/3}$ = 8 kHz (Figure 4.5b), the dynamic range of the map is higher than the previous case and the separation of the sources is more evident. In this case, the main source regions are distributed along the trailing edge of the airfoil, with a concentration in the right part of the sound map.

- At $f_{1/3}$ = 12.5 kHz (Figure 4.5c), the map shows a comparable energy level for both leading-edge and trailing-edge source regions. The CFDBF algorithm is able to localize the contributions of these sources and separate them but the dynamic range should be further reduced in order to visualize this separation. As previously mentioned, the presence of noise sources at the leading edge is attributable to the tripping procedure of the airfoil.

- Finally, at $f_{1/3}$ = 20 kHz (Figure 4.5d), the source region is distributed along the

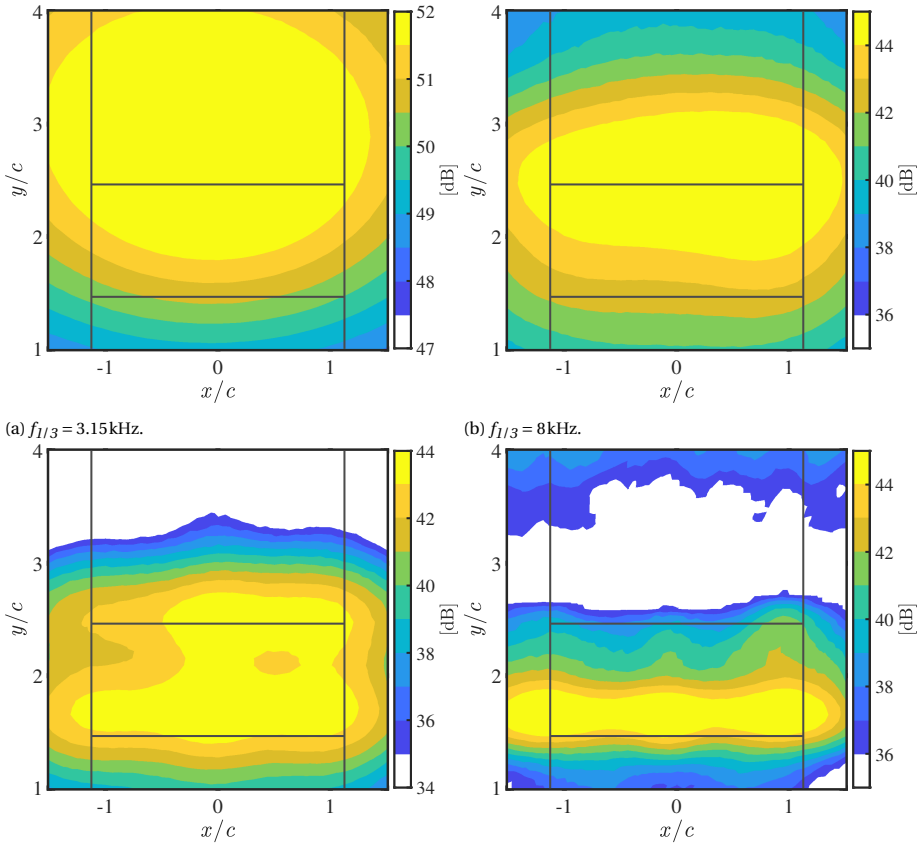

Figure 4.5: CFDBF source distribution maps of the NACA 63-215 Mod-B full-span airfoil. The vertical black lines indicate the test section side-walls, the horizontal ones indicate leading edge and trailing edge of the wing profile. The flow goes from bottom to top. The dynamic range is 10 dB computed with a reference pressure of $p_{\text{ref}} = 20\,\mu\text{Pa}$.

tripped leading edge in the spanwise direction. As expected, the high frequency leads to a better spatial resolution, although spurious side lobes seem to be present in the top part of the map.

In Figure 4.6, the corresponding GIBF sound maps are presented. For the visualization of the results, the same settings as those for the CFDBF cases are considered with the sole exception of the dynamic range, which is risen to 20 dB. All the maps feature a significant improvement in the readability and a reduction of the spurious sources. Likewise, the different frequencies are investigated individually.

- At $f_{1/3}$ = 3.15 kHz (Figure 4.6a), a downstream shift in the source distribution can be observed if compared with the results obtained by CFDBF. The position of the main lobe is now displaced in correspondence with the trailing-edge center, which

represents a more likely location for the noise source. The resolution of the source distribution significantly increases with respect to the CFDBF one in terms of SL.

- At $f_{1/3}$ = 8 kHz (Figure 4.6b), the sources are distributed along the entire trailing-edge length of the model. The position of the main lobe coincides with that retrieved by CFDBF. Low-level secondary sources can be observed at the bottom of the map in this case.

- At $f_{1/3}$ = 12.5 kHz (Figure 4.6c), the leading-edge and trailing-edge source regions are visually clearly separated and feature a similar level of source strength. The noise sources appear to have a distributed nature and, for the leading edge, it is possible to identify the same three peaks as the related CFDBF result. No artifacts are present in the map.

- At $f_{1/3}$ = 20 kHz (Figure 4.6d), GIBF provides a uniform visualization of the distributed sources along the leading edge. Three spots where the source region is more concentrated can be identified in the middle and in proximity of the external borders of the wing profile.

It is important to point out that inverse beamforming methods such as GIBF display the source-distribution contours instead of the peak source intensity, differently from direct techniques [14]. This feature is practically useful when dealing with multiple or distributed noise sources. Hence, the source-power integration [47] of the maps is required to assess the actual noise-source strength. This explains the relatively low levels of the sound maps in Figure 4.6 in comparison with the results of CFDBF.

Finally, the comparison between the maps obtained with GIBF and the results published by Bahr *et al.* [48] related to other advanced phased array techniques is shown in Figure 4.7. The contributions for the NASA2 benchmark test case come from three organizations: NASA Langley Research Center (using DAMAS), University of Lyon (using Sparse Bayesian Reconstruction [49] and DAMAS), and University of New South Wales (using CFDBF and CLEAN-SC). All the contributors processed the data corresponding to $f_{1/3}$ = 12.5 kHz. The reason behind this choice lies in the similar energetic level that the sources feature at the leading edge and at the trailing edge. In this way, the performances of each method in terms of source isolation can be assessed. However, the real source distribution is still not known with certainty due to the experimental nature of the benchmark. Sources are expected to occur just downstream of the leading edge and at the trailing edge of the airfoil. Both source regions are expected to feature distributed characteristics.

In general, all the methods are able to successfully isolate the two different source regions. The focus points of the comparison with GIBF are once again addressed separately.

- For CLEAN-SC, the acoustic source energy in the map, which is expected to be distributed along the leading edge and trailing edge, appears to be concentrated in isolated spots near the airfoil center and side walls. GIBF provides a better representation of the nature of the source region, whereas the position of the main lobes computed by the two algorithms coincides. At the lateral boundaries of the map,

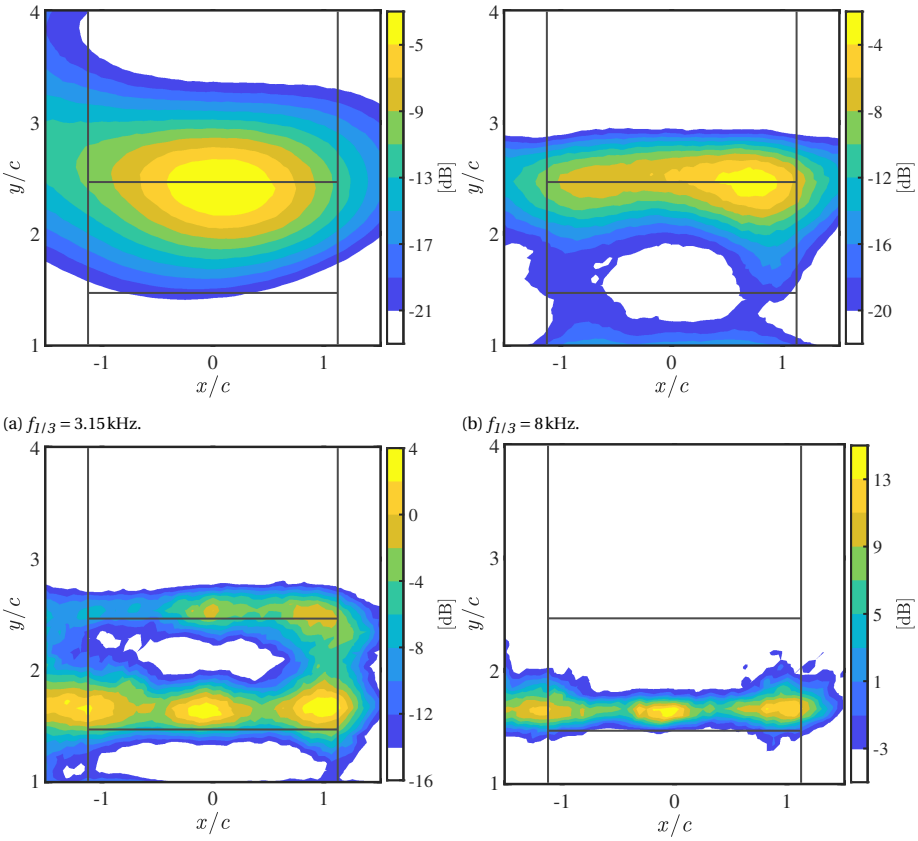

(a) $f_{1/3} = 3.15\,\text{kHz}$.

(b) $f_{1/3} = 8\,\text{kHz}$.

(c) $f_{1/3} = 12.5\,\text{kHz}$.

(d) $f_{1/3} = 20\,\text{kHz}$.

Figure 4.6: GIBF source distributions of the NACA 63-215 Mod-B full-span airfoil. The vertical black lines indicate the test section side-walls, the horizontal ones indicate leading edge and trailing edge of the wing profile. The flow goes from bottom to top. The algorithm is based on the quasi-optimality criterion for the determination of the optimized regularization parameter and on the minimization of $\mathscr{L}^1$ norm. The dynamic range of the maps is 20 dB computed with a reference pressure of $p_{\text{ref}} = 20\,\mu\text{Pa}$.

there are artifacts whose origin could be related to numerical issues. Finally, the peak level of the CLEAN-SC map is higher than that estimated by DAMAS, probably because of the more significant energy concentration.

- Bayesian reconstruction shows a better spatial resolution than GIBF and a total absence of spurious sources at the boundaries of the map. However, the source distribution is still more irregular, with a concentration of energy comparable to the previous case. Thus, conclusions similar to the comparison with CLEAN-SC case can be drawn. Concerning the sound power level estimation, the nature of the Bayesian method makes it difficult to directly relate the peak level of this technique to the other results [48]. An additional scaling factor is therefore required.

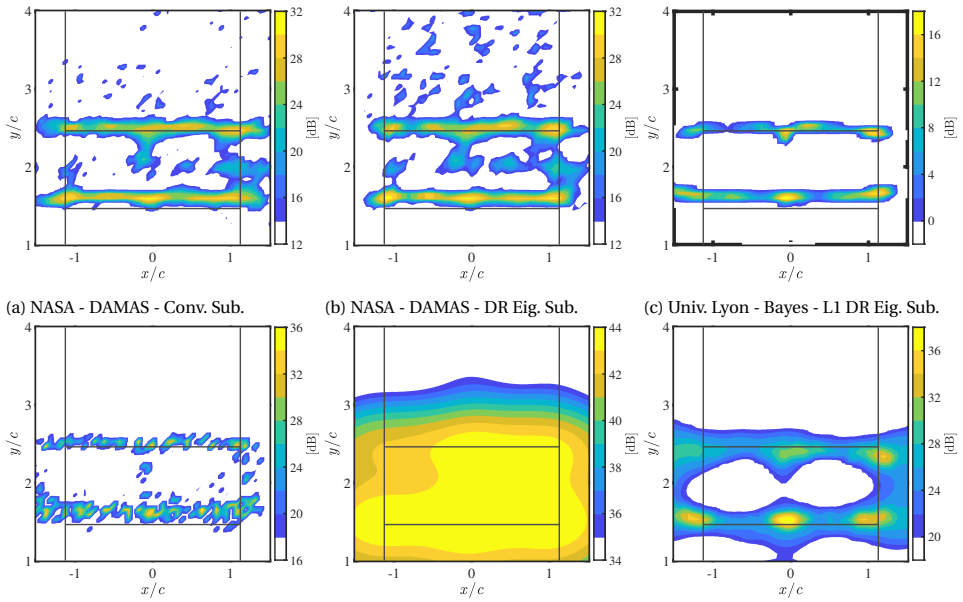

(a) NASA - DAMAS - Conv. Sub. (b) NASA - DAMAS - DR Eig. Sub. (c) Univ. Lyon - Bayes - L1 DR Eig. Sub.

(d) Univ. Lyon - DAMAS - Eig. Sub. (e) UNSW - CFDBF - DR Conv. Sub. (f) UNSW - CLEAN-SC - DR Conv. Sub.

Figure 4.7: Qualitative comparison of the NASA2 benchmark contributions corresponding to a one-third octave band frequency of 12.5 kHz. The algorithms used for the source distributions are: DAMAS, from NASA (no diagonal removal, conventional subtraction), DAMAS, from NASA (diagonal removal, eigenvalue subtraction), Bayesian reconstruction, from University of Lyon (diagonal removal, eigenvalue subtraction), DAMAS, from University of Lyon (no diagonal removal, eigenvalue subtraction), CFDBF, from UNSW (diagonal removal, conventional subtraction), and CLEAN-SC, from UNSW (diagonal removal, conventional subtraction). All maps aside from CFDBF are characterized by a 20 dB dynamic range computed with a reference pressure of $p_{\text{ref}} = 20\,\mu\text{Pa}$. Credit: Christopher Bahr.

- The source distribution processed by DAMAS features a better spatial resolution than GIBF for the source regions. However, for this algorithm, implementation plays a relevant role in the distribution of low-level spurious sources [48]. For instance, in the results from NASA, the effective aeroacoustic sources are homogeneously distributed along the leading and trailing edge with no significant variation of the sound-pressure level in the spanwise direction. The source distribution is therefore closer to the expected one if compared with GIBF. Nevertheless, the maps appear less readable due to the presence of spurious sources and artifacts at the lateral boundaries of the scanning grid. These artifacts are probably due to the effects of the acoustic reflection of the side-walls. The DAMAS source distributions from University of Lyon are instead cleaner and do not present artifacts at the lateral boundaries. However, the source distribution is sparse and with isolated peaks along the leading edge and trailing edge. NASA's DAMAS and GIBF provide therefore a better representation of the expected nature of the sources. Furthermore, the peak level of the map is higher than the levels of the two NASA's implementations.

- The comparison with CFDBF has already been discussed above. Additionally, due to the distributed characteristics of the sources, the peak levels of the map are significantly higher than any of the other beamforming techniques.

In Chapter 4.3.1, the discussion is extended to the quantitative analysis for the determination of the sound-pressure levels of the integrated spectra.

INTEGRATED SOURCE SPECTRA RESULTS

The quantitative estimation of the integrated power spectra of the leading-edge and trailing-edge regions computed at the center of the array is discussed in this section. The one-third octave spectra are determined by summing the pressure-squared values

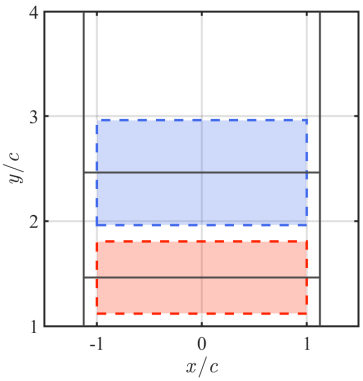

(a) Areas considered for the integration

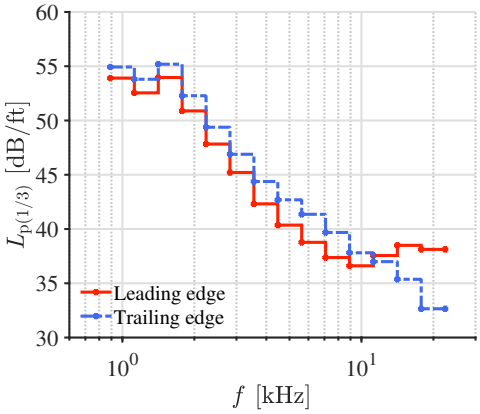

(b) Integrated one-third octave spectra per foot span computed with CFDBF

Figure 4.8: Quantitative analysis of the leading edge and trailing edge regions of the model per foot-span.

of each scanning-grid point within rectangular areas surrounding the leading edge and trailing edge of the airfoil. A visual representation of the integration regions is shown in Figure 4.8a. The leading-edge rectangular area has a width of 0.813 m (2 c) and a height of 0.279 m (0.7 c), while the trailing edge one has the same width and a height of 0.406 m 1 c. Since the region's spanwise length is 2.5 ft, the sums are divided by 2.5 in order to express the spectral results on a per-foot basis and, therefore, to allow for the comparison with the published data.

A first approach to the source-strength estimation of the leading-edge and trailing-edge regions is made by computing the one-third octave spectra with CFDBF (Figure 5.13). The trailing edge noise appears to be dominant for frequencies up to 11 kHz, below which the leading edge one prevails. This trend is visible also in the source-distribution maps in Figures 4.5 and 4.6. However, especially at low frequencies, leading-edge noise appears to be contaminated by the trailing-edge one, probably because of the beamwidth characteristics of the antenna. This is highlighted by the fact that the trend of the integrated leading-edge spectra follows that of the integrated trailing-edge ones. The use of more advanced algorithms makes it possible to solve this problem and determine a more reliable estimation of the source strength.

For GIBF, the integration procedure differs from that considered for direct methods and has to be performed in two stages. Given the assumption of source coherence, the pressure values of the scanning-grid points within the integration region are first summed and then squared for each eigenmode, resulting in as many squared-pressure values as the number of processed eigenmodes. These are subsequently summed in order to determine the final sound-pressure level.

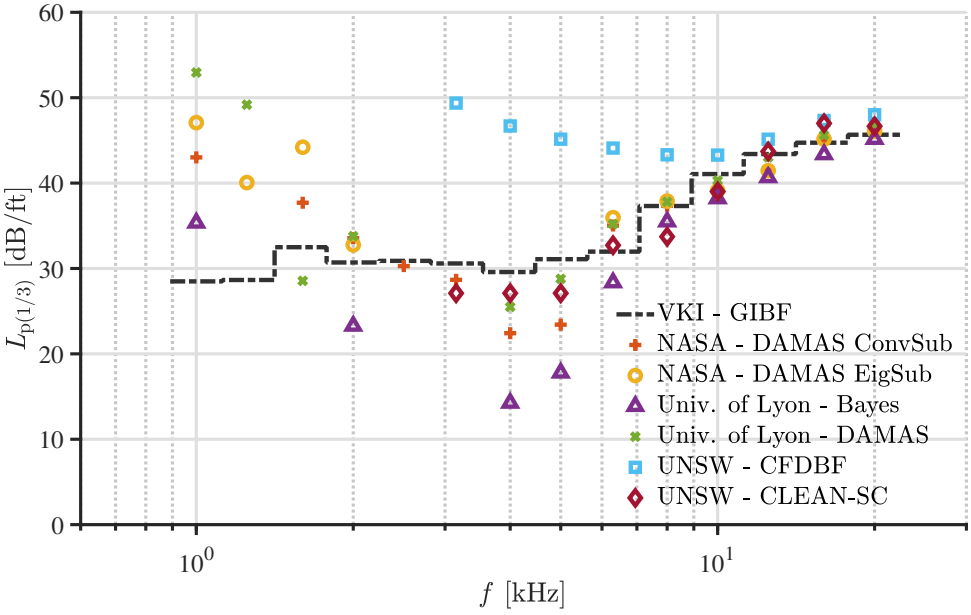

Figure 4.9: Integrated leading-edge one-third octave spectra per-foot-span computed with various analysis methods. Credit: Christopher Bahr [48].

Figure 4.9 shows the integrated one-third octave spectra per-foot-span referred to the leading-edge region and computed by the same algorithms discussed above in Figure 4.7. All the leading-edge spectra feature similar trends between 6 kHz and 20 kHz[2], suggesting that the differences in the qualitative maps at 12.5 kHz analyzed in the previous section tend to average out within the integration procedure. In this range of frequencies, GIBF follows successfully the trend of the other methods. Below approximately 6 kHz, the advanced techniques start showing a significant divergence in the resulting sound-pressure level. Thus, for lower frequencies, the integrated leading-edge one-third octave spectra do not represent a proper validation test case for the source-strength estimation. As stated by Bahr et al. [48], one of the reasons for this limitation can be related to the microphone antenna used for the measurement. Because of the frequency-dependent beamwidth characteristics of the SADA, indeed, separating multiple source contributions at frequencies above 5 kHz may be difficult even for advanced methods.

The integrated one-third octave spectra per-foot-span corresponding to the trailing-edge region are presented in Figure 4.10. Also in this case, GIBF follows successfully the

[2]The divergence experienced by CFDBF has been already discussed.

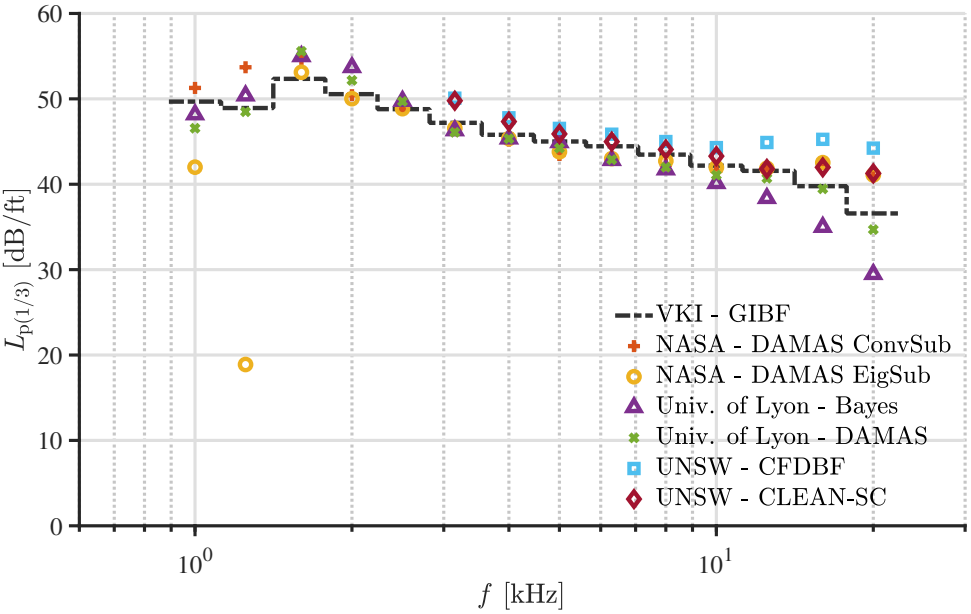

Figure 4.10: Integrated trailing-edge one-third octave spectra per-foot-span computed with various analysis methods. Credit: Christopher Bahr [48].

trend of the other methods. At low frequencies, the spectra computed by the different algorithms show a more uniform behavior in relationship to the leading-edge spectra, most probably because of the dominance of trailing-edge noise over the leading-edge one in this frequency range. Indeed, the calculation of the integrated levels of the dominant sources at low frequencies features less variability with respect to the array resolution when compared to the levels of a weaker source [48]. This observation is reinforced by the increased variability exhibited by the trailing-edge spectra in the frequency range where leading-edge noise is dominant (11 kHz – 20 kHz).

4.3.2. LOCALIZED-SOURCE MEASUREMENTS

The second benchmark dataset considered for the validation of GIBF features measurements of a single speaker emitting synthetic broadband noise and two speakers emitting incoherent synthetic broadband noise. The measurements have been designed and performed in the A-tunnel facility by R. Merino-Martínez [50].

EXPERIMENTAL SETUP

The microphone distribution employed for the measurements is optimized for frequencies ranging between 1 kHz and 10 kHz [51] and provides an array diameter of approximately 2 m. The location of the microphones and the relative position of the two Visaton *K 50 SQ* speakers are depicted in Figure 4.11a. Each speaker is employed for emitting a different incoherent synthetic broadband noise signal. Both of them are placed at a distance of 1 m from the array plane and have a baffle diameter of approximately 0.45 m.

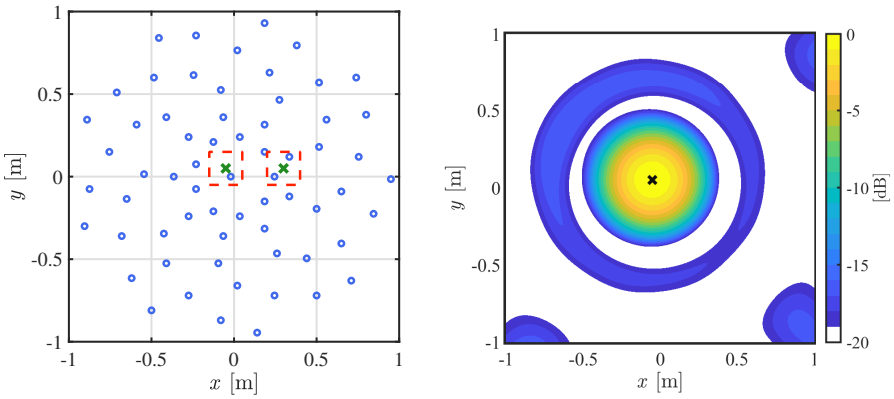

(a) Schematic of the microphone distribution of the array (blue dots) and relative position (green **x** symbols) and integration regions (red dashed squares) of the two speakers.

(b) PSF of the array for a point source at the left speaker location (denoted by the black **x** symbol) emitting sound within a 630 Hz one–third octave band.

Figure 4.11: Setup of the experimental campaign for the speaker measurements.

The (x, y, z) coordinates of the speakers, with the x- and y-axis centered at the array center microphone and the z-axis normal to the array plane pointing towards the speakers, are $(-0.05\,\text{m}, 0.05\,\text{m}, 1\,\text{m})$ for the left speaker and $(0.3\,\text{m}, 0.05\,\text{m}, 1\,\text{m})$ for the right one. The test cases featuring speakers are performed without flow in the wind tunnel, using the facility as an anechoic chamber. The PSF of this microphone array is shown in Figure 4.11b for a point source located at the left speaker position emitting sound within a one–third octave frequency band centered at 630 Hz.

For the acquisition, a sampling frequency of 50 kHz and 60 s of recording time are considered. The acoustic data are averaged in time blocks of 2^{13} samples, providing a frequency resolution of 6.10 Hz), and windowed using a Hanning weighting function with 50 % data overlap, following Welch method [52]. The frequency range of interest considered in this study extends from 500 Hz to 5 kHz.

For each test case, some considerations should be noted.

- **Case I: Single speaker.** For the first test case, only the left speaker (Figure 4.11a) emits sound. The same synthetic broadband noise signal is played at four different volumes, which provide four different values of signal-to-noise-ratio (SNR) with respect to the background noise of the facility. These SNR values are calculated by subtracting the background-noise spectrum of the wind–tunnel facility from the frequency spectrum of the speaker. The data are averaged over the 64 microphones. The background noise remains the same for all the cases involving speakers. The baseline pressure signal (labeled as SNR_1) is reduced in amplitude by a factor 10 (SNR_2), 50 (SNR_3), and 100 (SNR_4). For each SNR case, the signal is played 10 times to investigate the repeatability of the results. The average signal of all the microphones of the array is considered as the reference signal for comparison with the results of GIBF. The signal of each microphone is corrected for expressing the sound-pressure level at 1 m from the sound source. A scanning grid ranging from $x = -1$ m to $x = 1$ m and from $y = -1$ m to $y = 1$ m is used in the algo-

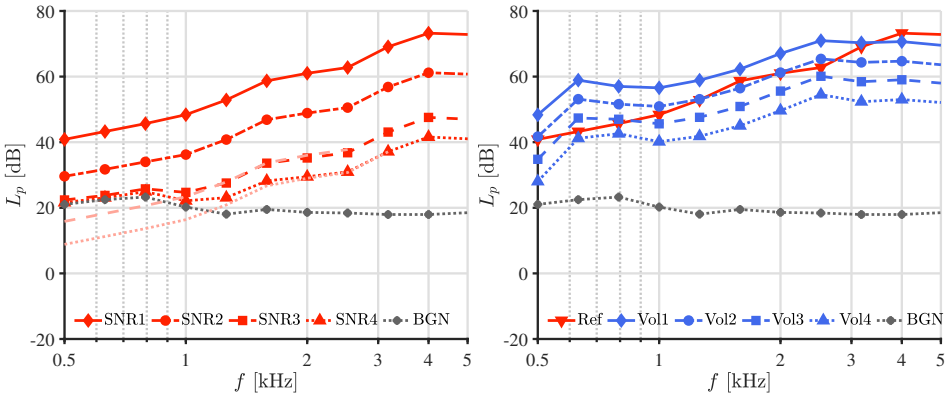

(a) The single-speaker case, with the four SNR cases. The opaque lines denote the predicted spectra for SNR_3 and SNR_4 at low frequencies.

(b) The two-speakers case, with the four volumes emitted by the right speaker and the SNR_1 case emitted by the left speaker.

Figure 4.12: One–third octave spectra averaged over the 64 microphones of the array. The background-noise spectrum (BGN) of the facility is also plotted. The spectra are computed with $p_{ref} = 20\,\mu Pa$.

rithm, with $z = 1\,m$ and spacing between the grid points of $\Delta x = \Delta y = 0.01\,m$. The resulting source-distribution maps are integrated over a square integration area centered at the left speaker (from $x = -0.15\,m$ to $x = 0.05\,m$ and from $y = -0.05\,m$ to $y = 0.15\,m$, with $z = 1\,m$), as the dashed square in Figure 4.13a depicts. The frequency spectra recorded by the array and averaged over all the microphones for the different SNR cases are presented in Figure 4.12a, as well as the background noise (BGN) of the facility. The values shown indicate the sound-pressure levels L_p expressed in decibels and computed with a reference pressure of $p_{ref} = 20\,\mu Pa$. It is observed that an almost constant offset over the whole frequency range is obtained when decreasing the volume of the left speaker. These offsets have approximate values of $-12\,dB$, $-25\,dB$, and $-32\,dB$ for SNR_2, SNR_3, and SNR_4, respectively, with respect to the maximum volume considered (SNR_1). It is also seen that the recorded signals for SNR_3 and SNR_4 collapse with the background noise spectrum of the facility for the lowest frequencies, which indicates that the speaker is emitting sound below the background noise in that frequency range, i.e. with a negative SNR. The sound spectra expected for these two SNR cases are depicted as opaque lines in the same figure, assuming the aforementioned offset values of $-25\,dB$ and $-32\,dB$, respectively.

- **Case II: Two speakers.** For the case with two speakers, both left and right speakers (Figure 4.11a) emit sound simultaneously. The same synthetic broadband noise signal as in Case I is played by the left speaker with the volume of the SNR_1 case, and another different synthetic broadband noise signal (incoherent with the first signal) is played by the right speaker at four different volumes. The baseline signal for the right speaker is referred to as Volume 1. Volumes 2, 3, and 4 denote cases with the right speaker emitting the signal of Volume 1 divided by a factor 4, 8, and 16, respectively. Additional recordings with just the right speaker are also

performed, and the corrected averaged array signal is once again taken as a reference. The challenge for this test case is to retrieve the correct signals emitted by each speaker when both speakers are emitting simultaneously. The same scanning grid as in Case I is employed, as well as the integration area for the left speaker. The integration area for the right speaker spans from from $x = 0.2\,\text{m}$ to $x = 0.4\,\text{m}$ and from $y = -0.05\,\text{m}$ to $y = 0.15\,\text{m}$, with $z = 1\,\text{m}$, as shown by the dashed squares in Figure 4.12b. The frequency spectra of the left (SNR_1) and right speaker (for the four different volumes) recorded by the array and averaged over all the microphones with only one of the speakers emitting sound at a time are plotted in Figure 4.12b. Similar to what already observed in Figure 4.12a, an almost constant offset over the whole frequency range is obtained when decreasing the volume of the right speaker. The offsets relative to Volume 1 have approximate values of $-6\,\text{dB}$, $-12\,\text{dB}$, and $-18\,\text{dB}$ for Volumes 2, 3, and 4, respectively. These four volumes provide a wide range of ratios between the signals emitted by both speakers, having the right speaker from being the loudest source to being almost negligible compared to the left speaker. For this case, both speaker signals are stronger than the background noise of the facility.

Finally, the same automatic procedure for the determination of the optimal regularization parameters described in Chapter 4.3.1 is used for the present test case. For the single speaker, only one eigenmode is found to be dominant with the sole exception of the lowest SNR case (SNR_4) in the frequency range where the background noise is dominant. For the two speakers, two dominant eigenmodes are considered for every volume due to the incoherence of the emitted broadband signals.

SOURCE LOCALIZATION RESULTS

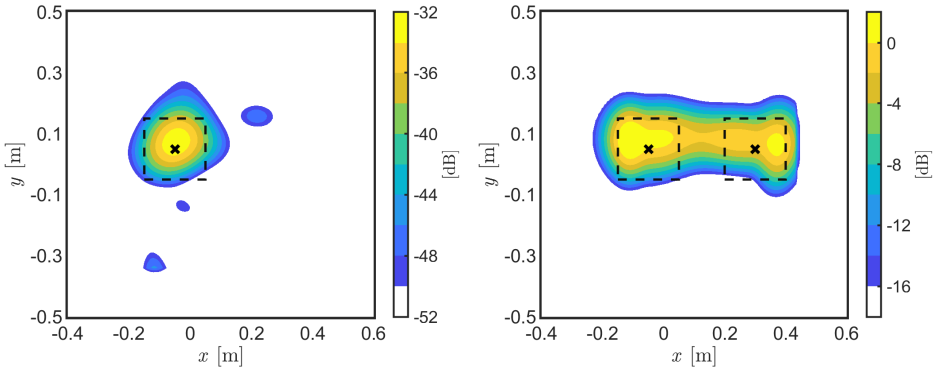

(a) Single speaker emitting noise with the lowest signal-to-noise ratio (SNR_4).

(b) Two speakers with the right speaker emitting noise with the lowest volume (Volume 4)

Figure 4.13: GIBF source-distribution maps for the two-speakers case for $f_{1/3} = 630\,\text{Hz}$. The dashed squares denote the integration regions, while the black **x** symbols indicate the positions of the speakers. The sound-pressure levels are computed with $p_{\text{ref}} = 20\,\mu\text{Pa}$ and presented with a dynamic range of 20 dB.

The first outcome of the application of GIBF to the speaker benchmark dataset con-

cerns the assessment of the accuracy of the noise-source localization in different testing conditions. Figure 4.13a presents one example source-distribution map obtained by the algorithm for the single-speaker case with the lowest SNR (SNR_4). The results correspond to a one–third–octave frequency band centered at 630 Hz and the map has a dynamic range of 20 dB computed with a reference pressure of $p_{ref} = 20\,\mu Pa$. This frequency band is selected because it represents one of the lowest SNR cases, as can be observed in Figure 4.12a, and the speaker signal is below the background noise, i.e. it has a negative SNR value amounting to approximately −11.5 dB. As a consequence, the noise source emitted by the speaker does not correspond to the dominant eigenmode but instead to the third largest one. This application shows the potentialities associated with the GIBF eigenmode analysis as a means to reduce the contribution of the background noise. Regarding the source-distribution map, the GIBF algorithm provides the correct localization of the speaker position.

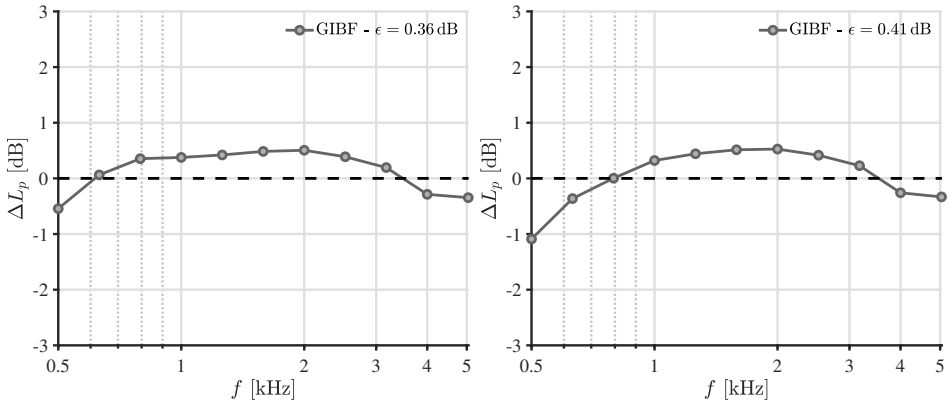

(a) SNR_1 case.

(b) SNR_2 case.

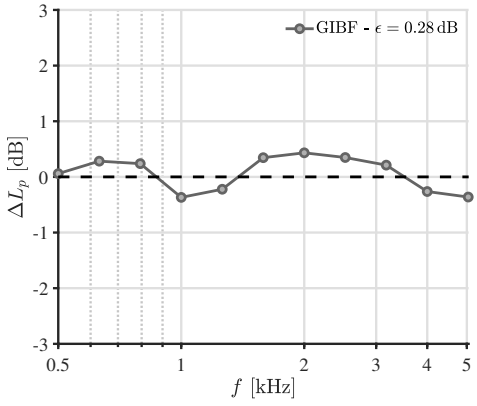

(c) SNR_3 case.

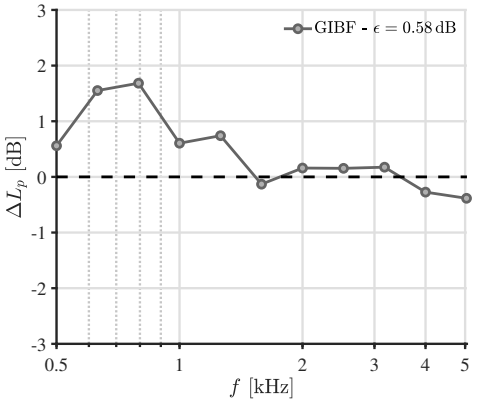

(d) SNR_4 case.

Figure 4.14: Error per third–octave band made by GIBF, with respect to the averaged microphone signal for the different SNRs of the single-speaker case. The absolute error ϵ averaged over the whole considered frequency range is specified in the legends.

Figure 4.13b contains one example source-distribution map obtained by GIBF for the case of two speakers with the lowest volume in the right one (Volume 4). Also these results correspond to a one–third–octave frequency band centered at 630 Hz. This frequency band is selected because, for the given array geometry and distance between the sources ($y = 0.35$ m), it approximately represents the resolution limit frequency f_R for which the two sources can be distinguished using conventional acoustic imaging methods. Indeed, according to the Rayleigh criterion [53], the minimum resolvable source separation R can be estimated as

$$R \simeq l_{p-n} \tan\left(\frac{1.22\, c_0}{f_R\, D_a}\right), \tag{4.15}$$

where l_{p-n} is the distance between microphone array and scanning grid and D_a is the array maximum aperture, resulting in $f_R \approx 645$ Hz. The sound-pressure levels emitted by both speakers are practically identical for these conditions, as can be seen in Figure 4.12b. The GIBF source-distribution map exhibits a somehow distributed line source with maximum levels at both ends of the segment. While the location of the left speaker is correctly reconstructed by the algorithm, the one of the right speaker appears to be slightly shifted. However, both source regions are included in the considered integration areas and this provides an accurate estimation of the source strength, as will be shown in the following section.

INTEGRATED SOURCE SPECTRA RESULTS

The results of the quantitative analysis on the speaker benchmark datasets are presented separately for Case I and Case II. Concerning the former, the one-third octave spectra are obtained with GIBF through the integration of the source-distribution maps within the integration area depicted in Figure 4.11a. The method described in Chapter 4.3.1 is adopted. In order to assess the accuracy in retrieving the correct sound spectra, the relative errors made by the algorithm with respect to the reference averaged microphone signal $\Delta L_p = L_{p,\mathrm{GIBF}} - L_{p,\mathrm{ref}}$ are calculated and shown in Figure 4.14 for all the SNRs. For clarity reasons, only the errors linked to the spectra averaged over the 10 repetitions are plotted. A positive value of ΔL_p corresponds to an over-prediction of the result by GIBF.

For the two lowest SNR cases SNR_3 and SNR_4, the errors below a threshold frequency of 1 kHz and 1.25 kHz, respectively, are estimated with respect to the predicted frequency spectra below the background noise, corresponding to the opaque lines in Figure 4.12a. In addition, the absolute error made by the algorithm averaged over the whole considered frequency range $\epsilon = |\Delta L_p|$, i.e. the average $\mathscr{L}_1$ norm of the differences, is also calculated and included in the legends of Figure 4.11a. For the first three SNRs (Figures 4.14a, 4.14b, and 4.14c), the ΔL_p values are contained within ± 0.5 dB for most frequencies. Interestingly, the best performance is achieved for SNR_3, for which $\epsilon = 0.28$ dB. For the lowest SNR case (Figure 4.14d), the errors made by GIBF increase at low frequencies, probably due to the influence of the background noise that dominates over the speaker source.

The repeatability of the results of GIBF is investigated considering the 10 repetitions recorded for each SNR case. Figure 4.15 depicts the standard deviation σ (in dB and per third–octave–band) of the estimated spectra from each method, as well as the standard

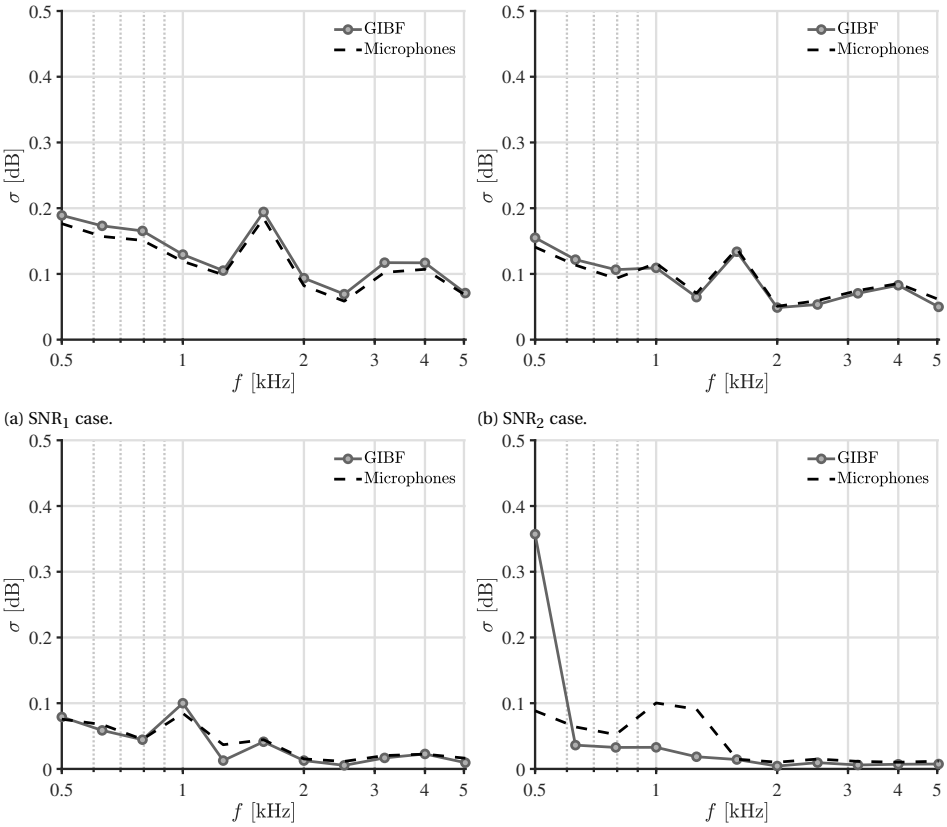

(a) SNR_1 case.

(b) SNR_2 case.

(c) SNR_3 case.

(d) SNR_4 case.

Figure 4.15: Standard deviation σ per third–octave band for GIBF and for the averaged microphone signal calculated over the 10 repetitions for the different SNRs of the single-speaker case.

deviation of the reference signal of the array averaged over all microphones. The latter is caused by small perturbations in the non–perfect measurement environment and the intrinsic uncertainties of the microphone and speaker. In general, most σ are below 0.2 dB for the highest SNR and become lower as the SNR decreases, reaching values of about 0.05 dB for the SNR_4 case (Figure 4.14d).

Furthermore, the standard deviations of GIBF collapse almost perfectly with those of the microphones of the array, suggesting that the deviations in the results are due to the nature of the recorded signals themselves and not due to a lack of robustness in the GIBF algorithm. In some cases, the variability exhibited by the algorithm is even lower than that of the microphones. The only exception to this common trend is represented by the 500 Hz band for the SNR_4 case, for which $\sigma \approx 0.4$ dB. This may depend on the presence of noise sources extraneous to the scanning grid plane due to the dominant background noise. Indeed, the algorithm reconstructs the external noise-source distributions recorded by the microphones through the generation of non–negligible ampli-

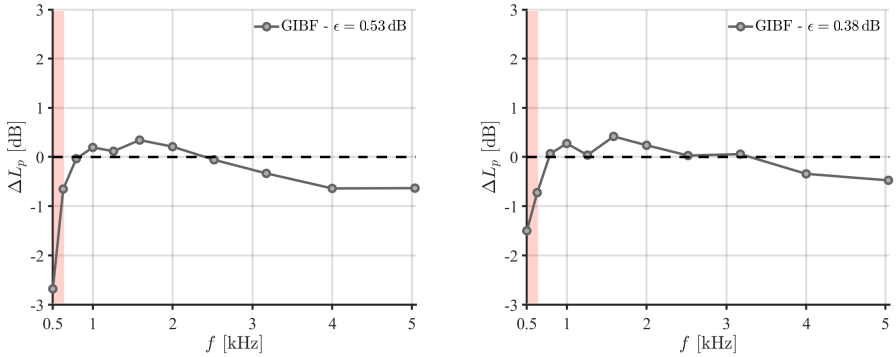

(a) Volume 1 case.

(b) Volume 2 case.

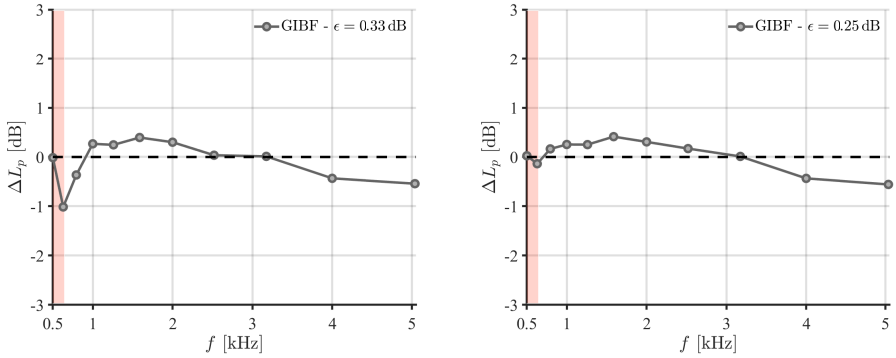

(c) Volume 3 case.

(d) Volume 4 case.

Figure 4.16: Error per third–octave band made by GIBF for the left speaker (with both speakers on), with respect to the averaged microphone signal (with only the left speaker on) for the different SNRs of the two-speakers case. The absolute error ϵ averaged over the whole considered frequency range is specified in the legends. The region beyond the Rayleigh resolution limit frequency f_c is denoted by the red area.

tudes that are concentrated around the border of the scanning-grid plane. This edge effect reduces the accuracy of the source intensity estimation and, therefore, increases its variability when the $\mathscr{L}_1$ norm approach is adopted since the sparsity of the solution is greater in this case (see Chapter 4.2.2). Increasing the extension of the scanning grid plane may represent a possible solution to improve the results at low frequencies with a negative SNR, with the consequent increase of the computational time required.

Similar to the single-speaker case, the integrated spectra computed from the two integration areas depicted in Figure 4.11a are compared to the reference signals of the left and right speaker recorded by the array and averaged over all microphones. As explained in Chapter 4.3.2, the left speaker is set to emit the exact same synthetic broadband noise signal as in the SNR_1 case, while the right speaker emits the same signal at four different volumes.

Figures 4.16 and 4.17 present the relative errors ΔL_p with respect to the averaged reference signal for the left and right speaker, respectively. The Rayleigh resolution limit for

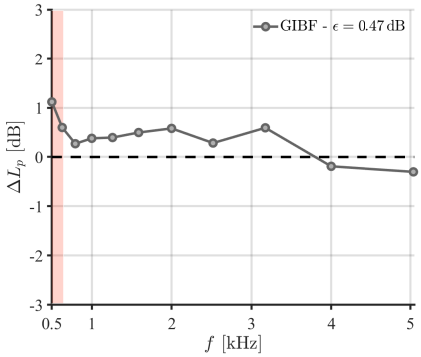

(a) Volume 1 case.

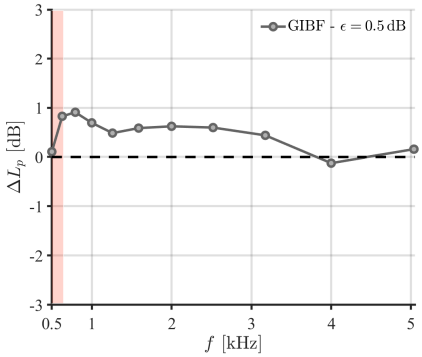

(b) Volume 2 case.

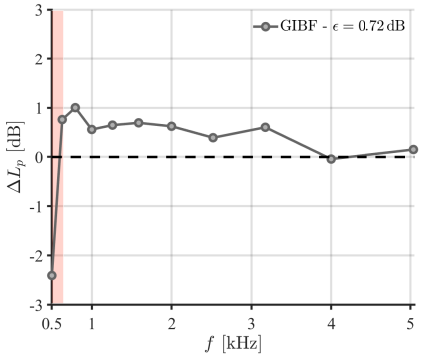

(c) Volume 3 case.

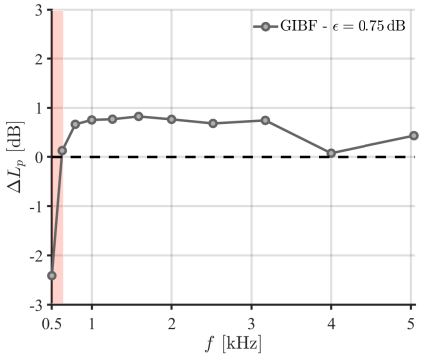

(d) Volume 4 case.

Figure 4.17: Error per third–octave band made by GIBF for the right speaker (with both speakers on), with respect to the averaged microphone signal (with only the right speaker on) for the different SNRs of the two-speakers case. The absolute error ϵ averaged over the whole considered frequency range is specified in the legends. The region beyond the Rayleigh resolution limit frequency f_c is denoted by the red area.

the given setup (≈ 645 Hz) is also indicated in the maps. Likewise, the average absolute error ϵ is reported in the legend. As a general trend for the left speaker, the values of ϵ decrease along with the volume of the right speaker. For the Volumes 1 (Figure 4.16a) and 2 (Figure 4.16b), the highest errors occur for frequencies below f_c. An opposite trend can be observed for the right speaker, for which the errors increase when its volume is reduced. This is an expected result since the right speaker becomes less dominant compared to the left speaker with a decreasing volume. Once again, the most significant deviations can be observed for frequencies less than the Rayleigh resolution limit frequency.

4.4. NOISE REDUCTION THROUGH POROSITY

In this section, the aeroacoustic results of the experimental campaign carried out in the A-tunnel facility are presented. The analysis of the effectiveness of the use of porous

materials as a sound-mitigation technique is performed by comparing the noise sources and sound-pressure levels radiated by the three airfoil configurations.

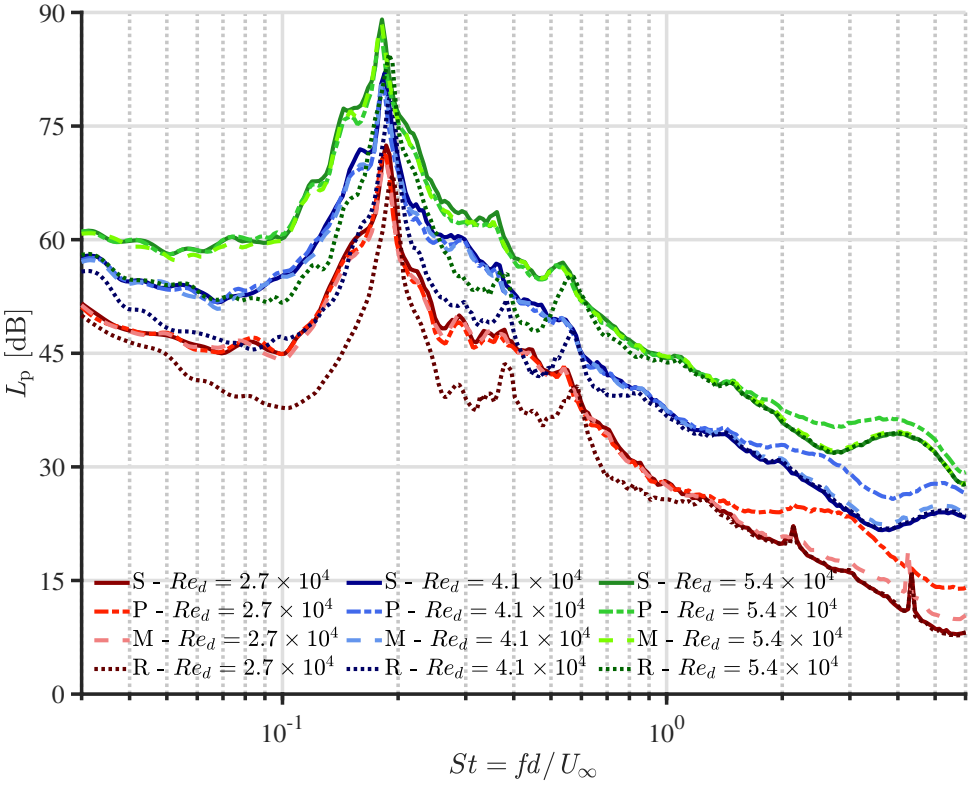

Figure 4.18: Sound-pressure level spectra acquired at 1 m from the airfoil installed downstream of the rod for different rod-based Reynolds numbers. The data are averaged over the 64 microphones of the array and refer to the solid (*S*), porous (*P*), melamine (*M*), and rod-alone (*R*) configuration. The reference pressure is $p_{\text{ref}} = 20\,\mu\text{Pa}$

4.4.1. FAR-FIELD ACOUSTIC MEASUREMENTS

The results of the far-field acoustic measurements are presented in Figure 4.18 for $Re_d = 2.7 \times 10^4$, $Re_d = 4.1 \times 10^4$, and $Re_d = 5.4 \times 10^4$. The acquired data related to the solid, porous, and melamine case and the background noise corresponding to the rod alone are averaged over the 64 microphones of the array and are presented with a reference pressure of $p_{\text{ref}} = 20\,\mu\text{Pa}$. The Strouhal number is based on the cylindrical rod diameter and free-stream velocity. The comparison of the sound-pressure levels L_p shows that the airfoil-turbulence interaction noise dominates over the noise coming from the rod in the low-St range for every rod-based Reynolds numbers, up to approximately $St = 1$. Therefore, the noise-reduction performance of the porous airfoil configurations can be evaluated directly from the far-field measurements only in this range, while acoustic beam-

forming techniques are required to characterize the performance at higher frequencies. The cases at low-St and high-St will be addressed separately.

LOW-FREQUENCY RANGE

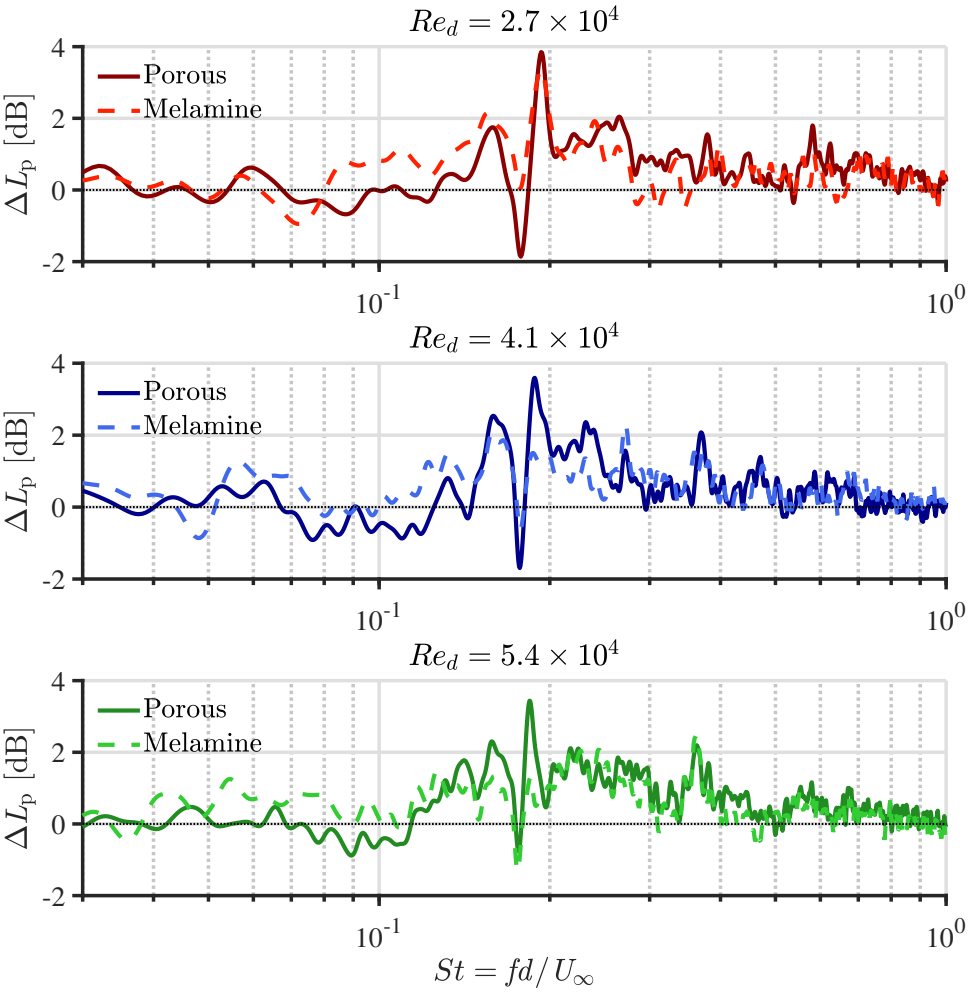

Figure 4.19: Sound-pressure level spectra of the porous and melamine airfoil configuration of Figure 4.18 relative to the solid one for different rod-based Reynolds numbers.

The porous treatment of the wing profile is found to alter the noise radiated due to inflow turbulence with a trend that is similar for the different rod-based Reynolds numbers. This can be visualized in Figure 4.19, which exhibits the relative sound-pressure levels ΔL_p of the porous and melamine cases with respect to the solid one. With this convention, a positive ΔL_p indicates a noise reduction, whereas a negative ΔL_p denotes

	$Re_d = 2.7 \times 10^4$		$Re_d = 4.1 \times 10^4$		$Re_d = 5.4 \times 10^4$	
Case	$L_{p,\mathrm{VS}}$ [dB]	St_{VS} [-]	$L_{p,\mathrm{VS}}$ [dB]	St_{VS} [-]	$L_{p,\mathrm{VS}}$ [dB]	St_{VS} [-]
Solid	72.4	0.186	82.2	0.184	89.1	0.182
Porous	71.1	0.184	80.8	0.182	87.4	0.180
Melamine	70.9	0.185	81.1	0.183	87.7	0.181
Rod	68.6	0.193	79.8	0.192	84.7	0.190

Table 4.2: Sound-pressure level $L_{p,\mathrm{VS}}$ and Strouhal number St_{VS} characterizing the vortex-shedding peak in the acoustic frequency spectra for the different rod-based Reynolds numbers and different airfoil configurations.

noise increase. In particular, the acoustic spectra related to the porous airfoil configuration feature a slight increase up to about $St = 0.15$ that is attenuated in the case of the melamine airfoil, especially for higher velocities. It must be specified that, at such low Strouhal numbers, the investigated frequencies are below the cutoff frequency of the A-Tunnel facility, which can be no more considered as anechoic. Nonetheless, as observed in Figure 4.18, the acoustic spectra for the three-airfoil configurations exhibit sufficiently higher values than their corresponding background noise and the relative turbulence-interaction noise emissions are not expected to be affected by the facility. Above the above-mentioned threshold, the porous treatments effectively reduce both tonal and broadband noise components, with a maximum abatement of about 2 dB, and no notable differences are reported for the two cases. The mitigation is generally more pronounced around the vortex-shedding peak at $St = 0.18$ and gradually decreases up to $St = 1$, where the porous spectra start converging with the solid one.

Moreover, the sudden transition occurring at $St = 0.18$ can be readily explained by a slight shift of the vortex-shedding peak due to the porous treatment of the airfoil. This evidence is supported by the data listed in Table 4.2, which reports the sound-pressure level $L_{p,\mathrm{VS}}$ and Strouhal number St_{VS} corresponding to the vortex-shedding frequency peak in the spectra of Figure 4.18. The first conclusion that can be drawn from the analysis of the tonal noise is that the porous treatments of the airfoil decrease the level of the vortex-shedding frequency peak by approximately 1.5 dB for each rod-based Reynolds number, with no significant impact of the exoskeleton. The second conclusion is that the presence of the airfoil reduces St_{VS} by about 4 %, most probably due to the higher blockage effect. As anticipated, also the porous treatments of the airfoil contribute to the further decrease of the Strouhal number at which the vortex shedding occurs. Interestingly, this effect is more important for the porous airfoil configuration for every considered rod-based Reynolds number, hinting at a possible increased blockage generated by the hard-plastic exoskeleton.

The noise reduction performance achieved in the present work appears to be low if compared to the results of the investigations discussed in Chapter 1.1.2. This limited efficiency is partially related to the presence of the exoskeleton that decreases the flow penetration into the melamine foam, as the noise increase in the low-frequency range in Figure 4.18 may indicate. Moreover, the hard-plastic extension that is designed to cover the full width of the wind tunnel and accounts for the 20 % of the full span con-

tributes to the far-field noise and decreases the overall effect of porosity. Another possible explanation for the lower performance of the porous treatments is represented by the center-plane. Indeed, the acoustic waves generated on the airfoil surface can potentially penetrate the porous medium and interact with the solid walls of this component, similar to the effect of the material junctions in the case of a porous leading-edge insert [54]. Further parametric studies will be performed in the near future to analyze the influence of the center-plane on noise reduction.

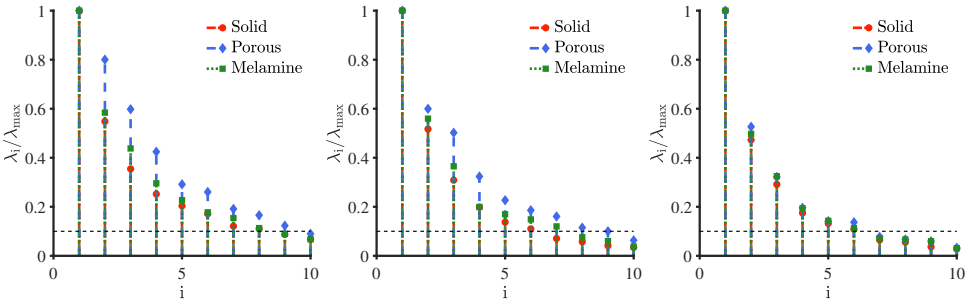

(a) $Re_d = 2.7 \times 10^4$. (b) $Re_d = 4.1 \times 10^4$. (c) $Re_d = 5.7 \times 10^4$.

Figure 4.20: Eigenvalues λ of the CSM for $f = 2.5\,\text{kHz}$ normalized with the maximum eigenvalue $\lambda_{\max}$ of each airfoil configuration. All the eigenvalues below the 10 % of $\lambda_{\max}$ are discarded.

HIGH-FREQUENCY RANGE

The characterization of the sound reduction performance of the porous treatments in the St-range where the rod-alone noise dominates can be achieved through the use of the GIBF algorithm, which allows for the isolation of the different sound sources on the airfoil and for proper handling of the background noise. In the present analysis, the advanced subtraction technique developed by Bahr and Horne [55] is employed. For a rod-airfoil configuration, the acquired background noise corresponds to a configuration where the airfoil has been removed. Indeed, the separation between rod and airfoil is such that the vortex shedding is not suppressed by the presence of the body and the changes in the vortex-shedding frequency are only marginal, making it feasible to perform the subtraction. Moreover, this distance determines also the frequency f_R above which the source distribution at the leading edge of the airfoil due to inflow turbulence is separated from that produced in correspondence with the rod. By imposing $R = d_{\text{TE-LE}}$ in Equation (4.15), where $d_{\text{TE-LE}}$ is the distance between trailing edge of the rod and leading edge of the airfoil, it follows from Rayleigh criterion that $f_R \approx 1.24\,\text{kHz}$. This value represents the lower frequency limit that is considered for the GIBF processing of the acoustic far-field data in order to have a successful background noise subtraction.

For the algorithm setting, the automatic procedure introduced in Chapter 4.2.2 for the NASA-2 benchmark dataset is employed for the determination of the optimal regularization parameters. Likewise, the number of eigenmodes processed for each configuration is found to be dependent on the frequency and free-stream velocity. The presence of porosity seems to slightly alter the relative weight of the amplitude of the different eigenvalues with reference to the dominant one. This effect decreases with increasing

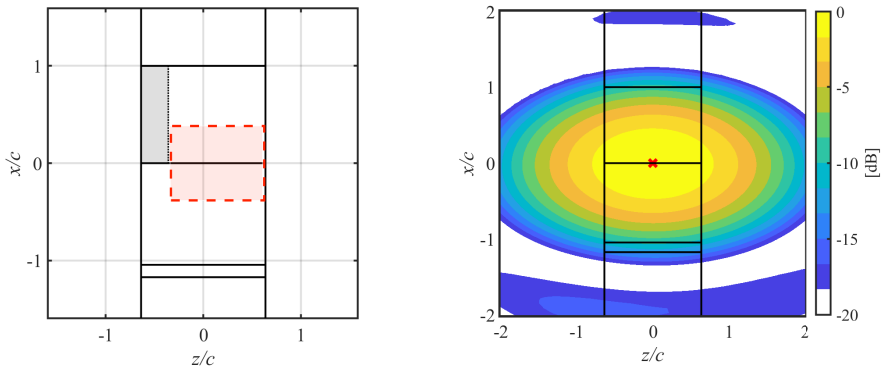

Figure 4.21: Configuration of the GIBF sound map, with the black lines indicating side-plates, rod, and airfoil leading edge and trailing edge and the red dashed lines denoting the source integration area. The gray area depicts the hard-plastic extension rigidly connected to the airfoil. The PSF of the array for a point source at the airfoil leading-edge center (denoted by the red x symbol) emitting sound within a 1250 Hz one–third octave band is reported.

Re_d, as can be observed in Figure 4.20, which shows the eigenvalues of the CSM corresponding to the narrow frequency $f = 2.5$ kHz for the different airfoil configurations and different free-stream velocities. The eigenvalues are normalized by the maximum eigenvalue $\lambda_{\max}$ related to each case.

The impact of porosity on the source distribution location is first evaluated by comparing the GIBF sound maps related to the solid, porous, and melamine airfoil at different Re_d. The results are presented considering the setup in Figure 4.21, which illustrates the relative position of the cylindrical rod and airfoil including the hard-plastic extension that rigidly connects the wing profile to the side plate. The dynamic range is set to 20 dB and is the same for the three airfoil configurations. The scanning grid ranges from $x = -0.5$ m to $x = 0.5$ m and from $y = -0.5$ m to $y = 0.5$ m, with $z = 1$ m and spacing between the grid points of $\Delta x = \Delta y = 0.005$ m. Figures 4.22, 4.23, and 4.24 show the maps for the one-third octave band frequencies $f_{1/3} = 1.25$ kHz, $f_{1/3} = 2.50$ kHz, and $f_{1/3} = 5$ kHz, respectively.

In general, for the lowest frequency band (Figure 4.22), the main lobe of the noise-source region does not appear to be distributed along the airfoil leading edge due to the beamwidth characteristics of the microphone array but it extends within a region in the center of the wing profile. Furthermore, additional noise sources are located in correspondence with the rod as a residual of the background-subtraction procedure that is not able to fully suppress the contribution of the rod noise, which is dominant. This effect may be due to a partial coherence between turbulence-interaction noise and background noise and varies with the considered airfoil configuration. However, the presence of these residual sources is not expected to alter the actual source of interest as they are not included in the integration region.

The analysis of the GIBF sound maps for $Re_d = 2.7 \times 10^4$ (Figure 4.22a) indicates that, at this frequency, the sound-pressure levels for the solid airfoil are higher than those for

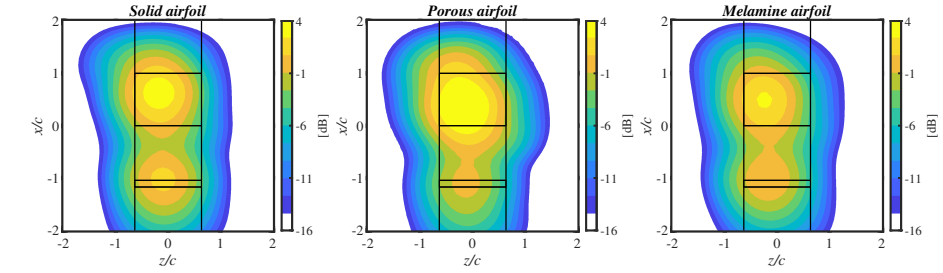

(a) $Re_d = 2.7 \times 10^4$

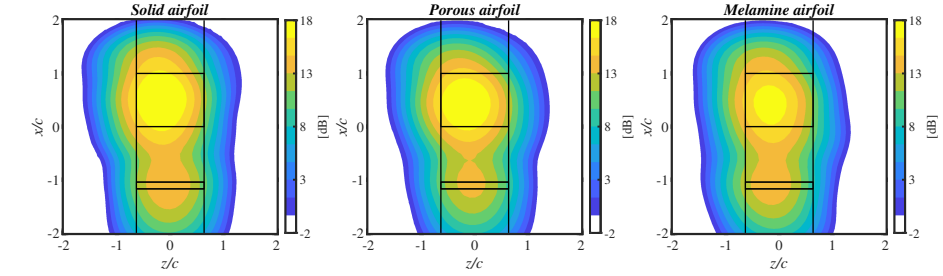

(b) $Re_d = 4.1 \times 10^4$

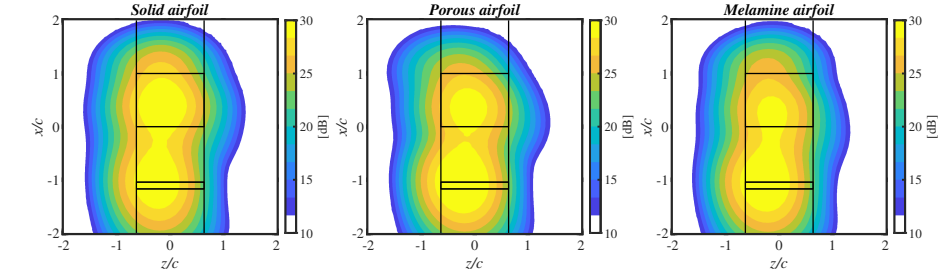

(c) $Re_d = 5.4 \times 10^4$

Figure 4.22: GIBF sound maps exhibiting the noise-source distribution contours for the solid, porous, and melamine airfoil at $f_{1/3} = 1.25\,\text{kHz}$ for different rod-based Reynolds number. The maps are plotted with the same 20 dB dynamic range for each velocity and computed with a reference pressure of $p_{\text{ref}} = 20\,\mu\text{Pa}$. A background subtraction technique is applied to reduce the rod-noise contribution.

the melamine airfoil, i.e. the melamine foam is still effective in reducing noise, but lower than those for the porous airfoil, i.e. the presence of the exoskeleton leads to a noise increase. For $Re_d = 4.1 \times 10^4$ (Figure 4.22b) and $Re_d = 5.7 \times 10^4$ (Figure 4.22b), the latter effect is not found and the source distribution regions for the solid and porous airfoils exhibit comparable values, whereas a noise mitigation is still present for the melamine configuration.

At $f_{1/3} = 2.50\,\text{kHz}$ (Figure 4.23), the localization of the distributed noise sources is more accurate due to the higher resolution achievable at this frequency band. Overall, noise regeneration is always present and increases for decreasing free-stream velocities. For $Re_d = 2.7 \times 10^4$ (Figure 4.23a), the noise emitted by the porous airfoil dominates over

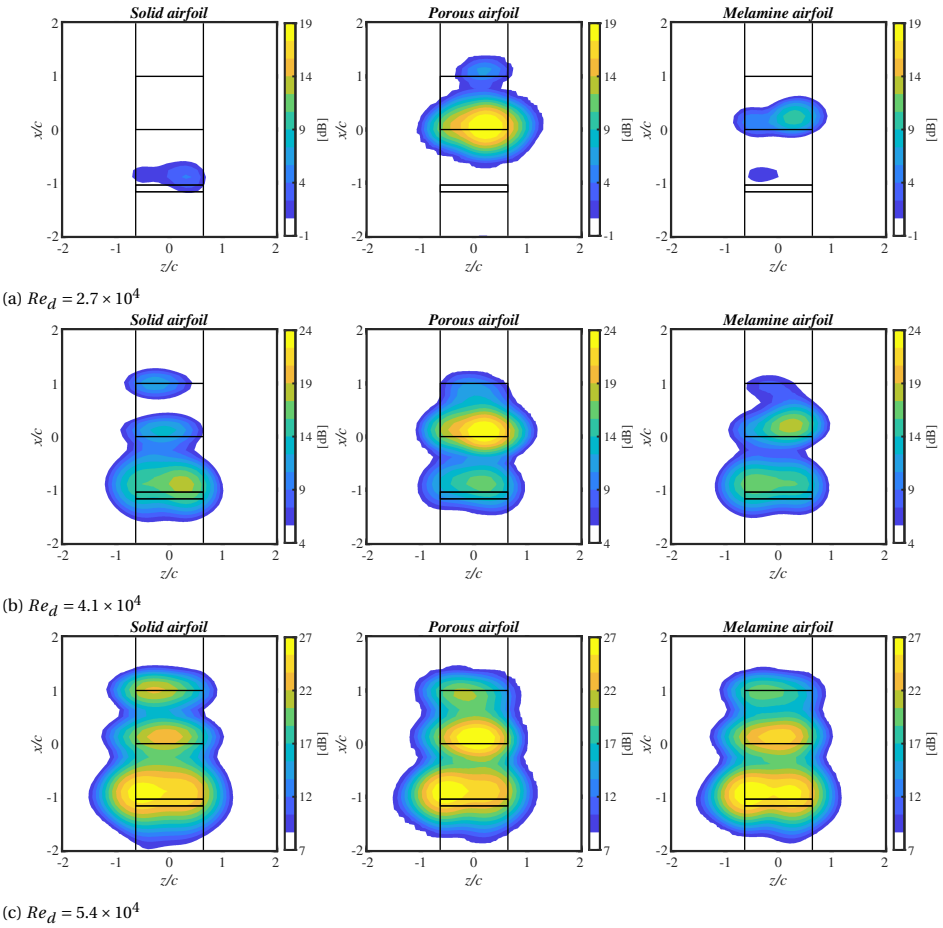

(a) $Re_d = 2.7 \times 10^4$

(b) $Re_d = 4.1 \times 10^4$

(c) $Re_d = 5.4 \times 10^4$

Figure 4.23: GIBF sound maps exhibiting the noise-source distribution contours for the solid, porous, and melamine airfoil at $f_{1/3} = 2.50\,\text{kHz}$ for different rod-based Reynolds numbers. The maps are plotted with the same 20 dB dynamic range for each velocity and computed with a reference pressure of $p_{\text{ref}} = 20\,\mu\text{Pa}$. A background subtraction technique is applied to reduce the rod-noise contribution.

that produced by the solid configuration, for which no sound sources can be located at the leading edge within the considered dynamic range. Noise regeneration occurs even for the melamine wing profile but with a significantly reduced impact. Interestingly, for both porous and melamine airfoils, the main lobes are situated slightly downstream of the leading edge. For $Re_d = 4.1 \times 10^4$ (Figure 4.23b), similar trends as those for the lower velocities can be observed. In this case, noise sources are also distributed at the trailing edge of the hard-plastic extension for the solid and melamine configuration. The fact that trailing-edge noise is not visible for the actual airfoil may be due to the presence of the metallic wire-mesh that acts on the boundary layer developing along the surface. Further studies would be required to improve the understanding of the present

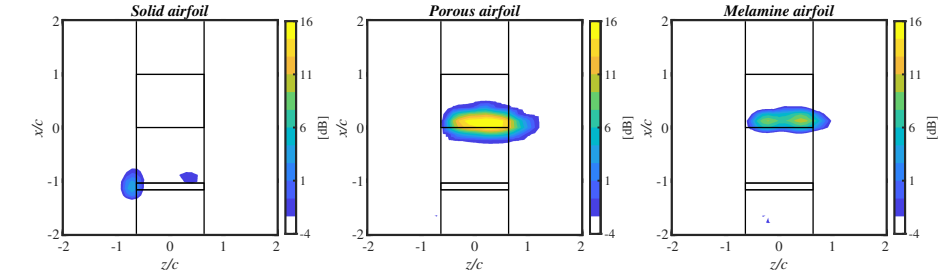

(a) $Re_d = 2.7 \times 10^4$

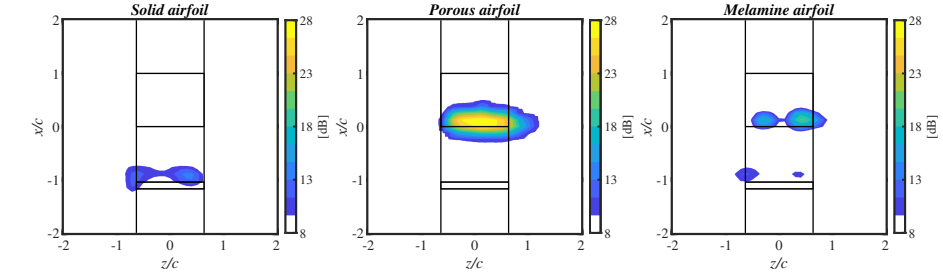

(b) $Re_d = 4.1 \times 10^4$

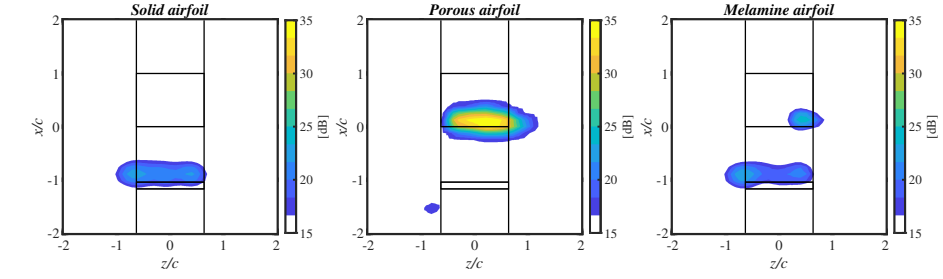

(c) $Re_d = 5.4 \times 10^4$

Figure 4.24: GIBF sound maps exhibiting the noise-source distribution contours for the solid, porous, and melamine airfoil at $f_{1/3} = 5.00\,\text{kHz}$ for different rod-based Reynolds numbers. The maps are plotted with the same 20 dB dynamic range for each velocity and computed with a reference pressure of $p_{\text{ref}} = 20\,\mu\text{Pa}$. A background subtraction technique is applied to reduce the rod-noise contribution.

mechanism. For $Re_d = 4.1 \times 10^4$ (Figure 4.23c), all the airfoils feature comparable sound-pressure levels, with a more pronounced noise increase for the porous one. Also in this case, trailing-edge noise is visible in correspondence with the rigid extension.

The present trends for the noise regeneration are enhanced at $f_{1/3} = 5\,\text{kHz}$ (Figure 4.24). In general, the porous configuration is significantly noisier than the solid one, for which the sound sources generated by turbulence interaction at the leading edge are not included in the considered dynamic range. In addition, the deviation between the noise regeneration for the melamine airfoil and that for the porous airfoil increases along with Re_d (Figures 4.24a, 4.24b, and 4.24c), differently from the previous cases. This trend can be further investigated through the evaluation of the integrated spectra.

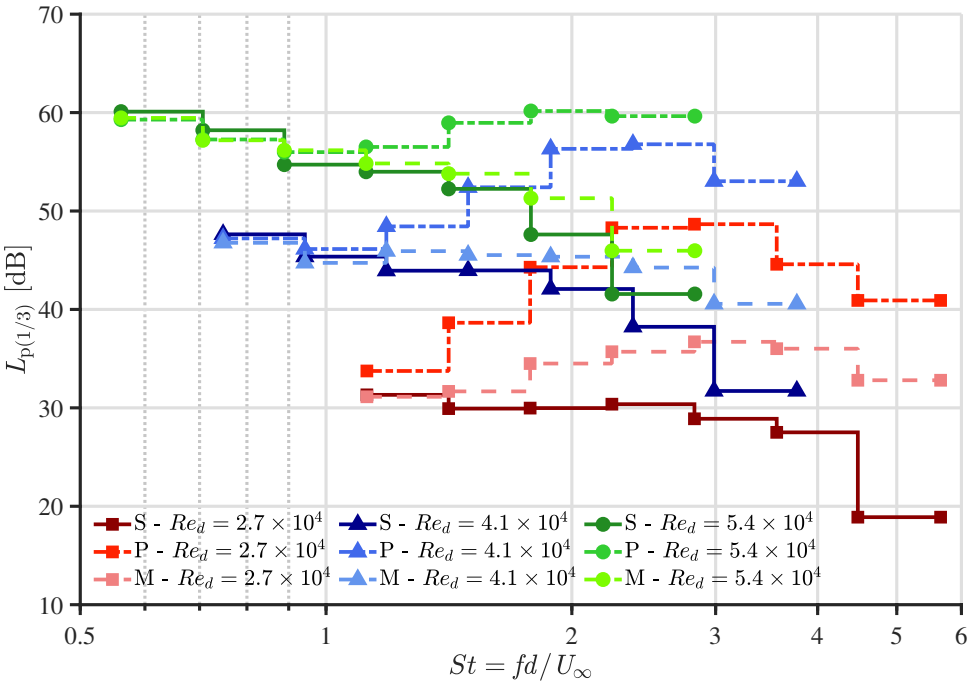

Figure 4.25: Integrated GIBF one-third octave spectra for different rod-based Reynolds numbers and presented with a reference pressure of $p_{ref} = 20\,\mu Pa$. The data refer to the solid (S), porous (P), and melamine (M) airfoil configuration.

The resulting sound maps for one-third octave band center frequencies ranging from 1.25 kHz to 5 kHz are subsequently integrated with reference to the center of the array by summing the pressure values of each scanning-grid point within a square region surrounding the airfoil leading edge, as described in Chapter 4.3.1. The integration region is depicted in Figure 4.21. In this way, the contribution of the hard-plastic extension can be removed. The integrated one-third octave spectra $L_{p(1/3)}$ for the three wing profiles are presented in Figure 4.25 for the different Re_d, while the corresponding relative spectra $\Delta L_{p(1/3)}$ of the porous and melamine airfoils with respect to the solid one are shown in Figure 4.26. The Strouhal number is based on the cylindrical rod diameter and free-stream velocity. For $St < 0.9$, a slight noise reduction due to the porous treatments of the airfoil still occurs, in agreement with the results shown in Figure 4.19. At higher Strouhal numbers, both porous and melamine airfoils feature noise regeneration and this effect is more pronounced for the porous configuration and with the increasing frequency, as already seen in the GIBF source-distribution maps in Figures 4.23 and 4.24. Interestingly, the trend of the noise increase appears to be independent of Re_d. At $St = 2$, for instance, $\Delta L_{p(1/3)} \approx -5$ dB and $\Delta L_{p(1/3)} \approx -14$ dB for the melamine and porous airfoil model, respectively.

The origin of the noise regeneration at high-St for the melamine airfoil is attributable

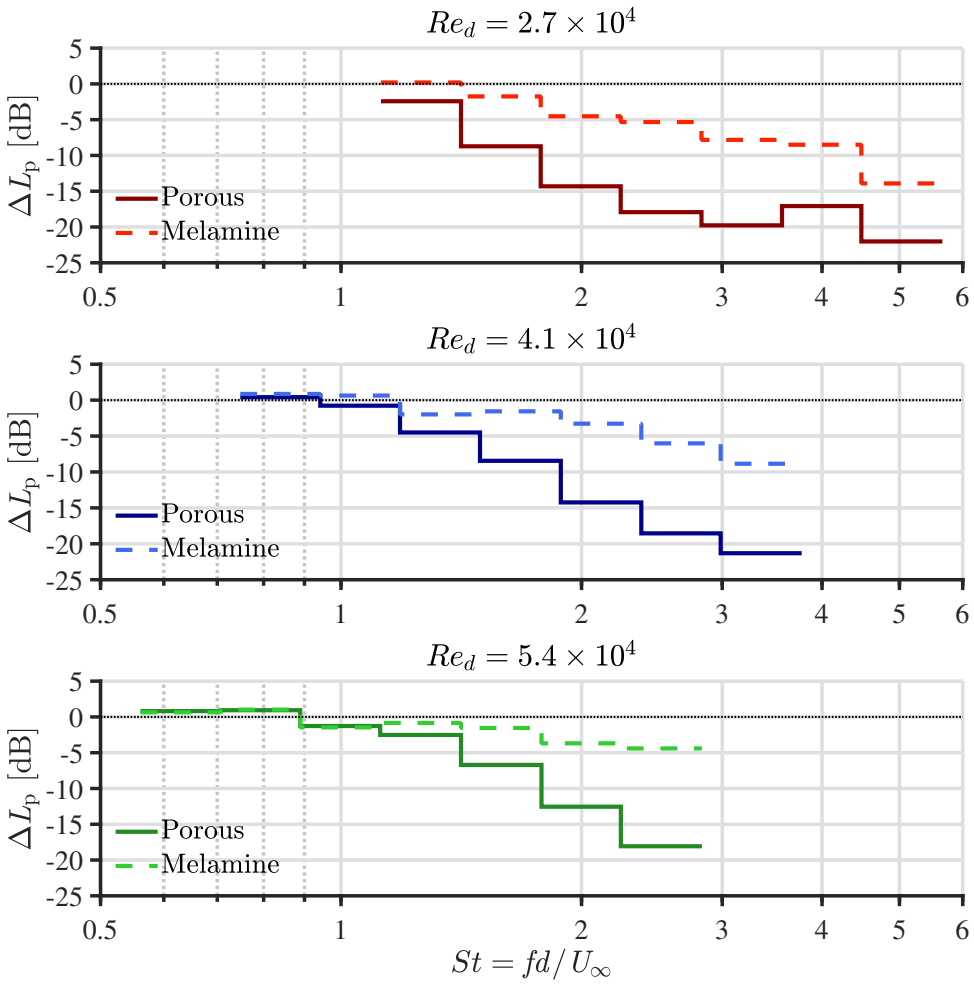

Figure 4.26: Integrated GIBF one-third octave spectra of the porous and melamine airfoil configuration of Figure 4.25 relative to the solid one for different rod-based Reynolds numbers.

to the more substantial surface roughness of the melamine foam. Indeed, the role played by surface-roughness noise [56–58] is more significant for materials characterized by low values of static air-flow resistivity due to the typically larger dimensions of the pores [59]. However, this mechanism cannot be directly transposed to the porous airfoil configuration since the presence of the woven wire mesh ensures the same surface roughness as the solid baseline. A possible explanation for the noise increase may come from the fluid-structure interaction between the flow and the hexagonal pores of the hard-plastic exoskeleton. The investigation of the flow field around the porous wing profile may clarify this mechanism and will be described in Chapter 5.

4.5. OVERVIEW AND CONCLUDING REMARKS

An improved version of the GIBF is developed and implemented. The use of automated methods for the determination of the regularization parameters involved in the solution of the inverse problem turns out to be essential for accurate localization of aeroacoustic distributed sources and for an accurate estimation of their strength.

For its validation, the algorithm is applied to two different experimental benchmark datasets that are relevant for aeroacoustic applications. The first one includes trailing-edge noise measurements conducted on a wing profile immersed in a clean flow at NASA Langley QFF open-jet wind tunnel. A detailed comparison with CFDBF and with other advanced beamforming techniques is performed in order to evaluate the capability of the method in localizing and quantifying distributed sound sources. Results indicate that GIBF provides a clear representation of the noise sources distributed at the leading edge and trailing edge of the airfoil with the absence of spurious sources when the innovative regularization technique developed in this work is employed. Moreover, the source-power integration of the resulting sound maps shows that the algorithm can correctly estimate the source strength of the dominant noise regions, featuring comparable trends in the integrated acoustic spectra with reference to the other advanced techniques.

The second dataset contains measurements of the broadband signal emitted by one speaker at different SNR with respect to the background noise (Case I) and of the incoherent broadband signals emitted by two closely–located speakers at different relative volumes (Case II) conducted in the A-Tunnel open-jet wind tunnel. The results for Case I point out that GIBF is able to successfully estimate the strength of the synthetic signal for a wide range of frequencies with errors below 0.6 dB also in the case of a negative SNR. Furthermore, the algorithm features high performance in terms of repeatability, with standard deviations of the integrated spectra over 10 acquisitions comparable with those of the microphones of the array. This indicates that the deviations in the spectra are due to the nature of the recorded signals themselves and not due to a lack of robustness in the method. The results for Case II show that GIBF can effectively separate incoherent sources and correctly quantify their strength with a maximum averaged error of 0.75 dB, even for frequencies below the Rayleigh resolution limit frequency.

GIBF is subsequently employed together with far-field acoustic measurements to investigate the turbulence-interaction noise radiated by the solid, porous, and melamine NACA-0024 profiles installed in a rod-airfoil configuration. A noise reduction of up to 2 dB is found for Strouhal numbers ranging from 0.18 to 1. The maximum attenuation occurs in correspondence with the vortex-shedding frequency peak at $St \approx 0.18$ and is independent of the Reynolds number upstream of the cylindrical rod. Above this value, the noise mitigation gradually decreases until it becomes negligible at $St \approx 1$. At higher frequencies, the porous treatment of the airfoil results in a pronounced noise regeneration that increases along with the frequency and is independent of Re_d. At $St = 3$, the porous airfoil configuration is noisier than the solid baseline by approximately 20 dB. The permeable hard-plastic exoskeleton only marginally affects the noise reduction but has a significant negative impact on the noise increase. The present deviation suggests a different physical mechanism at the basis of the regeneration. For the melamine airfoil configuration, this is probably related to the augmented surface roughness of the wing

profile, whereas for the porous airfoil configuration it may be linked to a fluid-structure interaction occurring between the flow and the hexagonal pores of the exoskeleton. In Chapter 5, the alterations in the flow field upstream of and around the airfoil caused by porosity will be investigated in order to evaluate potential correlations with the modifications in the acoustic field.

REFERENCES

[1] R. Zamponi, N. V. de Wyer, and C. Schram, *An Improved Regularization of the Generalized Inverse Beamforming Applied to a Benchmark Database,* in *7th Berlin Beamforming Conference* (BeBeC, Berlin, Germany, 2018).

[2] R. Zamponi, N. Van de Wyer, and C. Schram, *Benchmark Assessment of an Improved Regularization Technique for Generalized Inverse Beamforming,* in *2018 AIAA/CEAS Aeroacoustics Conference* (American Institute of Aeronautics and Astronautics, Atlanta, Georgia, 2018).

[3] R. Merino-Martínez, S. Luesutthiviboon, R. Zamponi, A. Rubio Carpio, D. Ragni, P. Sijtsma, M. Snellen, and C. Schram, *Assessment of the accuracy of microphone array methods for aeroacoustic measurements,* Journal of Sound and Vibration **470**, 115176 (2020).

[4] R. Zamponi, P. Chiariotti, G. Battista, C. Schram, and P. Castellini, *3D Generalized Inverse Beamforming in wind tunnel aeroacoustic testing: application to a Counter Rotating Open Rotor aircraft model,* Applied Acoustics **163**, 107229 (2020).

[5] S. Tamaro, R. Zamponi, D. Ragni, C. Teruna, and C. Schram, *Experimental investigation of turbulent coherent structures interacting with a porous airfoil,* Experiments in Fluids (2021), 10.1007/s00348-021-03170-2.

[6] B. Van Veen and K. Buckley, *Beamforming: a versatile approach to spatial filtering,* IEEE ASSP Magazine **5**, 4 (1988).

[7] D. H. Johnson and D. E. Dudgeon, *Array signal processing: concepts and techniques*, Prentice-Hall signal processing series (P T R Prentice Hall, Englewood Cliffs, NJ, 1993).

[8] C. S. Allen, W. K. Blake, R. P. Dougherty, D. Lynch, P. T. Soderman, and J. R. Underbrink, *Aeroacoustic Measurements* (Springer Berlin Heidelberg, Berlin, Heidelberg, 2002).

[9] S. Oerlemans and P. Sijtsma, *Determination of Absolute Levels from Phased Array Measurements Using Spatial Source Coherence,* in *8th AIAA/CEAS Aeroacoustics Conference & Exhibit* (American Institute of Aeronautics and Astronautics, Breckenridge, Colorado, 2002).

[10] E. Sarradj, *Three-Dimensional Acoustic Source Mapping with Different Beamforming Steering Vector Formulations,* Advances in Acoustics and Vibration **2012**, 1 (2012).

[11] Y. Liu, A. R. Quayle, A. P. Dowling, and P. Sijtsma, *Beamforming correction for dipole measurement using two-dimensional microphone arrays,* The Journal of the Acoustical Society of America **124**, 182 (2008).

[12] P. Sijtsma, S. Oerlemans, and H. Holthusen, *Location of rotating sources by phased array measurements,* in *7th AIAA/CEAS Aeroacoustics Conference and Exhibit* (American Institute of Aeronautics and Astronautics, Maastricht,Netherlands, 2001).

[13] O. Amoiridis, A. Zarri, R. Zamponi, J. Christophe, C. F. Schram, G. Yakhina, and S. Moreau, *Experimental Analysis of the Sound Radiated by an Automotive Cooling Module Working at Different Operational Conditions,* in *AIAA AVIATION 2020 FORUM* (American Institute of Aeronautics and Astronautics, VIRTUAL EVENT, 2020).

[14] T. Suzuki, *L1 generalized inverse beam-forming algorithm resolving coherent/incoherent, distributed and multipole sources,* Journal of Sound and Vibration **330**, 5835 (2011).

[15] P. Sijtsma, *CLEAN Based on Spatial Source Coherence,* International Journal of Aeroacoustics **6**, 357 (2007).

[16] P. Sijtsma, R. Merino-Martinez, A. M. Malgoezar, and M. Snellen, *High-resolution CLEAN-SC: Theory and experimental validation,* International Journal of Aeroacoustics **16**, 274 (2017).

[17] S. Luesutthiviboon, A. M. Malgoezar, R. Merino-Martinez, M. Snellen, P. Sijtsma, and D. G. Simons, *Enhanced HR-CLEAN-SC for resolving multiple closely spaced sound sources,* International Journal of Aeroacoustics **18**, 392 (2019).

[18] T. F. Brooks and W. M. Humphreys, *A deconvolution approach for the mapping of acoustic sources (DAMAS) determined from phased microphone arrays,* Journal of Sound and Vibration **294**, 856 (2006).

[19] T. Brooks and W. Humphreys, *Extension of DAMAS Phased Array Processing for Spatial Coherence Determination (DAMAS-C),* in *12th AIAA/CEAS Aeroacoustics Conference (27th AIAA Aeroacoustics Conference)* (American Institute of Aeronautics and Astronautics, Cambridge, Massachusetts, 2006).

[20] R. Dougherty, *Extensions of DAMAS and Benefits and Limitations of Deconvolution in Beamforming,* in *11th AIAA/CEAS Aeroacoustics Conference* (American Institute of Aeronautics and Astronautics, Monterey, California, 2005).

[21] K. Ehrenfried and L. Koop, *Comparison of Iterative Deconvolution Algorithms for the Mapping of Acoustic Sources,* AIAA Journal **45**, 1584 (2007).

[22] Z. Chu and Y. Yang, *Comparison of deconvolution methods for the visualization of acoustic sources based on cross-spectral imaging function beamforming,* Mechanical Systems and Signal Processing **48**, 404 (2014).

[23] K. Holland and P. Nelson, *The application of inverse methods to spatially-distributed acoustic sources,* Journal of Sound and Vibration **332**, 5727 (2013).

[24] P. Zavala, W. De Roeck, K. Janssens, J. Arruda, P. Sas, and W. Desmet, *Generalized inverse beamforming with optimized regularization strategy,* Mechanical Systems and Signal Processing **25**, 928 (2011).

[25] F. Presezniak, P. A. Zavala, G. Steenackers, K. Janssens, J. R. Arruda, W. Desmet, and P. Guillaume, *Acoustic source identification using a Generalized Weighted Inverse Beamforming technique,* Mechanical Systems and Signal Processing **32**, 349 (2012).

[26] C. Colangeli, P. Chiariotti, and K. Janssens, *Uncorrelated Noise Sources Separation Using Inverse Beamforming,* in *Experimental Techniques, Rotating Machinery, and Acoustics, Volume 8*, edited by J. De Clerck (Springer International Publishing, Cham, 2015) pp. 59–70.

[27] R. Merino-Martinez, *Microphone arrays for imaging of aerospace noise sources*, Ph.D. thesis, Delft University of Technology (2018).

[28] R. Merino-Martínez, P. Sijtsma, M. Snellen, T. Ahlefeldt, J. Antoni, C. J. Bahr, D. Blacodon, D. Ernst, A. Finez, S. Funke, T. F. Geyer, S. Haxter, G. Herold, X. Huang, W. M. Humphreys, Q. Leclère, A. Malgoezar, U. Michel, T. Padois, A. Pereira, C. Picard, E. Sarradj, H. Siller, D. G. Simons, and C. Spehr, *A review of acoustic imaging methods using phased microphone arrays,* CEAS Aeronautical Journal **10**, 197 (2019).

[29] P. Chiariotti, M. Martarelli, and P. Castellini, *Acoustic beamforming for noise source localization – Reviews, methodology and applications,* Mechanical Systems and Signal Processing **120**, 422 (2019).

[30] P. Sijtsma, *Phased Array Beamforming Applied to Wind Tunnel And Fly-Over Tests*, Tech. Rep. (National Aerospace Laboratory NLR, 2010).

[31] J. Hadamard, *Sur les problèmes aux dérivées partielles et leur signification physique (on the problems with partial derivatives and their physical meaning),* Princeton university bulletin , 49 (1902).

[32] P. C. Hansen, *REGULARIZATION TOOLS: A Matlab package for analysis and solution of discrete ill-posed problems,* Numerical Algorithms **6**, 1 (1994).

[33] T. Brooks and W. Humphreys, *Three-Dimensional Applications of DAMAS Methodology for Aeroacoustic Noise Source Definition,* in *11th AIAA/CEAS Aeroacoustics Conference* (American Institute of Aeronautics and Astronautics, Monterey, California, 2005).

[34] R. P. Dougherty, *Jet noise beamforming with several techniques,* in *Proceedings of the 3rd Berlin Beamforming Conference* (GFaI, Gesellschaft zur Förderung angewandter Informatik e.V., Berlin, 2010).

[35] M. Legg and S. Bradley, *Comparison of CLEAN-SC for 2d and 3d Scanning Surfaces,* in *Proceedings of the 4th Berlin Beamforming Conference* (GFaI, Gesellschaft zur Förderung angewandter Informatik e.V., Berlin, 2012).

[36] T. Geyer, E. Sarradj, and J. Giesler, *Application of a Beamforming Technique to the Measurement of Airfoil Leading Edge Noise,* Advances in Acoustics and Vibration **2012**, 1 (2012).

[37] R. Porteous, Z. Prime, C. Doolan, D. Moreau, and V. Valeau, *Three-dimensional beamforming of dipolar aeroacoustic sources,* Journal of Sound and Vibration **355**, 117 (2015).

[38] H. Ding, Y. Bao, Q. Huang, C. Li, and G. Chai, *Three-dimensional localization of point acoustic sources using a planar microphone array combined with beamforming,* Royal Society Open Science **5**, 181407 (2018).

[39] T. Padois and A. Berry, *Two and Three-Dimensional Sound Source Localization with Beamforming and Several Deconvolution Techniques,* Acta Acustica united with Acustica **103**, 392 (2017).

[40] G. Elias, *Source localization with a two-dimensional focused array: optimal signal processing for a cross-shaped array,* in *Proceedings of INTER-NOISE 95, the 1995 International Congress on Noise Control Engineering* (Noise Control Foundation, 1995).

[41] L. Lamotte, B. Beguet, C. Cariou, and O. Delverdier, *Qualifying the noise sources in term of localization and quantification during flight tests,* in *Proceedings of 3rd European Conference for Aeronautics and Space Sciences - EUCASS 2009* (EDP Sciences, 2009).

[42] L. Lamotte, O. Minck, and S. Paillasseur, *Interior noise source identification with multiple spherical arrays in aircraft and vehicle,* in *Proceedings of ICSV 20 – International Congress on Sound and Vibration* (International Institute of Acoustics and Vibration, 2013).

[43] R. Merino-Martinez, E. Neri, M. Snellen, J. Kennedy, D. G. Simons, and G. J. Bennett, *Analysis of nose landing gear noise comparing numerical computations, prediction models and flyover and wind-tunnel measurements,* in *2018 AIAA/CEAS Aeroacoustics Conference* (American Institute of Aeronautics and Astronautics, Atlanta, Georgia, 2018).

[44] *Arraybenchmark : Fachgebiet Technische Akustik - BTU Cottbus-Senftenberg - URL: https://www.b-tu.de/fg-akustik/lehre/aktuelles/arraybenchmark,* .

[45] F. V. Hutcheson and T. F. Brooks, *Measurement of trailing edge noise using directional array and coherent output power methods,* International Journal of Aeroacoustics **1**, 329 (2002).

[46] J. Hald, *Removal of incoherent noise from an averaged cross-spectral matrix,* The Journal of the Acoustical Society of America **142**, 846 (2017).

[47] R. Merino-Martínez, P. Sijtsma, A. R. Carpio, R. Zamponi, S. Luesutthiviboon, A. M. Malgoezar, M. Snellen, C. Schram, and D. G. Simons, *Integration methods for distributed sound sources,* International Journal of Aeroacoustics **18**, 444 (2019).

[48] C. J. Bahr, W. M. Humphreys, D. Ernst, T. Ahlefeldt, C. Spehr, A. Pereira, Q. Leclère, C. Picard, R. Porteous, D. Moreau, J. R. Fischer, and C. J. Doolan, *A Comparison of Microphone Phased Array Methods Applied to the Study of Airframe Noise in Wind Tunnel Testing,* in *23rd AIAA/CEAS Aeroacoustics Conference* (American Institute of Aeronautics and Astronautics, Denver, Colorado, 2017).

[49] A. Pereira, J. Antoni, and Q. Leclère, *Empirical Bayesian regularization of the inverse acoustic problem,* Applied Acoustics **97**, 11 (2015).

[50] R. Merino-Martínez, A. Rubio Carpio, L. T. Lima Pereira, S. van Herk, F. Avallone, D. Ragni, and M. Kotsonis, *Aeroacoustic design and characterization of the 3D-printed, open-jet, anechoic wind tunnel of Delft University of Technology,* Applied Acoustics **170**, 107504 (2020).

[51] S. Luesutthiviboon, A. Malgoezar, M. Snellen, P. Sijtsma, and D. G. Simons, *Improving source discrimination performance by using an optimized acoustic array and adaptive high-resolution clean-sc beamforming,* in *Proceedings of the 7th Berlin Beamforming Conference* (GFaI, Gesellschaft zur Förderung angewandter Informatik e.V., Berlin, 2018).

[52] P. Welch, *The use of fast Fourier transform for the estimation of power spectra: A method based on time averaging over short, modified periodograms,* IEEE Transactions on Audio and Electroacoustics **15**, 70 (1967).

[53] Rayleigh, *XXXI. Investigations in optics, with special reference to the spectroscope,* The London, Edinburgh, and Dublin Philosophical Magazine and Journal of Science **8**, 261 (1879).

[54] M. J. Priddin, C. C. Paruchuri, P. Joseph, and L. J. Ayton, *A Semi-analytic and Experimental Study of Porous Leading Edges,* in *25th AIAA/CEAS Aeroacoustics Conference* (American Institute of Aeronautics and Astronautics, Delft, The Netherlands, 2019).

[55] C. J. Bahr and W. C. Horne, *Advanced Background Subtraction Applied to Aeroacoustic Wind Tunnel Testing,* in *21st AIAA/CEAS Aeroacoustics Conference* (American Institute of Aeronautics and Astronautics, Dallas, TX, 2015).

[56] M. S. Howe, *Surface pressures and sound produced by turbulent flow over smooth and rough walls,* The Journal of the Acoustical Society of America **90**, 1041 (1991).

[57] Y. Liu, A. Dowling, and H.-C. Shin, *Effects of Surface Roughness on Airframe Noise,* in *12th AIAA/CEAS Aeroacoustics Conference (27th AIAA Aeroacoustics Conference)* (American Institute of Aeronautics and Astronautics, Cambridge, Massachusetts, 2006).

[58] Y. Liu, A. Dowling, H.-C. Shin, and A. Quayle, *Experimental Study of Surface Roughness Noise,* in *13th AIAA/CEAS Aeroacoustics Conference (28th AIAA Aeroacoustics Conference)* (American Institute of Aeronautics and Astronautics, Rome, Italy, 2007).

[59] T. Geyer, E. Sarradj, and C. Fritzsche, *Porous Airfoils: Noise Reduction and Boundary Layer Effects,* International Journal of Aeroacoustics **9**, 787 (2010).

5

FLOW-FIELD CHARACTERIZATION

The important thing is not to stop questioning.
Curiosity has its own reason for existence.

Albert Einstein

The present chapter illustrates the investigation of the turbulent flow around the airfoils. The porous and melamine NACA-0024 profiles are compared with the solid baseline, both airfoils being in turn subjected to the turbulence shed by an upstream circular rod at different Reynolds numbers. The mean wall-pressure distribution and mean-velocity and turbulence-intensity profiles along the airfoils are characterized to study the impact of the porous treatment on the airfoil potential effect and the evolution of the boundary layer. Subsequently, the flow field in the stagnation region is analyzed by means of hot-wire anemometry, PIV, and LES with the aim of elucidating the physical mechanisms involved in the airfoil-turbulence interaction noise mitigation and, particularly, how porosity affects the incoming turbulence characteristics in the immediate vicinity of the surface.

Parts of this chapter are included in [1–3].

5.1. EFFECT OF POROSITY IN CURLE'S ANALOGY

One of the main conclusions of the analysis carried out in Chapter 2.2 is that Curle's dipole-like sources can be considered *footprints* of the Reynolds stresses, resulting from their hydrodynamic and acoustic scattering by the body. They are a consequence of the manipulation of Lighthill's stress tensor. The presence of a rigid surface has an impact on the Reynolds stresses, especially in correspondence with geometrical singularities such as the leading edge of an airfoil. In the case of a porous body, both dipoles and Reynolds stresses are expected to be affected by the change of boundary conditions associated with the porous surface. The investigation on how porosity influences the Reynolds stresses in the vicinity of the airfoil leading edge can lead to a better understanding of the physical mechanisms involved in the turbulence-interaction noise reduction. This is the approach that has been followed in the present study.

It is also important to point out that for a porous body the assumptions $-\partial \rho u_i/\partial \tau = 0$ and $\rho u_i u_j = 0$ made in Equation (2.28) are no more valid due to the presence of a non-zero transpiration velocity at the surface. As a consequence, additional equivalent sources may be produced by the above-mentioned terms and contribute to the overall radiated noise. Particularly, the term $-\partial \rho u_i/\partial \tau$ may constitute a monopole-like source related to unsteady injection of mass in the volume, while the term $\rho u_i u_j$ may represent a dipole-like source generated by the evolution of the Reynolds stresses on the surface. The manipulation of Curle's analogy would be necessary to derive a suitable analytical formulation for evaluating these contributions and will be the object of future research.

5.2. MEAN WALL-PRESSURE DISTRIBUTION

The results of the measurements of the mean wall-pressure distribution are presented by defining the pressure coefficient C_p as

$$C_p = \frac{p - p_\infty}{p_{0,s} - p_\infty}, \tag{5.1}$$

where p is the measured mean wall-pressure and p_∞ and $p_{0,s}$ are the static pressure in the free-stream and stagnation pressure measured at the leading edge of the solid airfoil, respectively.

The C_p distributions along the chord for the solid and porous airfoil configurations for $Re_d = 4.1 \times 10^4$ are shown in Figure 5.1. Each point of the curve is calculated by averaging the mean wall-pressure acquired on the two sides of the airfoil at the same chordwise coordinate.

The alteration in the mean pressure field by the porous treatment appears to be mostly confined to the upstream 30% of the airfoil, although the melamine foam fills the porous airfoil up to 80% of the chord. Nonetheless, the pressure recovery experienced by the solid NACA-0024 profile downstream of the maximum thickness is slightly higher than that in the porous case, with a deviation that increases as the trailing edge is approached. The maximum difference at $x/c = 0.8$ is approximately $|\Delta C_p| = 0.03$. The present trend agrees with the thicker boundary layer that is observed in the aft part of the porous airfoil, as will be discussed in Chapter 5.3. Furthermore, the two configurations exhibit almost the same pressure at the stagnation point, although this value does

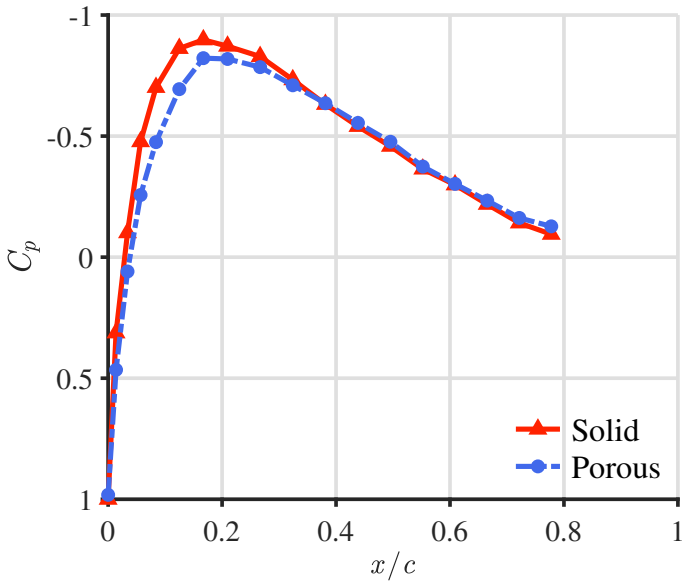

Figure 5.1: C_p distribution along the airfoil chord measured for the solid (red solid line) and porous (blue dash-dotted line) airfoil for $Re_d = 4.1 \times 10^4$ and for a 0° angle of attack.

not correspond to the free-stream dynamic pressure since the airfoil is immersed in the wake of the rod.

The negative C_p peak for the two airfoils occurs at 17% of the chord and is almost preserved, being its absolute value reduced by 6.7% in the porous case. Moreover, for the porous airfoil, this peak is reached in a more gradual way. The discrepancy can be explained by the partial penetration of the air flow through the pores of the melamine foam that tends to level out the pressure differences along the surface and reduces the flow displacement by the NACA-0024 profile. This would most likely degrade the lift of the airfoil if placed at some non-zero angles of attack, as reported in similar works [4, 5].

5.3. AIRFOIL BOUNDARY-LAYER CHARACTERIZATION

In this section, the results of the characterization of the flow field around the solid and porous airfoil configurations are presented. Profiles of mean velocity and turbulence intensity are shown at different chordwise locations to investigate how the porous treatment of the wing profile alters the evolution of the boundary layer. An estimation of the loss in the aerodynamic performance due to the porous treatment of the airfoil is provided in terms of drag increase by evaluating the mean-velocity deficit in the wake of the wing profiles.

5.3.1. MEAN-VELOCITY PROFILES

The mean-velocity profiles $\bar{U}$ for both airfoil configurations are presented in Figure 5.2. The y-axis reports the distance $y^\star$ from the airfoil surface and is normalized by the max-

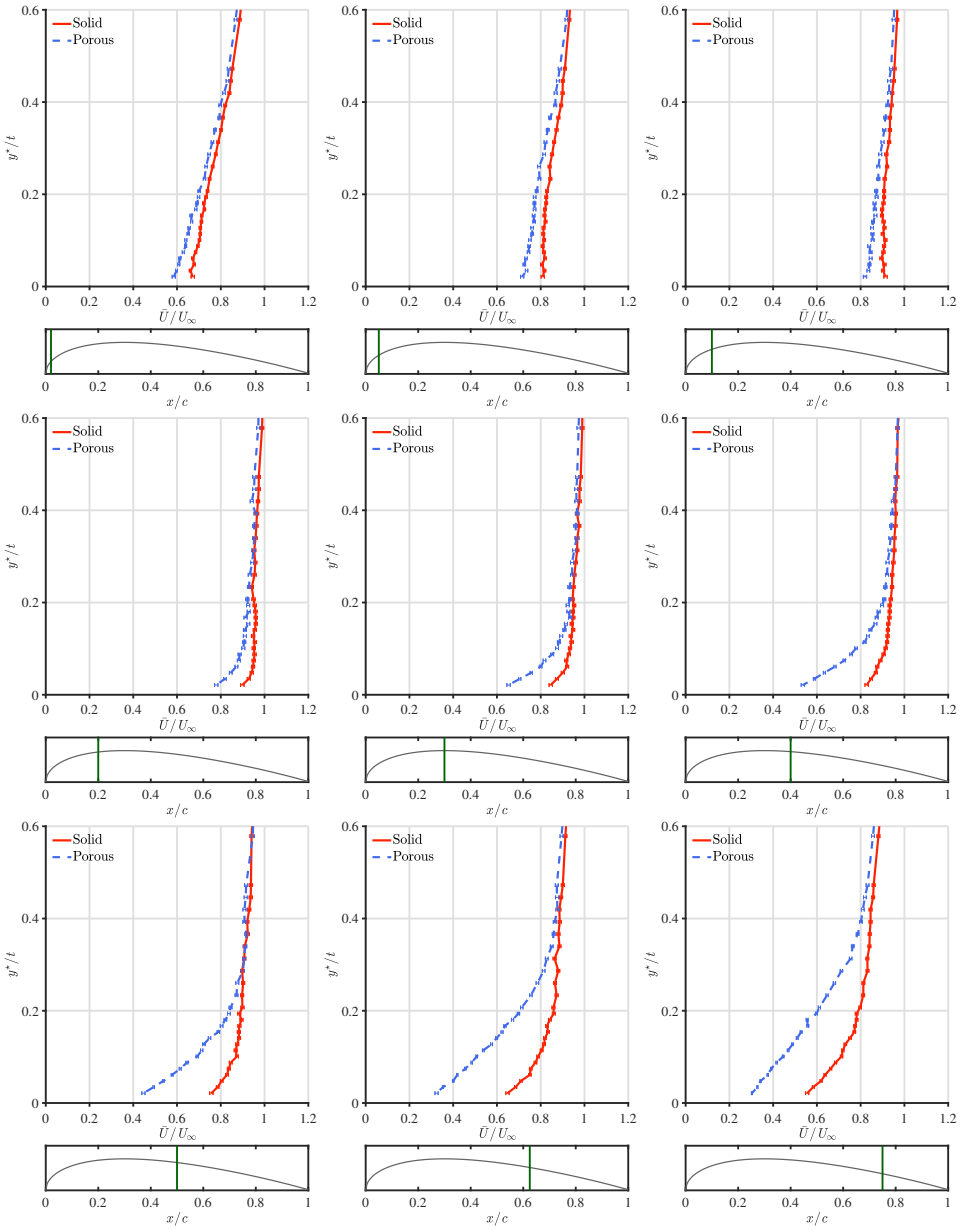

Figure 5.2: Mean-velocity profiles of the solid (red solid line) and porous (blue dashed line) airfoil for the different chordwise positions depicted in Figure 3.12. $y^\star$ is the distance from the airfoil surface, while t is the airfoil maximum thickness. The free-stream velocity is $U_\infty = 30\,\mathrm{m\,s^{-1}}$, corresponding to $Re_d = 4.1 \times 10^4$. The error bars denote the statistic uncertainty with a 97.5 % confidence level (see Appendix A.3).

imum thickness, $t = 0.038\,\mathrm{m}$. All the plots show the $\bar{U}$ profiles up to $0.678\,t$ (equivalent

to about 25 mm) from the surface, while the minimum distance between hot-wire probe and airfoil is 0.5 mm, as mentioned in Chapter 3.6. Before proceeding with a discussion of the results, it is important to point out that the profiles for the first three traverses ($x/c = 0.02$, $x/c = 0.05$, and $x/c = 0.10$) of both solid and porous cases do not exhibit the typical trends of the turbulent boundary layer over a flat plate. This divergence is attributable to the fact that the considered traverses are not perpendicular to the airfoil surface, making it difficult to relate the measured $\bar{U}$ profiles to a *standard* boundary-layer profile.

The comparison shows that the $\bar{U}$ distribution is generally lower in the boundary layer of the porous case with respect to the solid one. This leads to a mass-flow deficiency that is associated with a wider opening of the jet flow. Interestingly, the magnitude of the deficiency increases with the increasing chordwise position, reaching a maximum at $x/c = 0.75$. The present trend has also been observed by Geyer *et al.* [6] and Rubio-Carpio *et al.* [7] in the framework of trailing-edge noise reduction. In both studies, the measurements showed that the magnitude of velocity deficiency was linked to the parameters characterizing the employed porous material. In particular, the lower the static air-flow resistivity of the porous medium is, the greater the mass-flow loss within the airfoil boundary layer will be. This can be explained by the augmented dimension of the pores of the material that increases the surface roughness.

5.3.2. TURBULENCE-INTENSITY PROFILES

The turbulence-intensity profiles U' for both airfoil configurations are presented in Figure 5.3. The results show that, in the initial part of the wing profile, a reduction in turbulence intensity occurs in the proximity of the surface due to the porous treatment. The decrease in the r.m.s.of the velocity fluctuations is consistent with the conclusions that will be drawn in the investigation of the airfoil stagnation region in Chapter 5.4 and may be correlated to a less efficient turbulence-interaction noise generation mechanism. However, the discrepancy in the turbulence intensity profiles of the porous case with respect to the solid one reduces with the increasing chordwise position. At $x/c = 0.20$, the two profiles almost coincide. Notably, this trend reflects that observed in the C_p distribution shown in Figure 5.1.

For $x/c > 0.20$, a trend inversion is visible, with the turbulence-intensity profile for the porous configuration overcoming the turbulence-intensity profile for the solid one within the boundary layer. In this case, the magnitude of the discrepancy increases along with the chordwise direction. Moreover, for $x/c > 0.40$, the hump of the turbulence intensity profile for the porous configuration moves away from the airfoil surface and the peak is shifted towards higher $y^\star/t$. The increment in r.m.s. of the velocity fluctuations that the flow experiences for large x/c might also be linked to a possible circulation of flow generated in the first part of the airfoil and partially blowing in the second part from the pores of the melamine foam. Indeed, the presence of a steady cross-flow blowing within the measurement location has been proved to increase the turbulence intensity within the boundary layer [8]. This effect may also be generated by the fluid-structure interaction occurring between the flow and the hexagonal pores of the hard-plastic exoskeleton, as already hypothesized in Chapter 4.4 with reference to the noise regeneration experienced by the porous wing profile. However, from the GIBF sound maps,

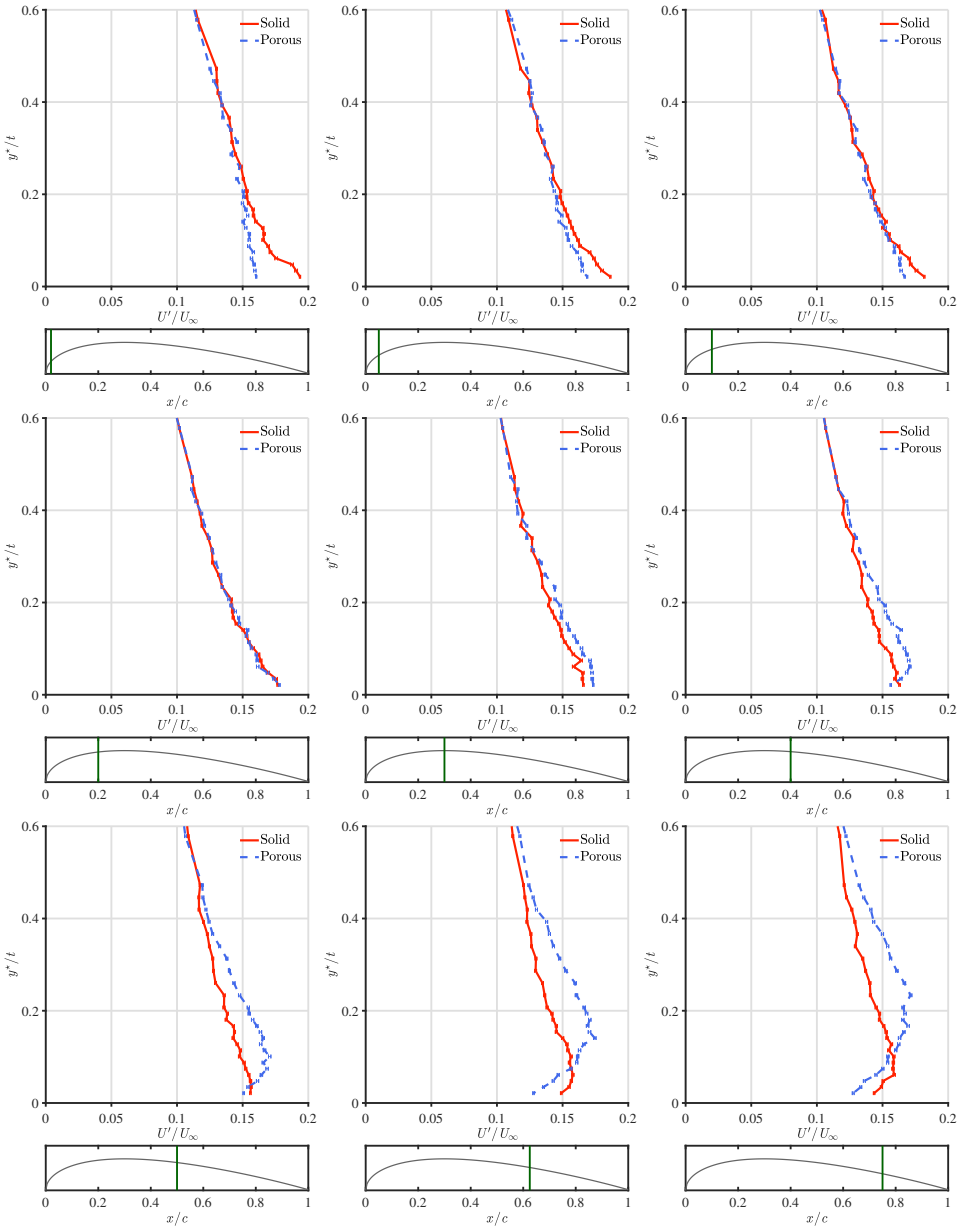

Figure 5.3: Turbulence-intensity profiles of the solid (red solid line) and porous (blue dashed line) airfoil for the different chordwise positions depicted in Figure 3.12. $y^\star$ is the distance from the airfoil surface, while t is the airfoil maximum thickness. The free-stream velocity is $U_\infty = 30\,\mathrm{m\,s^{-1}}$, corresponding to $Re_d = 4.1 \times 10^4$. The error bars denote the statistic uncertainty with a 97.5 % confidence level (see Appendix A.3).

the dominant high-frequency noise sources are found slightly downstream of the lead-

ing edge. In this region, the alterations in the turbulence intensity occurring within the boundary layer do not seem to confirm the above-mentioned hypothesis. Therefore, further investigations would be required to shed light upon the origin of the noise regeneration.

5.3.3. AIRFOIL WAKE

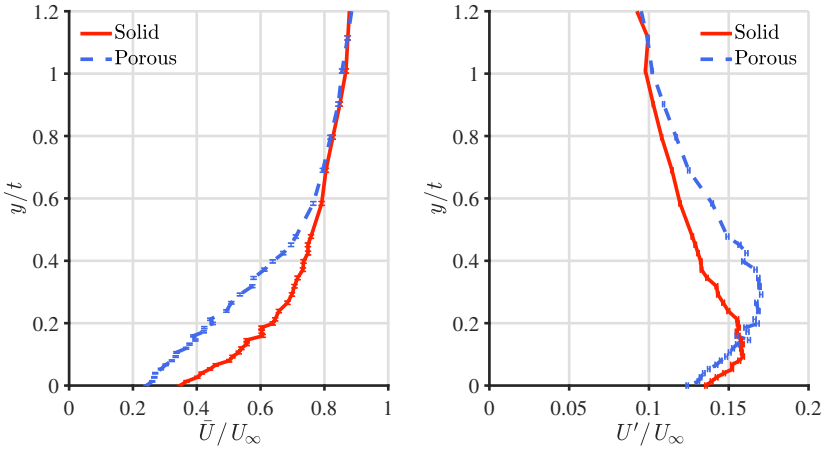

Figure 5.4: Mean-velocity (on the left) and turbulence-intensity (on the right) profile in the wake of the solid (red solid line) and porous (in blue dashed line) airfoil at $x/c = 1.05$. t is the airfoil maximum thickness (0.038 m). The free-stream velocity is $U_\infty = 30\,\mathrm{m\,s^{-1}}$, corresponding to $Re_d = 4.1 \times 10^4$. The error bars denote the statistic uncertainty with a 97.5% confidence level (see Appendix A.3).

The mean-velocity and turbulence-intensity profiles extracted at $x/c = 1.05$ are reported in Figure 5.4. Both solid and porous airfoil cases exhibit similar trends to those measured at $x/c = 0.75$ in Figure 5.3, with lower mean velocities and corresponding higher velocity deficits in the vicinity of the chord line, and a shift of the turbulence intensity bump towards larger y/t for the porous case with reference to the solid one.

Airfoil configuration	Solid	Porous
C_d [-]	0.0157	0.0204

Table 5.1: Zero-lift drag coefficients for the solid and porous airfoil.

The integration of the above mean-velocity profiles shows a significant 30% increment of drag experienced by the porous airfoil, as can be observed in the results listed in Table 5.1. This is a consequence of the increased surface roughness caused by the fluid-structure interaction with the hard-plastic exoskeleton already discussed.

5.4. STAGNATION REGION CHARACTERIZATION

In this section, the outcomes of the experimental and numerical investigation of the flow field alterations within the stagnation region of the solid and porous airfoil are discussed

by analyzing the mean and fluctuating velocity field and velocity spectra at several locations around the leading edge.

5.4.1. VELOCITY FIELD ALONG THE STAGNATION STREAMLINE

The experimental hot-wire data along the stagnation streamline presented in Chapter 3.6 are compared with the results of the LES presented by Satcunanathan *et al.* [9] that are based on the JAFAR experimental setup. This is performed by relating the statistics of the flow-velocity field acquired by the single-probe hot-wire anemometer and the simulated ones. For further information about the setting of the simulations, the reader is referred to the above-mentioned paper. This comparison is meant to validate the numerical results that will be presented in the following section of the manuscript.

The quantities u_1, u_2, and u_3 indicate the simulated velocity components in the x, y, and z direction and the symbols $\bar{}$ and $'$ denote the mean velocity and r.m.s. of the velocity fluctuations, respectively. Evaluating the magnitude of the two mean velocity components that are perpendicular to the wire in each sampling point, i.e. $\bar{u}_1$ and $\bar{u}_2$, $\bar{U}$ reads

$$\bar{U} = \sqrt{\bar{u}_1{}^2 + \bar{u}_2{}^2}. \tag{5.2}$$

Similarly, the formulation proposed in this work to estimate U' is

$$U' = \sqrt{(u_1' \cos\alpha)^2 + (u_2' \sin\alpha)^2} \qquad \text{with} \quad \alpha = \tan^{-1}\left(\frac{\bar{u}_2}{\bar{u}_1}\right). \tag{5.3}$$

This quantity does not correspond to the r.m.s. of the velocity fluctuations that are given by the magnitude of the two velocity components measured by the probe but rather represents a weighted average of u_1' and u_2' based on the local mean-flow direction, which is expressed by the parameter α. This is a consequence of the fact that, for small turbulence levels, a single normal hot-wire only responds to fluctuations in the direction of the mean velocity [10].

Nonetheless, the proposed method to evaluate the local mean-flow direction and, therefore, the contribution of the different velocity fluctuations components to U' could not be applicable if the numerical data were taken precisely on the stagnation streamline. Indeed, in such circumstances, $\bar{u}_2$ would be zero along the whole traverse and so would α due to the flow symmetry. Hence, U' would correspond to u_1' and no influence of u_2' would be detected. In order to tackle the problem, the LES data were extracted at $y = 8.8 \times 10^{-5}$ m. This distance was close enough to provide a negligible deviation from the flow field statistics computed on the stagnation streamline and far enough to have a non-zero value of $\bar{u}_2$ in the stagnation region.

The hot-wire anemometry results indicate that the implementation of the porous material in the airfoil structure preserves the potential effect with regard to the upstream flow. Figure 5.5a illustrates the mean-velocity profile along the stagnation streamline for the solid and porous airfoils. $\bar{U}$ is normalized by the free-stream velocity. As can be observed, the experimental data for the two cases follow the same trend up to the immediate vicinity of the leading edge. This conclusion is supported also by the relatively small deviation in the solid and porous C_p distributions of Figure 5.1.

Moreover, the hot-wire data are in a fairly satisfactory agreement with the numerical results corresponding to the solid airfoil for $\xi = x/r_{LE} \leq -1$. The deviation that occurs

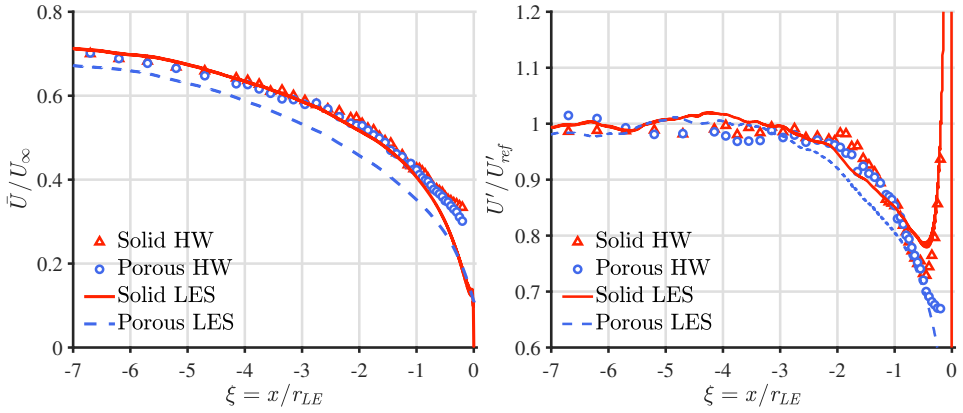

(a) Mean-velocity profile.

(b) Velocity-fluctuation profile.

Figure 5.5: Profiles of the solid (in red) and porous (in blue) airfoil along the stagnation streamline for $Re_d = 4.1 \times 10^4$ and for a 0° angle of attack. The solid and dash-dotted lines refer to the numerical results of the LES, whereas the triangle and dot symbols refer to the VKI experimental data. $\bar{U}$ is normalized by the free-stream velocity $U_\infty = 30\,\mathrm{m\,s^{-1}}$, corresponding to $Re_d = 4.1 \times 10^4$, while U'_{ref} denotes to the r.m.s. of the velocity fluctuations evaluated at $\xi = -7$ for the solid case. The dimension of the symbols for the hot-wire data is proportional to their statistic uncertainty with a confidence level of 97.5% (see Appendix A.3).

5

for $\xi > -1$ has been already reported by Bearman [11] and is probably due to a thermal effect produced by the proximity to the surface or due to the intrusiveness of the hot-wire probe that has moved the stagnation point slightly. By contrast, the numerical results computed for the porous case do not follow the same trend as the solid one, hinting at an alteration of the airfoil's potential effect. The discrepancy may be linked to the absence of the hard-plastic permeable exoskeleton and wire mesh in the numerical model of the porous medium, as suggested by Satcunanathan *et al.* [9].

The most striking effect of porosity is on the evolution of the turbulent-velocity fluctuations in the immediate vicinity of the leading edge. The velocity-fluctuations profile along the stagnation streamline for the solid and porous airfoil is depicted in Figure 5.5b. The velocity U' is normalized with an upstream reference value, U'_{ref}, which corresponds to the r.m.s. of the velocity fluctuations that have not been affected by the presence of the airfoil yet. This notation is consistent with that used by Batchelor and Proudman [12], Bearman [11], Hunt [13], and Britter *et al.* [14] in their investigations of turbulence distortion. U'_{ref} is evaluated at $\xi = -7$ and refers to the solid case. As can be seen from the plot, the experimental data present a similar trend up to about $0.5\,r_{LE}$ from the leading edge, with a constant value equal to 1 for $\xi < -2$ and a decrease in the region $-2 \leq \xi < -0.5$. Above this threshold, the solid and porous cases diverge significantly, the former starts to increase and the latter keeps decreasing.

Furthermore, a satisfactory agreement is found between numerical and experimental data for both solid and porous airfoils in this case, indicating that the previously mentioned thermal effects do not affect the measurement of the velocity fluctuations performed by the hot-wire. Notably, the slope with which U' increases in the immediate vicinity of the solid airfoil is well predicted by the simulations, although a slight underes-

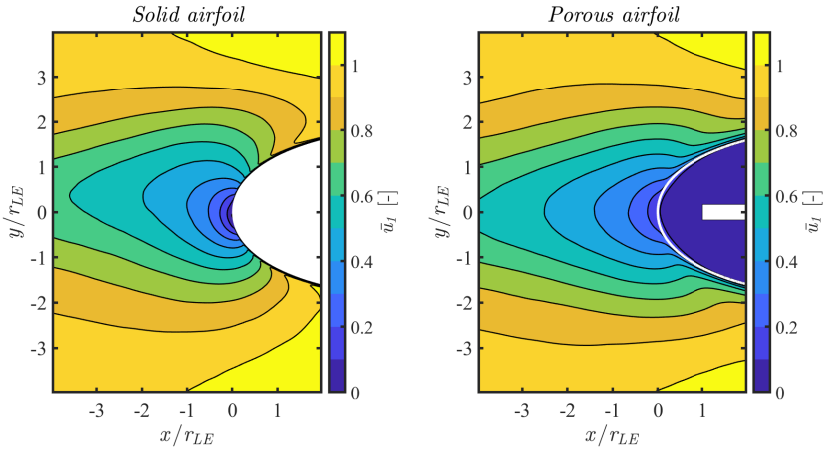

(a) Streamwise velocity component.

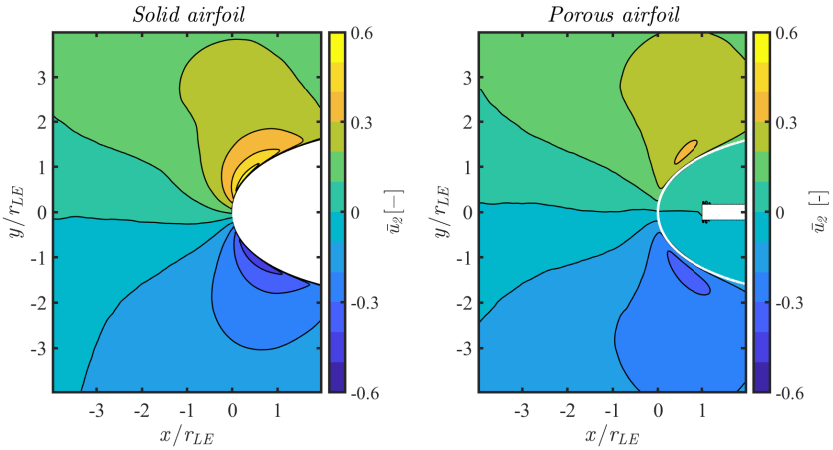

(b) Upwash velocity component.

Figure 5.6: Mean velocity for the solid (on the left) and porous airfoil (on the right) in the stagnation region extracted by the LES. The mean velocities are made dimensionless by the free-stream velocity, U_∞.

timation is observed for the minimum peak at $\xi = -0.5$. However, for the porous case, a small discrepancy is visible for $\xi > -0.5$. Analogously to the mean-velocity comparison, this may be associated with the fact that exoskeleton and wire mesh are not modeled in the numerical simulations.

5.4.2. FLOW FIELD IN THE STAGNATION REGION

Mean and r.m.s. velocities are extracted from the LES to analyze the velocity components independently and to explain the hot-wire trends in Figure 5.5. Figure 5.6 presents the mean velocity in the stagnation region for the solid and porous cases. As indicated by the white airfoil outline, the LES provide an estimation of the flow field partially penetrating

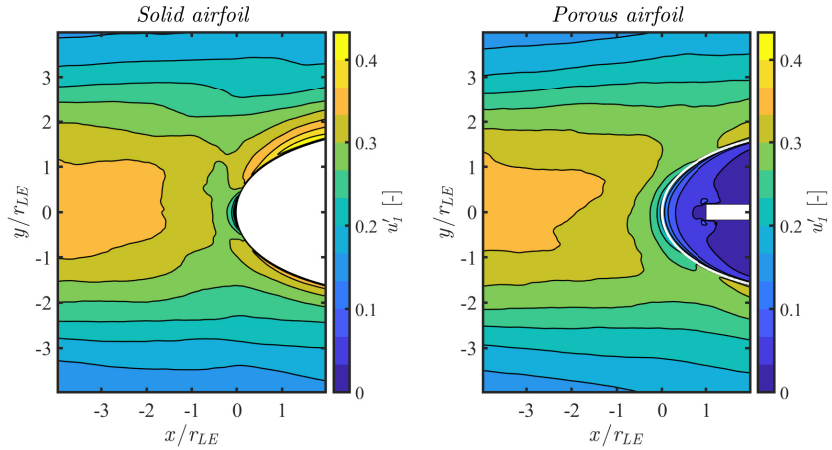

(a) Streamwise velocity component.

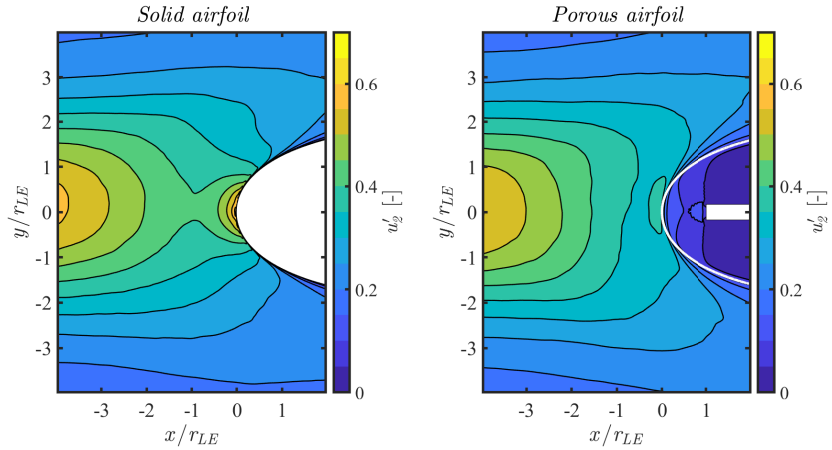

(b) Upwash velocity component.

Figure 5.7: Turbulence intensity for the solid (on the left) and porous airfoil (on the right) in the stagnation region extracted by the LES. The velocity fluctuations are made dimensionless by the free-stream velocity, U_∞.

into the inner porous volume. Specifically, the low-pressure spot that corresponds to the region of highest streamline curvature and flow acceleration (at $x/c = 0.17$ in Figure 5.1) attracts the surrounding fluid, generating an induced flow within the melamine foam. This phenomenon is explained in greater details by Satcunanathan *et al.* [9] and is at the origin of the pronounced momentum deficit of $\bar{u}_1$ and $\bar{u}_2$ that is visible in the maps for $x/c > 0$ and has already been addressed in Chapter 5.3. Lastly, the effective influence of the porosity on the mean-flow field is expected to be less pronounced than that shown in the maps. This supposition is based on the deviation between experiments and simulations observed in Figure 5.6a for the porous case.

The velocity fluctuations in the wake of the rod are primarily caused by the shed vor-

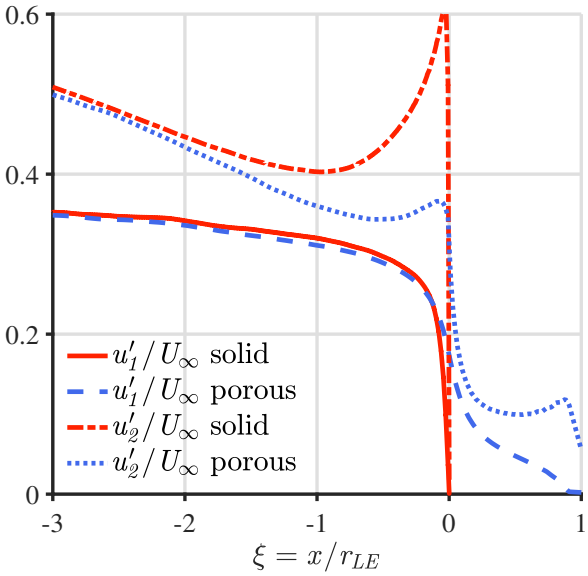

Figure 5.8: Turbulence intensity for the solid (red lines) and porous airfoil (blue lines) extracted by the LES along the stagnation streamline. The u_1'- and u_2'-components are made dimensionless by the free-stream velocity, U_∞.

tices, which lead to a much larger component in the normal direction than in the streamwise direction. In addition, the porous treatment of the airfoil has a significant effect on the evolution of the turbulent-velocity fluctuations as they are convected towards the leading edge. The u_1' and u_2' components in the stagnation region are illustrated in Figures 5.7a and 5.7b, respectively, whereas the values extracted at $y/r_{LE} = 0$ are reported in Figure 5.8.

Along the stagnation streamline of the solid airfoil, u_1' is suppressed due to the non-penetration condition, whereas this reduction is weakened in the porous case. Similarly, the increase of u_1' experienced on the solid airfoil surface in the surrounding region of the leading edge is mitigated by the presence of porosity. This trend has already been pointed out in Chapter 5.3 as a result of the boundary-layer characterization by hot-wire anemometry. Consequently, the main effect of the porous treatment on u_1' is to dampen the variation of velocity fluctuations near the airfoil.

Moreover, the significant amplification in the upwash component of the velocity fluctuations around the stagnation point that is observed for the solid case is significantly attenuated for the porous one. The reduction in u_2' is reflected in the turbulent kinetic energy (TKE), defined as

$$\mathrm{TKE} = \frac{1}{2}\left(u_1' + u_2'\right) \tag{5.4}$$

and reported in Figure 5.9. This constitutes a key point in understanding how the porous treatment of the airfoil affects the turbulence distortion. The upwash turbulent velocity is indeed the component that is responsible for the unsteady lift according to the lin-

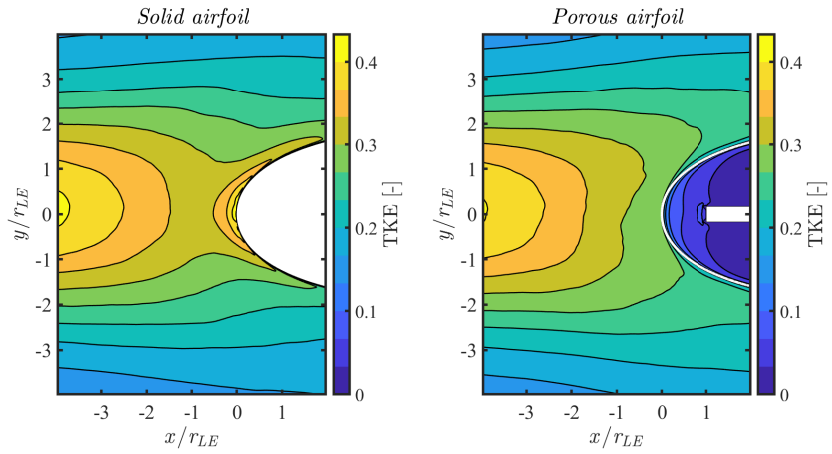

Figure 5.9: Turbulent kinetic energy for the solid (on the left) and porous airfoil (on the right) in the stagnation region extracted by the LES and made dimensionless by the free-stream velocity, U_∞.

earized airfoil theory [15] and for the associated noise following Amiet's model [16] (see Chapter 1.1.1). In addition, a second amplification in u_2' can be observed in the porous case within the inner volume of the melamine foam in proximity to the solid centerplane (Figure 5.8). The present trend confirms the relevance of the role played by this component on the acoustic field, as already mentioned in Chapter 4.4.

The results illustrated in Figure 5.5b can now be explained through the maps presented in Figures 5.6 and 5.7 and the trends reported in Figure 5.8. u_1' dominates the trend of U' in the upstream flow region where $\alpha \approx 0$. As the stagnation point is being approached, u_1' is reduced and so is U'. However, since the decrease in $\bar{u}_1$ is also associated with an increase in α (see Equation 5.3), the contribution of u_2' to U' becomes more significant in this region. Therefore, the relatively higher U' values in the solid case are caused by the transfer of momentum from the streamwise component to the upwash component of the velocity fluctuations due to the non-penetration condition imposed by the rigid surface. This increase in u_2' can be detected near the leading edge because the heat transfer of the hot-wire is no longer dominated by the mean flow. Likewise, the absence of the non-penetration condition at the porous surface makes it possible to have a non-zero value for the mean velocity at the stagnation point, which can be considered fictitious in this case. Hence, in the immediate vicinity of the leading edge, α is smaller for the porous airfoil than for the solid one, and this yields a further attenuation in U' for the porous case with respect to the solid one.

Finally, the above-discussed alterations in the velocity field induced by porosity are reflected in a modification in the vorticity near the surface. Figure 5.10 displays the mean spanwise vorticity, defined as

$$\Omega_3 = \frac{\partial \bar{u}_2}{\partial x} - \frac{\partial \bar{u}_1}{\partial y}, \tag{5.5}$$

for the two airfoil configurations. The lower velocity gradients observed in the boundary layer of the porous wing profile in Figures 5.2 and 5.6 result in an attenuation of the

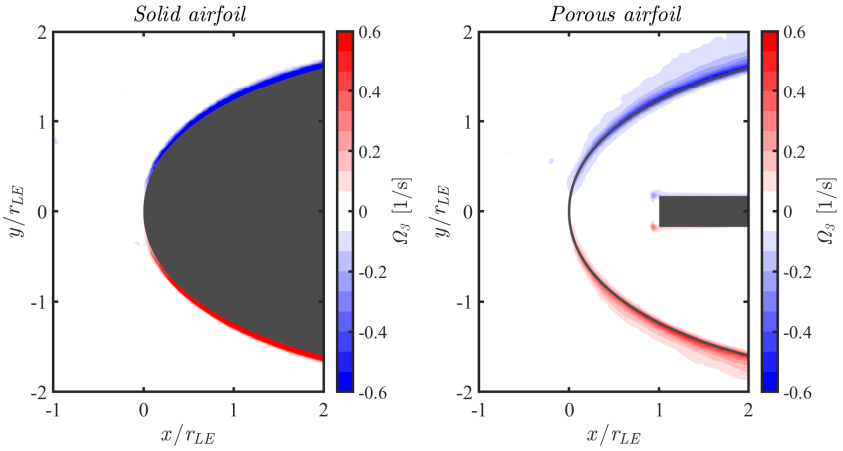

Figure 5.10: Mean spanwise vorticity for the solid (on the left) and porous airfoil (on the right) in the stagnation region extracted by the LES.

intensity of Ω_3, which is found to be spread over a wider region. Moreover, the mean spanwise vorticity is negligible within the inner volume of the airfoil but starts increasing at the front corners of the center-plane as a consequence of the separation experienced by the internal flow.

REYNOLDS NUMBER AND EXOSKELETON EFFECT ON TURBULENCE STATISTICS

The effect of the Reynolds number on the turbulence-distortion alterations due to the porous treatment of the wing profile can be evaluated through the PIV measurements, which are conducted at $Re_d = 2.7 \times 10^4$, $Re_d = 4.1 \times 10^4$, and $Re_d = 5.4 \times 10^4$. In addition, the PIV campaign provides the framework to investigate the influence of the permeable exoskeleton on the flow field since the experiments include the presence of the melamine airfoil configuration. The mean-flow velocity and turbulence-intensity maps are computed from an under-sampled dataset in order to ensure the uncorrelation of the samples. This procedure and the resulting PIV maps are illustrated in Appendix C, while the data extracted along the stagnation streamline related to the mean streamwise velocity and turbulent-velocity fluctuations are depicted in Figures 5.11 and 5.12, respectively.

In general, the results related to $Re_d = 4.1 \times 10^4$ exhibit the same trends as the LES in Figures 5.7 and 5.6, although the numerical data feature higher amplitudes in the velocity fluctuations. This can be attributable to the different inflow conditions existing in the A-Tunnel facility and in the LES boundary conditions, which are calibrated considering the nozzle-flow qualification of the JAFAR wind tunnel.

The trends of the streamwise component of the mean velocity (Figure 5.11) for the three NACA-0024 profiles do not appear to be significantly affected by the different free-stream flow velocities. For each configuration, porosity influences $\bar{u}_1$ in the stagnation region, particularly for $\xi > -1$, as a consequence of the flow entering the inner volume of the wing profile. No notable difference can be observed between porous and melamine

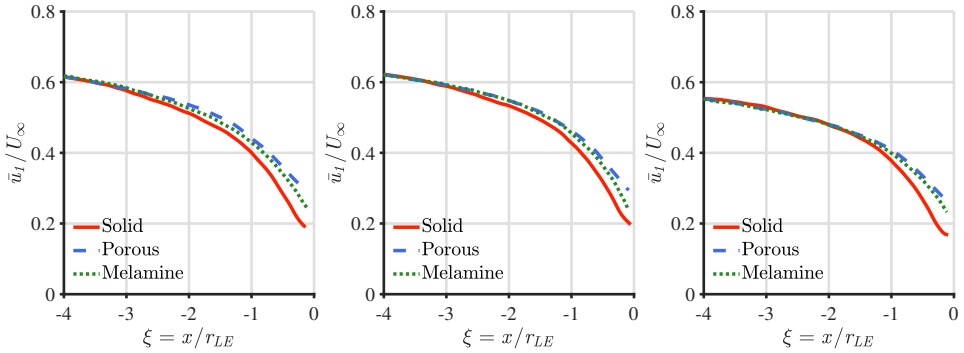

(a) $Re_d = 2.7 \times 10^4$. (b) $Re_d = 4.1 \times 10^4$. (c) $Re_d = 5.4 \times 10^4$.

Figure 5.11: Uncorrelated mean-velocity profiles of the streamwise velocity component extracted from the PIV maps along the stagnation line for the solid (solid red line), porous (dashed blue line), and melamine (dotted green line) airfoil. The data refer to different rod-based Reynolds numbers.

case except for the immediate vicinity of the surface, suggesting that the exoskeleton does not considerably limit the flow penetration at the stagnation point.

A strong effect of the rod-based Reynolds number and porous treatment is found on the evolution of the velocity fluctuations instead. These are presented in Figure 5.12. Both streamwise and upwash velocity components feature a maximum in the upstream region due to the presence of the coherent vortices shed by the rod. Getting closer to the stagnation point, a decrease in u'_1 and an increase in u'_2 are found, consistently with the hot-wire anemometry and LES results presented in Chapter 5.4.2. Interestingly, the streamwise position at which the deviations start, i.e. at which the distortion of turbulence by the airfoil begins, is independent of Re_d and occurs at $\xi \approx -1$, in line with the turbulent-velocity profiles in Figure 5.8 and with the conclusions drawn by de Santana *et al.* [17, 18].

In agreement with the previous results, porosity induces an attenuated reduction of turbulence intensities for the streamwise direction in the stagnation region. Similar to the case of the corresponding mean-velocity component, the presence of the exoskeleton does not appear to alter the present trend. On the contrary, the mitigation in the fluctuations of the upwash velocity component is more evident for the melamine airfoil configuration. Indeed, the pores of the hard-plastic exoskeleton allow for the penetration of the incident flow but most probably reduce the attenuation in the momentum transfer taking place between streamwise and upwash velocity.

The effect of Re_d is to extend the region where porosity has an impact on the turbulent field. In particular, the location from which the trends of u' and v' start diverging moves towards lower x/R_{LE} with the increasing Reynolds number. Moreover, the effect of porosity on the velocity fluctuations appears to be enhanced for higher values of Re_d with reference to the solid case, especially for the upwash component. The deviation in v' between porous and melamine case is also a function of the Reynolds number and increases along with Re_d.

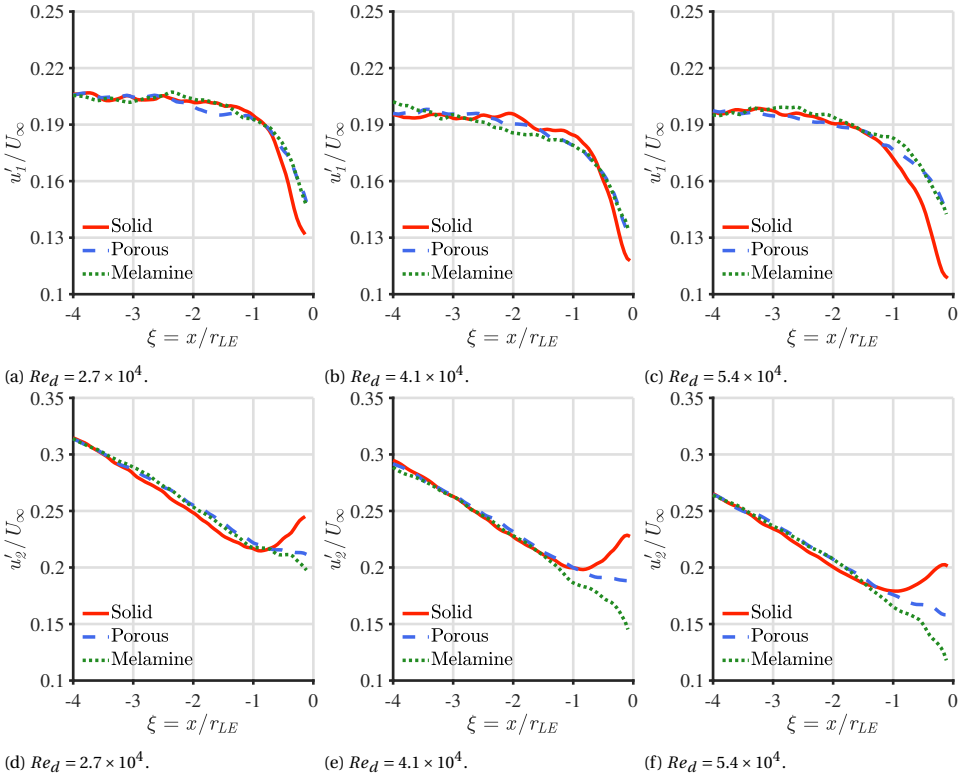

(a) $Re_d = 2.7 \times 10^4$. (b) $Re_d = 4.1 \times 10^4$. (c) $Re_d = 5.4 \times 10^4$.

(d) $Re_d = 2.7 \times 10^4$. (e) $Re_d = 4.1 \times 10^4$. (f) $Re_d = 5.4 \times 10^4$.

Figure 5.12: Uncorrelated turbulence-intensity profiles of the streamwise of upwash velocity components extracted from the PIV maps along the stagnation line for the solid (solid red line), porous (dashed blue line), and melamine (dotted green line) airfoil. The data refer to different rod-based Reynolds numbers.

5.4.3. TURBULENT-VELOCITY POWER SPECTRA

In this section, the flow field is investigated by evaluating the PSD of the turbulent velocity at different locations upstream and around the airfoils. Likewise, the influence of the Reynolds number and permeable exoskeleton is analyzed.

SPECTRA ALONG THE STAGNATION STREAMLINE

The PSDs of the velocity fluctuations for the solid and porous airfoil configuration from the hot-wire experimental data extracted at four specific locations along the stagnation streamline are computed. The results in Figure 5.13 are presented in dB/St with a reference of $1\,\mathrm{m^2\,s^{-1}}$. The Strouhal number is based on the cylindrical rod diameter and free-stream velocity.

The measured vortex-shedding frequency peak is found to occur at $St = 0.176 \pm 0.001$. This value is slightly lower than what is commonly reported for Reynolds numbers in the high sub-critical regime [19–21]. The discrepancy is most likely caused by the significant blockage of the rod with respect to the JAFAR wind-tunnel width. At $\xi = -6.7$ (Figure 5.13a), the velocity PSDs clearly present two peaks corresponding to the vortex-shedding

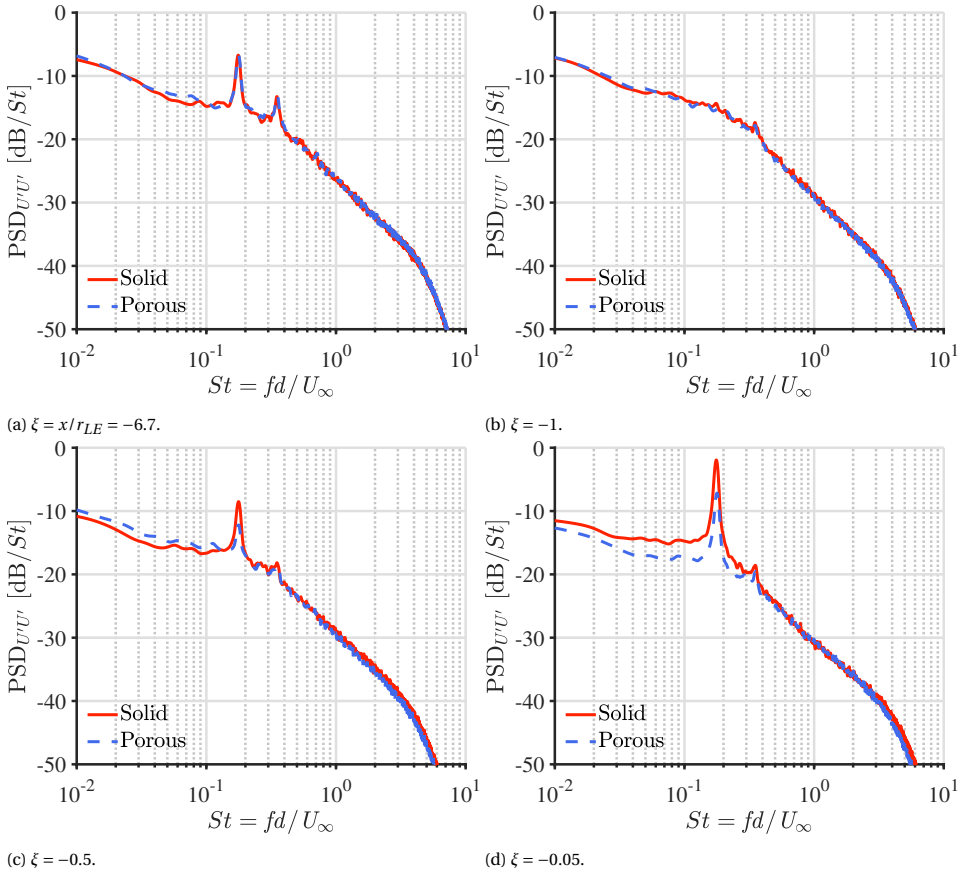

(a) $\xi = x/r_{LE} = -6.7$.

(b) $\xi = -1$.

(c) $\xi = -0.5$.

(d) $\xi = -0.05$.

Figure 5.13: Velocity fluctuations PSD for the solid (solid red line) and porous case (dashed blue line) computed from the hot-wire measurements at different dimensionless locations along the stagnation streamline with a reference of $1\,\mathrm{m}^2\,\mathrm{s}^{-1}$.

frequency and its first harmonic. At this position, no difference can be detected between solid and porous case, as already observed in Figure 5.5b.

At $\xi = -1$ (Figure 5.13b), the two considered cases still exhibit the same trend but now the vortex-shedding frequency peak turns out to be fully dampened and is no longer visible in the spectra. It is observed that this peak gradually decreases from the region downstream of the rod up to $\xi = -2$, where it disappears. Interestingly, at this location, the r.m.s. of the velocity fluctuations measured by the hot-wire starts reducing, as shown in Figure 5.5b.

Furthermore, in this intermediate region, the turbulence is not yet distorted and the turbulent fluctuations extracted from the numerical simulations are found to be comparable in the different components, hinting at local isotropic turbulence. Under this assumption, the size of the largest eddies of the turbulent flow in the streamwise direction can be estimated by evaluating the streamwise integral length scale L_x from the

integration of the auto-correlation function of the hot-wire time signal and from the local mean-flow velocity [22] considering Taylor's frozen turbulence assumption. Figure 5.14 depicts the auto-correlation of U' $R_{U'U'}$ defined as

$$R_{U'U'}(\tau) = \lim_{T\to\infty} \int_0^T U(t)U(t+\tau)\,dt \tag{5.6}$$

and computed at $\xi = -2$ for the two airfoil configurations. The resulting $L_x \approx 4.2\ r_{LE}$, which amounts to the same value for the solid and porous case since porosity has no effect on the flow field at this location, will be considered in Chapter 6.3.4 to interpret the velocity fluctuation trends by means of the RDT.

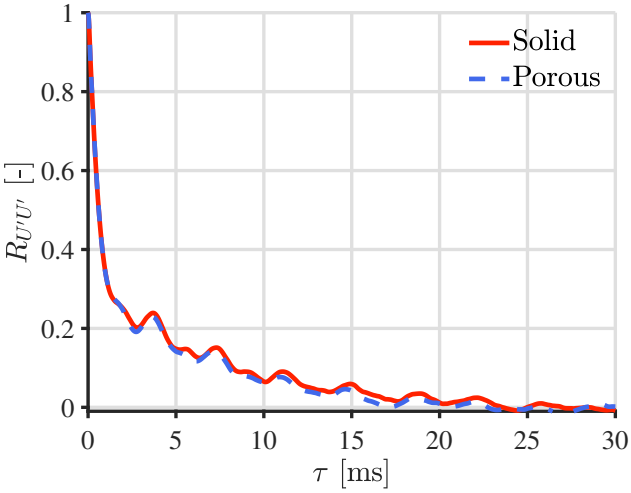

Figure 5.14: Auto-correlation function of the hot-wire time signal for the solid (in red) and porous (in blue) airfoil computed at $\xi = -2$.

At $\xi = -0.8$, the peak at $St = 0.176 \pm 0.001$ reappears for both airfoils and increases in magnitude as the stagnation point is approached. This phenomenon is typical for stagnation-point flows [23] and might be caused by the effect of the flow deceleration that excites the instability in the upstream cylinder wake associated with the vortex shedding. Indeed, sufficiently large-scale eddies properly oriented to be stretched can experience an amplification in their vorticity as they are convected towards the stagnation region. In particular, the vorticity that is present in the incoming turbulent flow with a small intensity can reappear near the body with increased intensity and induce substantial three-dimensional effects.

Moreover, the solid and porous PSDs start diverging from $\xi = -0.5$ on, consistently with the U' trends in Figure 5.5b. For the measurement point closest to the airfoil surface at $\xi = -0.05$ (Figure 5.13d), the part of the spectrum that is affected by the porosity is that at low Strouhal numbers, which corresponds to large vortical structures, whereas the high-St region is mostly unaltered.

Likewise, a better understanding of the turbulence distortion can be gained by the analysis of the LES velocity components separately. Figure 5.15 illustrates the PSD of the

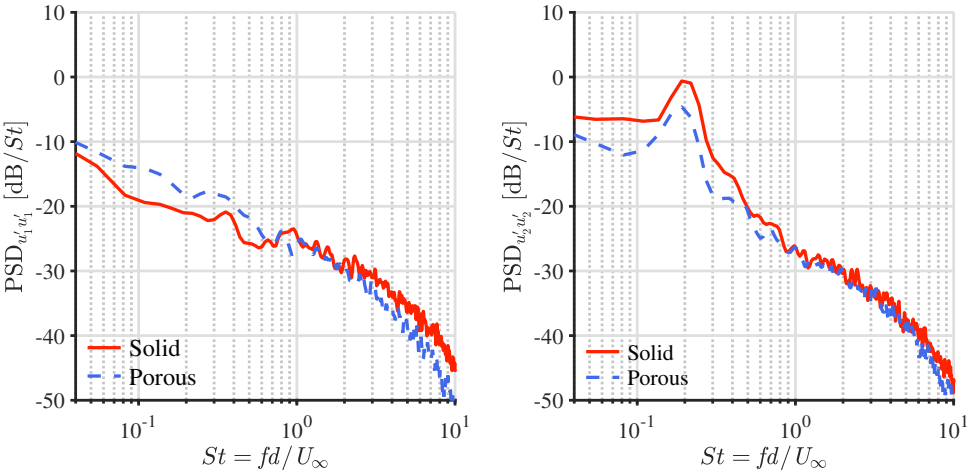

Figure 5.15: PSD of the streamwise component (on the left) and upwash component (on the right) of the velocity fluctuations for the solid (solid red lines) and porous case (dashed blue lines) extracted by the LES at $\xi = -0.05$. The reference is $1\,\mathrm{m^2\,s^{-1}}$.

5

streamwise ($\mathrm{PSD}_{u_1' u_1'}$) and upwash ($\mathrm{PSD}_{u_2' u_2'}$) component of the velocity fluctuations extracted at $\xi = -0.05$ for the solid and porous airfoil configurations. For both components, the porosity mostly alters the spectrum in the low-St region up to about $St = 0.05$, similar to the experimental trend. In this range, the limited decrease in u_1' observed in the stagnation region of the porous airfoil (Figure 5.8) is reflected in higher values of $\mathrm{PSD}_{u_1' u_1'}$ for this configuration with respect to the solid one. Conversely, the PSDs of the upwash component of the velocity fluctuations in the porous case are characterized by lower values of $\mathrm{PSD}_{u_2' u_2'}$ in the low-St region. The combination of these opposite trends can explain the quantitative difference reported in Figure 5.13d. This aspect will be further discussed in Chapter 6.3 by means of the RDT.

SPECTRA AROUND THE AIRFOIL

The extent of the influence of the porous treatment on the turbulence distortion can be investigated by analyzing the PSDs of the velocity fluctuations at several positions around the airfoil leading edge. Figure 5.16 reports the PSDs of the two velocity fluctuations components extracted by the LES at three different locations that gradually drift away from the stagnation streamline. Near the leading edge (Figure 5.16a), $\mathrm{PSD}_{u_1' u_1'}$ is generally higher in the porous case than in the solid one for the majority of the spectrum, reflecting the trend of u_1' shown in Figure 5.7a. Interestingly, the vortex-shedding frequency peak visible in the spectrum for the solid airfoil is not present in that for the porous airfoil. This absence may be linked to better damping of the vortical structures shed by the rod in the interaction with the porous surface and may clarify why the greatest noise abatement occurs around the vortex-shedding frequency peak (see Chapter 4.4). In contrast, the trend exhibited by $\mathrm{PSD}_{u_2' u_2'}$ is closer to that in Figure 5.15. The significant alteration in the PSD of the upwash component of the velocity fluctuations due to the porous treatment is confined to the low-St region, especially for $St < 0.3$. At the in-

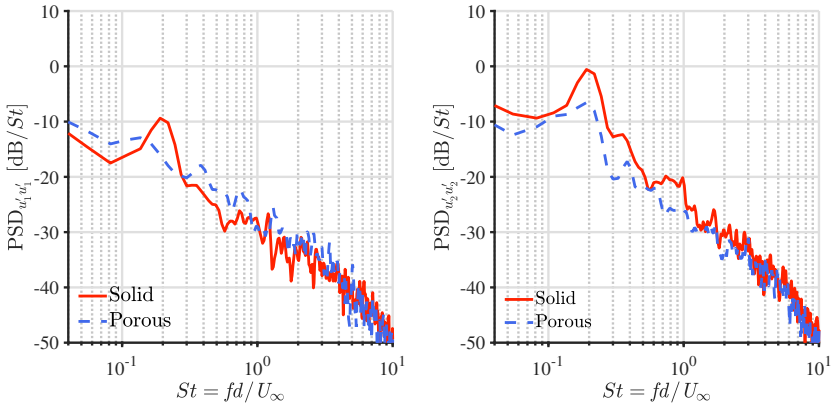

(a) $x/r_{LE} = 0.04$; $y/r_{LE} = 0.36$.

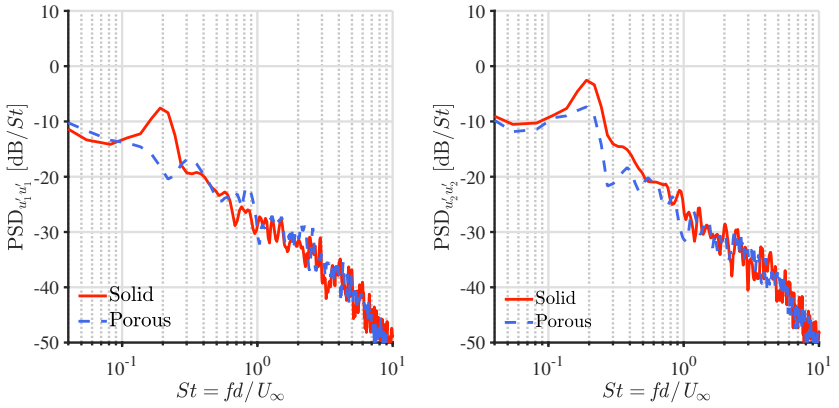

(b) $x/r_{LE} = 0.15$; $y/r_{LE} = 0.57$.

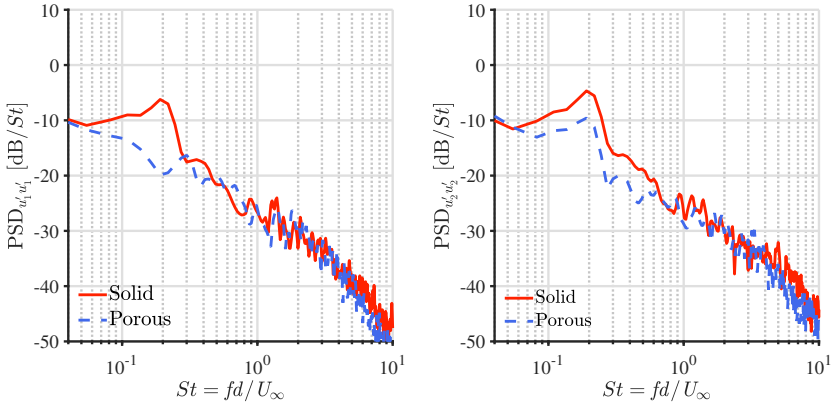

(c) $x/r_{LE} = 0.29$; $y/r_{LE} = 0.78$.

Figure 5.16: PSD of the streamwise component (on the left) and upwash component (on the right) of the velocity fluctuations for the solid (solid red lines) and porous case (dashed blue lines) extracted by the LES at different dimensionless locations around the airfoil leading edge. The reference is $1\,\mathrm{m}^2\,\mathrm{s}^{-1}$.

termediate location (Figure 5.16b), the deviation between the two airfoil configurations is reduced for both velocity components and the PSDs start converging, with the exception of the vortex-shedding frequency peak. The present trend is even more pronounced at the location farther from the leading edge (Figure 5.16c). In conclusion, the porosity is estimated to have an influence on the two components of the velocity fluctuations and, therefore, on the turbulence distortion up to about $\xi = 2$. This result is in agreement with the outcomes of the airfoil boundary-layer characterization presented in Chapter 5.3.

REYNOLDS NUMBER AND EXOSKELETON EFFECT ON VELOCITY SPECTRA

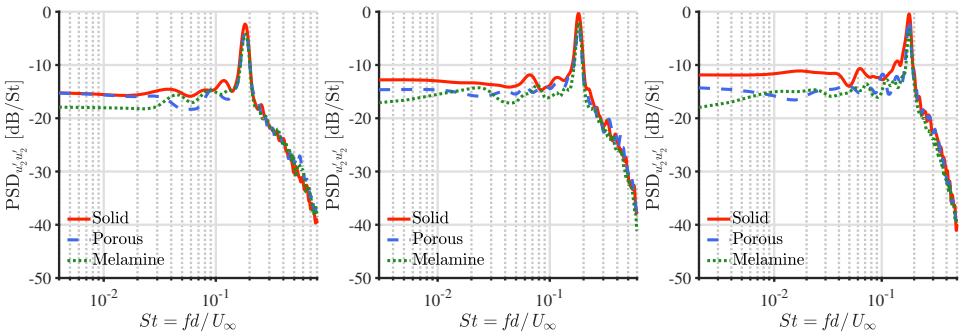

(a) $Re_d = 2.7 \times 10^4$. (b) $Re_d = 4.1 \times 10^4$. (c) $Re_d = 5.4 \times 10^4$.

Figure 5.17: PSD of the upwash component of the velocity fluctuations for the solid (solid red line), porous (dashed blue line), and melamine (dotted green line) airfoil from the PIV measured at $(x/R_{LE}, y/R_{LE}) = (-0.25, 0)$. The data refer to different rod-based Reynolds numbers. The reference is $1\,\mathrm{m}^2\,\mathrm{s}^{-1}$.

The dependence of the turbulent-field alterations due to porosity on the Reynolds number observed in the PIV measurements in Figure 5.12 can be further investigated by evaluating the turbulent-velocity spectrum at a location near the airfoil. Figure 5.17 depicts the PSD of the upwash component of the velocity fluctuations computed at $\xi = -0.25$ for the three airfoil configurations and different Re_d. This position is chosen as a trade-off between enhancement of the porosity effects and need to avoid invalid PIV data points due to reflections. Concerning the latter aspect, the number of valid points obtained at $\xi = -0.25$ is above 80 % for each airfoil configuration. The remaining points are either interpolated in time or reconstructed (see Chapter 3.8).

For all the PSDs, the vortex-shedding frequency peak occurs at $St \approx 0.18$, in agreement with the far-field acoustic spectra presented in Chapter 4.4. This value is slightly higher (and, thereby, closer to the theoretical $St = 0.2$) than that measured by the hot-wire anemometer, most likely due to the larger exit area of the A-Tunnel nozzle and the consequent smaller blockage effect produced by the airfoils. Similar to what previously observed, the effect of porosity is confined to the low-St range of the velocity PSDs, with a frequency extent and amplitude that increase along with the Reynolds number. The presence of the permeable exoskeleton does not appear to alter the magnitude of the reduction in PSD$_{u_2'u_2'}$ near the vortex-shedding frequency peak but has an impact at lower Strouhal numbers, which correspond to larger turbulent structures. This trend is par-

ticularly visible at $Re_d = 2.7 \times 10^4$ (Figure 5.17a), for which the spectrum related to the porous case starts converging with that of the solid airfoil for $St < 0.03$, differently from the spectrum of the melamine configuration that remains constant. The present low-frequency deviation between porous and melamine case may partly explain the difference in the r.m.s. of the upwash velocity fluctuations observed in Figure 5.12.

5.5. OVERVIEW AND CONCLUDING REMARKS

An extensive experimental campaign is carried out with the solid, porous, and melamine NACA-0024 profiles in order to explore the flow-field alterations due to porosity. First, the velocity around the solid and porous airfoil is characterized by means of hot-wire anemometry for $Re_d = 4.1 \times 10^4$. The porous treatment is found to alter the boundary layer in the aft part of the wing profile by reducing the mean velocity and increasing the turbulence intensity near the surface, with an amplitude that grows along with the chordwise position. The present mechanism yields a widening of the jet opening that, in turn, leads to an increase in the drag force. However, no definitive explanation for the origin of the noise regeneration at high frequencies can be found from the analysis of the flow field around the airfoil.

The focus of the investigation is then put on the stagnation region near the leading edge with the purpose of examining the effect of the porosity on the distortion of the turbulent vortical structures interacting with the wing profiles. Specifically, from the acquisition of the mean wall-pressure distributions on their surface, it is observed that the porous treatment leads to a slight reduction in the flow displacement by the airfoil due to the possibility for the incident velocity to penetrate the inner volume. This phenomenon influences the potential effect of the airfoil and levels out the pressure differences along the surface. However, the C_p deviation between the two cases seems to be limited by the presence of the exoskeleton that preserves the integrity of the NACA-0024 profile's shape.

Furthermore, the trends of mean velocity and turbulence intensity along the stagnation streamline measured by the hot-wire anemometer are compared with the LES results. A method to relate the hot-wire data to the two turbulent-velocity components calculated by the numerical simulations is proposed based on the local mean-flow direction. Results show that the fluctuating-velocity field is significantly affected by the porosity when the stagnation region is being approached. In particular, the substantial increase in the r.m.s. of the upwash velocity fluctuations experienced by flow in the immediate vicinity of the solid airfoil leading edge is not observed in the porous case, resulting in an attenuation of the TKE in the stagnation region. The mean spanwise vorticity in the boundary layer around the wing profile is also found to be mitigated by the porous treatment. Besides, the analysis of the turbulent-velocity PSDs along the stagnation streamline and around the leading edge suggests that the melamine foam has an effect mainly at low frequencies on the large scale structures, with a spatial extent up to about two leading-edge radii from the stagnation point. In addition, the vortex-shedding frequency peak in the PSD of the streamwise velocity fluctuations close to the airfoil surface is found to be suppressed due to the porous treatment.

Subsequently, time-resolved PIV measurements are conducted to characterize the flow field around solid, porous, and melamine airfoils at $Re_d = 2.7 \times 10^4$, $Re_d = 4.1 \times 10^4$,

and $Re_d = 5.4 \times 10^4$. By doing so, the influence of the different free-stream velocities and the presence of exoskeleton and wire mesh can be evaluated. The effect of increasing Re_d of the incoming flow on the turbulent-velocity alterations is to extend the region where the velocity fluctuations are affected by porosity. Specifically, higher free-stream velocities lead to a more pronounced low-frequency reduction in the PSD of the turbulent upwash velocity and a wider St range in which this reduction occurs. Moreover, the presence of the permeable hard-plastic exoskeleton does not impact the alteration of the fluctuations of the streamwise velocity but appears to limit the mitigation of the upwash velocity ones in the low-frequency range of the upwash velocity PSD.

In view of the above, it can be concluded that the flow penetration through the pores of the melamine foam in the porous airfoil softens the distortion of the large turbulent eddies by the presence of the body. This may play a role in the leading-edge noise reduction, as supported by the results of the acoustic measurements presented in Chapter 4.4 that indicate that the most appreciable noise attenuation is achieved in correspondence with the vortex-shedding frequency peak. In addition, no notable difference in the noise emissions between porous and melamine airfoil configuration is found in this St-range, similar to what is observed for the upwash component of the turbulent velocity. This hypothesis for explaining the role of porosity in the turbulence-interaction noise mitigation has been already formed in the past, but, to the author's knowledge, no experimental evidence of it has ever been provided for a relatively thick airfoil. In Chapter 6, a theoretical model based on the RDT will be derived in order to improve the physical understanding of the turbulence-distortion alterations due to porosity.

REFERENCES

[1] R. Zamponi, D. Ragni, N. Van de Wyer, and C. Schram, *Experimental Investigation of Airfoil Turbulence-Impingement Noise Reduction Using Porous Treatment*, in *25th AIAA/CEAS Aeroacoustics Conference* (American Institute of Aeronautics and Astronautics, Delft, The Netherlands, 2019).

[2] R. Zamponi, S. Satcunanathan, S. Moreau, D. Ragni, M. Meinke, W. Schröder, and C. Schram, *On the role of turbulence distortion on leading-edge noise reduction by means of porosity*, Journal of Sound and Vibration **485**, 115561 (2020).

[3] S. Tamaro, R. Zamponi, D. Ragni, C. Teruna, and C. Schram, *Experimental investigation of turbulent coherent structures interacting with a porous airfoil*, Experiments in Fluids (2021), 10.1007/s00348-021-03170-2.

[4] E. Sarradj and T. Geyer, *Noise Generation by Porous Airfoils*, in *13th AIAA/CEAS Aeroacoustics Conference (28th AIAA Aeroacoustics Conference)* (American Institute of Aeronautics and Astronautics, Rome, Italy, 2007).

[5] T. Geyer, E. Sarradj, and C. Fritzsche, *Measurement of the noise generation at the trailing edge of porous airfoils*, Experiments in Fluids **48**, 291 (2010).

[6] T. Geyer, E. Sarradj, and C. Fritzsche, *Porous Airfoils: Noise Reduction and Boundary Layer Effects*, International Journal of Aeroacoustics **9**, 787 (2010).

[7] A. Rubio Carpio, R. Merino Martínez, F. Avallone, D. Ragni, M. Snellen, and S. van der Zwaag, *Experimental characterization of the turbulent boundary layer over a porous trailing edge for noise abatement,* Journal of Sound and Vibration **443**, 537 (2019).

[8] Y. Kametani, K. Fukagata, R. Örlü, and P. Schlatter, *Effect of uniform blowing/suction in a turbulent boundary layer at moderate Reynolds number,* International Journal of Heat and Fluid Flow **55**, 132 (2015).

[9] S. Satcunanathan, M. H. Meinke, and W. Schröder, *Prediction of Noise Mitigation by Porous Media based on a Direct-Hybrid CFD/CAA Method,* in *25th AIAA/CEAS Aeroacoustics Conference* (American Institute of Aeronautics and Astronautics, Delft, The Netherlands, 2019).

[10] J.-D. Vagt, *Hot-wire probes in low speed flow,* Progress in Aerospace Sciences **18**, 271 (1979).

[11] P. W. Bearman, *Some measurements of the distortion of turbulence approaching a two-dimensional bluff body,* Journal of Fluid Mechanics **53**, 451 (1972).

[12] G. K. Batchelor and I. Proudman, *The effect of rapid distortion of a fluid in turbulent motion,* The Quarterly Journal of Mechanics and Applied Mathematics **7**, 83 (1954).

[13] J. C. R. Hunt, *A theory of turbulent flow round two-dimensional bluff bodies,* Journal of Fluid Mechanics **61**, 625 (1973).

[14] R. E. Britter, J. C. R. Hunt, and J. C. Mumford, *The distortion of turbulence by a circular cylinder,* Journal of Fluid Mechanics **92**, 269 (1979).

[15] M. E. Goldstein and H. Atassi, *A complete second-order theory for the unsteady flow about an airfoil due to a periodic gust,* Journal of Fluid Mechanics **74**, 741 (1976).

[16] R. K. Amiet, *Acoustic radiation from an airfoil in a turbulent stream,* Journal of Sound and Vibration **41**, 407 (1975).

[17] L. D. de Santana, *Semi-analytical methodologies for airfoil noise prediction*, Ph.D. thesis, KU Leuven (2015).

[18] L. D. de Santana, J. Christophe, C. Schram, and W. Desmet, *A Rapid Distortion Theory modified turbulence spectra for semi-analytical airfoil noise prediction,* Journal of Sound and Vibration **383**, 349 (2016).

[19] E. Achenbach, *Vortex shedding from spheres,* Journal of Fluid Mechanics **62**, 209 (1974).

[20] J.-C. Giret, A. Sengissen, S. Moreau, M. Sanjose, and J.-C. Jouhaud, *Noise source analysis of a rod–airfoil configuration using unstructured large-eddy simulation,* AIAA Journal **53**, 1062 (2015).

[21] C. Zhang, M. Sanjose, and S. Moreau, *Turbulent flow and noise sources on a circular cylinder in the critical regime,* Advances **9**, 085009 1 (2019).

[22] N. V. C. Swamy, B. H. L. Gowda, and V. R. Lakshminath, *Auto-correlation measurements and integral time scales in three-dimensional turbulent boundary layers,* Applied Scientific Research **35**, 237 (1979).

[23] S. P. Sutera, P. F. Maeder, and J. Kestin, *On the sensitivity of heat transfer in the stagnation-point boundary layer to free-stream vorticity,* Journal of Fluid Mechanics **16**, 497 (1963).

6

EXTENSION OF THE RDT TO POROUS MATERIALS

In times of turbulence and rapid change,
you must constantly be re-evaluating yourself
relative to the new realities.

Brian Tracy

In this chapter, the distortion of homogeneous isotropic turbulence interacting with a porous cylinder is calculated by means of the RDT. The porous treatment, characterized by a constant static permeability, is modeled as a varying impedance boundary condition applied to the potential component of the velocity. The RDT implementation is first validated through comparisons with published velocity measurements in the stagnation region of an impermeable cylinder placed downstream of a turbulence grid. Subsequently, the impact of porosity on the velocity field is investigated through the analysis of the one-dimensional spectra at different locations near the body and the velocity variance along the stagnation streamline. The porous RDT is finally adapted to model the turbulence distortion in the vicinity of the leading edge of the porous NACA-0024 profile fitted with melamine foam.

Parts of this chapter are included in [1].

6.1. PROBLEM STATEMENT

The RDT, introduced in Chapter 2.3, describes the sudden changes in turbulence experienced by a turbulent flow impinging on a bluff body and has been applied by Hunt [2] for the case of a circular cylinder. The calculations of the turbulent flow for this application may be also considered to evaluate the distortion of turbulence as it approaches the leading edge of a wing profile. Indeed, in a region sufficiently close to the stagnation point, the inflow distortion produced by an airfoil is similar to that produced by a cylinder having the same radius as the leading-edge circle [3]. This makes it possible to use RDT to account for the effective geometry of the wing profile in semi-analytical noise prediction methods, like the theory of Amiet [4] (see Chapter 1.1.1). According to this model and with reference to Figure 6.1, the far-field acoustic PSD S_{pp} produced by a thin airfoil in a subsonic turbulent flow for a receiver located at $\mathbf{x} = (x, y, z)$ is given by

$$S_{pp}(\mathbf{x},\omega) = \left(\frac{\omega y \rho_0 b}{c_0 \sigma_0^2}\right) \pi U_\infty d \int_{-\infty}^{+\infty} \frac{\sin^2[(K_3 - k_3)d]}{(K_3 - k_3)^2} |\mathscr{L}(\mathbf{x}, K_1, k_3)|^2 \Psi_{22}(K_z, k_r)\, dk_3, \quad (6.1)$$

where $\sigma_0 = \sqrt{x^2 + \beta^2(y^2 + z^2)}$, $K_1 = \omega/U_\infty$, $K_3 = \omega z/(c_0\sigma_0)$, $\mathscr{L}$ is an aeroacosutic transfer function that relates the amplitude and phase of an incoming periodic gust to the respective unsteady-lift response [5], and Ψ_{22} is the upstream two-dimensional energy spectrum of the upwash turbulent-velocity component. A possible formulation to consider the effective geometry of the wing profile in the latter term is provided by Equation (2.65).

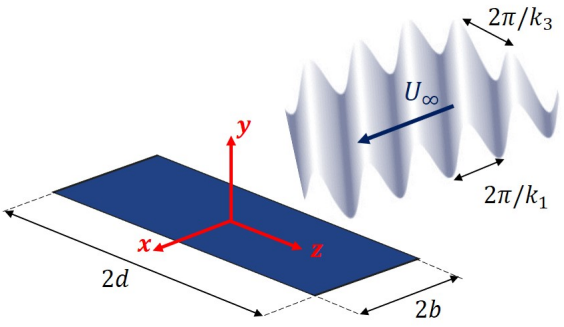

Figure 6.1: Coordinate system and notation considered in the Amiet's model, with a single skewed gust sweeping over a thin airfoil [4].

Such an approach was followed by Moreau and Roger [6], who formulated a semi-empirical RDT-based correction for taking into consideration the turbulence distortion occurring at the leading edge of a NACA-0012 profile. The results showed a better agreement between calculations and aeroacoustic far-field measurements. Christophe [7], De Santana [8], De Santana *et al.* [9], and Miotto *et al.* [10] implemented a similar correction to model Ψ_{22} as input to Amiet's theory by considering the asymptotic results for large-scale and small-scale turbulence and assuming the conservation of the variance of the velocity fluctuations. Likewise, the present methodology resulted in improved noise predictions compared with Amiet's original formulation.

In view of the above, the correction of the two-dimensional turbulence spectrum to account for porosity at the leading edge of the airfoil may lead to the development of novel semi-analytical methods for the prediction of the turbulence-interaction noise produced by porous wing profiles. The porous RDT model proposed in the manuscript has the potential to achieve this objective by providing a porosity-corrected turbulence spectrum. In the present work, the experimental investigation on the porous NACA-0024 profile described in Chapter 5.4 is considered as a test case for the theoretical model in order to explore this possibility. In particular, the RDT calculations will be compared with the one-dimensional spectra measured by the hot-wire anemometer near the airfoil leading edge in Chapter 6.3.4 in order to evaluate whether the analytical prediction provides an accurate description of the turbulence energy spectrum.

Finally, it is important to point out that porosity is expected to have an influence also on the airfoil unsteady-lift response and, thereby, on $\mathscr{L}$. The correction of this term for accounting for a porous treatment of the wing profile is not addressed in the present research project.

6.2. SOLUTION FOR A SOLID AND POROUS CYLINDER

The solution of the turbulent flow around a solid and porous cylinder is outlined following the approach of Hunt [2]. The derivations for the porous case are carried out assuming that the cylinder is characterized by a constant static permeability k_0.

6.2.1. POTENTIAL FLOW PAST A CIRCULAR CYLINDER

A cylindrical coordinate system (r, θ, z) is adopted, with $x = r\cos\theta$, $y = r\sin\theta$, and z being the spanwise direction (Figure 2.3). As mentioned in Chapter 2.3, these quantities are non-dimensionalized by the cylinder radius a. The standard potential flow solution for a circular cylinder, obtained by the solution of Equation (2.38) subjected to the boundary conditions in Equation (2.39), is represented by the following velocity potential Φ and streamfunction Ψ:

$$\Phi = \left(1 + \frac{1}{r^2}\right) r\cos\theta; \qquad \Psi = \left(1 - \frac{1}{r^2}\right) r\sin\theta. \tag{6.2}$$

Consequently, the mean-velocity components are

$$\begin{aligned} U_r &= \frac{\partial\Phi}{\partial r} = \frac{1}{r}\frac{\partial\Psi}{\partial\theta} = \left(1 - \frac{1}{r^2}\right)\cos\theta; \\ U_\theta &= \frac{1}{r}\frac{\partial\Phi}{\partial\theta} = -\frac{\partial\Psi}{\partial r} = -\left(1 + \frac{1}{r^2}\right)\sin\theta. \end{aligned} \tag{6.3}$$

The resulting flow pattern computed for an impermeable cylinder is depicted in Figure 6.2. While potential theory cannot account for the flow separation that occurs downstream of the cylinder for Reynolds numbers of practical interest, the present model however provides a fair description of the flow field over the region (E) of Figure 2.3, which is also the region of interest at an airfoil leading edge. In any case, the assumption that the flow remains attached over the whole domain is required to proceed with the mathematical treatment that is pursued below [2].

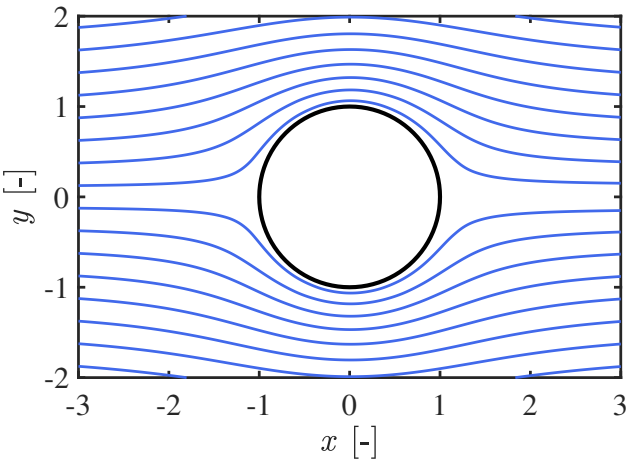

Figure 6.2: Pattern of the potential flow around a solid cylinder computed with the potential-flow solution.

A possible formulation to derive Δ_T as a function of Ψ has been proposed by Darwin [11], i.e.

$$\Delta_T(\theta,\Psi) = \frac{1}{\xi}\left\{\left(1-\frac{1}{2}\xi^2\right)\left[\mathrm{K}_L\left(\xi^2\right)-\mathrm{F}_L\left(\theta-\frac{\pi}{2},\xi^2\right)\right]-\left[\mathrm{E}_L\left(\xi^2\right)-\mathrm{E}_L\left(\theta-\frac{\pi}{2},\xi^2\right)\right]\right\}, \tag{6.4}$$

where

$$\xi^2 = \frac{4}{4+\Psi^2}. \tag{6.5}$$

$\mathrm{F}_L\left(\theta-\frac{\pi}{2},\xi^2\right)$ and $\mathrm{E}_L\left(\theta-\frac{\pi}{2},\xi^2\right)$ are the incomplete elliptic integrals of the first and second kind, respectively, while $\mathrm{K}_L\left(\xi^2\right)$ and $\mathrm{E}_L\left(\xi^2\right)$ are the complete elliptic integrals of the first and second kind, respectively. However, $\mathrm{K}_L\left(\xi^2\right)$ is not defined for $\xi^2=1$, which occurs at $\theta=0$ and $\theta=\pi$. As a consequence, Δ_T cannot be computed along the stagnation streamline, as is the case for $\Omega^\star$ in Equation (2.60). Hunt [2] tackled this problem by introducing the assumption that within a small angle $\delta\theta$ on either side of $\theta=\pi$, $\Omega^\star$ is a linear function of θ determined by its values at $\theta=\pi\pm\delta\theta$. The same procedure is also applied for $\theta=0$.

6.2.2. BOUNDARY CONDITIONS FOR A POROUS CYLINDER

When the circular cylinder is not impermeable, the incident velocity does not vanish at the surface and a substitute to Equation (2.39) must be found. The velocity potential of the irrotational mean flow around a porous cylinder characterized by a constant k_0 computed by Power *et al.* [12] is

$$\Phi_p = \left(1+\frac{1}{r^2}\right) r\cos\theta + K^\star\frac{1}{r^2}\cos 2\theta + O(K^{\star 2}), \tag{6.6}$$

where $K^\star$ is a dimensionless physical parameter linked to k_0 by the relation

$$K^\star = \frac{k_0 U_\infty}{\nu a}. \tag{6.7}$$

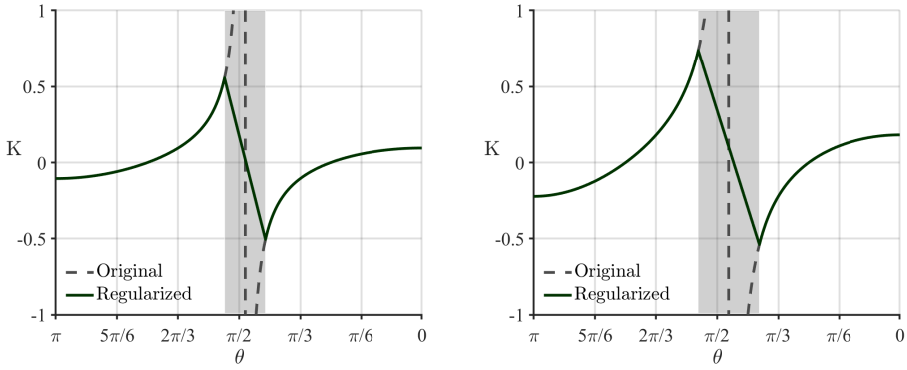

(a) $K^\star = 0.1$. (b) $K^\star = 0.2$.

Figure 6.3: Variation of K over θ for a porous cylinder for different values of normalized static permeability. The solid and the dashed lines indicate the original and the regularized K, respectively, while the gray areas denote the θ range at which the regularization procedure is applied.

If $K^\star$ is small, i.e. in the case of a low-permeability large cylinder immersed in a low-speed turbulent flow, Equation (6.6) may be simplified by neglecting the second-order terms and Φ_p is represented as a combination of the corresponding velocity potential for an impermeable body having the same geometry of the porous one and a term that is linearly proportional to $K^\star$. The radial and angular component of the velocity field are then computed as $U_r = \partial\Phi_p/\partial r$ and $U_\theta = \partial\Phi_p/r\partial\theta$:

$$\begin{aligned} U_r &= \left(1 - \frac{1}{r^2}\right)\cos\theta - 2K^\star\frac{1}{r^3}\cos 2\theta; \\ U_\theta &= -\left(1 + \frac{1}{r^2}\right)\sin\theta - 2K^\star\frac{1}{r^3}\sin 2\theta. \end{aligned} \tag{6.8}$$

Likewise, it is possible to derive an analogous formulation for the streamfunction from the integration of the velocity components, resulting in

$$\Psi_p = \left(1 - \frac{1}{r^2}\right) r\sin\theta - K^\star\frac{1}{r^2}\sin 2\theta. \tag{6.9}$$

Ψ_p can be used in Equation (6.4) to compute the drift function $\Delta_T\left(\theta, \Psi_p\right)$ and fluid particle deviation $\Delta_y = y + \Psi_p$ for the case of a porous cylinder.

The mean irrotational flow expressed by Equation (6.6) may also be produced by imposing a Neumann boundary condition at the surface, such as

$$\frac{\partial\Phi}{\partial r} = K\Phi \qquad \text{at} \quad r = 1 \qquad \text{with} \qquad K = -\frac{2K^\star\cos 2\theta}{2\cos\theta + K^\star\cos 2\theta}. \tag{6.10}$$

Equation (6.10) is equivalent to an impedance boundary condition, similar to the one Kisil and Ayton [13] suggested on flat plates, determined by a porous parameter K that smoothly varies over the cylinder surface. As a consequence, the Darcy's flow within

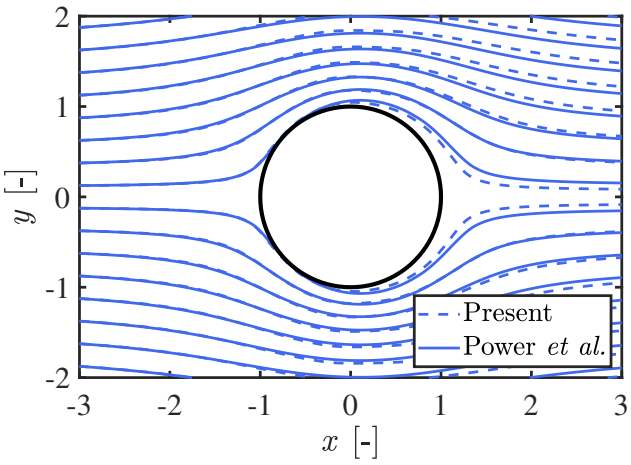

(a) $K^\star = 0.1$.

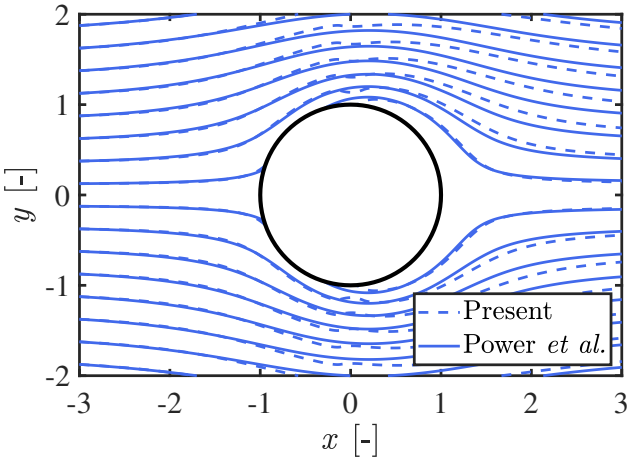

(b) $K^\star = 0.2$.

Figure 6.4: Pattern of the mean flow around a porous cylinder computed using an impedance boundary condition approach and following Power *et al.* [12] for different values of normalized static permeability.

the body is indirectly modeled. However, this expression exhibits a singular point at $\theta^\star = \arccos(-1/2K^\star + \sqrt{1+2K^{\star 2}}/2K^\star) \approx \pi/2$, for which the denominator is zero. The issue is overcome by a regularization procedure similar to that employed for $\Omega^\star$. In this case, the value of $\delta\theta$ depends on the static permeability of the cylinder: larger values of $K^\star$ lead to smaller $\theta^\star$ and to a broader range of angles θ where regularization is required. The strategy adopted in the present study is to determine $\delta\theta$ in order to maintain $K^\star > -0.5$. The results computed for $K^\star = 0.1$ and $K^\star = 0.2$, corresponding to $\delta\theta \approx \pi/18$ and $\delta\theta \approx \pi/12$, respectively, are shown in Figure 6.3, while the comparison between the two approaches for the evaluation of the mean-flow pattern is reported in Figure 6.4 and will be discussed in Chapter 6.3.1.

A proper boundary condition has to be applied to ϕ and $\boldsymbol{\psi}$ at the porous cylinder surface. For the former, the same approach as that followed in Equation (6.10) is adopted, yielding

$$\frac{\partial \phi}{\partial r} = u_{r\infty} + K\phi \qquad \text{at} \quad r = 1, \tag{6.11}$$

$u_{r\infty}$ being the radial component of the upstream velocity. For the latter, an assumption about the flow field inside the body is required. If the porous medium is homogeneous and the temperature variation is negligible, the internal flow may be represented as irrotational and be determined by the corresponding pressure related to the seepage velocity at the surface following Darcy's law [14]. This is a consequence of the averaging procedure performed over the flow within the porous medium and agrees with the analysis carried out by Power *et al.* [12]. Indeed, although the flow inside each pore is viscous and thus rotational, the local rotations average out to an irrotational global motion. Therefore, the vortical term of the turbulent velocity can be assumed to be negligible at the surface and the boundary condition in Equation (2.46) is employed also for the porous configuration. The present hypothesis is meant to be valid for wavenumbers of the turbulent flow significantly smaller than the spatial resolution associated with the effective pore diameter of the porous medium.

6.2.3. SOLUTION IN TERMS OF FOURIER SERIES

The expression of Equations (2.59) and (2.60) in cylindrical coordinates yields

$$\left[\frac{\partial^2}{\partial r^2} + \frac{1}{r}\frac{\partial}{\partial r} + \frac{1}{r^2}\frac{\partial^2}{\partial \theta^2} - \kappa_3^2\right]\beta_\mathrm{j} = 0 \tag{6.12}$$

and

$$\begin{cases} \left[\dfrac{\partial^2}{\partial r^2} + \dfrac{1}{r}\dfrac{\partial}{\partial r} + \dfrac{1}{r^2}\dfrac{\partial^2}{\partial \theta^2} - \dfrac{2}{r^2}\dfrac{\partial}{\partial \theta} - \left(\dfrac{1}{r^2} + \kappa_3^2\right)\right]\tilde{\alpha}_{1\mathrm{j}} = -\tilde{\Omega}_{1\mathrm{j}} \\ \left[\dfrac{\partial^2}{\partial r^2} + \dfrac{1}{r}\dfrac{\partial}{\partial r} + \dfrac{1}{r^2}\dfrac{\partial^2}{\partial \theta^2} - \dfrac{2}{r^2}\dfrac{\partial}{\partial \theta} - \left(\dfrac{1}{r^2} + \kappa_3^2\right)\right]\tilde{\alpha}_{2\mathrm{j}} = -\tilde{\Omega}_{2\mathrm{j}} \\ \left[\dfrac{\partial^2}{\partial r^2} + \dfrac{1}{r}\dfrac{\partial}{\partial r} + \dfrac{1}{r^2}\dfrac{\partial^2}{\partial \theta^2} - \kappa_3^2\right]\tilde{\alpha}_{3\mathrm{j}} = -\tilde{\Omega}_{3\mathrm{j}}, \end{cases} \tag{6.13}$$

where $\tilde{\alpha}$ is obtained by a rotation in Euclidean space and is defined as

$$\tilde{\alpha}_{1\mathrm{j}} = \alpha_{1\mathrm{j}}\cos\theta + \alpha_{2\mathrm{j}}\sin\theta; \quad \tilde{\alpha}_{2\mathrm{j}} = -\alpha_{1\mathrm{j}}\sin\theta + \alpha_{2\mathrm{j}}\cos\theta; \quad \tilde{\alpha}_{3\mathrm{j}} = \alpha_{3\mathrm{j}}, \tag{6.14}$$

while $\tilde{\Omega}$ is calculated from the distortion tensor in cylindrical coordinates:

$$\tilde{\Omega}_{\mathrm{ij}} = \left[\tilde{\gamma}_{\mathrm{ij}}\, e^{i(\kappa_1\Delta_t - \kappa_2\Delta_y)} - \tilde{\gamma}_{\infty,\mathrm{j}}\right] e^{ir(\kappa_1\cos\theta + \kappa_2\sin\theta)} \tag{6.15}$$

with

$$\tilde{\gamma}_{\mathrm{ij}} = \begin{bmatrix} U_r & \sin\theta - \partial\Delta_T/r\partial\theta & 0 \\ U_\theta & \cos\theta + \partial\Delta_T/\partial r & 0 \\ 0 & 0 & 1 \end{bmatrix}; \qquad \tilde{\gamma}_{\infty,\mathrm{ij}} = \begin{bmatrix} \cos\theta & \sin\theta & 0 \\ -\sin\theta & \cos\theta & 0 \\ 0 & 0 & 1 \end{bmatrix}. \tag{6.16}$$

The present expression for $\tilde{\gamma}_\infty$ represents the transpose of that reported by Hunt [2] in Equation (4.7) of his paper.

One possible way to solve Equations (6.12) and (6.13) is to avoid the dependence on θ and express $\boldsymbol{\beta}$, $\tilde{\alpha}$, and $\tilde{\Omega}$ as Fourier series [2]:

$$\begin{pmatrix} \beta_\mathrm{j} \\ \tilde{\alpha}_\mathrm{ij} \\ \tilde{\Omega}_\mathrm{ij} \end{pmatrix} = \sum_{n=0}^{\infty} \left\{ \begin{pmatrix} \beta_\mathrm{j}^{cn} \\ \alpha_\mathrm{ij}^{cn} \\ \Omega_\mathrm{ij}^{cn} \end{pmatrix} (r;\boldsymbol{\kappa}) \cos n\theta + \begin{pmatrix} \beta_\mathrm{j}^{sn} \\ \alpha_\mathrm{ij}^{sn} \\ \Omega_\mathrm{ij}^{sn} \end{pmatrix} (r;\boldsymbol{\kappa}) \sin n\theta \right\}. \tag{6.17}$$

The computation of the Fourier coefficients implies that the aforementioned variables are defined all over the domain and that the boundary conditions at the cylinder surface are valid for $0 \leq \theta \leq 2\pi$. This is made possible through the assumption of no-flow separation introduced in Chapter 6.2.1.

By substituting Equation (6.17) into Equation (6.12) and Equation (6.13), it follows that

$$\left\{ \frac{\partial^2}{\partial r^2} + \frac{1}{r}\frac{\partial}{\partial r} - \left(\frac{n^2}{r^2} + \kappa_3^2 \right) \right\} \begin{pmatrix} \beta_\mathrm{j}^{cn} \\ \beta_\mathrm{j}^{sn} \end{pmatrix} = 0 \tag{6.18}$$

and

$$\begin{cases} \left[\dfrac{\partial^2}{\partial r^2} + \dfrac{1}{r}\dfrac{\partial}{\partial r} - \dfrac{1}{r^2} - \left(\dfrac{n^2}{r^2} + \kappa_3^2 \right) \right] \begin{pmatrix} \alpha_\mathrm{1j}^{cn} \\ \alpha_\mathrm{1j}^{sn} \end{pmatrix} = - \begin{pmatrix} \Omega_\mathrm{1j}^{cn} \\ \Omega_\mathrm{1j}^{sn} \end{pmatrix} + \dfrac{2n}{r^2} \begin{pmatrix} \alpha_\mathrm{2j}^{sn} \\ -\alpha_\mathrm{2j}^{cn} \end{pmatrix} \\ \left[\dfrac{\partial^2}{\partial r^2} + \dfrac{1}{r}\dfrac{\partial}{\partial r} - \dfrac{1}{r^2} - \left(\dfrac{n^2}{r^2} + \kappa_3^2 \right) \right] \begin{pmatrix} \alpha_\mathrm{2j}^{cn} \\ \alpha_\mathrm{2j}^{sn} \end{pmatrix} = - \begin{pmatrix} \Omega_\mathrm{2j}^{cn} \\ \Omega_\mathrm{2j}^{sn} \end{pmatrix} - \dfrac{2n}{r^2} \begin{pmatrix} \alpha_\mathrm{1j}^{sn} \\ -\alpha_\mathrm{1j}^{cn} \end{pmatrix} \\ \left[\dfrac{\partial^2}{\partial r^2} + \dfrac{1}{r}\dfrac{\partial}{\partial r} - \left(\dfrac{n^2}{r^2} + \kappa_3^2 \right) \right] \begin{pmatrix} \alpha_\mathrm{3j}^{cn} \\ \alpha_\mathrm{3j}^{sn} \end{pmatrix} = - \begin{pmatrix} \Omega_\mathrm{3j}^{cn} \\ \Omega_\mathrm{3j}^{sn} \end{pmatrix} \end{cases}. \tag{6.19}$$

The boundary conditions need to be converted into equations for the Fourier coefficients of $\boldsymbol{\beta}$ and $\tilde{\alpha}$. For the former, it is possible to reformulate Equations (2.46) and (6.11) considering the outward-pointing normal to the cylinder surface $\boldsymbol{n} = (1,0,0)^\intercal$ as

$$\begin{aligned} &\textit{Solid cylinder:} && \frac{\partial \beta_\mathrm{j}}{\partial r} = (\cos\theta, \sin\theta, 0)^\intercal \, e^{i(\kappa_1 \cos\theta + \kappa_2 \sin\theta)} && \text{at} \quad r = 1; \\ &\textit{Porous cylinder:} && \frac{\partial \beta_\mathrm{j}}{\partial r} = (\cos\theta, \sin\theta, 0)^\intercal \, e^{i(\kappa_1 \cos\theta + \kappa_2 \sin\theta)} + K\beta_\mathrm{j} && \text{at} \quad r = 1, \end{aligned} \tag{6.20}$$

which yields

$$\begin{aligned} &\textit{Solid cylinder:} && \frac{\partial}{\partial r} \begin{pmatrix} \beta_\mathrm{j}^{cn} \\ \beta_\mathrm{j}^{sn} \end{pmatrix} = \begin{pmatrix} G_\mathrm{j}^{cn} \\ G_\mathrm{j}^{sn} \end{pmatrix} && \text{at} \quad r = 1; \\ &\textit{Porous cylinder:} && \frac{\partial}{\partial r} \begin{pmatrix} \beta_\mathrm{j}^{cn} \\ \beta_\mathrm{j}^{sn} \end{pmatrix} = \begin{pmatrix} G_\mathrm{j}^{cn} \\ G_\mathrm{j}^{sn} \end{pmatrix} + K_\theta \begin{pmatrix} \beta_\mathrm{j}^{cn} \\ \beta_\mathrm{j}^{sn} \end{pmatrix} && \text{at} \quad r = 1, \end{aligned} \tag{6.21}$$

where

$$\begin{pmatrix} G_\mathrm{j}^{cn} \\ G_\mathrm{j}^{sn} \end{pmatrix} = \frac{I}{2\pi} \int_0^{2\pi} \begin{pmatrix} \cos n\theta \\ \sin n\theta \end{pmatrix} (\cos\theta, \sin\theta, 0)^\intercal \, e^{i(\kappa_1 \cos\theta + \kappa_2 \sin\theta)} \, d\theta. \tag{6.22}$$

$I = 1$ if $n = 0$ and $I = 2$ if $n > 0$ as a consequence of the Fourier coefficients calculation. In this case, K_θ is the value of K corresponding to the angular position of interest, which must be defined *a priori*. Furthermore, as $r \to \infty$, Equation (2.47) implies that

$$\begin{pmatrix} \beta_{\mathrm{j}}^{cn} \\ \beta_{\mathrm{j}}^{sn} \end{pmatrix} \to 0. \tag{6.23}$$

For the latter, Equation (2.48) at $r = 1$ can be rewritten similar to the previous case as

$$\left[n \begin{pmatrix} \alpha_{3\mathrm{j}}^{sn} \\ -\alpha_{3\mathrm{j}}^{cn} \end{pmatrix} - i\kappa_3 \begin{pmatrix} \alpha_{2\mathrm{j}}^{cn} \\ -\alpha_{2\mathrm{j}}^{sn} \end{pmatrix} \right]_{r=1} = 0. \tag{6.24}$$

Likewise, Equation (2.49) for $x \to \infty$ leads to

$$\begin{cases} \dfrac{n}{r} \begin{pmatrix} \alpha_{3\mathrm{j}}^{sn} \\ -\alpha_{3\mathrm{j}}^{cn} \end{pmatrix} - i\kappa_3 \begin{pmatrix} \alpha_{2\mathrm{j}}^{cn} \\ \alpha_{2\mathrm{j}}^{sn} \end{pmatrix} = 0 \\ i\kappa_3 \begin{pmatrix} \alpha_{1\mathrm{j}}^{cn} \\ \alpha_{1\mathrm{j}}^{sn} \end{pmatrix} - \dfrac{\partial}{r} \begin{pmatrix} \alpha_{3\mathrm{j}}^{cn} \\ \alpha_{3\mathrm{j}}^{sn} \end{pmatrix} = 0 \\ \dfrac{1}{r}\dfrac{\partial}{r} \left\{ r \begin{pmatrix} \alpha_{2\mathrm{j}}^{cn} \\ -\alpha_{2\mathrm{j}}^{sn} \end{pmatrix} \right\} - \dfrac{n}{r} \begin{pmatrix} \alpha_{1\mathrm{j}}^{sn} \\ -\alpha_{1\mathrm{j}}^{cn} \end{pmatrix} = 0 \end{cases}, \tag{6.25}$$

while the application of the gauge condition (2.50) for $r = 1$ and as $x \to \infty$ yields

$$\frac{1}{r}\frac{\partial}{\partial r} \left\{ r \begin{pmatrix} \alpha_{1\mathrm{j}}^{cn} \\ \alpha_{1\mathrm{j}}^{sn} \end{pmatrix} \right\} + \frac{n}{r} \begin{pmatrix} \alpha_{2\mathrm{j}}^{sn} \\ -\alpha_{2\mathrm{j}}^{cn} \end{pmatrix} + i\kappa_3 \begin{pmatrix} \alpha_{3\mathrm{j}}^{cn} \\ \alpha_{3\mathrm{j}}^{sn} \end{pmatrix} = 0. \tag{6.26}$$

As discussed in Chapter 6.2.2, the present equations have to be satisfied for both cylinder configurations.

Equations (6.18) and (6.19) can be solved by means of the modified Bessel functions and the method of variation of parameters. The detailed derivations are reported in Appendix D. Once the different components of $\boldsymbol{\beta}$ and $\tilde{\alpha}$ are obtained, $\boldsymbol{M}$ is found in Cartesian coordinates. In this case, $\boldsymbol{\alpha}$ is computed from Equation (6.14) by inverting the rotation matrix.

6.2.4. TURBULENCE-DISTORTION MECHANISMS

A bluff body affects the incoming turbulent flow in two ways: (i) through the distortion of the vorticity field that alters the mean-velocity field both around and upstream of the body, and (ii) through the pressure exerted by the body, which blocks, partially or completely, the wall-normal turbulence velocity fluctuations. The influence of the vorticity distortion on the evolution of the velocity fluctuations is typically negligible if the integral length scale of the turbulent flow, L_x, is much larger than the characteristic dimension of the cylinder, a. In contrast, the body always exerts a reaction pressure field on the flow, regardless of the scales being considered. The present mechanism is evident for a flat plate, which is characterized by $L_x/a \to \infty$. In this extreme case, the vorticity

field is almost unaffected by the presence of the body and the only contribution to the alteration of the turbulent-velocity field comes from the second effect.

The Helmholtz decomposition expressed by Equation (2.43) is instrumental in investigating the two turbulence-distortion mechanisms. Indeed, the first effect is linked to the component $\nabla \times \boldsymbol{\psi}$ and mostly alters the velocities of small-scale eddies ($k \gg 1$), whereas the second one is associated with the component $\nabla\phi$ and mainly impacts the velocity of the large-scale eddies ($k \ll 1$). The same decomposition is applied to the velocity distortion tensor, which, from Equation (2.64), can be seen as the sum of (i) a term $\boldsymbol{M}^{(s)}$ that is related to the blocking of velocity fluctuations by the pressure of the body, (ii) a term $\boldsymbol{M}^{(d)}$ that depends on the distortion of vorticity by the mean flow, and (iii) a term $\boldsymbol{M}^{(\infty)}$ that is fully determined by the upstream conditions. In Chapter 6.3, the influence of porosity on the turbulence distortion will be analyzed in terms of these quantities.

6.2.5. COMPUTATIONAL METHODOLOGY

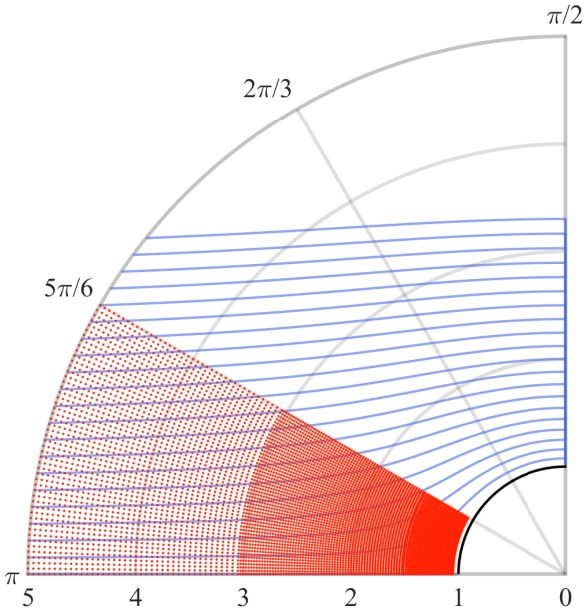

Figure 6.5: Domain for the computation of the velocity distortion tensor. The dots define the calculation locations, while the solid lines represent the mean-flow pattern for the case of a solid cylinder.

The distortion tensor $\boldsymbol{M}$ is calculated following the approach proposed by Hunt [2] but with a finer discretization of the calculation domain, which proved to yield a better accuracy. A total of 380 values of r from $r = 1.05$ to $r = 10$ and 50 angular positions from $\theta = 5\pi/6$ to $\theta = \pi$ are considered, with a resolution ranging from 0.01 near the stagnation point to 0.025 for $r > 3$ and 0.05 for $r > 5$ for the radial coordinate and a uniform resolution of about $\pi/300$ for the angular one. Therefore, the resulting grid consists of a total

of 16500 points and is depicted in Figure 6.5 for $0 < r < 5$.

The wavenumber domain used for the integration of $\boldsymbol{M}$ according to Equations (2.66) and (2.67) must be truncated in order to ensure that all wavenumber components can be adequately represented on the grid shown in Figure 6.5. The maximum value of the non-dimensional streamwise wavenumber κ_1 is set to 5. In addition, instabilities in the energy spectra occur when $\kappa_1, \kappa_2 > 1$ and $\kappa_3 \to 0$. Hence, $\boldsymbol{M}$ is only calculated for normalized wavenumbers greater than 0.001. Convergence tests showed that 25 values for each component are sufficient, leading to a total of 15625 points.

Solid	$r = 1.01$			$r = 3.60$		
$\kappa_1 = \kappa_2$	$(\Omega_{11}^{cn})_{\max}$	$n_{\max}$	λ_c	$(\Omega_{11}^{cn})_{\max}$	$n_{\max}$	λ_c
0.1	$-0.976 + 0.005\mathrm{i}$	1	3.25×10^5	$-0.072 + 0.022\mathrm{i}$	1	4.48×10^2
1.0	$-0.559 + 0.009\mathrm{i}$	1	1.82×10^4	$0.160 - 0.091\mathrm{i}$	3	1.04×10^2
3.0	$0.365 - 0.008\mathrm{i}$	1	2.68×10^3	$-0.214 + 0.071\mathrm{i}$	3	3.88×10^1
10	$0.001 + 0.290\mathrm{i}$	4	9.16×10^2	$0.232 + 0.070\mathrm{i}$	5	1.23×10^1

Porous	$r = 1.01$			$r = 3.60$		
$\kappa_1 = \kappa_2$	$(\Omega_{11}^{cn})_{\max}$	$n_{\max}$	λ_c	$(\Omega_{11}^{cn})_{\max}$	$n_{\max}$	λ_c
0.1	$-0.972 - 0.026\mathrm{i}$	1	4.44×10^3	$-0.072 + 0.020\mathrm{i}$	1	4.49×10^2
1.0	$-0.071 - 0.639\mathrm{i}$	2	3.49×10^2	$0.160 - 0.089\mathrm{i}$	3	1.04×10^2
3.0	$0.433 + 0.027\mathrm{i}$	1	2.98×10^2	$-0.212 + 0.076\mathrm{i}$	3	3.87×10^1
10	$0.300 + 0.018\mathrm{i}$	11	2.06×10^1	$0.240 + 0.053\mathrm{i}$	5	1.23×10^1

Table 6.1: Properties of the Fourier series of Ω_{11}^{cn} for a solid ($K^\star = 0$) and porous ($K^\star = 0.2$) cylinder. $(\Omega_{11}^{cn})_{\max}$ is the largest term of the series, $n_{\max}$ is the Fourier mode at which Ω_{11}^{cn} is maximum, and $\lambda_c = \left|(\Omega_{11}^{cn})_{\max}\right| / |\Omega_{11}^{c100}|$.

All the functions are calculated by means of routines implemented in MATLAB. The integrations are performed through the Simpson's rule, while the modified Bessel functions are computed by means of standard subroutines with a tolerance of the order of 2×10^{-16}. The Fourier series approach in Equation (6.17) requires $\boldsymbol{\Omega}$ to be estimated for $0 < \theta < \pi$ in order to determine Ω^{cn} and Ω^{sn}. The calculation is performed considering 1000 values of θ with regular spacings of $\pi/500$ and a $\delta\theta$ of $\pi/100$.

For the Fourier series decomposition, $n_{\max}$ is set to 100 in order to ensure an accurate reconstruction of the original function. The convergence is evaluated by estimating the ratio λ_c of the modulus of the largest Ω_{11}^{cn} in the series to the modulus of the last term. Values of λ_c, evaluated at $r = 1.01$ and $r = 3.6$ for different wavenumbers, are reported in Table 6.1 for $K^\star = 0$ (solid cylinder) and $K^\star = 0.2$ (porous cylinder). The table also shows the values of the largest Ω_{11}^{cn} and the value of n at which Ω_{11}^{cn} is maximum. The chosen locations and presented parameters allow for a direct comparison with the results listed in Table 3 of the original paper of Hunt [2].

Conclusions similar to those of Hunt can be drawn in this case. For both cylinders, λ_c decreases as the wavenumber increases as a consequence of the more rapid varia-

tions in Ω_{11}^{cn} occurring over smaller distances. Likewise, the convergence is slower for higher values of r due to the larger distance in the angular direction and leads to more significant inaccuracies in the reconstruction of the function. However, the values of λ_c are notably higher than those computed by Hunt [2] for every considered case and this justifies the choice of an increased n, especially for $\kappa_1 = \kappa_2 = 10$.

Moreover, the comparison with the porous case exhibits two different trends. At $r = 1.01$, the convergence for $K^\star = 0.2$ is considerably slower than that for the corresponding solid case due to the additional terms in the velocity components of Equation (6.8). Therefore, more Fourier series modes would be required to reach the same accuracy in the reconstruction of Ω_{11}^{cn} as in the case of $K^\star = 0$. Yet, at least one order of magnitude of difference is seen between $\left|\left(\Omega_{11}^{cn}\right)_{\max}\right|$ and $\left|\Omega_{11}^{c100}\right|$ in the most critical case at $\kappa_1 = \kappa_2 = 10$, allowing for a satisfactory convergence in the computation of the turbulent flow near the porous cylinder for high wavenumbers. At $r = 3.60$, the deviation between solid and porous cases is negligible, hinting at an effect of porosity localized in the proximity of the body surface. This trend is confirmed by the lines of constant Δ_T and by the results of the incident velocity spectra presented in Chapter 6.3.2.

6.2.6. ALGORITHM VALIDATION

The validation of the adopted methodology is carried out by comparing the RDT one-dimensional velocity spectra with the experimental results of Britter *et al.* [15], who performed velocity measurements on a circular cylinder placed downstream of square grids that produced approximately homogeneous isotropic turbulence with different length scales. The spectra are presented using the following scaling in order to avoid the dependence on the parameter L_x/a:

$$\hat{\boldsymbol{\Theta}}(x, y; \hat{\boldsymbol{\kappa}}) = \frac{a}{L_x}\boldsymbol{\Theta}(x, y; \boldsymbol{\kappa}); \qquad \hat{\boldsymbol{\kappa}} = \frac{L_x}{a}\boldsymbol{\kappa}. \tag{6.27}$$

With this notation, the transition between energy-containing eddies and inertial subrange occurs at $\hat{\kappa}_1 \approx 1$. Furthermore, it indicates that the lower the ratio of L_x/a that is considered is, the higher the maximum κ_1 that must be computed to have an accurate description of the velocity field will be. This provides a limitation on the turbulence scales calculated in the present analysis, which focuses on the case $L_x > a$. It is important to point out that $\hat{\kappa}_1$ corresponds to a normalized frequency made dimensionless by L_x and $\bar{u}_\infty$ throughout the flow. It effectively represents a convective wavenumber only in the undisturbed flow, whereas, near the cylinder, it would be considered as a true convective wavenumber if it were normalized with the local mean velocity.

The comparison between RDT calculations for an impermeable cylinder and data taken at $x = -4$ and $x = -1.2$ along the stagnation streamline is shown in Figure 6.6. These refer to three values of L_x/a, namely $L_x/a = 9.09$, $L_x/a = 2.86$, and $L_x/a = 1.56$. The results are supplemented by the expressions computed through the von Kármán model in Equation (2.68) that are meant to approximate the upstream spectra. The first observation is that the measured undisturbed RDT spectra at $x = -4$ almost coincide with the von Kármán model over the whole frequency range. This is related to the fact that in the considered wavenumber range $\boldsymbol{M}$ reduces to the identity matrix at a location sufficiently far from the cylinder surface.

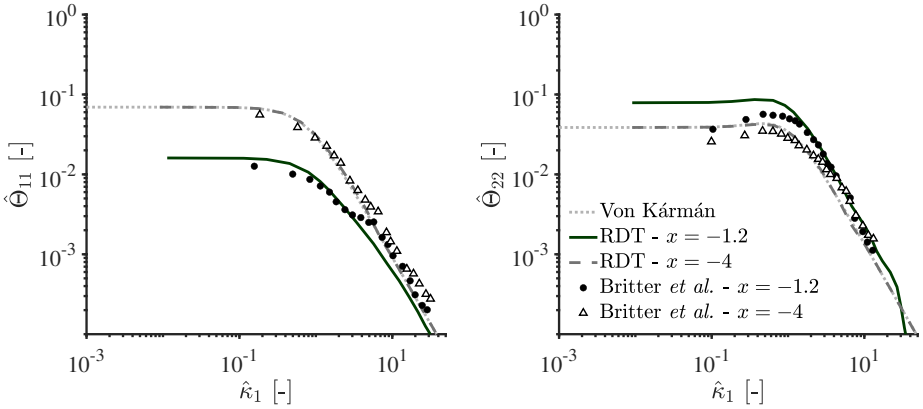

(a) $L_x/a = 9.09$.

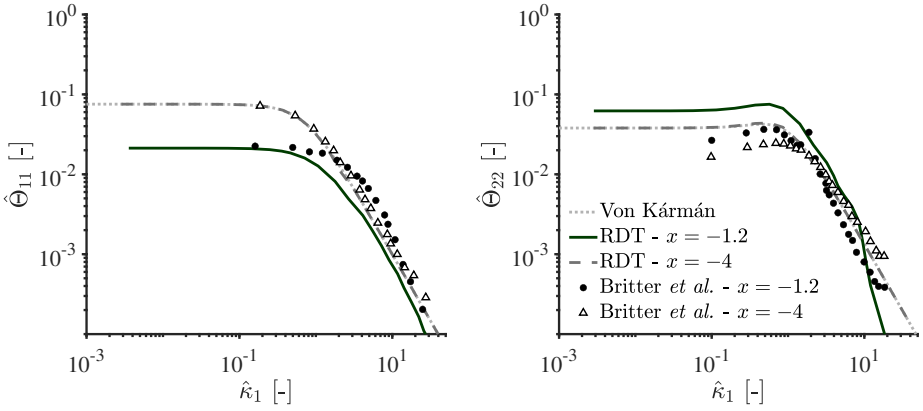

(b) $L_x/a = 2.86$.

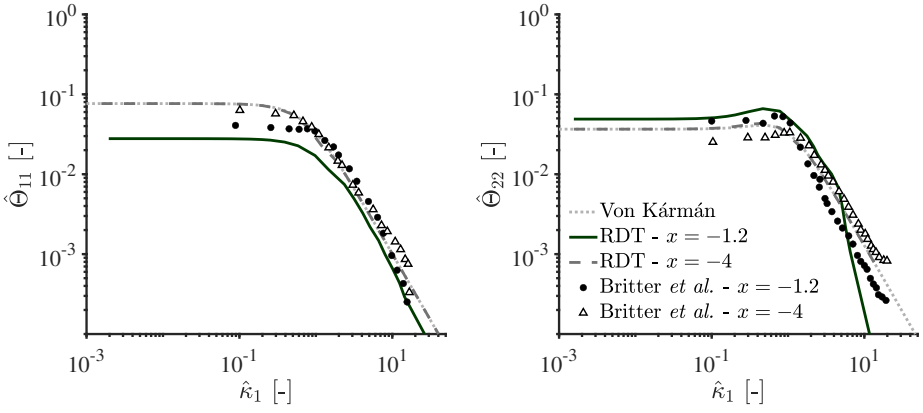

(c) $L_x/a = 1.56$.

Figure 6.6: Comparison among the RDT spectra of streamwise (on the left) and upwash (on the right) velocity components, the measurements of Britter *et al.* [15] at two locations along the stagnation streamline for different turbulence scales, and the von Kármán model. The velocity is normalized by u'_∞.

In the second place, while the agreement between experimental results and von Kármán model is satisfactory for the streamwise component everywhere, the spectra of the upwash velocity component exhibit a deviation in the low-frequency range. The present trend has been already pointed out by Britter *et al.* [15] and Jackson *et al.* [16] and is due to the finite ratio of the wind-tunnel width to the grid mesh size. However, the effect of the aspect ratio is mainly significant in the low-frequency range and the von Kármán model agrees with the measurements elsewhere.

Furthermore, at the most upstream location, the two velocity components exhibit opposite evolutions for all the considered values of L_x/a. The streamwise velocity decreases, whereas the upwash component increases. This is a consequence of the energy transfer that occurs between $\hat{\Theta}_{11}$ and $\hat{\Theta}_{22}$ due to the blocking effect of the impermeable body. The present trend is more pronounced for larger turbulence scales due to the dominance of this turbulence-distortion mechanism for $k \gg 1$.

Comparing the RDT calculations with the experimental results leads to interesting conclusions. For the streamwise velocity component, the agreement is generally better for larger values of L_x/a, with the distorted spectra that show a comparable $\Delta\hat{\Theta}_{11}$ with the upstream ones at lower $\hat{\kappa}_1$ and start converging at higher $\hat{\kappa}_1$. Yet, the overlapping occurs at lower frequencies for the experimental results than for the RDT prediction. The magnitude of this deviation increases with the decreasing value of L_x/a and can be attributed to the truncation of the wavenumber domain at $\boldsymbol{\kappa} = [5,5,5]$. This affects the integration in Equation (2.66) and yields an energy deficit in the disturbed spectra that modifies the slope with which they decay. Moreover, the deficit decreases for larger turbulence scales with respect to the lower ones since higher values of L_x/a correspond to augmented normalized frequencies according to Equation (6.27).

For the upwash velocity components, only a qualitative comparison can be carried out due to the effect of the wind-tunnel width. Likewise, the RDT calculations and the measurements feature analogous trends in terms of $\Delta\hat{\Theta}_{22}$ and frequency-dependence behavior, with a better correspondence for larger values of L_x/a. In this case, the spectra at $x = -1.2$ exhibit lower values than the upstream ones at higher frequencies and the trade-off point moves towards lower $\hat{\kappa}_1$ with the decreasing turbulence scale.

6.3. RDT RESULTS IN PRESENCE OF POROSITY

The results of the RDT calculations describing the turbulent flow around a solid and porous cylinder are presented by comparing the computations obtained with two values of the normalized static permeability (namely $K^\star = 0.1$ and $K^\star = 0.2$) with the impermeable configuration.

6.3.1. MEAN FLOW DEFLECTION

The porosity alters the mean-flow field near the cylinder surface due to the flow penetration. Figures 6.4a and 6.4b illustrate the mean-flow streamlines computed by the velocity potential of Equation (6.6) and by the impedance boundary condition in Equation (6.10) for $K^\star = 0.1$ and $K^\star = 0.2$, respectively. For both cases, the two approaches provide approximately the same flow pattern for $x < 0$, whereas increasing deviations occur for $x > 0$. In particular, the streamline closest to the body exhibits the most significant

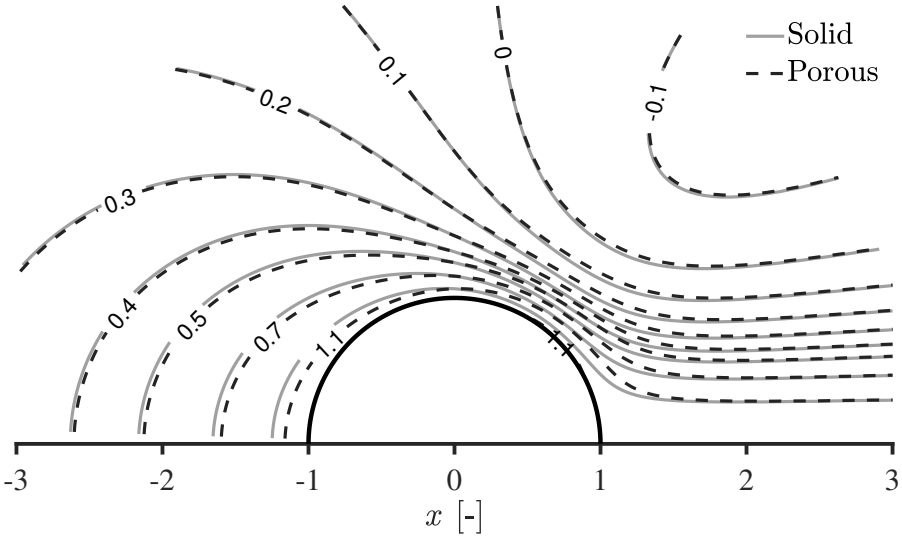

(a) $K^\star = 0.1$.

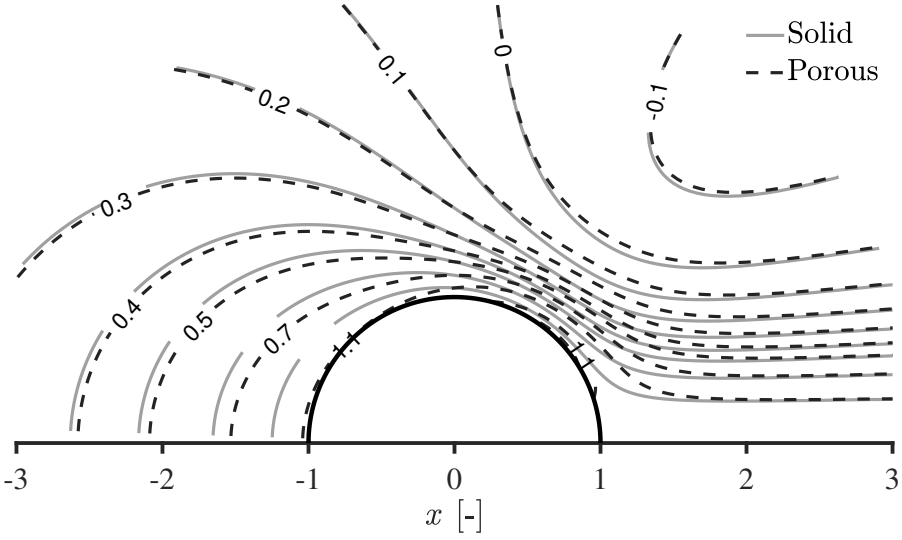

(b) $K^\star = 0.2$.

Figure 6.7: Lines of constant Δ_T for a solid ($K^\star = 0$) and porous cylinder characterized by different values of static permeability.

difference between the two methods, probably due to the limitations of the impedance boundary condition approach in effectively modeling the internal Darcy's flow in the rear part of the body. Moreover, the deviations increase with increasing $K^\star$ since the regularization procedure extends over a wider range of θ. In any case, the present region of interest is centered around the cylinder stagnation point, where the agreement

between the two methods is satisfactory.

The altered deflection of the mean flow in the presence of porosity has an impact on $\boldsymbol{\gamma}$ and, thereby, on $\boldsymbol{\omega}$. Indeed, the second term that appears in the mean-velocity field expressed by Equation (6.8) affects γ_{11} and γ_{21}, whereas the formulation of Δ_T for the porous case modifies γ_{12} and γ_{22}. This last aspect is made evident in Figures 6.7a and 6.7b, which display lines of constant Δ_T for a solid and porous cylinder with $K^\star = 0.1$ and $K^\star = 0.2$, respectively. In fact, the possibility of the incident velocity penetrating the inner volume leads to a reduction in the time taken for a fluid particle to reach a point in the vicinity of the body surface, which constitutes a reduced geometrical discontinuity with respect to a solid wall. The deviation in Δ_T is more evident in the proximity of the stagnation region and reflects the trend of K in Figure 6.3a that features a local minimum at $\theta = \pi$. As expected, the effect of porosity is more pronounced in terms of amplitude and extension in the case of $K^\star = 0.2$. In addition, the results for the solid cylinder closely reproduce those shown in Figure 4 in the original paper of Hunt [2] and validate the implementation of this function.

6.3.2. ONE-DIMENSIONAL SPECTRA

The modifications in the one-dimensional velocity spectra due to the presence of porosity exhibit two opposite trends. Figure 6.8 illustrates the spectra of the streamwise and upwash component of the turbulent velocity computed at $x = -1.1$ and $\theta = \pi$ (stagnation streamline) for $L_x/a = 9.09$, $L_x/a = 2.86$, and $L_x/a = 1.56$. These are compared with the undistorted spectra calculated at $x = -5$, which coincide for all the cylinder configurations. The velocity is made dimensionless by u'_∞, while the results are presented on a logarithmic scale in order to better visualize the deviations between solid and porous cases.

The influence of porosity is seen to take place close to the cylinder surface and is more significant for larger turbulence scales, as exemplified by the case $L_x/a = 9.09$. The decrease in the streamwise component (Figure 6.8a, on the left) is attenuated in the porous cases and the effect is mostly confined to low normalized frequencies. Similarly, the upwash component (Figure 6.8a, on the right) exhibits lower values in the same range. As expected, the deviation is higher for the case with the larger $K^\star$. However, at high normalized frequencies, the porous spectra start diverging from the solid one and this occurs at the intersection point with the undisturbed spectra. $K^\star$ does not affect the normalized frequency at which the deviation starts but alters the slope with which the spectra diverge from the solid configuration.

Similar conclusions can be drawn for $L_x/a = 2.86$, although, in this case, the impact of porosity is less pronounced in the low-frequency range for both streamwise (Figure 6.8b, on the left) and upwash (Figure 6.8b, on the right) velocity components. As already pointed out in Chapter 6.2.6, the amplification in $\hat{\Theta}_{22}$ due to the energy transfer is less than for larger turbulent scales, and this yields a shift of the above-mentioned intersection point towards lower normalized frequencies. Likewise, the slope gets closer to that of the undisturbed case for frequencies beyond the intersection point and the deviation is more significant for $K^\star = 0.2$ than for $K^\star = 0.1$. The trends discussed above about the effect of reducing the turbulence scales are still observed when further decreasing L_x/a from 2.86 to 1.56, as seen in Figure 6.8c.

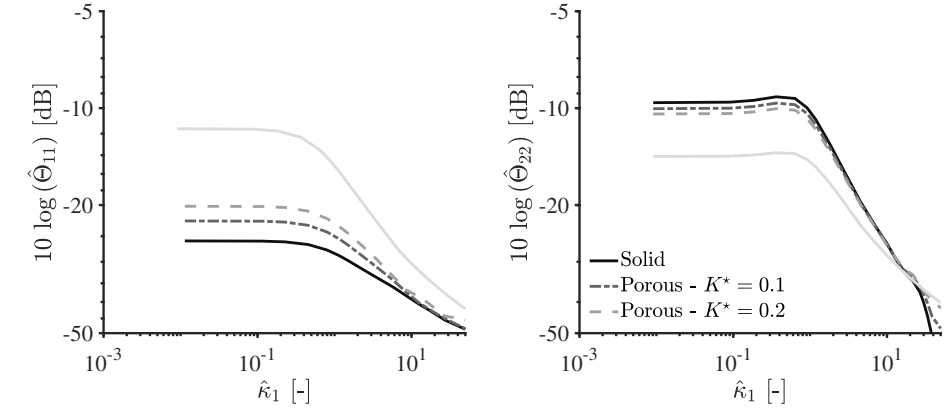

(a) $L_x/a = 9.09$.

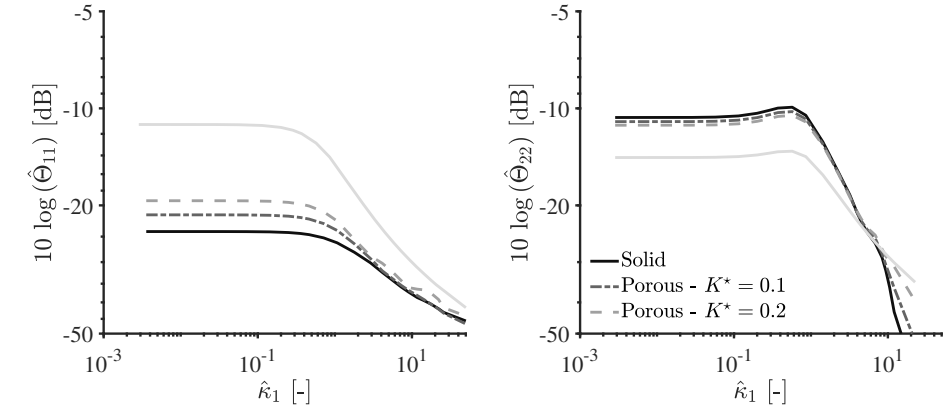

(b) $L_x/a = 2.86$.

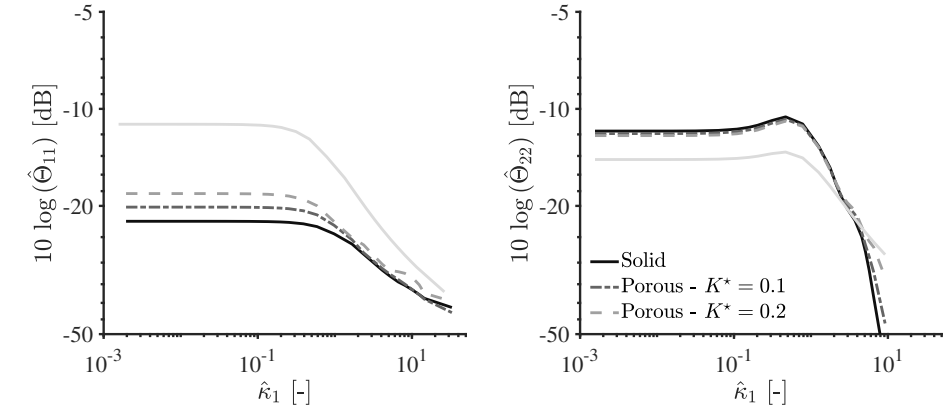

(c) $L_x/a = 1.56$.

Figure 6.8: Solid and porous ($K^\star = 0.1$ and 0.2) spectra of streamwise (on the left) and upwash (on the right) velocity components computed at $x = -1.1$ and $\theta = \pi$ for different turbulence scales. The undisturbed spectra are shown as opaque lines. The velocity is normalized by u'_∞.

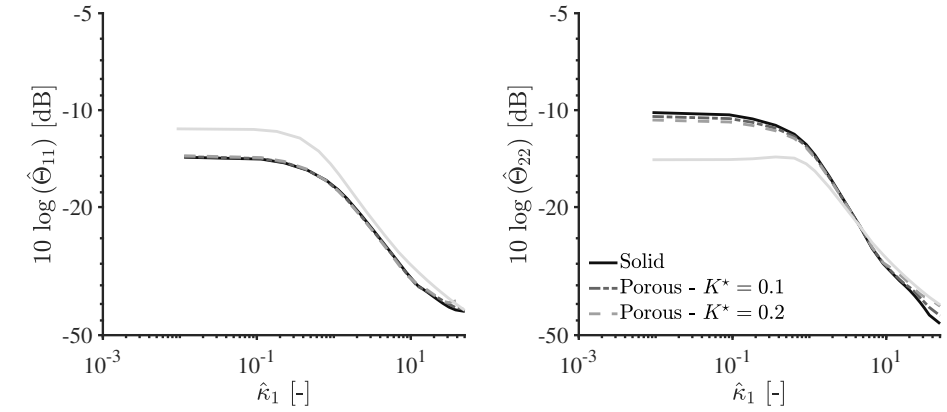

(a) $L_x/a = 9.09$.

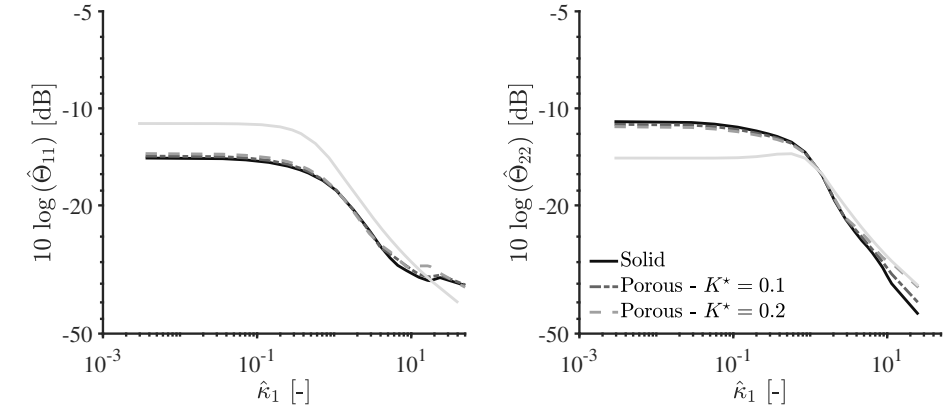

(b) $L_x/a = 2.86$.

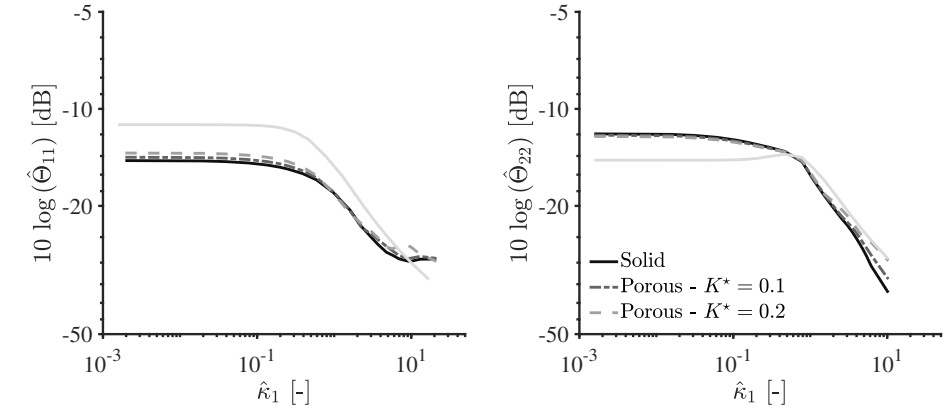

(c) $L_x/a = 1.56$.

Figure 6.9: Solid and porous ($K^\star = 0.1$ and 0.2) spectra of streamwise (on the left) and upwash (on the right) velocity components computed at $x = -1.1$ and $\theta = 5\pi/6$ for different turbulence scales. The undisturbed spectra are shown as opaque lines. The velocity is normalized by u'_∞.

Additional remarks can be made when the velocity spectra are evaluated at an angular position slightly away from the stagnation point. Figure 6.9 presents the results of the RDT calculations performed at $\theta = 5\pi/6$. The first observation is that the attenuation in $\hat{\Theta}_{11}$ from the upstream values is less than that at $\theta = \pi$, thereby mimicking the behavior of the mean streamwise velocity. The second observation is that the impact of porosity is reduced in the low-frequency range as a consequence of the trend of K illustrated in Figure 6.3, which features values of the dimensionless porous parameter closer to zero at $\theta = 5\pi/6$. Interestingly, while for the upwash velocity component the same conclusions as for the case at $\theta = \pi$ are drawn for the dependence of the energy attenuation on the turbulence scale, a different trend is observed for the streamwise component. Indeed, no substantial difference between solid and porous cases can be appreciated for $\hat{\Theta}_{11}$ at $L_x/a = 9.09$, whereas increasing deviations occur for $L_x/a = 2.86$ and $L_x/a = 1.56$. The third observation is that the high-frequency deviation for the upwash velocity spectra still occurs at the intersection point with the undisturbed ones but, notably, this phenomenon extends also to the streamwise velocity spectra, which start diverging from normalized frequencies that reduce with decreasing L_x/a. Likewise, the divergence is more pronounced for the larger value of $K^\star$.

The trends seen in Figures 6.8 and 6.9 may be analyzed in terms of the velocity distortion tensors $\boldsymbol{M}^{(\mathrm{d})}$ and $\boldsymbol{M}^{(\mathrm{s})}$. When the scale of the incoming turbulence is large compared with the characteristic length of the body, the possibility of the potential component of the incident velocity penetrating the cylinder's inner volume alters the blocking effect of the surface and affects $\boldsymbol{M}^{(\mathrm{s})}$. This phenomenon has an impact mostly on the low-frequency range of the spectra and results in a damping of the turbulence distortion and a reduction in the change of the streamwise and upwash velocity fluctuations near the stagnation point. When $L_x \approx a$ or, in general, at high normalized frequencies, the effect of the porosity on $\boldsymbol{M}^{(\mathrm{s})}$ is limited and does not yield a significant alteration in the turbulent velocity.

Nevertheless, the modification of the mean flow due to the porous surface indirectly modifies $\boldsymbol{M}^{(\mathrm{d})}$ and is responsible for the high-frequency deviation occurring in the one-dimensional spectra at the intersection point with the undisturbed spectra. This trend can be qualitatively explained by considering the evolution of a fluid line element approaching the cylinder along the stagnation streamline. As this is advected towards the body by the mean flow, its lengths $\mathrm{d}l_1$, $\mathrm{d}l_2$, and $\mathrm{d}l_3$ undergo a change and so do the different components of the vorticity associated with the element [2]. In particular, $\mathrm{d}l_1$ is compressed and $\mathrm{d}l_2$ is stretched due to the blockage effect of the obstacle, leading to an attenuation of ω_1 and an amplification of ω_2, respectively, whereas no modification in $\mathrm{d}l_3$ and, therefore, in ω_3 is expected[1]. The mitigation of ω_1 and the invariance of ω_3 will, in turn, induce a reduction in the upwash component of the turbulent velocity that is localized in the high-frequency range of the spectrum, as mentioned in Chapter 6.2.4. The present mechanism is weakened for the case of a porous cylinder and the decrease in Θ_{22} is lesser than that for the solid configuration. This is at the basis of the high-frequency deviation in the one-dimensional spectra.

Figure 6.10 illustrates those effects through the evolution of $|M_{11}^{(\mathrm{s})}|$, $|M_{11}^{(\mathrm{d})}|$, $|M_{22}^{(\mathrm{s})}|$, and

[1] The vorticity field is solenoidal, i.e. $\nabla \cdot \boldsymbol{\omega} = 0$: a compression of the fluid element in one direction results in an increase in $\boldsymbol{\omega}$ in the other directions.

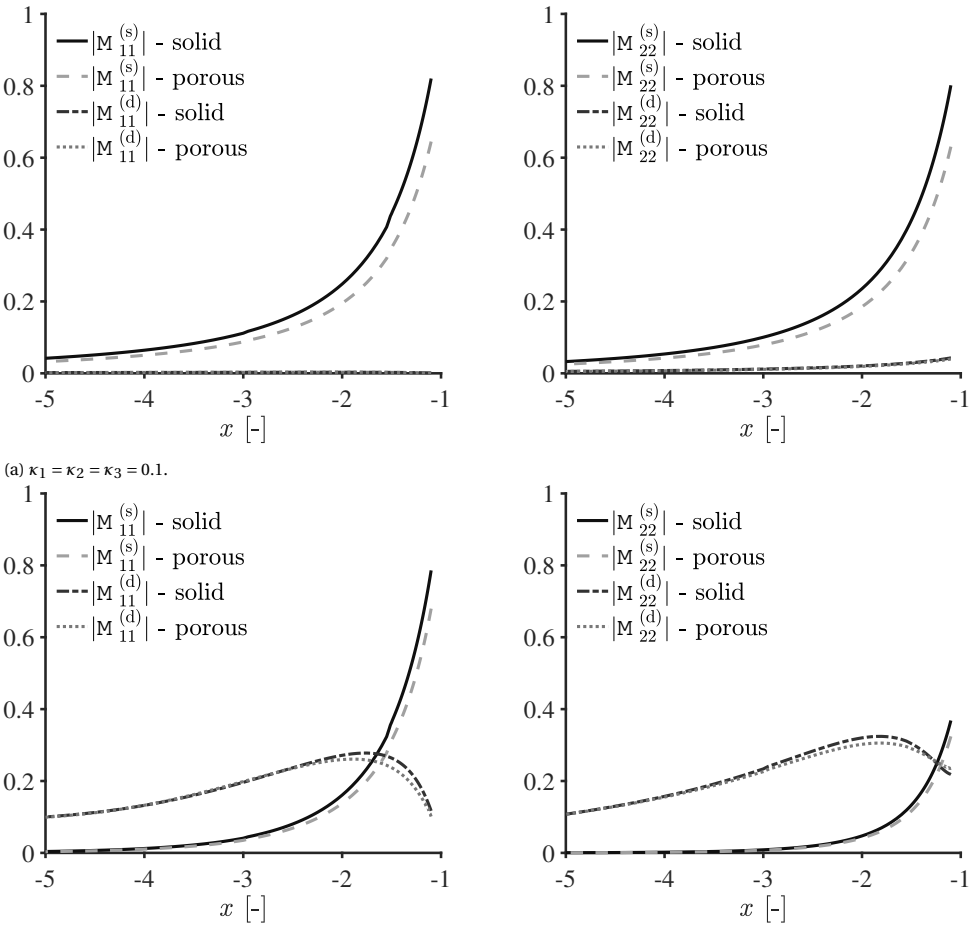

(a) $\kappa_1 = \kappa_2 = \kappa_3 = 0.1$.

(b) $\kappa_1 = \kappa_2 = \kappa_3 = 1$.

Figure 6.10: Evolution of the different components of $\boldsymbol{M}$ along the stagnation streamline computed for different wavenumbers and for a solid ($K^\star = 0$) and porous ($K^\star = 0.2$) cylinder.

$|M_{22}^{(d)}|$ along the stagnation streamline for a solid and porous cylinder characterized by $K^\star = 0.2$. Two different wavenumber vectors are computed in this case: $\boldsymbol{\kappa}$ = [0.1,0.1,0.1] and $\boldsymbol{\kappa}$ = [1,1,1]. For the former (Figure 6.10a), the distortion generated by $\boldsymbol{M}^{(d)}$ can be considered negligible and the porous surface has a substantial influence on $\boldsymbol{M}^{(s)}$, the magnitude of which is reduced in absolute terms. For the latter (Figure 6.10b), the two turbulence-distortion mechanisms feature comparable values near the body and the porosity alters both $\boldsymbol{M}^{(s)}$ (yet, with less impact than for the lowest wavenumber amplitude) and $\boldsymbol{M}^{(d)}$.

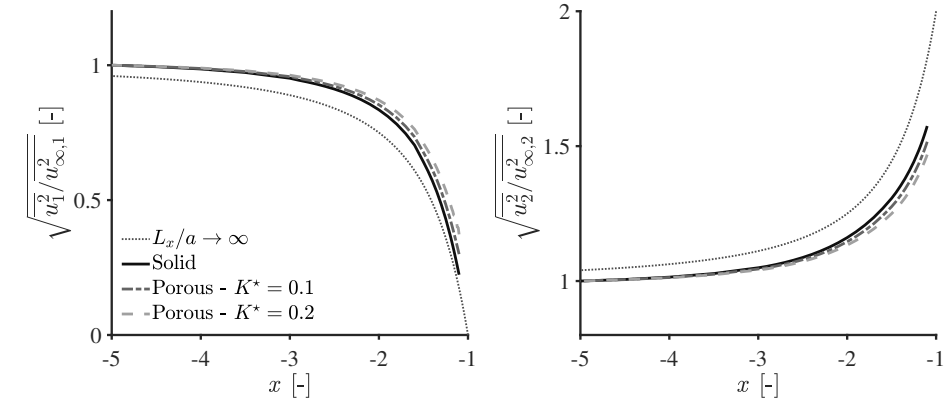

(a) $L_x/a = 9.09$.

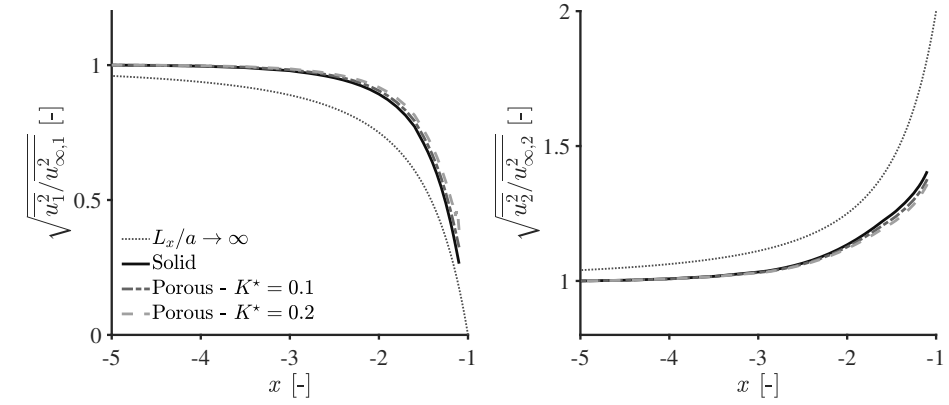

(b) $L_x/a = 2.86$.

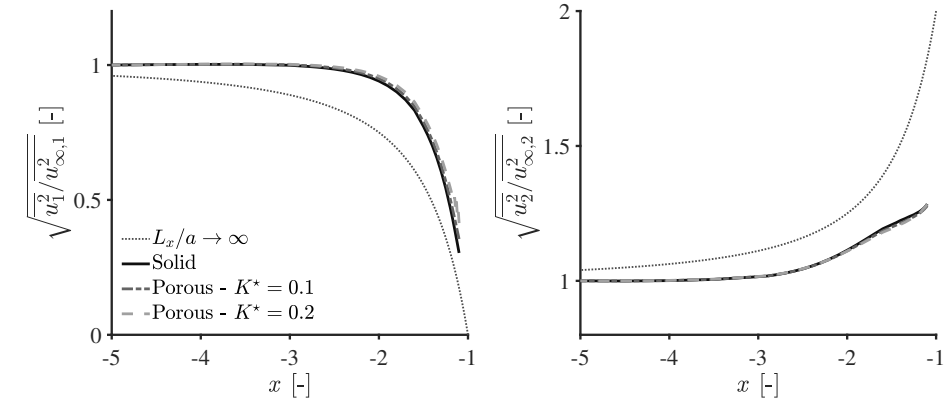

(c) $L_x/a = 1.56$.

Figure 6.11: Solid and porous ($K^\star = 0.1$ and 0.2) variances of streamwise (on the left) and upwash (on the right) velocity components computed along the stagnation streamline for different turbulence scales, and normalized by their upstream values. The asymptotic case for $L_x/a \to \infty$ is also reported.

6.3.3. VARIANCE ALONG THE STAGNATION STREAMLINE

The integration of the turbulent-velocity spectra of Figure 6.8 at each position of the domain along the stagnation streamline allows for the evaluation of the variance of the turbulent-velocity components. Figure 6.11 illustrates the square root of the normalized variance of the streamwise and the upwash turbulent-velocity components for the solid and the porous cylinders computed for different values of L_x/a. In addition, the asymptotic limit for $L_x/a \to \infty$ is plotted. Indeed, a closed-form expression of the RDT for this case describing the fluctuating-velocity field around the body can be derived given the mean-velocity field and its rate of change due to small alterations in the direction of the incident flow. Following Bearman [17], the r.m.s. of the turbulent-velocity components are then given by

$$\begin{cases} \sqrt{\overline{u_1^2}} = M_{11}^{(0)} \sqrt{\overline{u_{\infty,1}^2}} + M_{12}^{(0)} \sqrt{\overline{u_{\infty,2}^2}} \\ \sqrt{\overline{u^2}} = M_{21}^{(0)} \sqrt{\overline{u_{\infty,1}^2}} + M_{22}^{(0)} \sqrt{\overline{u_{\infty,2}^2}} \end{cases} \tag{6.28}$$

with

$$M_{ij}^{(0)} = \begin{bmatrix} 1 - \frac{x^2-y^2}{(x^2+y^2)^2} & \frac{2xy}{(x^2+y^2)^2} \\ \frac{-2xy}{(x^2+y^2)^2} & 1 + \frac{x^2-y^2}{(x^2+y^2)^2} \end{bmatrix}. \tag{6.29}$$

Along the stagnation streamline, Equations (6.28) and (6.29) reduce to

$$\sqrt{\frac{\overline{u_1^2}}{u_{\infty,1}^2}} = \left(1 - \frac{1}{x^2}\right); \qquad \sqrt{\frac{\overline{u_2^2}}{u_{\infty,2}^2}} = \left(1 + \frac{1}{x^2}\right). \tag{6.30}$$

The normalized variances for $L_x/a = 9.09$ (Figure 6.11a) are effectively approximated by the asymptotic analysis for every configuration. Yet, the porous cases exhibit increasingly higher values in the streamwise component and increasingly lower values in the upwash component when the stagnation point is approached, reflecting the trend observed in the one-dimensional spectra in Chapter 6.3.2. In particular, the maximum deviation in $\overline{u_1^2}$ between solid and porous configurations occurs at the location nearest to the cylinder and amounts to approximately 7.5 % for $K^\star = 0.1$ and 15 % for $K^\star = 0.2$, whereas that in $\overline{u_2^2}$ amounts to approximately 5 % for $K^\star = 0.1$ and 10 % for $K^\star = 0.2$.

Furthermore, the reduction in the upwash velocity component is a result of the partial compensation between low-frequency decrease and high-frequency increase due to the porosity illustrated in Figures 6.8 and 6.9. This, in turn, can potentially trigger mitigation of the turbulence-interaction noise mechanism, as will be shown in the NACA-0024 airfoil case described in Chapter 6.3.4.

At $L_x/a = 2.86$ (Figure 6.11b), the normalized variances deviate farther away from the asymptotic behavior, while the effect of the porosity is reduced. Indeed, the maximum deviation in $\overline{u_1^2}$ decreases to about 6 % and 12.5 % for $K^\star = 0.1$ and $K^\star = 0.2$, respectively, whereas that in $\overline{u_2^2}$ decreases to about 3 % and 5.5 % for $K^\star = 0.1$ and 0.2, respectively. The present trend is further accentuated at $L_x/a = 1.56$ (Figure 6.11c), for which the streamwise velocity component remains unaltered up to $x = -2$ and then drops to zero in the vicinity of the cylinder surface. Only marginal differences can be observed between solid

and both porous configurations in this case, amounting to approximately 5 % and 10 % for $K^\star = 0.1$ and $K^\star = 0.2$, respectively.

Conversely, the normalized variances of the upwash velocity component almost coincide for all the considered cases as a result of the compensation between the two opposite turbulence-distortion mechanisms that occur when $L_x \approx a$. Moreover, the decreased amplification in the one-dimensional spectra for the solid configuration, already discussed in Chapter 6.3.2, is reflected in lower $\overline{u_2^2}$ near the cylinder surface. This is in agreement with the asymptotic analysis for small-scale turbulence [2, 17, 18], which shows that for $L_x \ll a$ the upwash component of the turbulent velocity undergoes reduction when the stagnation point is approached due to the fast *pile-up* of vortex lines of opposite signs occurring at high wavenumbers.

6.3.4. APPLICATION CASE: POROUS NACA-0024 AIRFOIL

The modeling of the porous NACA-0024 profile case is based on the design introduced in Chapter 3.3 that is considered for the integration of the melamine foam in its inner volume. As seen in Chapter 5.4, the presence of the permeable exoskeleton allows for an alteration of the velocity fluctuations and has a limited impact on the mean-velocity field in the stagnation region, preserving the potential effect of the body. This makes it possible to model the porous airfoil by imposing the same deviation in mean flow produced by the solid configuration and applying the impedance boundary condition (6.11). In this case, the porous parameter is tuned considering (i) the static permeability of the melamine foam, $k_0 = 1.410 \times 10^{-9}\,\mathrm{m}^2$ (see Chapter 3.4), which is assumed to be homogeneous, (ii) the leading-edge radius, $a = r_{LE} = 0.01\,\mathrm{m}$, and (iii) the mean-flow speed downstream of the cylindrical rod, $U_\infty = 23\,\mathrm{m\,s}^{-1}$, resulting in $K^\star \approx 0.22$ (see Figure 5.5a). This value still makes it possible to neglect the higher-order terms in Equation (6.11).

Figure 6.12 depicts the one-dimensional spectra of the upwash velocity component computed at $x = -1.05$ for $L_x/a = 4.2$ (see Chapter 5.4). These are compared with the power spectra for the solid and the porous airfoil configuration of Figure 5.13d. Indeed, at this location near the surface, the fluctuations of the upwash velocity dominate over those of the streamwise velocity and the hot-wire probe is sensitive only to the former component. The spectra exhibit a relative agreement with the measurements in the frequency range at which the porosity has an impact, highlighting the key role played by the altered blocking effect of the porous airfoil in the low-frequency mitigation of $\hat{\Theta}_{22}$. A reduction of approximately 1.5 dB can be observed up to about the transition between energy-containing eddies and inertial subrange at $\hat{\kappa}_1 \approx 1$ in the RDT calculations. Beyond this wavenumber, the solid and porous spectra start gradually converging and the influence of porosity on the flow field diminishes.

The experimental results feature the same trend and the same $\Delta\hat{\Theta}_{22}$ at low normalized frequencies, although the turbulence downstream of the rod does not meet the condition of homogeneity and isotropy assumed by the theory. This suggests that the relative alterations in turbulence distortion due to porosity are independent of the nature of the upstream flow. However, deviations occur in correspondence with the frequency peak related to the vortex shedding in the wake of the upstream circular rod, which is not modeled in the present case. Interestingly, the reduction in $\hat{\Theta}_{22}$ around the afore-

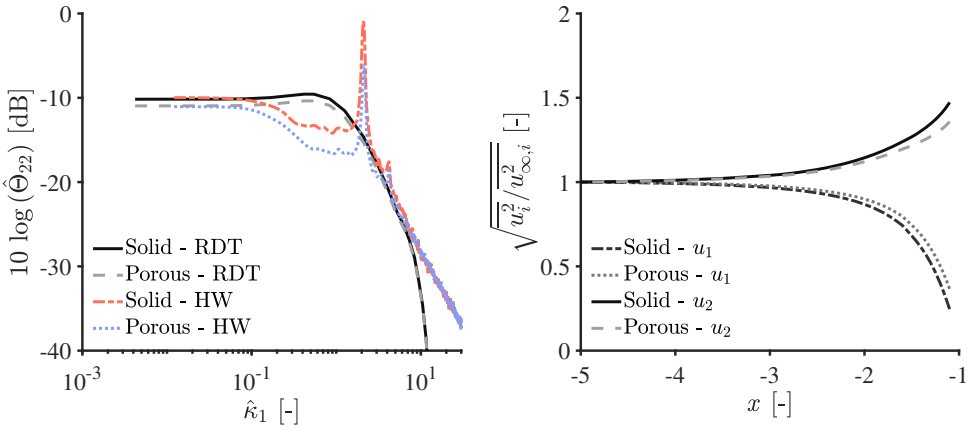

Figure 6.12: On the left, the solid and porous ($K^\star = 0.22$) spectra of the upwash velocity component computed at $x = -1.05$ for $L_x/a = 4.2$. The RDT calculations are compared with the hot-wire anemometry measurements presented in Figure 5.13d. On the right, the solid and porous ($K^\star = 0.22$) normalized variances of the streamwise and upwash velocity components computed along the stagnation streamline for $L_x/a = 4.2$.

mentioned peak is more pronounced in the measurements, probably due to the better hydrodynamic absorption of the large turbulent eddies shed by the circular rod. Since the vortex shedding mostly affects the upwash turbulent-velocity component, a better agreement is expected for the streamwise component in general. In addition, the RDT calculations approximate well the experimental results in the inertial subrange but exhibit an underprediction at high normalized frequencies. This could be related to the truncation of the wavenumber domain that has already been addressed in Chapter 6.2.6. An extension of the computed wavenumber range would most likely lead to a more accurate description of the turbulent-velocity field in this region. Moreover, the presence of the exoskeleton is expected to have an effect also at lower normalized frequencies, as suggested by the PIV measurements in Chapter 5.4, that is not accounted for in the model.

Figure 6.12 also illustrates the variance of turbulent velocities computed along the stagnation streamline for both solid and porous cylinder configurations. Trends analogous to the case $L_x/a = 9.09$ can be observed in this instance, even though the mitigation of the velocity fluctuations is stronger than the one that would be present without the exoskeleton due to the absence of the high-frequency amplification previously discussed. In particular, both an increase in $\overline{u_1^2}$ and decrease in $\overline{u_2^2}$ amount to approximately 12 %. Likewise, the predictions qualitatively agree with the conclusions drawn by the investigation of the measured turbulent-velocity fluctuations (Figure 5.5b) and of the LES (Figures 5.8). Nevertheless, the porous RDT model described in this work is not suitable for providing a quantitative estimation of the evolution of the r.m.s. of the velocity fluctuations along the stagnation streamline in the case of a wing profile. Indeed, the potential flow around a circular cylinder starts to increasingly differ from that around the airfoil moving away from the leading edge and the inflow distortion is no longer representative of the considered test case. The use of the actual potential solution for the wing profile

could possibly tackle this problem. In addition, the inhomogeneity and anisotropy of the incoming turbulence given by the presence of the vortex shedding are believed to alter the variation of the variances from their upstream values.

6.4. OVERVIEW AND CONCLUDING REMARKS

Detailed RDT calculations are performed to predict the distortion of the homogeneous isotropic turbulent flow approaching a porous cylinder characterized by a constant static permeability. The porous treatment is modeled as an impedance boundary condition applied to the potential component of the velocity and linked to the physical static permeability of the material. Two distortion mechanisms are addressed: the blocking of turbulent fluctuations by the pressure of the body and the distortion of the vorticity field by the mean flow. The RDT implementation is validated by comparing the results computed for an impermeable cylinder with published turbulence-distortion measurements taken at different locations along the stagnation streamline. Three ratios of the turbulence streamwise integral length scale L_x to the cylinder radius a are investigated under the condition $L_x/a > 1$.

One-dimensional spectra at two polar locations close to the surface and normalized variances of the streamwise and upwash velocity components along the stagnation streamline are computed for solid and porous cylinder configurations. Two values of static permeability are considered in order to analyze the influence of this parameter. The results show that the porosity affects the incoming turbulence distortion near the stagnation point in two ways. First, it reduces the blocking effect of the body, which leads to an attenuation of the transfer of energy from the streamwise to the upwash components at low normalized frequencies. Second, the vorticity deformation by the altered mean flow results in an amplification of the upwash velocity component at high normalized frequencies. As expected, the impact of porosity increases with its static permeability, resulting in a stronger low-frequency attenuation and a more significant high-frequency deviation. Moreover, the former effect is more pronounced for large turbulence scales, while the latter concerns the smaller ones. This influences the evolution of the fluctuating velocity components along the stagnation streamline. In particular, for $L_x \gg a$, the variation in the turbulent-velocity fluctuations turns out to be dampened moving towards the stagnation point as a consequence of the dominance of the blocking effect over the vorticity field distortion. Conversely, for $L_x \approx a$, the two effects approximately compensate each other, resulting in no notable difference between the different configurations. Furthermore, at angular positions slightly away from the stagnation point, the penetration of the flow into the inner volume of the cylinder decreases due to the lower mean pressure exerted by the surface, which further reduces the effect of porosity.

Finally, the porous RDT model is employed to analyze the distortion of turbulence as it approaches the stagnation region of the porous NACA-0024 profile immersed in the turbulent wake shed by the upstream circular rod. The model is based on the conclusions drawn from the experimental campaign and considers the static permeability of the melamine foam, the upstream mean velocity and the streamwise integral length scale measured by the hot-wire anemometer, and the assumption that the potential effect of the solid airfoil in the stagnation region is preserved in the porous case due to the

presence of the exoskeleton. The analytical predictions are shown to be in satisfactory relative agreement with the velocity measurements, although the vortex shedding is not accounted for in the prediction. The frequency range at which the porosity has an impact on the velocity fluctuations appears to be independent of the homogeneity and the isotropy of the incoming turbulence. Moreover, the assumed conservation of the potential effect of the airfoil ensured by the presence of the permeable exoskeleton yields more efficient damping of the turbulent-velocity variation in the stagnation region due to the absence of the high-frequency deviation in the one-dimensional spectra. Nonetheless, this component is expected to have an influence on the turbulent-velocity spectrum also at lower normalized frequencies, as suggested by the PIV measurements. The present aspect is not taken into consideration in the theory.

The results detailed above support a scenario in which the damping of the distortion of incoming turbulence is a plausible explanation for the noise reduction that is observed experimentally and from scale-resolved simulations. Indeed, it appears that an attenuation of the incoming turbulence distortion leads to a smaller variation of the inertia of the turbulent structures interacting with the airfoil and, thereby, to a less efficient conversion of their kinetic energy into sound waves. The present evidence is in line with the outcome of the acoustic far-field measurements outlined in Chapter 4.4 and reported in Figure 4.19, which feature a noise-abatement trend similar to the one with which $\hat{\Theta}_{22}$ is reduced by porosity. Specifically, the most appreciable decrease occurs at low normalized frequencies, while the spectra gradually converge with increasing $\hat{\kappa}_1$.

In addition, the possibility of reducing the high-frequency amplification shown in this analysis for the case $L_x/a > 1$ represents a potential indication for a porous treatment design that efficiently dampens the turbulent-velocity fluctuations while maintaining the integrity of the wing profile. Indeed, preserving the mean-flow field around the airfoil can be beneficial for limiting the possible degradation in the aerodynamic performance caused by the porous surface. The present theory is therefore suitable for modeling such a configuration and provides a simple method to predict the turbulent-velocity field in the stagnation region of a porous wing profile that could be employed for the pre-design of permeable leading-edge inserts as passive noise-mitigation treatments.

REFERENCES

[1] R. Zamponi, S. Moreau, and C. Schram, *Rapid distortion theory of turbulent flow around a porous cylinder,* Journal of Fluid Mechanics **915**, A27 (2021).

[2] J. C. R. Hunt, *A theory of turbulent flow round two-dimensional bluff bodies,* Journal of Fluid Mechanics **61**, 625 (1973).

[3] P. F. Mish and W. J. Devenport, *An experimental investigation of unsteady surface pressure on an airfoil in turbulence—Part 2: Sources and prediction of mean loading effects,* Journal of Sound and Vibration **296**, 447 (2006).

[4] R. K. Amiet, *Acoustic radiation from an airfoil in a turbulent stream,* Journal of Sound and Vibration **41**, 407 (1975).

[5] R. F. Miotto, W. R. Wolf, and L. D. de Santana, *Numerical computation of aeroacoustic transfer functions for realistic airfoils,* Journal of Sound and Vibration **407**, 253 (2017).

[6] S. Moreau and M. Roger, *Effect of Angle of Attack and Airfoil Shape on Turbulence-Interaction Noise,* in *11th AIAA/CEAS Aeroacoustics Conference* (American Institute of Aeronautics and Astronautics, Monterey, California, 2005).

[7] J. Christophe, *Application of Hybrid Methods to High Frequency Aeroacoustics*, Ph.D. thesis, Université Libre de Bruxelles (2011).

[8] L. D. de Santana, *Semi-analytical methodologies for airfoil noise prediction*, Ph.D. thesis, KU Leuven (2015).

[9] L. D. de Santana, J. Christophe, C. Schram, and W. Desmet, *A Rapid Distortion Theory modified turbulence spectra for semi-analytical airfoil noise prediction,* Journal of Sound and Vibration **383**, 349 (2016).

[10] R. F. Miotto, W. R. Wolf, and L. D. de Santana, *Leading-Edge Noise Prediction of General Airfoil Profiles with Spanwise-Varying Inflow Conditions,* AIAA Journal **56**, 1711 (2018).

[11] C. Darwin, *Note on hydrodynamics,* Mathematical Proceedings of the Cambridge Philosophical Society **49**, 342 (1953).

[12] H. Power, G. Miranda, and V. Villamizar, *Integral-equation solution of potential flow past a porous body of arbitrary shape,* Journal of Fluid Mechanics **149**, 59 (1984).

[13] A. Kisil and L. J. Ayton, *Aerodynamic noise from rigid trailing edges with finite porous extensions,* Journal of Fluid Mechanics **836**, 117 (2018).

[14] J. Bear, *Dynamics of Fluids in Porous Media* (Dover Publications, 1972).

[15] R. E. Britter, J. C. R. Hunt, and J. C. Mumford, *The distortion of turbulence by a circular cylinder,* Journal of Fluid Mechanics **92**, 269 (1979).

[16] R. Jackson, J. M. R. Graham, and D. J. Maull, *The Lift on a Wing in a Turbulent Flow,* Aeronautical Quarterly **24**, 155 (1973).

[17] P. W. Bearman, *Some measurements of the distortion of turbulence approaching a two-dimensional bluff body,* Journal of Fluid Mechanics **53**, 451 (1972).

[18] G. K. Batchelor and I. Proudman, *The effect of rapid distortion of a fluid in turbulent motion,* The Quarterly Journal of Mechanics and Applied Mathematics **7**, 83 (1954).

7

CONCLUSIONS AND PERSPECTIVES

Life is like riding a bicycle.
To keep your balance you must keep moving.

Albert Einstein

7.1. OVERVIEW AND DISCUSSION

An extensive study on airfoil-turbulence interaction noise reduction by means of porosity is carried out in this research project. The main conclusions are summarized according to the three research objectives stated in Chapter 1 in order to estimate to what extent these have been achieved.

1. **Perform detailed experiments to characterize the alterations in the distortion of turbulence interacting with the airfoil due to porosity and the corresponding noise attenuation**

   An innovative design for the manufacturing of a porous NACA-0024 profile integrated with melamine foam is proposed to experimentally investigate the turbulence-interaction noise reduction achievable with this technology. The porous parameters defining the foam and its sound-absorbing behavior are estimated by means of impedance tube measurements (see Chapter 3). The airfoils are tested in a rod-airfoil configuration at rod-based Reynolds numbers of $Re_d = 2.7 \times 10^4$, $Re_d = 4.1 \times 10^4$, and $Re_d = 5.4 \times 10^4$.

   The far-field acoustic measurements results (see Chapter 4) show that the presence of porosity in the wing-profile structure is effective in mitigating noise up to 2 dB for $0.18 < St < 1$, particularly in correspondence with the vortex-shedding frequency peak, but at the same time leads to pronounced noise regeneration at higher frequencies. The flow field around the airfoils is subsequently investigated

in order to study the origin of the noise reduction (see Chapter 5). The main effect of the porous treatment is found to be the damping of the variation of velocity fluctuations from their upstream, undistorted values. In particular, the increase in the r.m.s. of the upwash velocity fluctuations experienced by the solid airfoil in the immediate vicinity of the leading edge is notably attenuated in the porous case, resulting in a decrease of the TKE in the stagnation region. Porosity has an influence on the turbulent-velocity PSDs mainly at low frequencies on the large-scale structures. In addition, the vortex-shedding frequency peak in the PSDs of the streamwise velocity fluctuations close to the airfoil surface is found to be suppressed due to the porous treatment.

In view of the above, it can be concluded that the flow penetration through the pores of the melamine foam in the porous airfoil softens the distortion of the large turbulent eddies caused by the presence of the body. This may play a role in the corresponding leading-edge noise reduction, as supported by the results of the acoustic measurements that indicate that the most appreciable noise attenuation is achieved in correspondence with the vortex-shedding frequency peak. This hypothesis for explaining the role of porosity in the turbulence-interaction noise mitigation has been already formed in the past, but, to the author's knowledge, no experimental evidence of it has ever been provided for a relatively thick airfoil.

2. **Implement an accurate and robust acoustic beamforming technique for the localization and quantification of the noise sources generated by the impingement of a turbulent flow on a wing profile**

An innovative implementation of the GIBF algorithm is proposed (see Chapter 4). The method is based on an automated procedure for the determination of the regularization parameters involved in the $\mathscr{L}^1$ norm minimization problem. This strategy constitutes an original contribution to the scientific community.

The performance of the technique is investigated through the processing of experimental benchmark datasets that are relevant for aeroacoustic applications (see Chapter 4). In particular, the capability of the method to correctly reconstruct and quantify distributed sound sources is evaluated by means of trailing-edge noise measurements conducted on a wing profile immersed in a clean flow. In this case, GIBF is compared with other advanced beamforming techniques, showing improvements in the localization of the distributed noise sources and comparable trends in the corresponding integrated noise spectra. The accuracy and variability of the algorithm are assessed by analyzing the broadband signal emitted by one speaker at different SNRs with respect to the background noise and incoherent broadband signals emitted by two closely–located speakers at different relative volumes. The results indicate that GIBF is able to successfully retrieve the sound-pressure level of the synthetic signals with errors generally below 0.7 dB even in the most challenging conditions, i.e. in the case of a negative SNR or below the Rayleigh resolution limit frequency. Furthermore, the algorithm achieves high performance in terms of repeatability, with standard deviations of the integrated spectra over 10 acquisitions comparable with those of the microphones of the array. This study validates the algorithm implementation and makes GIBF a suit-

able post-processing technique for the evaluation of airfoil turbulence-interaction noise and other relevant aeroacoustic applications.

3. **Develop an analytical model based on the RDT to predict the turbulent flow around a porous bluff body and apply it to interpret the experimental results of the turbulence distortion in the vicinity of the airfoil**

   A theoretical RDT-based model for the calculation of the homogeneous isotropic turbulent flow around a porous cylinder with a constant static permeability is proposed (see Chapter 6). The algorithm's implementation is successfully validated by comparing the results computed for a solid cylinder with published velocity measurements. Three ratios of the turbulence streamwise integral length scale L_x to the cylinder radius a are investigated under the condition $L_x/a > 1$.

   Results show that the presence of the porous surface affects the incoming turbulence distortion near the stagnation point by reducing the blocking effect of the body. This yields an attenuation of the transfer of energy from the streamwise to the upwash components at low normalized frequencies. Moreover, the mean flow around the cylinder is altered by porosity, resulting in the deformation of the vorticity field that leads to an amplification in the one-dimensional spectra of the upwash velocity component at high normalized frequencies. The impact of porosity increases with its static permeability, leading to a stronger low-frequency attenuation and a more significant high-frequency deviation. Furthermore, the turbulence-distortion mechanisms are strongly dependent on the considered turbulence scale and this influences the evolution of the fluctuating-velocity components in the stagnation region. For $L_x \gg a$, the attenuated blockage effect of the body dominates over the vorticity deformation, whereas for $L_x \approx a$ the two effects approximately compensate each other.

   The porous RDT model is subsequently adapted to predict the turbulence distortion in the vicinity of the porous NACA-0024 airfoil installed in the rod-airfoil configuration. The RDT computations show satisfactory relative agreement with the velocity measurements, suggesting that the frequency range at which the porosity has an impact on the velocity fluctuations may be considered independent of the homogeneity and isotropy of the incoming turbulence. According to the calculations, the presence of the exoskeleton can reduce the alterations in vorticity distortion caused by the mean flow and the consequent high-frequency deviation in the one-dimensional spectra, resulting in more efficient damping of the turbulent-velocity variation in the stagnation region.

   In conclusion, the model proposed in this work represents an original contribution that adapts the theoretical framework first developed by Hunt in order to account for a porous bluff body. It provides a deeper understanding of the physical mechanisms involved in the turbulence-interaction noise reduction by means of porosity and represents a potential pre-design tool for the development of innovative noise-mitigation techniques. In addition, it constitutes a possible basis for the formulation of novel semi-analytical methods for the prediction of the leading-edge noise produced by porous wing profiles. The latter possibility would certainly provide a contribution that the aeroacoustic community can benefit from.

7.2. OPEN QUESTIONS AND FUTURE WORK

This section aims to present some recommendations for future works following the main results of the thesis.

- The localization and quantification of the leading-edge noise sources by means of the GIBF algorithm could be further improved by designing a three-dimensional scanning grid situated on the surface of the airfoil and by considering a dipole-like sound propagation model for the Green's function.

- An extensive experimental investigation of the flow-field alterations caused by porosity is described in the manuscript for a thick NACA-0024 profile installed in a rod-airfoil configuration. New interesting insights would possibly be gained if the experiments would include a thinner airfoil or different upstream turbulent-flow conditions, i.e employing a turbulence grid. The latter modification would also allow for a more quantitative comparison with the porous RDT calculations.

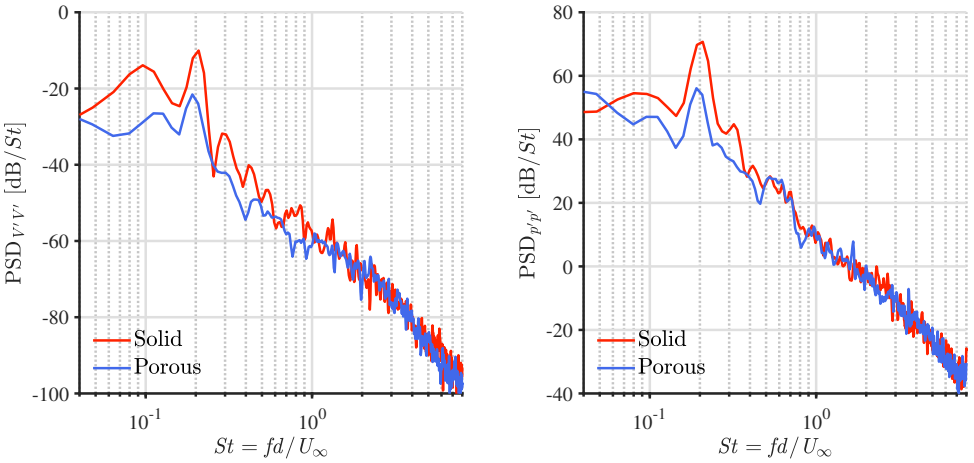

Figure 7.1: PSD of the wall-normal turbulent velocity (on the left) and wall-pressure fluctuations (on the right) for the solid (solid red lines) and porous case (dashed blue lines) extracted by the LES at $x/r_{LE} = 0.34$ and $y/r_{LE} = 0.79$. The reference is $1\,\mathrm{m^2\,s^{-1}}$ for the velocity spectra and $1\,\mathrm{Pa^2\,s^{-1}}$ for the pressure spectra.

- The connection between the attenuated turbulence distortion and the reduced noise achieved by the porous treatment has still to be clarified and verified. This objective could be pursued by comparing the pressure fluctuations on the surface of the solid and porous airfoils from numerical simulations. Preliminary results from the LES data processed in the thesis suggest that porosity induces mitigation in the PSD of the wall-pressure fluctuations p' in a frequency range similar to the reduction occurring in the PSD of the wall-normal turbulent velocity V' evaluated near the surface. This correspondence appears to confirm the above-mentioned link. An example of the present trend is illustrated in Figure 7.1. Furthermore, such an approach would make it possible to evaluate the monopole-like and dipole-like sources related to the transpiration velocity and Reynolds stresses at the porous

body surface following Curle's analogy. To the author's knowledge, no studies involving this kind of investigation are reported in the literature.

- The porous RDT model proposed in this thesis can be refined by imposing a proper impedance boundary condition for the turbulent stream function in order to relax the assumption of a negligible vortical velocity component at the surface. Moreover, the implementation of a more accurate procedure for describing the porous medium, e.g. based on the JCAL model, would be beneficial for a comparison with the experiments. At the moment, the only parameter involved in the definition of the properties of the material is the static air-flow resistivity, which plays the most important role in the noise-mitigation performance achievable with the treatment but is not sufficient to fully characterize the porous medium. Finally, the theory is formulated for homogeneous isotropic turbulence. The RDT has already been extended in literature for taking into account different inflow turbulence. Such an extension could be applied also to the present case.

- The RDT calculations performed in this study for a circular cylinder need to be validated. There is therefore a strong need for detailed velocity measurements of the distortion experienced by turbulence in the interaction with a porous bluff body. The ideal experimental campaign would feature PIV measurements of a grid-generated turbulent flow around a cylinder characterized by constant static air-flow resistivity. This would make it possible to perform a quantitative comparison between RDT calculations and experiments.

- The porous RDT model should be implemented in Amiet's theory to explore the possibility of predicting the reduction in airfoil-turbulence interaction noise due to porosity. The use of a new (or existing) experimental dataset featuring far-field acoustic measurements of solid and porous wing profiles impinged by homogeneous isotropic turbulence would be also required for validation purposes.

A

APPENDIX A - INSTRUMENTATION OF JAFAR FACILITY

This appendix presents the experimental setup designed for the flow-velocity measurements that are performed in the VKI JAFAR facility by means of hot-wire anemometry.

A.1. FLOW-VELOCITY DETERMINATION PROCEDURE

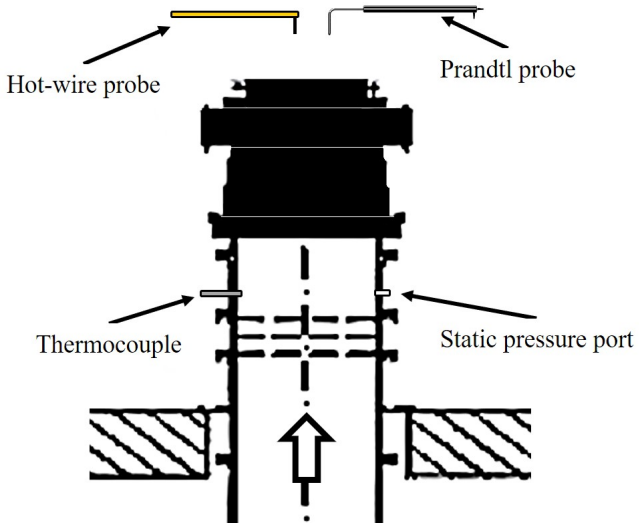

Figure A.1: Experimental setup installed in the JAFAR facility for the determination of the flow velocity and calibration of the hot-wire anemometry methodology. The direction of the flow is denoted by the arrow.

Figure A.1 illustrates the experimental apparatus that equips the wind tunnel in the JAFAR facility. A pressure port and Type E (NiCr - CuNi) thermocouple are installed in

the inner surface of the jet to measure the static wall-pressure P_s and flow temperature T, respectively. The port is connected to the positive terminal of a Validyne DP15 differential pressure transducer, the negative terminal measuring the atmospheric pressure. The transducer is calibrated by means of a Betz-type water manometer, while the thermocouple is calibrated in an oil bath.

For a preliminary estimation of the wind-tunnel mean-flow velocity, a Prandtl probe is located in the potential core of the jet. The total-pressure and static-pressure ports of the probe communicate with the positive and negative terminals of a second Validyne *DP15* differential pressure transducer, respectively, making it possible to directly measure the dynamic pressure P_d of the flow and, thereby, the flow speed according to the relation $U_\infty = (2P_d/\rho_0)^{0.5}$. The two Validyne transducers and thermocouple are connected to the same NI *cDAQ 9234* card employed for the hot-wire anemometry measurements (see Chapter 3.5.1). In this way, the simultaneous acquisition of the different parameters characterizing the flow field as well as the flow velocity can be performed. Figure A.2 shows the time signals of the gauge static-pressure and temperature of the flow over a period of 20 min from the instant in which the flow reaches the nominal dynamic pressure. Interestingly, the temperature signal features a significant variation over the time period, with a sudden initial reduction up to approximately 16° and a more gradual increase afterward. This trend can be explained by the difference in temperature existing between the tank where the pressurized air is stored and the anechoic chamber. Indeed, the thermocouple is initially cooled down by the colder air that flows through the wind tunnel. Subsequently, the flow temperature starts gradually increasing until the thermal balance in the chamber is restored.

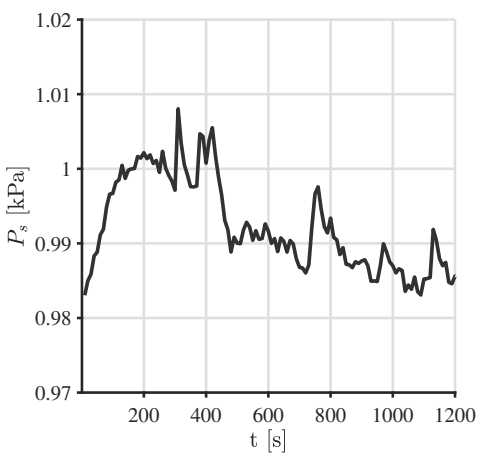

(a) Flow static gauge pressure.

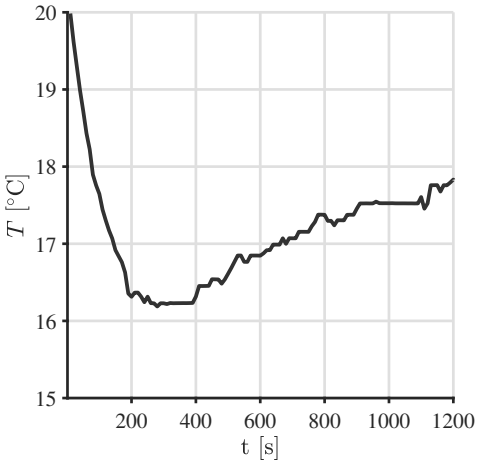

(b) Flow temperature.

Figure A.2: Simultaneous time signals recorded by the transducers installed in the inner surface of the wind tunnel. $t = 0$ s corresponds to the instant in which the flow reaches the desired dynamic pressure.

When the hot-wire L-shaped probe in the traverse system described in Chapter 3.5.1 is employed for the qualification of the nozzle flow, a different procedure for the determination of the mean-flow speed has to be considered. Indeed, the Prandtl probe con-

stitutes an intrusive measurement technique that interferes with the automatic movement of the anemometer. One possible way to tackle this problem is to calibrate the static pressure signal in the jet with the dynamic pressure signal of the Prandtl probe for different mean-flow velocities. The calibration of the facility is performed daily during the in-situ calibration of the hot-wire probe using an ad-hoc routine implemented in the commercial software LabVIEW by NI. The relation between the two pressures is expected to be linear, i.e. a first-order polynomial curve is used to fit the data points. An example of the present procedure is reported in Figure A.3a, while the resulting mean-flow velocity is depicted in Figure A.3b. As expected, the trend of the velocity matches with that of the static pressure in Figure A.2a and exhibits a mean value close to the desired flow speed $U_\infty = 30\,\mathrm{m\,s^{-1}}$, standard deviation of $\sigma = 0.08\,\mathrm{m\,s^{-1}}$, and maximum deviation of $\pm 1.4\,\%$. The same calibration procedure is adopted also to estimate and monitor the mean-flow velocity during the measurements with rod and airfoil.

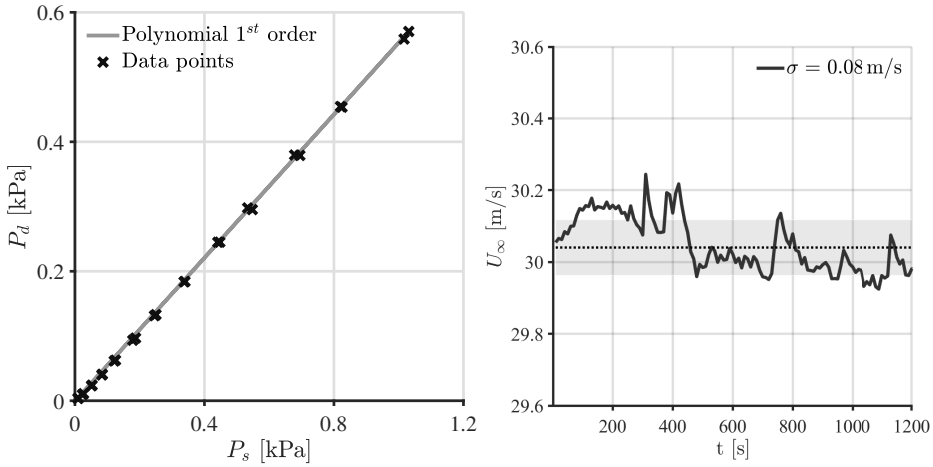

(a) Calibration curve between static pressure P_s in the internal wall of the jet and dynamic pressure P_d of the Prandtl probe.

(b) Time signal of the mean-flow velocity measurement. The dashed line indicates the time average of the velocity, while the gray area is determined by its standard deviation σ.

Figure A.3: Calibration procedure for the estimation of the mean flow velocity.

A.2. HOT-WIRE CALIBRATION AND TEMPERATURE EFFECT

The in-situ static calibration of the hot-wire probe is performed by comparing the acquired hot-wire Wheatstone bridge imbalanced voltage E_w with the velocity measured by the Prandtl probe for different flow speeds. The data are then fitted using a third-order polynomial curve by a routine implemented in LabVIEW.

One important aspect that requires attention during the calibration procedure to avoid inconsistent results on flow-velocity measurements is the temperature-drift effect. As seen in Figure A.2b, the air flow is subjected to a significant temperature variation that can have a substantial effect on E_w. This motivates the use of a temperature compensation model like that proposed by Bruun [1], which consists of defining a reference

temperature at which the imbalanced voltage measured by the anemometer has to be referred to. The model is given by the equation

$$E_{w,\mathrm{ref}} = E_w \left(\frac{T_w - T_{a,\mathrm{ref}}}{T_w - T_a} \right)^{0.5}, \tag{A.1}$$

where $E_{w,\mathrm{ref}}$ is the reference voltage, T_w is the temperature of the wire, T_a is the flow temperature, and $T_{a,\mathrm{ref}}$ is the ambient reference temperature, whose choice is arbitrary. In the experimental campaigns performed in this work, $T_{a,\mathrm{ref}}$ is determined as the average value of the flow temperatures acquired during the static calibration procedure. A possible way to estimate T_w is to measure the imbalanced voltages $E_{w,1}$ and $E_{w,2}$ corresponding to one flow speed at two different flow temperatures $T_{a,1}$ and $T_{a,2}$. It then follows from Equation (A.1) that [1]

$$T_w = \frac{E_{w,1}^2 T_{a,2} - E_{w,2}^2 T_{a,1}}{E_{w,1}^2 - E_{w,2}^2}. \tag{A.2}$$

The present method delivers accurate results only if the temperature difference between $T_{a,1}$ and $T_{a,2}$ is such to have substantial variations in the imbalanced voltage acquired by the hot-wire probe. The significant temperature variations occurring in the first minutes of operation of the facility (see Figure A.2b) makes it possible to apply this technique.

A.3. HOT-WIRE STATISTICAL UNCERTAINTY

Statistical uncertainties arise from random fluctuations occurring during a measurement. These tend to average to zero when a large number of samples is considered. It is possible to estimate the statistical uncertainty on the mean velocity $\bar{U}$ measured by the hot-wire anemometer by considering a standard normal distribution as [2]

$$\bar{U} - \varepsilon_{\mathrm{CL}} \frac{\sigma_U}{\sqrt{N}} < \bar{U} < \bar{U} + \varepsilon_{\mathrm{CL}} \frac{\sigma_U}{\sqrt{N}}, \tag{A.3}$$

where σ_U is the standard deviation of the dataset, N the number of samples, and $\varepsilon_{\mathrm{CL}}$ can be chosen according to the standard distribution in order to determine the desired confidence level α_{CL}. For a $\alpha_{\mathrm{CL}} = 97.5\,\%$, $\varepsilon = 1.96$.

Conversely, the statistical uncertainty for the r.m.s. of the velocity fluctuations U' can be calculated through the Chi-square distribution as [2]

$$\sqrt{\frac{(N-1)\sigma_U^2}{\chi^2_{N-1,\alpha_{\mathrm{CL}}/2}}} < U' < \sqrt{\frac{(N-1)\sigma_U^2}{\chi^2_{N-1,1-\alpha_{\mathrm{CL}}/2}}}. \tag{A.4}$$

Equations (A.3) and (A.4) are employed to assess the random error in the qualification of the nozzle flow described in the following section and in the flow-field characterization presented in Chapter 5.

A.4. EXTENDED NOZZLE-FLOW QUALIFICATION

The flow-nozzle qualification of the wind tunnel in the JAFAR facility is performed at two different heights with reference to the coordinate system shown in Figure 3.3a, namely

at $x/d = -10.65$ (0.001 m downstream of the nozzle exit) and $x/d = -5$ (0.100 m downstream of the cylindrical rod). As already mentioned in Chapter 3.5.1, the results of the qualification are used as inputs for the LES described in [3].

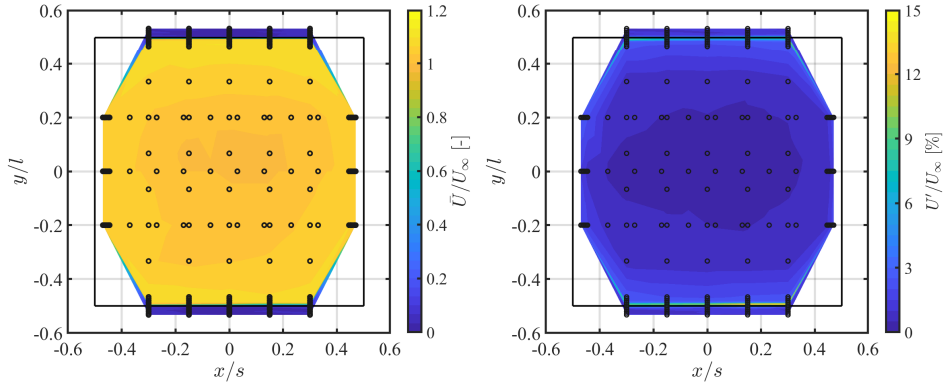

(a) Mean-velocity profile.

(b) Turbulence-intensity profile.

Figure A.4: Velocity map measured at the nozzle exit in presence of side-plates. The solid lines indicate the nozzle-exit position, while the dots denote the hot-wire measurements positions. The mean and fluctuating velocities are normalized by the free-stream velocity $U_\infty = 30\,\mathrm{m\,s^{-1}}$, while the axis by the wind-tunnel width l and span s.

The measurement-point distribution designed for the characterization covers a two-dimensional area in the yz-plane and features a higher refinement at regions where larger velocity gradients are expected, i.e. in correspondence with the shear layer of the jet. A total of 250 points are considered per each map. The measurement sequence is designed accounting for the speed of the brushless DC electric motors moving the probe with the aim of minimizing the overall acquisition time.

Figures A.4a and A.4b show the mean-velocity map and turbulence-intensity map with the hot-wire probe located at the nozzle exit, respectively. Only the side plates are installed in this configuration, which is denoted as *free-jet*. The same conclusions drawn from Figure 3.11, which has been generated by extracting the data of these maps at $x/s = 0$, can be extended also in the spanwise direction. In particular, the mean velocity is found to be uniform within most part of the nozzle-exit area, with a slight increase occurring in proximity to the outlet nozzle edges, while the turbulence intensity is generally below 0.5 % in the potential core of the jet.

The same uniformity is observed also at $x/d = -5$ in the free-jet configuration (Figure A.5). In this case, the mean-flow velocity amounts to the nominal value of U_∞ for most of the nozzle-exit area. The expansion of the flow mixing layer is indicated by a more gradual transition of the mean velocity from the potential core of the jet to the zero-velocity region. This area is characterized by an increase in turbulence intensity up to 18 %.

Finally, the presence of the rod in the configuration (Figure A.6) affects the velocity field in a region comparable to the surface swept by the cylinder, resulting in a 30 % re-

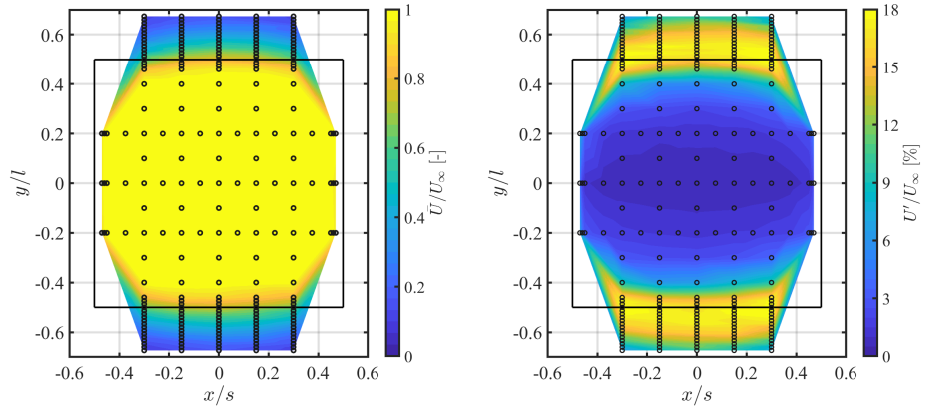

(a) Mean-velocity profile.

(b) Turbulence-intensity profile.

Figure A.5: Velocity map measured at $x/d = -5$ in presence of side-plates and in absence of the rod. The solid lines indicate the nozzle-exit position, while the dots denote the hot-wire measurements positions. The mean and fluctuating velocities are normalized by the free-stream velocity $U_\infty = 30\,\mathrm{m\,s^{-1}}$, while the axis by the wind-tunnel width l and span s.

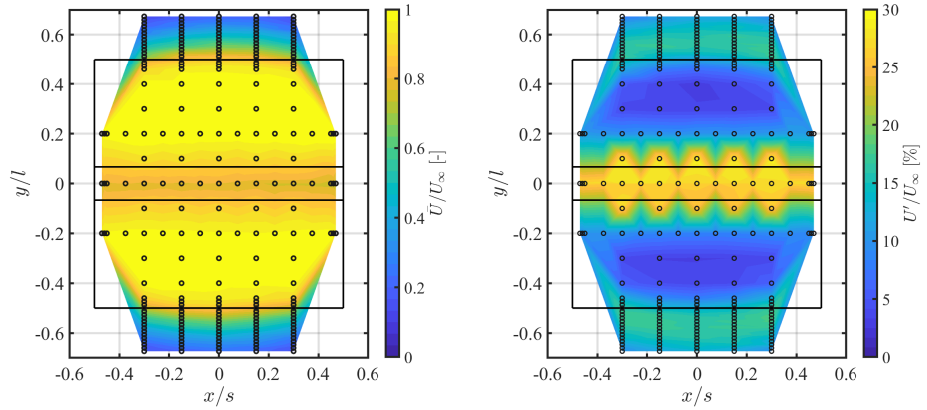

(a) Mean-velocity profile.

(b) Turbulence-intensity profile.

Figure A.6: Velocity map measured at $x/d = -5$ in presence of side-plates and rod. The solid lines indicate the nozzle-exit position and rod, while the dots denote the hot-wire measurements positions. The mean and fluctuating velocities are normalized by the free-stream velocity $U_\infty = 30\,\mathrm{m\,s^{-1}}$, corresponding to $Re_d = 4.1 \times 10^4$, while the axis by the wind-tunnel width l and span s.

duction in the mean-flow velocity and a significant increase in the turbulence intensity (up to $U'/U_\infty = 30\,\%$) due to the vortex shedding. These trends are also found in the mean-velocity and turbulence-intensity profiles along the stagnation streamline shown in Figure 5.5.

REFERENCES

[1] H. H. Bruun, *Hot-Wire Anemometry: Principles and Signal Analysis,* Measurement Science and Technology **7** (1996), 10.1088/0957-0233/7/10/024.

[2] J. S. Bendat and A. G. Piersol, *Random data: analysis and measurement procedures*, 4th ed., Wiley series in probability and statistics (Wiley, Hoboken, N.J, 2010).

[3] S. Satcunanathan, M. H. Meinke, and W. Schröder, *Prediction of Noise Mitigation by Porous Media based on a Direct-Hybrid CFD/CAA Method,* in *25th AIAA/CEAS Aeroacoustics Conference* (American Institute of Aeronautics and Astronautics, Delft, The Netherlands, 2019).

B

APPENDIX B - POROUS LINER CONFIGURATION

In this appendix, the effects of the flow on the transmission and reflection of the sound waves in the different layers of the porous NACA-0024 airfoil are investigated considering a liner configuration. The present measurements, conducted at LAUM in collaboration with T. Humbert, provide an additional test case for the calibration of the porous model implemented by Satcunanathan *et al.* [2] in their direct hybrid LES/CAA method.

B.1. EXPERIMENTAL SETUP

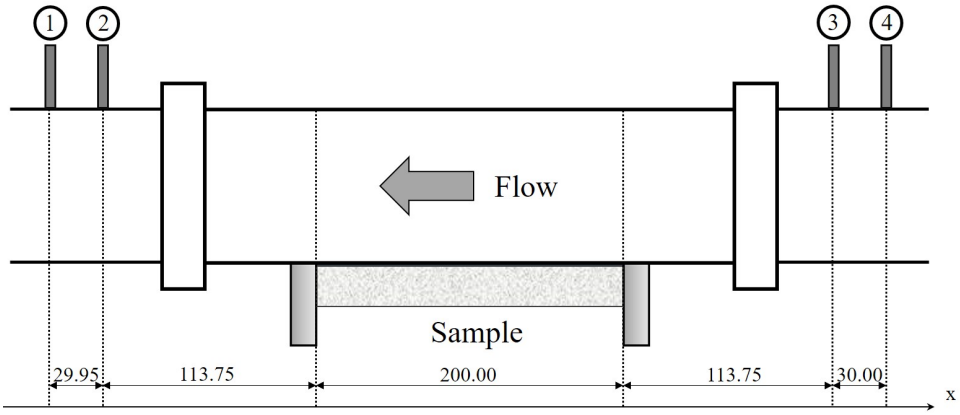

Figure B.1: Schematic of the melamine foam sample flush-mounted on the wind tunnel wall. The distances are expressed in mm.

Parts of this appendix are included in [1].

A sketch of the setup considered for the investigation is shown in Figure B.1. The melamine foam sample is cut in the form of a 0.200 m × 0.100 m rectangular plate with a thickness of 15.5 mm and flush-mounted in a metallic box, forming a liner configuration that is placed in a rectangular duct with a 0.400 m × 0.500 m cross-section [3]. The box is situated in the central part of the wind tunnel and is held in position by a series of metallic bars having the same thickness as the plate. This setup allows for the acoustic propagation of sound waves in the duct superimposed to a grazing flow over the acoustic liner. A picture of the facility is shown in Figure B.2, while further information about the wind tunnel is provided in [4].

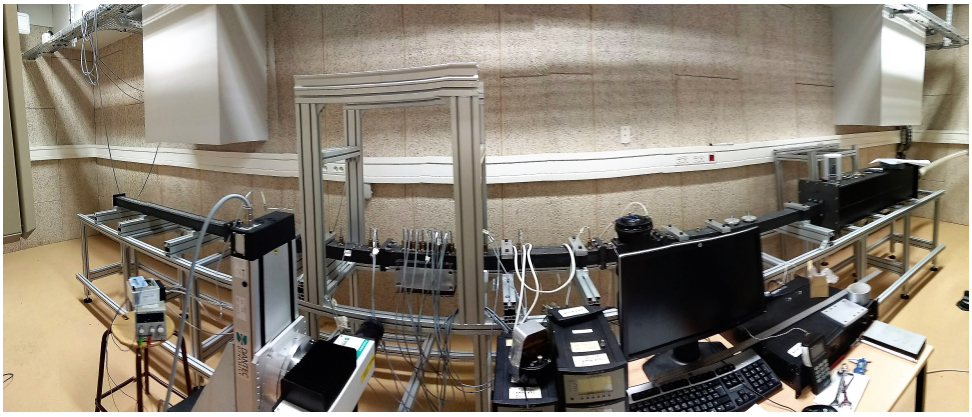

Figure B.2: Facility at LAUM for the determination of the anechoic-transmission and anechoic-reflection coefficients of the melamine foam sample installed in a liner configuration. Credits: T. Humbert.

The tunnel is equipped with anechoic terminations in order to avoid acoustic reflection. Two 1/4" *4938-A-011* pressure field Brüel & Kjær microphones are flush-mounted in the hard wall at each side of the liner test section. An acoustical source generated by two compression chambers Beyma *CP850Nd* is located upstream of the sample and emits a logarithmic-swept sine signal over the frequency range of 100 Hz–4.3 kHz with a frequency increment of 5 Hz. Its position can be modified in order to invert the direction of the sound propagation in relation to the position of the sample. The signal is acquired by means of an Agilent *VXI 1432*, which drives the excitation of the sound source synchronously with the microphone recording. The amplitude of the signal is automatically tuned to provide constant pressure, independently of the frequency, on the microphone that is situated in front of the transition between duct wall and porous material, i.e. on the upstream side of the liner test section when the upstream source is on (and vice versa with the downstream side).

The experimental test is conducted in the absence of flow and with a mean-flow speed of approximately $U_\infty = 30\,\mathrm{m\,s^{-1}}$. In the latter case, the flow goes from the right to the left of the tunnel. The comparison of the signals recorded by the upstream microphones with those downstream of the sample leads to the estimation of the anechoic transmission and anechoic reflection, as shown by Equation (3.10).

B.2. TRANSMISSION AND REFLECTION COEFFICIENTS

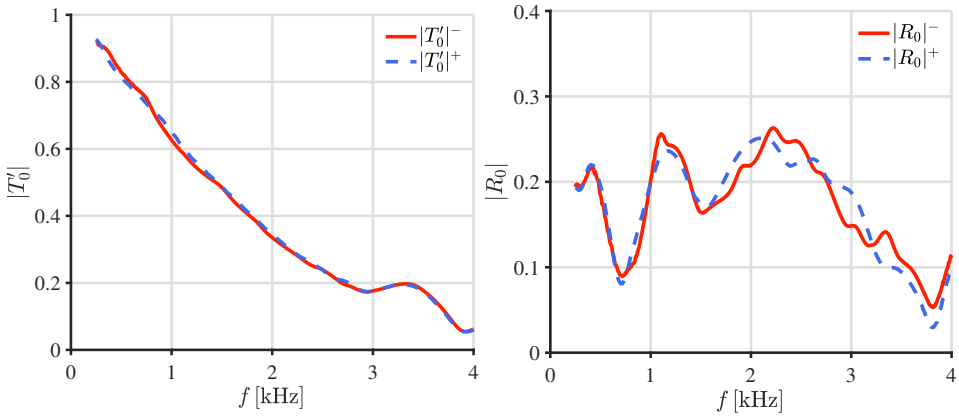

Figure B.3: Transmission and reflection coefficients for the two loudspeaker positions and for $U_\infty = 0\,\mathrm{m\,s^{-1}}$. The superscripts + and − indicate concordance and discordance with the direction of the flow, respectively.

In Figures B.3 and B.4, the absolute values of the anechoic transmission and reflection coefficients over the frequency for the two different positions of the acoustical source and for the two flow velocities are shown. In the present configuration, the incoming plane acoustic waves are diffracted at the edge of the sample and can penetrate the porous medium, in which they get attenuated. In addition, waves are reflected at both ends of the box containing the porous sample, where a standing wave can form. For $U_\infty = 0\,\mathrm{m\,s^{-1}}$ (Figure B.3), $|T_0'|$ and $|R_0|$ are expected to match due to the reciprocity principle that exists in the absence of flow. The transmission coefficient decreases smoothly with the increasing frequency, while the reflection coefficient oscillates around $|R_0| = 0.2$ up to about $f = 3\,\mathrm{kHz}$. These oscillations are probably related to the wave reflection occurring at the end of the porous material [3]. While the trends of the transmission coefficients for the positive and negative sound waves almost coincide (the superscripts + and − refer to an incident wave in concordance and discordance with the direction of the flow, respectively), the reflection coefficients feature a more significant scattering, in general below 10 %. This may be due to the inhomogeneity of the melamine foam that slightly breaks the symmetry [3].

For $U_\infty = 30\,\mathrm{m\,s^{-1}}$ (Figure B.4), the effect of the convection of the flow is clear in the deviation between positive and negative coefficients. $|T'|$ is generally enhanced by the flow when this goes in the same direction as the sound-wave propagation of the signal emitted by the acoustical source. However, an inversion in the trend is observed for $f > 3.2\,\mathrm{kHz}$, for which $|T_{30}'|^+$ features lower values than $|T_{30}'|^-$. Similar conclusions can be drawn also for $|R_{30}|$ but in this case $|R_{30}|^+$ always exhibits higher values than $|R_{30}|^-$. A possible formulation to estimate the amplification and reduction of the reflection coefficients with respect to the case at zero-flow velocity is [3]

$$|R_{30}|^+ \approx |R_0|\frac{1+M}{1-M}; \qquad |R_{30}|^- \approx |R_0|\frac{1-M}{1+M}, \tag{B.1}$$

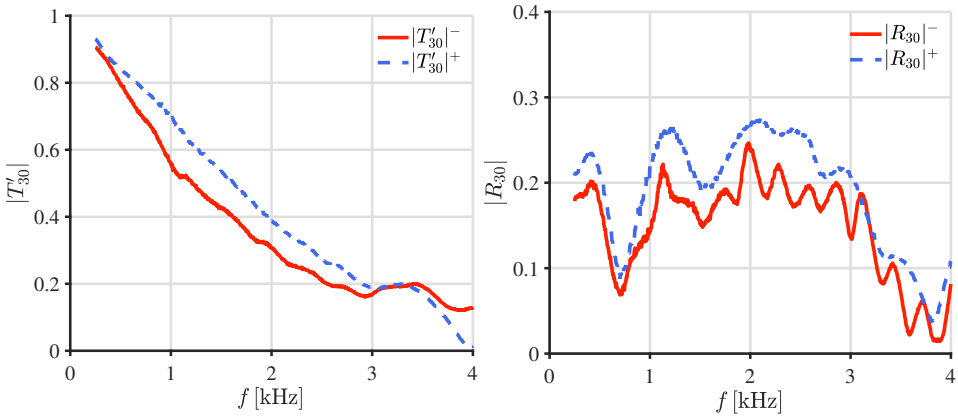

Figure B.4: Transmission and reflection coefficients for the two loudspeaker positions and for $U_\infty = 30\,\mathrm{m\,s^{-1}}$. The superscripts + and − indicate concordance and discordance with the direction of the flow, respectively.

where M is the Mach number. The application of Equation (B.1) in the present case yields $|R_{30}|^+ \approx 1.10|R_0|$ and $|R_{30}|^- \approx 0.84|R_0|$.

Moreover, the maximum attenuation corresponding to the minimum peak of the anechoic-transmission coefficient takes place at high frequencies, close to the cutoff frequency of the duct ($\approx 4.2\,\mathrm{kHz}$). This value is determined by the thickness of the porous layers as a consequence of the liner properties. Indeed, a drop in the anechoic transmission is expected at the frequency at which the complex impedance of the porous material reaches zero [5]. This occurs when $Z_s = -iZ_{ce}\cot(kL) = 0$, resulting in $kL = \pi/2$. Considering the definition of acoustic wavenumber, it follows that $Z_s = 0$ when $\lambda = 4L$, i.e. $|T'|$ is minimum at the frequency at which a quarter of the wavelength amounts to the sample thickness. For $L = 15.5\,\mathrm{mm}$, the present condition results in $f \approx 5.5\,\mathrm{kHz}$.

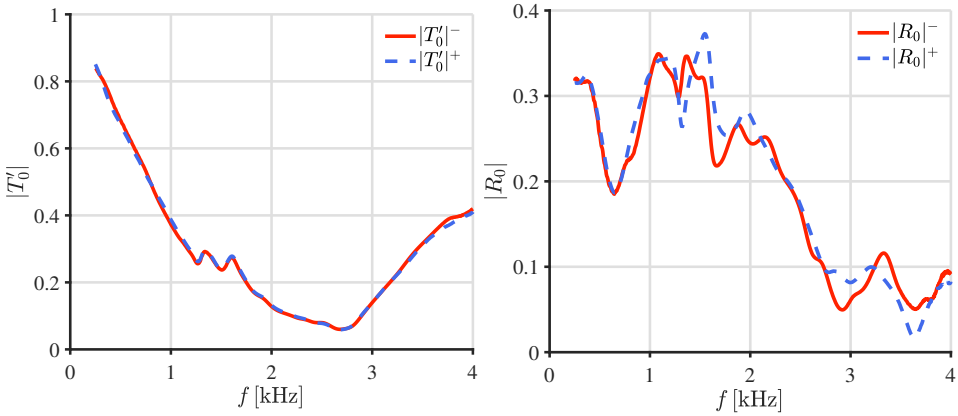

Figure B.5: Transmission and reflection coefficients for the two loudspeaker positions and for $U = 0\,\mathrm{m\,s^{-1}}$ and with the thicker porous layer. The superscripts + and − indicate concordance and discordance with the direction of the flow, respectively.

Therefore, a second test has been performed by placing an additional layer of melamine foam with a thickness of 15.5 mm on the top of the sample installed in the metallic box. In this way, the minimum in the anechoic-transmission is expected to occur at lower frequencies. The results of the measurement for $U_\infty = 0\,\mathrm{m\,s^{-1}}$ are shown in Figure B.5. In this case, the maximum attenuation occurs at about 2.7 kHz, close to the theoretical value ($f \approx 2.75\,\mathrm{kHz}$). Moreover, two peaks in the trend are visible at 1.4 kHz and 1.6 kHz. These are probably due to the resonance in the air and the porous media in the horizontal direction of the sample, whose length (0.2 m) approximately amounts to the wavelength (corresponding to $f = 1.7\,\mathrm{kHz}$). The results of the numerical simulations based on the experiments that have been presented above are discussed in [1].

REFERENCES

[1] S. Satcunathan, R. Zamponi, M. Meinke, N. Van de Wyer, C. Schram, and W. Schröder, *Validation of a model for acoustic absorption in porous media,* in *48th International Congress and Exhibition on Noise Control Engineering* (Institute of Noise Control Engineering, Madrid, Spain, 2019) pp. 4329–4344.

[2] S. Satcunanathan, M. H. Meinke, and W. Schröder, *Prediction of Noise Mitigation by Porous Media based on a Direct-Hybrid CFD/CAA Method,* in *25th AIAA/CEAS Aeroacoustics Conference* (American Institute of Aeronautics and Astronautics, Delft, The Netherlands, 2019).

[3] Y. Aurégan and D. Kumar Singh, *Experimental observation of a hydrodynamic mode in a flow duct with a porous material,* The Journal of the Acoustical Society of America **136**, 567 (2014).

[4] M. E. D'Elia, T. Humbert, and Y. Auregan, *Direct impedance eduction of liners from Laser Doppler Velocimetry measurements,* in *25th AIAA/CEAS Aeroacoustics Conference* (American Institute of Aeronautics and Astronautics, Delft, The Netherlands, 2019).

[5] Y. Aurégan and M. Leroux, *Experimental evidence of an instability over an impedance wall in a duct with flow,* Journal of Sound and Vibration **317**, 432 (2008).

C

APPENDIX C - DETERMINATION OF PIV TURBULENCE STATISTICS

This appendix illustrates the procedure followed for obtaining the mean- and turbulent-velocity fields from the PIV measurements for the different rod-based Reynolds numbers and the three airfoil configurations.

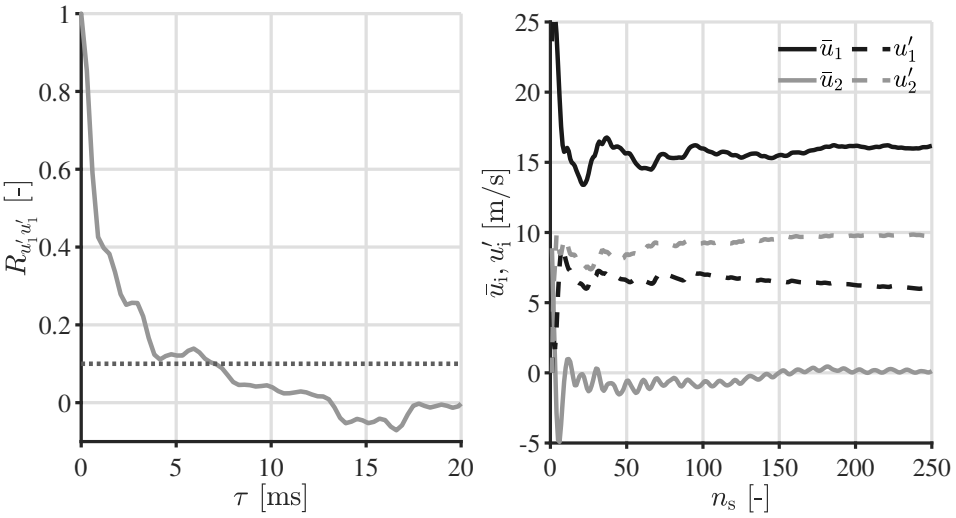

(a) Auto-correlation function of the streamwise velocity fluctuations from the PIV time signal. f_{us} is chosen as the τ at which $R_{u_1'u_1'}$ is reduced by 90%.

(b) Convergence of mean velocity and r.m.s. of the velocity fluctuations with increasing number of samples n_s within the reduced dataset.

Figure C.1: Procedure for the under-sampling of the PIV correlated dataset. The data refer to the solid airfoil at $Re_d = 4.1 \times 10^4$ and are computed at $(x/R_{LE}, y/R_{LE}) = (-4, 0)$.

Parts of this chapter are included in [1].

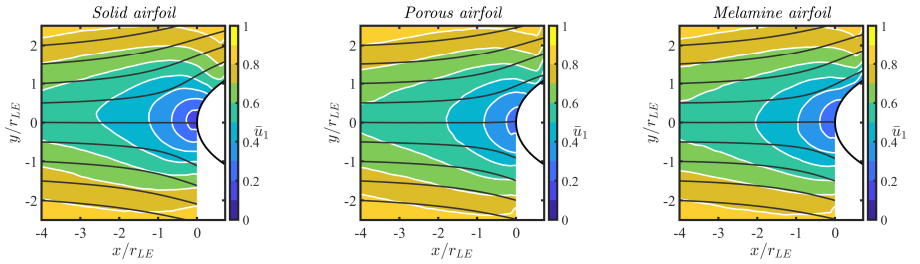

(a) Mean values of streamwise velocity component.

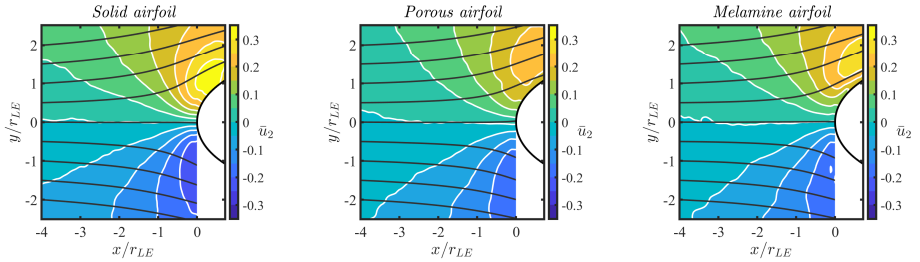

(b) Mean values of upwash velocity component.

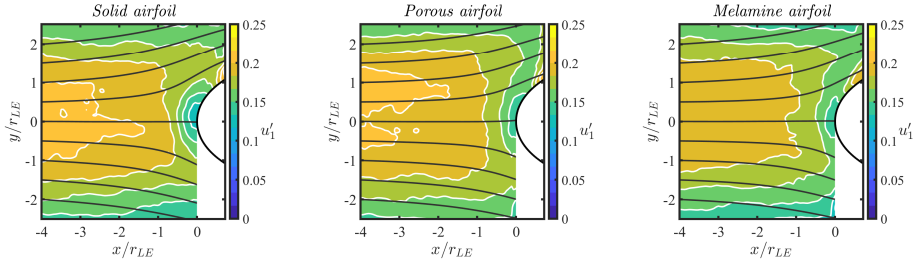

(c) Turbulence intensity of streamwise velocity component.

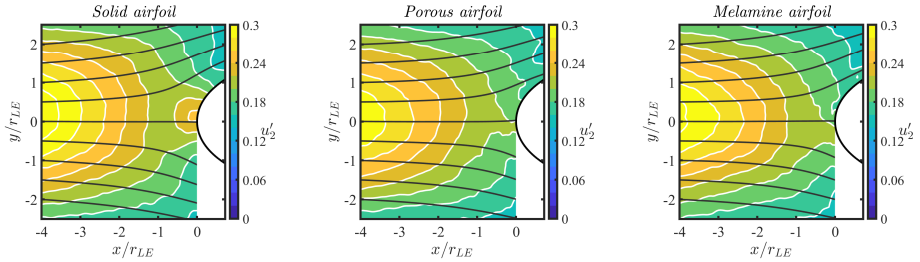

(d) Turbulence intensity velocity component.

Figure C.2: Velocity fields from PIV measurements for $Re_d = 2.7 \times 10^4$ for the three airfoil configurations. The black lines denote the mean-flow streamlines. The maps are normalized by the free-stream velocity, $U_\infty = 20\,\mathrm{m\,s^{-1}}$.

The PIV fields are computed by under-sampling the correlated dataset with a frequency $f_{\mathrm{us}} = 250\,\mathrm{Hz}$, thus leading to 250 PIV snapshots. This frequency is estimated by

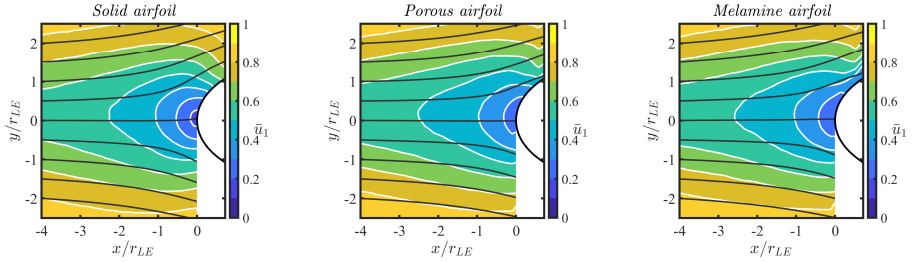

(a) Mean values of streamwise velocity component.

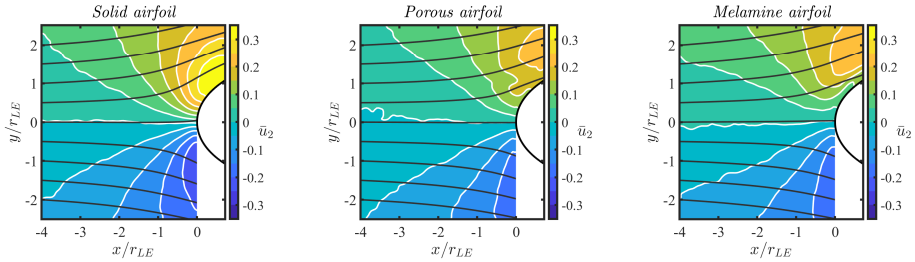

(b) Mean values of upwash velocity component.

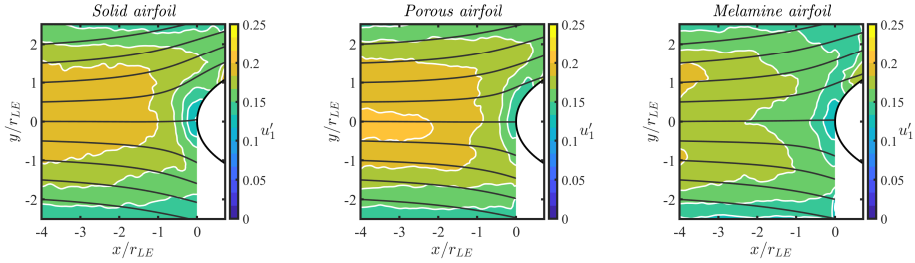

(c) Turbulence intensity of streamwise velocity component.

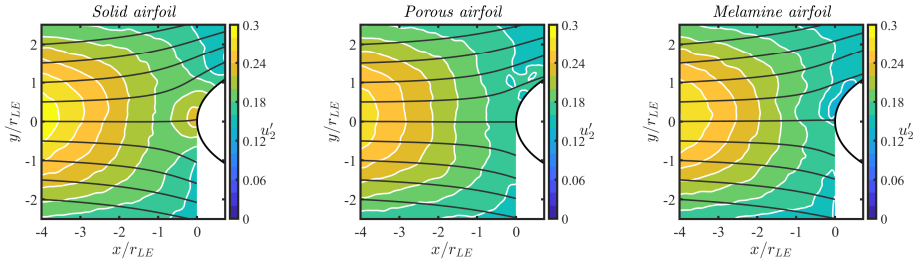

(d) Turbulence intensity velocity component.

Figure C.3: Velocity fields from PIV measurements for $Re_d = 4.1 \times 10^4$ for the three airfoil configurations. The black lines denote the mean-flow streamlines. The maps are normalized by the free-stream velocity, U_∞ = 30 m s^{-1}.

investigating the auto-correlation function of the streamwise component of the velocity fluctuations $R_{u'_1 u'_1}$, defined by Equation (5.6), at the upstream location (x/R_{LE}, y/R_{LE}) =

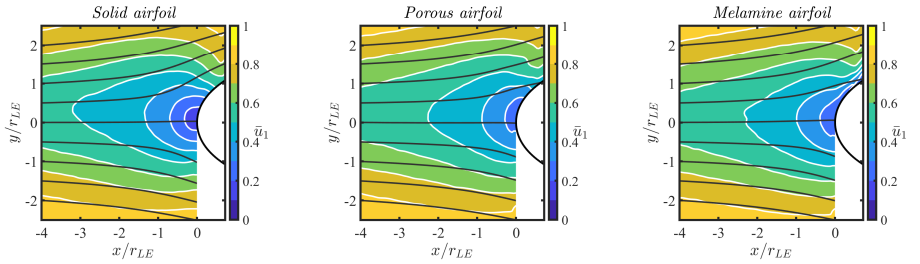

(a) Mean values of streamwise velocity component.

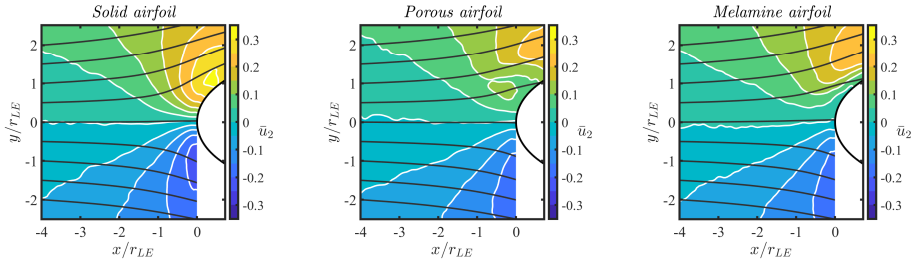

(b) Mean values of upwash velocity component.

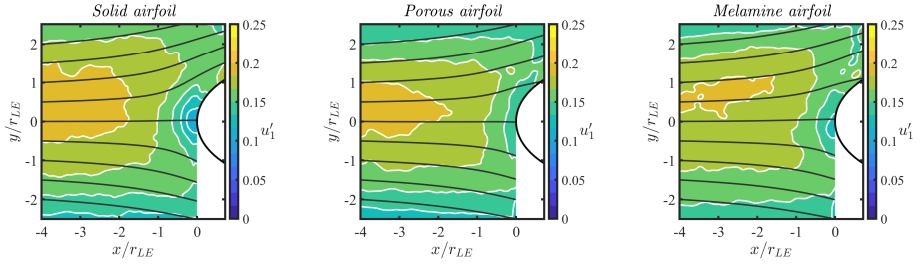

(c) Turbulence intensity of streamwise velocity component.

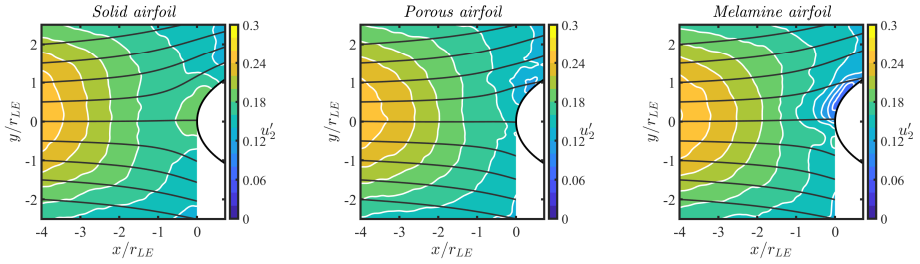

(d) Turbulence intensity velocity component.

Figure C.4: Velocity fields from PIV measurements for $Re_d = 5.4 \times 10^4$ for the three airfoil configurations. The black lines denote the mean-flow streamlines. The maps are normalized by the free-stream velocity, $U_\infty = 40\,\mathrm{m\,s^{-1}}$.

$(-4, 0)$. As can be observed in Figure C.1a, which refers to the solid airfoil configuration, $R_{u_1' u_1'}$ decreases by 90% at the time delay $\tau_{\mathrm{us}} = 4\,\mathrm{ms}$. The present threshold is chosen

to determine $f_{us} = 1/\tau_{us}$. The same procedure cannot be applied to the upwash velocity component since the presence of a strong coherent phenomenon such as the vortex shedding does not allow for convergence in the auto-correlation function. Nonetheless, 250 samples are sufficient to ensure the turbulence statistics to tend towards asymptotic values, as the mean velocities $\bar{u}_1$ and $\bar{u}_2$ and r.m.s. of the velocity fluctuations u'_1 and u'_2 computed for different numbers of samples n_s in Figure C.1b demonstrate.

The resulting velocity fields for $Re_d = 2.7 \times 10^4$, $Re_d = 4.1 \times 10^4$, and $Re_d = 5.4 \times 10^4$ are shown in Figures C.2, C.3, and C.4, respectively. The mean-flow streamlines are also reported. The extraction of the data along the stagnation streamline from the above maps provides the framework to evaluate the effect of Re_d on the flow-field alterations due to porosity, as discussed in Chapter 5.4.2.

REFERENCES

[1] S. Tamaro, R. Zamponi, D. Ragni, C. Teruna, and C. Schram, *Experimental investigation of turbulent coherent structures interacting with a porous airfoil,* Experiments in Fluids (2021), 10.1007/s00348-021-03170-2.

D

APPENDIX D - RDT DERIVATIONS

The detailed derivations for the solution of the equations presented in Chapter 6.2 are reported in this appendix. Minor differences with the original formulation of Hunt [2] for an impermeable cylinder are found and highlighted.

Turbulent-velocity potential. The first step to calculate the Fourier coefficients of $\boldsymbol{\beta}$ is to solve the integral in Equation (6.22). Defining $k_{12} = \sqrt{\kappa_1^2 + \kappa_2^2}$ and $\sigma_3 = \arctan \kappa_2/\kappa_1$, it follows that

$$\begin{pmatrix} G_1^{cn} \\ G_1^{sn} \\ G_2^{cn} \\ G_2^{sn} \\ G_3^{cn} \\ G_3^{sn} \end{pmatrix} = i^{n+1}\frac{I}{2}\left\{ \begin{pmatrix} \cos(n+1)\sigma_3 \\ \sin(n+1)\sigma_3 \\ \sin(n+1)\sigma_3 \\ \cos(n+1)\sigma_3 \\ 0 \\ 0 \end{pmatrix} \mathrm{J}_{n+1}(k_{12}) - \begin{pmatrix} \cos(n-1)\sigma_3 \\ \sin(n-1)\sigma_3 \\ -\sin(n-1)\sigma_3 \\ \cos(n-1)\sigma_3 \\ 0 \\ 0 \end{pmatrix} \mathrm{J}_{n-1}(k_{12}) \right\}, \tag{D.1}$$

J_n being the Bessel function of the first kind. In this case, the value of G_2^{sn} is found to be the opposite of that reported by Hunt [2]. The general solution for Equation (6.18) is

$$\begin{pmatrix} \beta_{\mathrm{j}}^{cn} \\ \beta_{\mathrm{j}}^{sn} \end{pmatrix}(r) = c_1 \mathrm{I}_n(|r\kappa_3|) + c_2 \mathrm{K}_n(|r\kappa_3|), \tag{D.2}$$

where c_1 and c_2 are constants of integration determined by the application of the boundary conditions and I_n and K_n are the modified Bessel function of the first and second kind, respectively. From Equation (6.23), it follows that $c_1 = 0$ since I_n grows exponentially with the increasing argument. Considering the identities

$$\begin{aligned} \frac{\partial}{\partial r}\mathrm{K}_n(|r\kappa_3|) &= -\kappa_3 \mathrm{K}_{n-1}(|r\kappa_3|) - \frac{n}{r}\mathrm{K}_n(|r\kappa_3|) = \frac{n}{r}\mathrm{K}_n(|r\kappa_3|) - \kappa_3 \mathrm{K}_{n+1}(|r\kappa_3|); \\ \frac{\partial}{\partial r}\mathrm{I}_n(|r\kappa_3|) &= \kappa_3 \mathrm{I}_{n-1}(|r\kappa_3|) - \frac{n}{r}\mathrm{I}_n(|r\kappa_3|) = \frac{n}{r}\mathrm{I}_n(|r\kappa_3|) + \kappa_3 \mathrm{I}_{n+1}(|r\kappa_3|), \end{aligned} \tag{D.3}$$

Parts of this chapter are included in [1].

c_2 may be determined by Equation (6.21), resulting in

$$\begin{aligned} &\textit{Solid cylinder:} \quad \begin{pmatrix} \beta_{\mathrm{j}}^{cn} \\ \beta_{\mathrm{j}}^{sn} \end{pmatrix} = \begin{pmatrix} G_{\mathrm{j}}^{cn} \\ G_{\mathrm{j}}^{sn} \end{pmatrix} \frac{\mathrm{K}_n(|r\kappa_3|)}{-\kappa_3 \mathrm{K}_{n+1}(|r\kappa_3|) + n\mathrm{K}_n(|r\kappa_3|)}; \\ &\textit{Porous cylinder:} \quad \begin{pmatrix} \beta_{\mathrm{j}}^{cn} \\ \beta_{\mathrm{j}}^{sn} \end{pmatrix} = \begin{pmatrix} G_{\mathrm{j}}^{cn} \\ G_{\mathrm{j}}^{sn} \end{pmatrix} \frac{\mathrm{K}_n(|r\kappa_3|)}{-\kappa_3 \mathrm{K}_{n+1}(|r\kappa_3|) + \left[n - K_\theta\right] \mathrm{K}_n(|r\kappa_3|)}. \end{aligned} \tag{D.4}$$

Here, the results of β_{j}^{cn} and β_{j}^{sn} for the solid cylinder differ from those of Hunt [2] by a minus sign.

Turbulent streamfunction. The solution of Equation (6.19) is calculated starting from $\alpha_{3\mathrm{j}}$. The application of the method of variation of parameters yields

$$\begin{aligned} \begin{pmatrix} \alpha_{3\mathrm{j}}^{cn} \\ \alpha_{3\mathrm{j}}^{sn} \end{pmatrix} = \mathrm{K}_n(|r\kappa_3|) \int_{r_1}^{r} \bar{r} \begin{pmatrix} \Omega_{3\mathrm{j}}^{cn} \\ \Omega_{3\mathrm{j}}^{sn} \end{pmatrix} \mathrm{I}_n(|\bar{r}\kappa_3|)\, d\bar{r} \\ + \mathrm{I}_n(|r\kappa_3) \int_{r}^{r_2} \bar{r} \begin{pmatrix} \Omega_{3\mathrm{j}}^{cn} \\ \Omega_{3\mathrm{j}}^{sn} \end{pmatrix} \mathrm{K}_n(|\bar{r}\kappa_3|)\, d\bar{r}. \end{aligned} \tag{D.5}$$

The constant of integration r_2 can be determined by the application of the boundary condition in Equation (6.25) and is equal to ∞. For numerical calculations, r_2 assumes the value of a large number R, which amounts to 10 in the present case. Conversely, the boundary conditions at the surface do not allow for the estimation of r_1. According to Hunt [2], this constant of integration can be chosen to simplify the following algebra and is set to 1. To find $\alpha_{1\mathrm{j}}$ and $\alpha_{2\mathrm{j}}$, it is necessary to decouple the equations. If the gauge condition is satisfied at $r = 1$ and as $r \to \infty$, then Equation (6.26) is valid for every r and $\alpha_2 j$ can be found in terms of $\alpha_{1\mathrm{j}}$ and $\alpha_{3\mathrm{j}}$ for $n \geq 1$:

$$\begin{pmatrix} \alpha_{2\mathrm{j}}^{sn} \\ -\alpha_{2\mathrm{j}}^{cn} \end{pmatrix} = -\frac{1}{n} \frac{\partial}{\partial r} \left\{ r \begin{pmatrix} \alpha_{1\mathrm{j}}^{cn} \\ \alpha_{1\mathrm{j}}^{sn} \end{pmatrix} \right\} - \frac{i\kappa_3 r}{n} \begin{pmatrix} \alpha_{3\mathrm{j}}^{cn} \\ \alpha_{3\mathrm{j}}^{sn} \end{pmatrix}. \tag{D.6}$$

Equation (D.6) can now be substituted into Equation (6.19) to yield

$$\left\{ \frac{\partial^2}{\partial r^2} + \frac{3}{r} \frac{\partial}{\partial r} - \left(\frac{n^2 - 1}{r^2} + \kappa_3^2 \right) \right\} \begin{pmatrix} \alpha_{1\mathrm{j}}^{cn} \\ \alpha_{1\mathrm{j}}^{sn} \end{pmatrix} = - \begin{pmatrix} F_{1\mathrm{j}}^{cn} \\ F_{1\mathrm{j}}^{sn} \end{pmatrix}, \tag{D.7}$$

where

$$\begin{pmatrix} F_{1\mathrm{j}}^{cn} \\ F_{1\mathrm{j}}^{sn} \end{pmatrix} = \begin{pmatrix} \Omega_{1\mathrm{j}}^{cn} \\ \Omega_{1\mathrm{j}}^{sn} \end{pmatrix} + \frac{2i\kappa_3}{r} \begin{pmatrix} \alpha_{3\mathrm{j}}^{cn} \\ \alpha_{3\mathrm{j}}^{sn} \end{pmatrix}. \tag{D.8}$$

When $n = 0$, it follows from Equation (6.26) that

$$\begin{aligned} \left\{ \frac{\partial^2}{\partial r^2} + \frac{1}{r} \frac{\partial}{\partial r} - \left(\frac{1}{r^2} + \kappa_3^2 \right) \right\} \alpha_{1\mathrm{j}}^{c0} = -\Omega_{1\mathrm{j}}^{c0}; \\ \left\{ \frac{\partial^2}{\partial r^2} + \frac{1}{r} \frac{\partial}{\partial r} - \left(\frac{1}{r^2} + \kappa_3^2 \right) \right\} \alpha_{2\mathrm{j}}^{c0} = -\Omega_{2\mathrm{j}}^{c0}. \end{aligned} \tag{D.9}$$

The general solutions of Equation (D.9) are

$$\begin{aligned}\alpha_{1j}^{c0} &= \mathrm{K}_1(|r\kappa_3|)\left[C_{1j}^{c0} + \int_1^r \bar{r}\Omega_{1j}^{c0}\mathrm{I}_1(|\bar{r}\kappa_3|)\,d\bar{r}\right] + \mathrm{I}_1(|r\kappa_3|)\int_r^R \bar{r}\Omega_{1j}^{c0}\mathrm{K}_1(|\bar{r}\kappa_3|)\,d\bar{r};\\ \alpha_{2j}^{c0} &= \mathrm{K}_1(|r\kappa_3|)\left\{C_{2j}^{c0} + \int_1^r \bar{r}\Omega_{2j}^{c0}\mathrm{I}_1(|\bar{r}\kappa_3|)\,d\bar{r}\right\} + \mathrm{I}_1(|r\kappa_3|)\int_r^R \bar{r}\Omega_{2j}^{c0}\mathrm{K}_1(|\bar{r}\kappa_3|)\,d\bar{r}.\end{aligned} \tag{D.10}$$

C_{1j}^{c0} has to be determined from Equation (6.26):

$$\begin{aligned}&\frac{\partial}{\partial r}\left\{\mathrm{K}_1(|\kappa_3|)C_{1j}^{c0} + \mathrm{I}_1(|\kappa_3|)\int_1^R \bar{r}\Omega_{1j}^{c0}\mathrm{K}_1(|\bar{r}\kappa_3|)\,d\bar{r}\right\} + \mathrm{K}_1(|\kappa_3|)C_{1j}^{c0}\\ &+\mathrm{I}_1(|\kappa_3|)\int_1^R \bar{r}\Omega_{1j}^{c0}\mathrm{K}_1(|\bar{r}\kappa_3|)\,d\bar{r} + i\kappa_3\left\{\mathrm{I}_0(|\kappa_3|)\int_1^R \bar{r}\Omega_{1j}^{c0}\mathrm{K}_0(|\bar{r}\kappa_3|)\,d\bar{r}\right\} = 0\end{aligned} \tag{D.11}$$

Considering the identities in Equation (D.3) and taking into account the relation [2]

$$\frac{\partial\Omega_{1j}^{c0}}{\partial r} + \frac{\Omega_{1j}^{c0}}{r} + i\kappa_3\Omega_{3j}^{c0} = 0, \tag{D.12}$$

it follows

$$\begin{aligned}&-\kappa_3\mathrm{K}_0(|\kappa_3|)C_{1j}^{c0} + \kappa_3\mathrm{I}_0(|\kappa_3|)\int_1^R \bar{r}\Omega_{1j}^{c0}\mathrm{K}_1(|\bar{r}\kappa_3|)\,d\bar{r} + \mathrm{I}_0(|\kappa_3|)\int_1^R \bar{r}\left\{i\kappa_3\Omega_{3j}^{c0}\right\}\mathrm{K}_0(|\bar{r}\kappa_3|)\,d\bar{r}\\ &= -\kappa_3\mathrm{K}_0(|\kappa_3|)C_{1j}^{c0} - \mathrm{I}_0(|\kappa_3|)\int_1^R\left\{\bar{r}\Omega_{1j}^{c0}\frac{\partial\mathrm{K}_0(|\bar{r}\kappa_3|)}{\partial r} + \bar{r}\frac{\partial\Omega_{1j}^{c0}}{\partial r}\mathrm{K}_0(|\bar{r}\kappa_3|) + \Omega_{1j}^{c0}\mathrm{K}_0(|\bar{r}\kappa_3|)\right\}d\bar{r}\\ &= -\kappa_3\mathrm{K}_0(|\kappa_3|)C_{1j}^{c0} - \mathrm{I}_0(|\kappa_3|)\Omega_{1j}^{c0}(r=1)\mathrm{K}_0(|\kappa_3|) = 0,\end{aligned} \tag{D.13}$$

resulting in

$$C_{1j}^{c0} = -\frac{\mathrm{I}_0(|\kappa_3|)\Omega_{1j}^{c0}(r=1)}{\kappa_3}. \tag{D.14}$$

Also in this case, a minus sign differentiates the present formulation from the original one.

Likewise, C_{2j}^{c0} can be derived from Equation (6.24) for $n = 0$, leading to

$$C_{2j}^{c0} = -\frac{\mathrm{I}_1(|\kappa_3|)}{\mathrm{K}_1(|\kappa_3|)}\int_1^R \bar{r}\Omega_{2j}^{c0}\mathrm{K}_1(|\bar{r}\kappa_3|)\,d\bar{r}. \tag{D.15}$$

When $n \geq 1$, the solution of Equation (D.7) is

$$\begin{aligned}\begin{pmatrix}\alpha_{1j}^{cn}\\ \alpha_{1j}^{sn}\end{pmatrix} = \frac{1}{r}\mathrm{K}_n(|r\kappa_3|)\left[\begin{pmatrix}C_{1j}^{cn}\\ C_{1j}^{sn}\end{pmatrix} + \int_1^r \bar{r}^2\begin{pmatrix}F_{1j}^{cn}\\ F_{1j}^{sn}\end{pmatrix}\mathrm{I}_n(|\bar{r}\kappa_3|)\,d\bar{r}\right]\\ +\frac{1}{r}\mathrm{I}_n(|r\kappa_3|)\int_r^R \bar{r}^2\begin{pmatrix}F_{1j}^{cn}\\ F_{1j}^{sn}\end{pmatrix}\mathrm{K}_n(|\bar{r}\kappa_3|)\,d\bar{r},\end{aligned} \tag{D.16}$$

D

while Equations (D.5) and (D.16) can be substituted into Equation (D.6) to calculate the solution for the Fourier coefficients of $\alpha_{2\mathrm{j}}$:

$$\begin{aligned}\begin{pmatrix} \alpha_{2\mathrm{j}}^{sn} \\ -\alpha_{2\mathrm{j}}^{cn} \end{pmatrix} &= -\frac{r}{n}\frac{\partial}{\partial r}\begin{pmatrix} \alpha_{1\mathrm{j}}^{cn} \\ \alpha_{1\mathrm{j}}^{sn} \end{pmatrix} - \frac{1}{n}\begin{pmatrix} \alpha_{1\mathrm{j}}^{cn} \\ \alpha_{1\mathrm{j}}^{sn} \end{pmatrix} - \frac{i\kappa_3 r}{n}\begin{pmatrix} \alpha_{3\mathrm{j}}^{cn} \\ \alpha_{3\mathrm{j}}^{sn} \end{pmatrix} \\ = -\frac{1}{nr}\Bigg\{ &- [n\mathrm{K}_n(|r\kappa_3|) + r\kappa_3\mathrm{K}_{n-1}(|r\kappa_3|)] \times \left[\begin{pmatrix} C_{1\mathrm{j}}^{cn} \\ C_{1\mathrm{j}}^{sn} \end{pmatrix} + \int_1^r \bar{r}^2 \begin{pmatrix} F_{1\mathrm{j}}^{cn} \\ F_{1\mathrm{j}}^{sn} \end{pmatrix} \mathrm{I}_n(|\bar{r}\kappa_3|)\, d\bar{r} \right] \\ &+ [r\kappa_3\mathrm{I}_{n-1}(|r\kappa_3|) - n\mathrm{I}_n(|r\kappa_3|)] \times \int_r^R \bar{r}^2 \begin{pmatrix} F_{1\mathrm{j}}^{cn} \\ F_{1\mathrm{j}}^{sn} \end{pmatrix} \mathrm{K}_n(|\bar{r}\kappa_3|)\, d\bar{r} + i\kappa_3 r^2 \begin{pmatrix} \alpha_{3\mathrm{j}}^{cn} \\ \alpha_{3\mathrm{j}}^{sn} \end{pmatrix} \Bigg\}. \end{aligned} \tag{D.17}$$

Once again, this result is equivalent to the opposite of that presented by Hunt [2].

Finally, it is possible to determine the last constants of integration $C_{1\mathrm{j}}^{cn}$ and $C_{1\mathrm{j}}^{sn}$ by substituting Equations (D.5) and (D.17) into Equation (6.24), yielding

$$\begin{pmatrix} C_{1\mathrm{j}}^{cn} \\ C_{1\mathrm{j}}^{sn} \end{pmatrix} = \frac{i\frac{\kappa_3^2+n^2}{\kappa_3}\mathrm{I}_n(|\kappa_3|)\begin{pmatrix} \Gamma_{3\mathrm{j}}^{cn} \\ \Gamma_{3\mathrm{j}}^{sn} \end{pmatrix} + [\kappa_3\mathrm{I}_{n-1}(|\kappa_3|) - n\mathrm{I}_n(|\kappa_3|)]\begin{pmatrix} \Gamma_{1\mathrm{j}}^{cn} \\ \Gamma_{1\mathrm{j}}^{sn} \end{pmatrix}}{n\mathrm{K}_n(|\kappa_3|) + \kappa_3\mathrm{K}_{n-1}(|\kappa_3|)}, \tag{D.18}$$

where

$$\begin{aligned}\begin{pmatrix} \Gamma_{3\mathrm{j}}^{cn} \\ \Gamma_{3\mathrm{j}}^{sn} \end{pmatrix} &= \int_1^R \bar{r}\begin{pmatrix} \Omega_{3\mathrm{j}}^{cn} \\ \Omega_{3\mathrm{j}}^{sn} \end{pmatrix} \mathrm{K}_n(|\bar{r}\kappa_3|)\, d\bar{r}; \\ \begin{pmatrix} \Gamma_{1\mathrm{j}}^{cn} \\ \Gamma_{1\mathrm{j}}^{sn} \end{pmatrix} &= \int_1^R \bar{r}^2 \begin{pmatrix} F_{1\mathrm{j}}^{cn} \\ F_{1\mathrm{j}}^{sn} \end{pmatrix} \mathrm{K}_n(|\bar{r}\kappa_3|)\, d\bar{r}. \end{aligned} \tag{D.19}$$

The solutions for $\boldsymbol{\beta}^{cn}$, $\boldsymbol{\beta}^{sn}$, $\boldsymbol{\alpha}^{cn}$, and $\boldsymbol{\alpha}^{sn}$ can now be used to determine $\boldsymbol{\beta}$ and $\tilde{\boldsymbol{\alpha}}$ from the Fourier series in Equation (6.17) and, thereby, $\boldsymbol{M}^{(\mathrm{s})}$ and $\boldsymbol{M}^{(\mathrm{d})}$ from Equations (2.62) and (2.63).

REFERENCES

[1] R. Zamponi, S. Moreau, and C. Schram, *Rapid distortion theory of turbulent flow around a porous cylinder,* Journal of Fluid Mechanics **915**, A27 (2021).

[2] J. C. R. Hunt, *A theory of turbulent flow round two-dimensional bluff bodies,* Journal of Fluid Mechanics **61**, 625 (1973).

ACKNOWLEDGMENTS

There are many people who helped me along the way on this journey. I want to take a moment to thank them.

First, I wish to acknowledge my promotion committee. I would like to thank my promoter Prof. Fulvio Scarano for sharing his expertise with me. Your critical feedback and stimulating questions during our meetings have considerably helped me improve my work. I also want to express my sincere gratitude to my supervisor Prof. Christophe Schram for offering me the opportunity to be part of this project. Your scientific curiosity and enthusiasm for research have been a true inspiration to me, while your insight and knowledge into the subject matter have steered me through the Ph.D. work. Special thanks go to my supervisor Dr. Daniele Ragni too for his never-ending support and constant guidance. Thank you for believing in me and trusting my abilities, I feel lucky to be a member of your team. I would like to especially thank Prof. Stéphane Moreau from UdeS for our prolific collaboration and interesting discussions. Doing research with you has been a great honor. Thanks also for welcoming me to Sherbrooke for my secondment.

VKI has been a second family to me. Without the support of my colleagues and friends, I would not have made it. Thanks to the aeroacoustic group (Julien, Nicolas, Cansev, Joachim, etc.), and in particular to my office mate and member of the *ZaZa* team Alessandro, who really deserves special praise for being able to bear with me for more than three years. I much enjoyed our talks and travels around the world, my Ph.D. would have been more difficult without our friendship. A huge and dutiful thanks to my dear friend Maria, to whom I probably owe more than a simple mention in the acknowledgments. Thank you for the precious suggestions with the presentations, the fun road trip across Europe, the help with the design of the thesis cover, and, more in general, the endless support that I know I can always rely on. To the tune of "Happy together" by The Turtles, I want to acknowledge Michele. Thank you for all the laughs, the serious discussions, the enjoyable moments, the beers, and the references to popular culture that have accompanied me during this journey. Special thanks to my amazing housemates Francisco and Simon. Our dinners and parties have certainly helped me cope with the Ph.D. workload. Thanks also to the rest of the VKI gang (Vincent, Domenico, Andrea A., Andrea F., Zoé, Iván, Florian, etc.) for making the last three years much more entertaining.

Being a part of the ITN SmartAnswer not only expanded my horizons but gave me the opportunity to meet stimulating and funny people. Thanks to all the ESRs for the scientific and social events we attended together. I will never forget our kart racing in Le Mans.

Despite the long distance, I must acknowledge the leading role that my many friends in Italy play in my life. Thanks for making me feel at home every time I come back. I greatly enjoy each moment we manage to spend together.

My deepest and sincere gratitude goes to my wonderful girlfriend Rebecca. Thanks for all the beautiful experiences we shared and the stunning memories we built in the last years. Thanks for carefully and relentlessly correcting the English of my manuscripts. Thanks for being by my side in every moment of this journey. I am forever grateful for the patience and understanding you showed to me while I was writing my dissertation. You earned this degree right along with me. *Tá grá agam duit.*

Per concludere, un ringraziamento doveroso e sentito alla mia famiglia, ai miei genitori, a mia sorella e, soprattutto, ai miei nonni. Vorrei che questo mio traguardo raggiunto, per quanto possibile, fosse un premio anche per voi e per i sacrifici che avete fatto. Grazie per esserci sempre stati.

CURRICULUM VITÆ

Riccardo ZAMPONI

10-01-1992 Born in Macerata, Italy.

EDUCATION

2011–2014 Bachelor Degree in Mechanical Engineering
Università Politecnica delle Marche (UNIVPM)
Ancona, Italy
Final mark: 110/110 with honours

2014–2017 Master of Science Degree in Mechanical Engineering
Università Politecnica delle Marche (UNIVPM)
Ancona, Italy
Final mark: 110/110 with honours and commendation

2016 Master of Science Thesis in Mechanical Engineering
von Karman Institute for Fluid Dynamics (VKI)
Sint-Genesius-Rode, Belgium
within an Erasmus scholarship
Thesis: Development of Acoustic Beamforming Techniques for Accurate Wind-tunnel Tests
Promotor: Prof. C. Schram

2017–2021 Doctor of Philosophy in Aeroacoustics,
von Karman Institute for Fluid Dynamics (VKI)
Sint-Genesius-Rode, Belgium
within Marie Skłodowska-Curie ITN "SmartAnswer"
Thesis: Investigation of turbulence-surface interaction noise mechanisms and their reduction using porous materials
Promotor: Prof. F. Scarano

List of Publications

Journal papers

9. **R. Zamponi**, S. Satcunathan, S. Moreau, D. Ragni, M. Meinke, W. Schröder, C. Schram, *Effect of porosity on the surface pressure fluctuations on an airfoil in turbulent flow*, Journal of Sound and Vibration. Manuscript in preparation.

8. O. Amoiridis, A. Zarri, **R. Zamponi**, Y. Pasco, G. Yakhina, J. Christophe, S. Moreau, C. Schram, *Sound localization and quantification analysis of an automotive engine cooling module*, Under review for the Journal of Sound and Vibration.

7. S. Tamaro, **R. Zamponi**, D. Ragni, C. Teruna, C. Schram, *Experimental investigation of turbulent coherent structures interacting with a porous airfoil*, Experiments in Fluids.

6. **R. Zamponi**, S. Moreau, C. Schram, *Rapid Distortion Theory of turbulent flow around a porous cylinder*, Journal of Fluid Mechanics **915**, A27 (2021).

5. L. Rego, D. Ragni, F. Avallone, D. Casalino, **R. Zamponi**, C. Schram, *Jet-installation noise reduction through flow-permeable materials*, Journal of Sound and Vibration **498**, 115959 (2021).

4. **R. Zamponi**, S. Satcunathan, S. Moreau, D. Ragni, M. Meinke, W. Schröder, C. Schram, *On the role of turbulence distortion on leading-edge noise reduction by means of porosity*, Journal of Sound and Vibration **485**, 115561 (2020).

3. **R. Zamponi**, P. Chiariotti, G. Battista, C. Schram, P. Castellini, *3D Generalized Inverse Beamforming in wind tunnel aeroacoustic testing: application to a Counter Rotating Open Rotor aircraft model*, Applied Acoustics **163**, 107229 (2020).

2. R. Merino-Martínez, S. Luesutthiviboon, **R. Zamponi**, A. Rubio-Carpio, D. Ragni, P. Sijtsma, M. Snellen, C. Schram, *Assessment of the accuracy of microphone array methods for aeroacoustic measurements*, Journal of Sound and Vibration **470**, 115176 (2020).

1. R. Merino- Martínez, P. Sijtsma, A. Rubio-Carpio, **R. Zamponi**, S. Luesutthiviboon, A. MN Malgoezar, M. Snellen, C. Schram, D. G Simons, *Integration methods for distributed sound sources*, International Journal of Aeroacoustics **18** (4-5), 444 (2020).

Conference papers

7. **R. Zamponi**, S. Moreau, D. Ragni, C. Schram, *Experimental and Analytical Investigation of the Distortion of Turbulence Interacting with a Porous Airfoil*, Accepted for presentation in the 27th AIAA/CEAS Aeroacoustics Conference, American Institute of Aeronautics and Astronautics, (2021).

6. O. Amoiridis, **R. Zamponi**, A. Zarri, J. Christophe, C. Schram, *Localization and characterization of rotating noise sources on axial fans by means of an irregularly shaped microphone array*, 18th ISROMAC Conference Proceedings, Virtual Event, (2020).

5. O. Amoiridis, A. Zarri, **R. Zamponi**, C. Schram, G. Yakhina, S. Moreau, *Experimental Analysis of the Sound Radiated by an Automotive Cooling Module Working at Different Operational Conditions*, 26th AIAA/CEAS Aeroacoustics Conference, American Institute of Aeronautics and Astronautics, Virtual Event, (2020).

4. S. Satcunathan, **R. Zamponi**, M. Meinke, N. Van de Wyer, C. Schram, W. Schröder, *Validation of a model for acoustic absorption in porous media*, 48th International Congress and Exhibition on Noise Control Engineering, INTER-NOISE, Madrid (ES), (2019).

3. **R. Zamponi**, D. Ragni, N. Van de Wyer, C. Schram, *Experimental Investigation of Airfoil Turbulence-Impingement Noise Reduction Using Porous Treatment*, 25th AIAA/CEAS Aeroacoustics Conference, American Institute of Aeronautics and Astronautics, Delft (NL), (2019).

2. **R. Zamponi**, N. Van de Wyer, C. Schram, *Benchmark Assessment of an Improved Regularization Technique for Generalized In-verse Beamforming*, 24th AIAA/CEAS Aeroacoustics Conference, American Institute of Aeronautics and Astronautics, Atlanta (GA), (2018).

1. **R. Zamponi**, N. Van de Wyer, C. Schram, *An Improved Regularization of the Generalized Inverse Beamforming Applied to a Benchmark Database*, 7th Berlin Beamforming Conference, BeBeC, Berlin (DE), (2018).

OTHER CONTRIBUTIONS

2. Lecture titled *Porous materials for the damping of turbulence-airfoil interaction* held during the von Karman Institute online lecture series *Advanced concepts for the reduction of flow-induced noise generation, propagation and transmission*, 23rd-26th November 2020.

1. Contribution titled *Improved Generalized Inverse Beamforming for Airframe Noise Applications* published in *Aeroacoustics research in Europe: The CEAS-ASC report on 2018 highlights*, Journal of Sound and Vibration **463**, 114950 (2019).